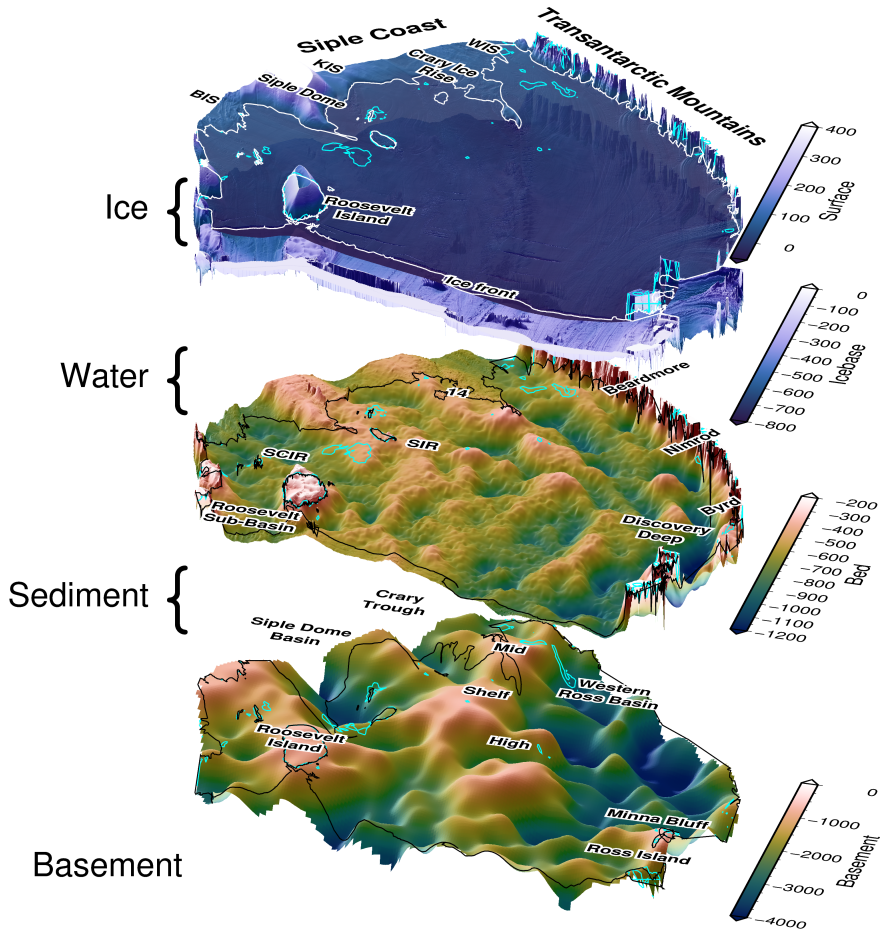


1

# Airborne Geophysical Investigation 2 beneath Antarctica's Ross Ice Shelf



3 A thesis presented for the degree of  
4 Doctor of Philosophy in Geophysics  
5

6 Matthew Tankersley



7  
8 Antarctic Research Centre  
9 Victoria University of Wellington  
10 New Zealand  
11 June 30, 2023



# <sup>12</sup> Abstract

<sup>13</sup> The Ross Ice Shelf controls the flow of ice into the ocean from catchments consisting  
<sup>14</sup> of both the East and West Antarctic Ice Sheets. These catchments hold a volume  
<sup>15</sup> of ice equivalent to  $\sim$ 12 m of global sea level rise. To adequately understand how  
<sup>16</sup> this ice will respond to a warming world requires knowledge of the properties and  
<sup>17</sup> parameters which influence how the ice sheet behaves. These boundary conditions  
<sup>18</sup> include fundamental knowledge of the Earth, such as the shape of the bed beneath  
<sup>19</sup> the ice, the seafloor, and the geologic structures of the upper crust. Knowledge of  
<sup>20</sup> the physiography and sub-surface geology is severely lacking beneath ice shelves due  
<sup>21</sup> to their inaccessibility.

<sup>22</sup> Here, we use airborne geophysical data from an extensive survey over the Ross Ice  
<sup>23</sup> Shelf to better understand these boundary conditions. From the analysis of airborne  
<sup>24</sup> magnetics data, we model the thickness of sediment, the shape of the crystalline  
<sup>25</sup> basement, and the likely locations of faults throughout the crust under the Ross Ice  
<sup>26</sup> Shelf. We find a continuous drape of sediment over the seafloor, including deep and  
<sup>27</sup> narrow fault-bound sedimentary basins beneath the Siple Coast.

<sup>28</sup> Using airborne gravity data, and distributed seismic constraints over the ice  
<sup>29</sup> shelf, we develop and implement a gravity inversion to recover a higher-resolution  
<sup>30</sup> bathymetry model beneath the ice shelf. This bathymetry model and our quantifica-  
<sup>31</sup> tion of spatial uncertainty highlight locations likely important for sub-ice shelf ocean  
<sup>32</sup> circulation and possible recent pinning points. In the process of these geophysical  
<sup>33</sup> investigations, we reveal a wide range of insights relating to how bathymetry and  
<sup>34</sup> geology play a critical role in the past, present, and future dynamics of the ice sheet,  
<sup>35</sup> and how this region has developed over its tectonic history.

## <sup>36</sup> Plain language summary

<sup>37</sup> The Ross Ice Shelf in Antarctica is a vast expanse of floating ice, hundreds of meters  
<sup>38</sup> thick, which is connected to the ice on land. It plays a crucial role in slowing down  
<sup>39</sup> the flow of ice from the Antarctic Ice Sheet into the ocean. Understanding how this  
<sup>40</sup> ice will respond to a warming world requires knowledge of the Earth's properties that  
<sup>41</sup> influence its behaviour. These properties include the depth of the seafloor beneath  
<sup>42</sup> the ice shelf, the topography beneath the ice on land, and geological features like  
<sup>43</sup> faults and rock types. However, accessing and surveying the sub-Ross Ice Shelf is  
<sup>44</sup> challenging, leading to limited knowledge.

<sup>45</sup> In this thesis, we utilized data collected during an airborne survey of the entire  
<sup>46</sup> Ross Ice Shelf to investigate the depths of the seafloor and the underlying geology.  
<sup>47</sup> By analyzing measurements of Earth's magnetic field across the ice shelf, we reveal  
<sup>48</sup> the thickness of sediment beneath the seafloor. This is possible due to variations  
<sup>49</sup> in magnetic properties between sediment and bedrock. The thickness of this layer

---

50 of sediment ranges from tens of meters to several kilometers. Additionally, we de-  
51 termine the shape of the underlying bedrock, which helps identify probable fault  
52 locations.

53 We also utilized measurements of changes in Earth's gravity field across the ice  
54 shelf to estimate the depth of the seafloor, in a process called a gravity inversion.  
55 This method is feasible since variations in the underwater topography (bathymetry)  
56 result in small, measurable changes in Earth's gravity, due to the density difference  
57 between the seafloor and the water. This bathymetry model, along with our as-  
58 sessment of uncertainties, identifies areas beneath the ice shelf that likely influence  
59 ocean currents as well as potential locations where the ice shelf was anchored to the  
60 bedrock in the recent past.

61 Through these geophysical investigations, we gained valuable insights into how  
62 features of the underlying Earth have influenced the behaviour of the overlying ice  
63 in the Ross Ice Shelf region, both historically and in the future. This information  
64 enhances our understanding of the Ross Ice Shelf region and its interaction with the  
65 underlying Earth.

# <sup>66</sup> Acknowledgements

<sup>67</sup> I would like to express my gratitude to the following individuals and organizations  
<sup>68</sup> for their invaluable support and guidance throughout this thesis.

<sup>69</sup>  
<sup>70</sup> First and foremost I would like to thank my advisors, Huw Horgan and Fabio  
<sup>71</sup> Caratori-Tontini for their unwavering support, patience, and mentorship. Huw, I  
<sup>72</sup> will always appreciate your effort to include me in the two field seasons to Antarc-  
<sup>73</sup> tica. Those trips included some of my most valued experiences, which I have you to  
<sup>74</sup> thank for. You have had an immeasurable impact on my development as a scien-  
<sup>75</sup> tist yet gave me space to pursue my own interests and styles. Fabio, through your  
<sup>76</sup> continuous encouragement and belief in my abilities you gave me the confidence to  
<sup>77</sup> explore many challenging aspects of this thesis I would have otherwise omitted.

<sup>78</sup>  
<sup>79</sup> To two of my supporting academics, Christine Siddoway and Kirsty Tinto. With-  
<sup>80</sup> out witnessing your dedication and enthusiasm for Antarctic science I would not have  
<sup>81</sup> pursued this PhD. I hope for years of collaboration to come! To the various members  
<sup>82</sup> of K863; Andrew, Jenny, Hamish, Will, Bob, and Caitlin, there couldn't have been  
<sup>83</sup> a better group to spend so much time with in the deep field. Thank you for making  
<sup>84</sup> those two trips such an incredible part of my PhD. To the open-source coding com-  
<sup>85</sup> munities, including Fatiando, PyGMT and Software Underground, especially Wei Ji  
<sup>86</sup> Leong, Santi Soler and Leo Uieda, thank you for the wonderful tools, tutorials, and  
<sup>87</sup> individual support you have offered me throughout my journey of learning to code.

<sup>88</sup>  
<sup>89</sup> To the various academics and staff on the 5th floor of the Cotton Building, thank  
<sup>90</sup> you for years of great conversations over lunch, beers, or bike rides. Thank you to  
<sup>91</sup> the friends who made living in and exploring NZ so great; Fran, Chris, Alanna,  
<sup>92</sup> Marjo, Knut, Callum, Dina, Flo. Charlotte, thank you for the unconditional sup-  
<sup>93</sup> port throughout this journey, it would not have been possible or as enjoyable without  
<sup>94</sup> you. To my family, thanks for the continuous encouragement and love from afar.  
<sup>95</sup> Knowing I always had you all to count on back home gave me the stability I needed.

<sup>96</sup>  
<sup>97</sup> Lastly, to the various funders of this research including several grants I have  
<sup>98</sup> received, thank you for the support; GNS Science, the Antarctic Research Centre  
<sup>99</sup> and Antarctica New Zealand.



# 100 Contents

<b>101 1 Introduction</b>	<b>15</b>
102    1.1 Motivation . . . . .	15
103    1.2 Influences on ice dynamics . . . . .	15
104     1.2.1 Bedrock topography . . . . .	15
105     1.2.2 Geologic structures . . . . .	18
106     1.2.3 Basal roughness . . . . .	19
107    1.3 Ross Ice Shelf . . . . .	20
108     1.3.1 Past investigations . . . . .	20
109    1.4 Research questions . . . . .	21
110    1.5 Outline . . . . .	22
111    1.6 Data and Code . . . . .	23
<b>112 2 Airborne magnetic analysis: Basement depths and sediment thickness</b>	<b>25</b>
113    2.1 Introduction . . . . .	26
114    2.2 Data and Methods . . . . .	28
115    2.3 Results . . . . .	29
116    2.4 Discussion . . . . .	31
117     2.4.1 West Antarctic Rift System extensional basins . . . . .	31
118     2.4.2 Consequences for ice sheet dynamics . . . . .	33
119     2.4.3 Mid-Shelf High - Central High . . . . .	33
120     2.4.4 Thermal subsidence and sedimentation . . . . .	34
121    2.5 Conclusions . . . . .	35
122    2.6 Open Research . . . . .	35
123    2.7 Acknowledgements . . . . .	35
<b>125 3 Gravity inversion: a tool for bathymetry modelling</b>	<b>37</b>
126    3.1 Introduction . . . . .	38
127    3.2 Methods . . . . .	40
128     3.2.1 Geophysical inversion . . . . .	40
129       3.2.1.1 Non-Linear inversions . . . . .	42
130       3.2.1.2 Geometric inversions . . . . .	42
131     3.2.2 Forward modelling . . . . .	43
132       3.2.2.1 Discretization . . . . .	43
133       3.2.2.2 Gravity edge effects . . . . .	43
134     3.2.3 Isolating anomalies . . . . .	44
135     3.2.4 Regional vs. Residual gravity . . . . .	45
136     3.2.5 Running the inversion . . . . .	46
137       3.2.5.1 Jacobian matrix . . . . .	46

138	3.2.5.2	Least-squares solver . . . . .	48
139	3.2.5.3	Regularization . . . . .	48
140	3.2.6	Stopping Criteria . . . . .	50
141	3.2.7	Software implementation . . . . .	51
142	3.3	Synthetic models . . . . .	51
143	3.3.1	Simple model . . . . .	52
144	3.3.1.1	Model setup . . . . .	52
145	3.3.1.2	Cross validation . . . . .	53
146	3.3.1.3	Comparing vertical derivative methods . . . . .	54
147	3.3.1.4	Added noise . . . . .	55
148	3.3.1.5	Down-sampled data . . . . .	56
149	3.3.2	Ensemble of Noise and Sampling values . . . . .	58
150	3.4	Adding a regional component . . . . .	60
151	3.4.1	Regional separation methods . . . . .	60
152	3.4.2	Constraint point minimization . . . . .	62
153	3.4.2.1	Tensioned minimum curvature . . . . .	63
154	3.4.2.2	Bi-harmonic splines . . . . .	63
155	3.4.2.3	Gridding comparison . . . . .	63
156	3.4.3	Inversion results . . . . .	65
157	3.4.4	Ensemble of Noise and Sampling values . . . . .	66
158	3.4.5	Simple model comparison . . . . .	66
159	3.5	Ross Sea model . . . . .	67
160	3.5.1	Observed gravity . . . . .	67
161	3.5.2	Starting bathymetry . . . . .	69
162	3.5.3	Gravity misfit . . . . .	70
163	3.5.4	Inversion . . . . .	71
164	3.5.5	Uncertainty analysis . . . . .	71
165	3.5.6	Effects of constraint spacing . . . . .	73
166	3.5.7	Effects of gravity data . . . . .	75
167	3.6	Discussion . . . . .	76
168	3.6.1	Simple synthetic model . . . . .	76
169	3.6.1.1	Inversion results . . . . .	77
170	3.6.1.2	Ensemble results . . . . .	77
171	3.6.2	Regional component . . . . .	79
172	3.6.2.1	Regional separation methods . . . . .	79
173	3.6.2.2	Constraint point minimization . . . . .	79
174	3.6.2.3	Inversion results . . . . .	80
175	3.6.2.4	Ensemble results . . . . .	80
176	3.6.3	Ross Sea model . . . . .	81
177	3.6.3.1	Effects of the gravity data . . . . .	82
178	3.6.3.2	Effects of the constraints . . . . .	83
179	3.6.3.3	Uncertainties . . . . .	84
180	3.7	Future work . . . . .	85
181	3.8	Conclusion . . . . .	85
182	<b>4</b>	<b>Ross Ice Shelf bathymetry inversion</b>	<b>89</b>
183	4.1	Introduction . . . . .	90
184	4.2	Methods . . . . .	92
185	4.2.1	Gravity reduction . . . . .	92

186	4.2.1.1	Attraction of normal Earth . . . . .	93
187	4.2.1.2	Topographic mass effects . . . . .	94
188	4.2.1.3	Regional separation . . . . .	98
189	4.2.2	Bathymetry inversion . . . . .	99
190	4.2.3	Starting bathymetry . . . . .	100
191	4.2.4	Uncertainty quantification . . . . .	100
192	4.3	Past inversions . . . . .	103
193	4.3.1	Gravity reduction comparison . . . . .	103
194	4.3.1.1	Regional separation . . . . .	105
195	4.3.2	Inversion comparison . . . . .	106
196	4.3.3	Uncertainty comparison . . . . .	107
197	4.4	Results . . . . .	107
198	4.4.1	Starting bathymetry . . . . .	107
199	4.4.2	Gravity processing results . . . . .	110
200	4.4.3	Gravity reduction results . . . . .	112
201	4.4.4	Inversion results . . . . .	114
202	4.4.5	Uncertainty . . . . .	114
203	4.4.5.1	Partitioning uncertainty . . . . .	119
204	4.5	Discussion . . . . .	119
205	4.5.1	Uncertainties and parameter importance . . . . .	119
206	4.5.1.1	Gravity component . . . . .	119
207	4.5.1.2	Constraints component . . . . .	121
208	4.5.1.3	Density component . . . . .	121
209	4.5.1.4	Interpolation component . . . . .	122
210	4.5.1.5	Reducing uncertainties . . . . .	123
211	4.5.1.6	Past estimations of uncertainty . . . . .	123
212	4.5.2	Past bathymetry models . . . . .	124
213	4.5.2.1	Starting model comparison . . . . .	124
214	4.5.2.2	Inversion result comparisons . . . . .	125
215	4.5.2.3	Ocean cavity comparison . . . . .	129
216	4.5.3	Implications . . . . .	130
217	4.5.3.1	New pinning points . . . . .	131
218	4.5.3.2	Basal melting . . . . .	131
219	4.5.3.3	Geologic and tectonic significance . . . . .	133
220	4.6	Conclusion . . . . .	134
221	<b>5</b>	<b>Synthesis</b>	<b>137</b>
222	5.1	Geologic structures . . . . .	138
223	5.2	Inversion . . . . .	138
224	5.3	Ross Ice Shelf bathymetry . . . . .	140
225	5.4	Geologic controls . . . . .	141
226	5.4.1	Present controls . . . . .	141
227	5.4.1.1	Basal melt . . . . .	141
228	5.4.1.2	Modern pinning points . . . . .	142
229	5.4.1.3	Sediment distribution . . . . .	144
230	5.4.1.4	Geothermal heat flux at Siple Coast . . . . .	144
231	5.4.2	Past and future implications . . . . .	145
232	5.4.2.1	Retreat dynamics . . . . .	146
233	5.4.2.2	Glacial initialization . . . . .	147

234	5.5 Future work . . . . .	148
235	5.6 Concluding remark . . . . .	150
236	<b>Appendix A</b>	<b>151</b>
237	A.1 Introduction . . . . .	151
238	A.2 Depth to basement assumptions . . . . .	151
239	A.3 Magnetic data collection, processing, and Werner deconvolution . . . . .	152
240	A.4 Tying magnetic basement to seismic basement . . . . .	153
241	A.5 Tying Ross Sea magnetic basement to Ross Ice Shelf magnetic basement	154
242	A.6 Gridding, merging, and filtering . . . . .	154
243	A.7 Sediment thickness and $\beta$ -factor calculations . . . . .	155
244	A.8 Uncertainties . . . . .	156
245	<b>Appendix B</b>	<b>163</b>
246	B.1 Synthetic inversion with a regional field . . . . .	163
247	B.2 Ross Sea synthetic model . . . . .	164
248	<b>Appendix C</b>	<b>169</b>
249	C.1 Gravity disturbance vs anomaly . . . . .	169
250	<b>Appendix D Antarctic-Plots</b>	<b>171</b>
251	D.1 Fetch . . . . .	171
252	D.2 Map . . . . .	172
253	D.3 Profile . . . . .	172
254	D.4 Regions . . . . .	172

# <sup>255</sup> List of Figures

256	1.1	Past observations and future predictions of sea level rise . . . . .	16
257	1.2	Summary of existing geologic and geophysical data for Antarctica . .	17
258	2.1	Bathymetry, magnetics, and acoustic basement . . . . .	27
259	2.2	Ross Sea magnetic and seismic basement comparison . . . . .	29
260	2.3	Basement elevation and sediment thickness . . . . .	30
261	2.4	Tectonic interpretation of the sub-Ross Ice Shelf . . . . .	32
262	3.1	Ice shelves of Antarctica . . . . .	39
263	3.2	Equivalent methods of discretizing a density contrast . . . . .	44
264	3.3	Annulus approximation of a vertical prism . . . . .	47
265	3.4	Training and testing set configuration . . . . .	49
266	3.5	Weighting grid for the simple synthetic inversion . . . . .	50
267	3.6	Simple synthetic model bathymetry . . . . .	52
268	3.7	Simple synthetic gravity anomalies . . . . .	53
269	3.8	Annulus approximation inversion results . . . . .	54
270	3.9	Annulus approximation inversion cross-validation and profile . . . .	54
271	3.10	Finite differences inversion results . . . . .	55
272	3.11	Finite differences and annulus approximation convergence curves . .	55
273	3.12	Synthetic inversion with noise . . . . .	56
274	3.13	Synthetic inversion with noise, CV and profile . . . . .	56
275	3.14	Creating a low-resolution observed gravity survey . . . . .	57
276	3.15	Synthetic inversion with sampled gravity . . . . .	58
277	3.16	Synthetic inversion with sampled gravity, CV and profile . . . . .	59
278	3.17	Gravity data ensemble for synthetic model . . . . .	59
279	3.18	Gravity anomalies with a regional field . . . . .	61
280	3.19	Regional separation methods . . . . .	62
281	3.20	Constraint point minimization gridding techniques . . . . .	64
282	3.21	Synthetic inversion with regional component, CV and profile . . . .	65
283	3.22	Synthetic inversion with regional component results . . . . .	65
284	3.23	Gravity data ensemble with regional component . . . . .	66
285	3.24	Ross Sea semi-synthetic model . . . . .	68
286	3.25	Ross Sea synthetic airborne survey . . . . .	69
287	3.26	Ross Sea starting bathymetry . . . . .	70
288	3.27	Ross Sea synthetic gravity anomalies . . . . .	71
289	3.28	Ross Sea inversion, CV and convergence . . . . .	72
290	3.29	Ross Sea inversion results . . . . .	72
291	3.30	Ross Sea Monte Carlo simulation . . . . .	74
292	3.31	Constraint spacing effects . . . . .	75
293	3.32	Ross Sea ensemble of noise levels and gravity spacing . . . . .	76

294	3.33 Grouped synthetic inversion ensemble . . . . .	78
295	3.34 Synthetic inversion error and regional error . . . . .	80
296	3.35 Grouped synthetic inversion with regional ensemble . . . . .	81
297	3.36 Ross Sea inversion error and regional error . . . . .	82
298	3.37 Grouped Ross Sea inversion with regional ensemble . . . . .	83
299	4.1 Ross Ice Shelf inversion inputs . . . . .	91
300	4.2 Schematic inversion workflow diagram . . . . .	93
301	4.3 Observed gravity data reduction for Antarctica . . . . .	95
302	4.4 Components of the topographic mass effect . . . . .	96
303	4.5 Discretizing the topographic mass effect . . . . .	97
304	4.6 Topographic mass effect for Antarctica . . . . .	98
305	4.7 Schematic Monte Carlo workflow diagram . . . . .	102
306	4.8 Random vs Latin hypercube sampling . . . . .	103
307	4.9 Ross Ice Shelf starting bathymetry . . . . .	109
308	4.10 Ross Ice Shelf weighting grid . . . . .	110
309	4.11 Re-levelling of the ROSETTA-Ice gravity data . . . . .	111
310	4.12 Gravity reduction results for the Ross Ice Shelf . . . . .	113
311	4.13 Ross Ice Shelf singular bathymetry inversion results . . . . .	115
312	4.14 Latin hypercube sampling distributions and correlations . . . . .	116
313	4.15 Ross Ice Shelf inverted bathymetry and uncertainty . . . . .	117
314	4.16 Monte Carlo results . . . . .	118
315	4.17 Inverted bathymetry comparisons . . . . .	125
316	4.18 Ross Ice Shelf assorted cross-sections . . . . .	128
317	4.19 Water column thickness comparisons . . . . .	130
318	4.20 Basal melt . . . . .	132
319	5.1 Ross Embayment geophysical and geologic information . . . . .	139
320	5.2 Uncertainty bounds for Ross Ice Shelf bathymetry and ocean cavity .	142
321	5.3 3D perspective view of Ross Ice Shelf . . . . .	146
322	A.1 Various Ross Ice Shelf grids . . . . .	157
323	A.2 OIB 403.3 magnetic and seismic basement comparison . . . . .	158
324	A.3 Werner deconvolution solutions for ROSETTA-Ice lines . . . . .	159
325	A.4 Unfiltered magnetic basement and point solutions . . . . .	160
326	A.5 Uncertainty limits of basement and sediment thickness . . . . .	161
327	A.6 Misfit distributions between magnetic and seismic basement . . . . .	162
328	B.1 Comparison of four methods of regional separation . . . . .	163
329	B.2 Constraint point minimization gridding comparison profiles . . . . .	164
330	B.3 Synthetic inversion with regional and noise, CV and profile . . . . .	165
331	B.4 Synthetic inversion with regional and noise, results . . . . .	165
332	B.5 Inversion and regional error for model with regional and noise . . . . .	165
333	B.6 Synthetic inversion with regional and re-sampling, CV and profile . . . . .	166
334	B.7 Synthetic inversion with regional and re-sampling, results . . . . .	166
335	B.8 Inversion and regional error for model with regional and low-res gravity	166
336	B.9 Inversion and regional error for Ross Sea constraint ensemble . . . . .	167
337	C.1 Gravity disturbance vs. anomaly . . . . .	169

# <sup>338</sup> List of Tables

<sup>339</sup>	3.1 Simple synthetic model summary . . . . .	67
<sup>340</sup>	4.1 Bathymetry uncertainties comparison . . . . .	120
<sup>341</sup>	A.1 Previous Ross Ice Shelf seismic sediment thickness measurements . .	156



# <sup>342</sup> Chapter 1

## <sup>343</sup> Introduction

### <sup>344</sup> 1.1 Motivation

<sup>345</sup> Improving projections of the rate of global sea level rise in response to a warming  
<sup>346</sup> world is vital for effectively mitigating future environment and socio-economic im-  
<sup>347</sup> pacts (Durand et al., 2022). A large portion of the uncertainties in modern and  
<sup>348</sup> projected sea level rise is related to the contribution from the Antarctic Ice Sheet  
<sup>349</sup> (Figure 1.1b, Bamber et al., 2022; Edwards et al., 2021; Otosaka et al., 2023; Slater  
<sup>350</sup> & Shepherd, 2018). The Antarctic Ice Sheet contains a total volume of ice equivalent  
<sup>351</sup> to 57.2 m of sea level rise (Fretwell et al., 2013). Satellite observations show that  
<sup>352</sup> Antarctica contributed  $\sim$  7.4 mm to mean sea level since 1992 (Otosaka et al., 2023),  
<sup>353</sup> and of the various components of sea level rise, the contribution from Antarctica is  
<sup>354</sup> accelerating the fastest (Figure 1.1a, Nerem et al., 2018). Since the early 1990s, the  
<sup>355</sup> sea level contribution from Antarctica has increased by 25% (Otosaka et al., 2023).  
<sup>356</sup> By the end of the century, Antarctica is projected to contribute between 0.03 and  
<sup>357</sup> 0.28 m to mean sea level (RCP 8.5, Intergovernmental Panel on Climate Change  
<sup>358</sup> (IPCC), 2022). Optimal strategies for preparing coastal communities to best miti-  
<sup>359</sup> gate the impacts of rising sea level depends on where in this range of uncertainties  
<sup>360</sup> the true sea level rise will be. Some of the uncertainty in how the Antarctic Ice  
<sup>361</sup> Sheet will respond to a warming world stems from a lack of understanding of the  
<sup>362</sup> complex interactions between the ice and the underlying earth (e.g. Schlegel et al.,  
<sup>363</sup> 2018; Zhao et al., 2018).

### <sup>364</sup> 1.2 Influence of bathymetry, topography, and geol- <sup>365</sup> ogy on ice dynamics

<sup>366</sup> The underlying Earth influences ice sheets through several mechanisms, which we  
<sup>367</sup> group as those resulting from bedrock topography, geologic structures, and bedrock  
<sup>368</sup> physical properties. Here we describe each of these categories of influences on the  
<sup>369</sup> Antarctic Ice Sheet, followed by introducing our specific study area, the Ross Ice  
<sup>370</sup> Shelf.

#### <sup>371</sup> 1.2.1 Bedrock topography

<sup>372</sup> Offshore bathymetry and onshore bed topography exert several fundamental con-  
<sup>373</sup> trols on how the Antarctic Ice Sheet behaves. Offshore, where the ice is floating, the

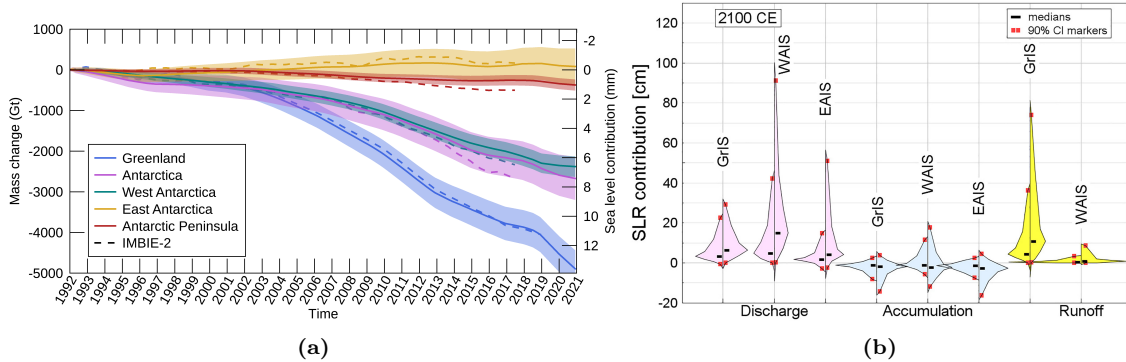


**Figure 1.1:** Past observations and future predictions of sea level rise. **a)** Observed cumulative mass change and sea level contributions from the various ice sheets. Data comes from satellite-altimetry estimates of volume changes, gravimetric estimates of mass changes, and quantification of input-output fluxes. Figure from Otosaka et al. (2023). **b)** Probability distributions for projected global sea level rise contributions for the year 2100 from the Greenland Ice Sheet (GrIS), West Antarctic Ice Sheet (WAIS), and East Antarctic Ice Sheet (EAIS), separated into three processes; discharge, accumulation, and runoff. Left and right sides of each distribution show the +2°C and +5°C global temperature trajectories, respectively. Figure from Bamber et al. (2022).

374 influence of the bathymetry is limited to the guiding of ocean circulations. Bathymetric ridges have been shown to block, or re-direct, the inflow of melt-inducing  
 375 waters to the ocean cavity beneath floating ice shelves (De Rydt et al., 2014; Gold-  
 376 berg et al., 2020; Zhao et al., 2019). Approximately 75% of Antarctica's coastline  
 377 is composed of these floating ice shelves, and 83% of total ice discharged into the  
 378 Southern Ocean from Antarctica is through these shelves, highlighting their signifi-  
 379 cance to Antarctica's ice budget (Rignot et al., 2013). Of the 83% of total ice loss  
 380 from Antarctica through ice shelves, basal melt is responsible for approximately half  
 381 (Greene et al., 2022; Rignot et al., 2013). Some of this melt occurs from surface  
 382 waters, where bathymetry has little effect, but for many of the largest ice shelves,  
 383 the majority of basal melt occurs along the deep grounding zone (Adusumilli et al.,  
 384 2020). Here, the melt-inducing water bodies are dense and flow into the ice shelf  
 385 cavities along the seafloor (Holland, 2008; Tinto et al., 2015). Therefore, bathy-  
 386 metric features act to guide or block these circulations from reaching the grounding  
 387 zone where they can melt the ice base. In addition to steering ocean currents, bed  
 388 topography, in regions of grounded ice, acts to steer the ice flow.  
 389

390 As revealed by extensive seismic and swath bathymetry data in Antarctica's Ross  
 391 Sea (Figure 1.2a), the dynamics of an advancing or retreating ice sheet are predomi-  
 392 nantly controlled by the physiography of the bed (Anderson et al., 2019; Halberstadt  
 393 et al., 2016). If large troughs and banks exist, advancing ice is initially confined by  
 394 these features, while the banks remain ice-free (Anderson et al., 2014). Eventually,  
 395 after the ice has covered the entire region, the retreat is initially confined to these  
 396 narrow troughs, while the banks retain grounded ice for much longer (Anderson  
 397 et al., 2019; Halberstadt et al., 2016). As the ice thins or retreats into regions of  
 398 deeper bed topography, these banks remain grounded, while the rest of the ice sheet  
 399 decouples from the bed, begins floating and forms an ice shelf (Shipp et al., 1999).  
 400 This remaining grounded ice on bathymetric highs forms pinning points.  
 401

402 Pinning points are regions of locally grounded ice within a floating ice shelf  
 403 (Matsuoka et al., 2015). The friction between the bed and ice base at these points

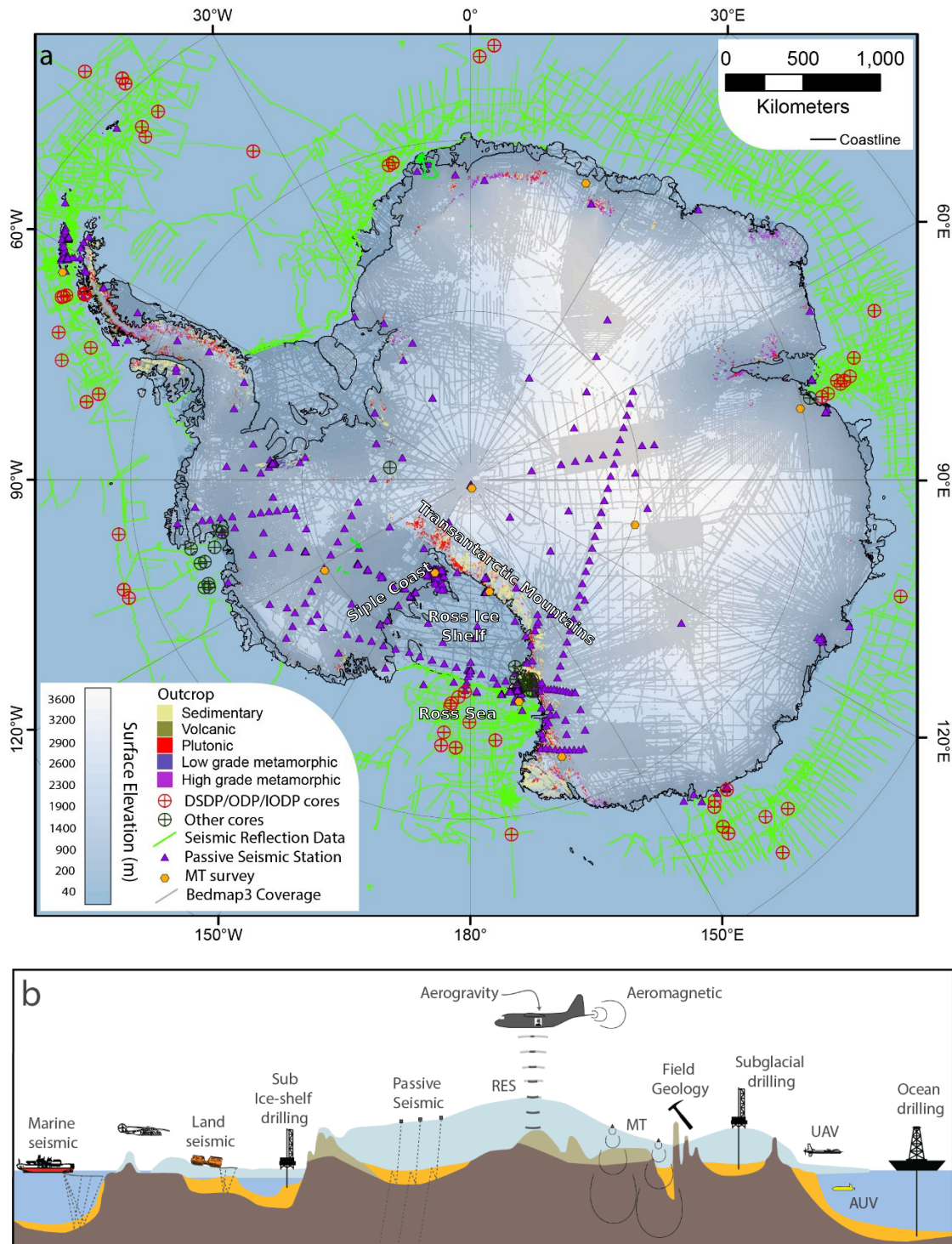


**Figure 1.2:** Summary of existing geologic and geophysical data for Antarctica. **a)** Map of data coverage in Antarctica indicating outcropping regions, drill core sites, seismic and magnetotelluric surveys, and bed elevation data points of Bedmap3, mostly from airborne radio-echo sounding (Frémand et al., 2022). **b)** Various methods of acquiring information sub-surface geology. Figure adapted from Aitken et al. (2023b).

405 impart a critical resisting force to the discharge of upstream ice; an effect known as  
 406 buttressing (Dupont & Alley, 2005; Thomas, 1979). Since the base of ice shelves  
 407 is flat relative to the underlying bathymetry, the morphology of the seafloor is the  
 408 dominant control of the location and geometry of these pinning points. The bedrock  
 409 topography has been thought to be relatively constant over a millennial timescale,

meaning that pinning points geometries vary mostly by temporal changes in the ice thickness. However, recent studies of glacial isostatic adjustment, the vertical rebound of the Earth following deglaciation, throughout West Antarctica have demonstrated high spatial variability and short (multi-centennial-to-millennial) timescales for these vertical land movements (Barletta et al., 2018; Coulon et al., 2021; Kachuck et al., 2020). As the bedrock beneath portions of West Antarctica continues to rebounds, the number and extent of these pinning points will likely increase, possibly providing a stabilizing effect to the ice sheet.

418

All of these above controls on ice dynamics imparted by the physiography of the bed rely on accurate knowledge of bed topography and bathymetry. Due to the inherently challenging nature of Antarctic fieldwork, and the logistical challenge of measuring bed elevations beneath thick ice, 50% of the Antarctic Ice Sheet is more than 5 km from the nearest measurement of bed elevation (Figure 1.2a, Morlighem et al., 2020). This value increases greatly if the floating ice shelves are included. For grounded ice, the dominant techniques for direct measurements of bed elevation data are airborne radio-echo sounding, over-snow radar, and seismic surveying (Figure 1.2b, Fretwell et al., 2013). In the open ocean, bathymetry data is typically collected with ship-borne multibeam echo sounding, seismic surveying (Figure 1.2b), or from satellite-altimetry. Acquiring bathymetry data beneath floating ice shelves presents a particular challenge. The efficient shipborne methods are unavailable since the ice shelves are persistent year-round, unlike the sea ice in the open ocean. Radio-echo sounding, either ground-based or airborne, cannot image through the water column. Direct observations through drilling are possible and exist, but typically require drilling through 100's to 1000's of meters of ice (Figure 1.2, Clough & Hansen, 1979; Patterson et al., 2022). Autonomous underwater vehicles (Figure 1.2b) present another option, but are expensive and have limited range (Dowdeswell et al., 2008; Nicholls et al., 2006). The only feasible method of direct observations of sub-ice shelf bathymetry is over-snow seismic surveying (Figure 1.2b). However, for the vast area of many ice shelves, even sparse coverage ( $\sim 50$  km spacing) of seismic points across the ice shelf takes several field seasons of data acquisition (Bentley, 1984).

### 1.2.2 Geologic structures

Additional influences on the overriding ice include the delivery of geothermal heat and subglacial water to the ice base and the vertical deformation of the bedrock in response to changing ice loads. Geothermal heat influences ice dynamics through several mechanisms; 1) increasing the temperature of the ice which lowers its viscosity, leading to enhanced flow via internal deformation (Llubes et al., 2006), 2) meltwater lubrication of the bed reduces friction, enhancing flow (Pollard et al., 2005), and 3) increasing the ability of the bed to deform via increased pore-fluid pressure, which increases ice flow (Tulaczyk et al., 2000). The latter two effects, while enhanced by geothermal heat through the melting of ice, also occur with simply the presence of liquid water at the ice-bed interface. As briefly mentioned in the above section, glacial isostatic adjustments of the bedrock following changes in ice load can influence the ice by altering the geometry and locations of grounded ice.

454

Each of these effects; geothermal heat flow, subglacial water availability, and glacial isostatic adjustment, are in turn influenced by geologic structures within the

457 upper crust. A portion of subglacial water comes from either transport along the  
458 ice-bed interface, or from the melting of the ice base. However, an often overlooked  
459 component of the subglacial hydrologic system is groundwater stored in deep sedimentary  
460 aquifers. For example, hydrologic modelling of the ice streams of the Siple  
461 Coast (Figure 1.2a) estimated the components of the hydrologic budget to be 8%  
462 from local basal melting, 47% from inflow from the ice sheet interior, and 45% from  
463 groundwater reservoirs (Christoffersen et al., 2014). These modelling observations of  
464 extensive groundwater have been recently verified beneath the Whillans Ice Stream  
465 by a magnetotelluric survey. This survey imaged an extensive groundwater aquifer  
466 within a sedimentary basin, containing at least an order of magnitude more water  
467 than the shallow hydrologic system (Gustafson et al., 2022). The vertical flow of this  
468 basinal groundwater is controlled by the pressure of the overriding ice sheet. As this  
469 overburden pressure decreases with thinning ice, groundwater is discharged to the  
470 ice base (Gooch et al., 2016; Li et al., 2022). This discharge is likely concentrated  
471 along pre-existing weaknesses or impermeable surfaces, such as fault damage zones,  
472 or the margins of crystalline basement (Jolie et al., 2021). During this ice-induced  
473 hydraulic unloading, regional geothermal heat is advected along the fluid pathways,  
474 leading to potentially highly elevated heat flow delivered to the ice base (Li et al.,  
475 2022; Ravier & Buoncristiani, 2018). In addition to concentrating both subglacial  
476 water and geothermal heat, these faults, or more generically, regions of the crust  
477 which have experienced recent faulting, will respond differently to stresses induced  
478 by glacial isostatic adjustment. To a first order, the isostatic response of the solid-  
479 earth to changing ice load is controlled by the rheology of the mantle (Whitehouse  
480 et al., 2019). However, on a more local scale, pre-existing faults are shown to ac-  
481 commodate glacial isostatic rebound-induced stresses (Peltier et al., 2022; Steffen  
482 et al., 2021).

483

484 To be able to understand the above influences on the ice, we must have some  
485 fundamental knowledge of the geologic structures beneath the ice. This includes  
486 knowing where sedimentary basins, and possible aquifers within, are located, where  
487 faults likely intersect the ice base, and the geometry of the crystalline basement.  
488 Each of these components is difficult to image directly. Drilling, seismic surveys,  
489 or geologic analysis of rock outcrops all provide valuable information but are not  
490 feasible to cover wide regions (Figure 1.2). Indirect methods are therefore needed.  
491 These include techniques such as gravity, magnetic, or electromagnetic methods.  
492 Each of these techniques records measurements of the spatial variation of a poten-  
493 tial field, such as the Earth's gravity, magnetic, or electromagnetic fields. These  
494 fields are all partially dependant on a physical Earth property, such as rock density,  
495 magnetic susceptibility, or resistivity. From these relationships, sub-surface geologic  
496 information can be learned.

### 497 1.2.3 Basal roughness

498 The last major influence on the ice from the underlying Earth we present is the  
499 roughness of the bed which the ice sheet flows over. This bed roughness is impor-  
500 tant on both a micro and macro scale. At a micro-scale, roughness is determined  
501 by the material which the bed is composed of. A bed of erosion-resistance crys-  
502 talline basement, for example, can greatly hinder the flow of ice. This material  
503 results in high friction with the ice base, slowing the sliding of ice (Bell et al., 1998).

504 Conversely, beds composed of fine-grained tills allow fast ice flow. This fast flow  
505 is predominantly due to deformation within the till as the ice flows (Alley et al.,  
506 1986). In between the end members of crystalline basement and fine grain till are  
507 lithified sedimentary rocks, for example. This type of bed may initially lead to high  
508 friction with the ice, but due to their high erodability, sedimentary rock will quickly  
509 generate till (Anandakrishnan et al., 1998). A macro-scale view of basal roughness  
510 is also important for ice dynamics. As observed at the Siple Coast (Figure 1.2a) ice  
511 streams, there is a strong inverse relation between bed roughness, from scales of 5  
512 km to >40km, and ice stream velocities (Siegert et al., 2004). The composition of  
513 the bed also plays an important role in the total effective resistance imparted on ice  
514 flow from pinning points (Still et al., 2019).

515  
516 To best quantify the effect of basal roughness on ice dynamics, information on  
517 the material properties of the bed is needed. While sediment samples beneath the ice  
518 yield valuable information, they may only represent the bed at the specific location  
519 where they were sampled. The most fundamental information needed is the generic  
520 rock type of the bed, namely, is the bed loose, unconsolidated sediment, lithified  
521 sedimentary rock, or crystalline rock? Aitken et al. (2023b) provide a detailed  
522 review of Antarctica's sedimentary basins, and the methods employed to determine  
523 both the presence of sediment and the sediment thickness. These methods, as well as  
524 the methods described in the above sections, are shown in Figure 1.2, as reproduced  
525 from Aitken et al. (2023b).

526 With the dominant influences from the underlying Earth on ice dynamics laid  
527 out, we will now introduce the study area of this thesis, Antarctica's Ross Ice Shelf.

## 528 1.3 Ross Ice Shelf

529 The Ross Ice Shelf is Antarctica's largest ice shelf ( $\sim 480,000 \text{ km}^2$ ), Figure 1.2).  
530 It is situated between the Transantarctic Mountains and Marie Byrd Land. It  
531 buttresses a catchment of ice that flows from both the East and West Antarctic  
532 Ice Sheets. This catchment contains 11.6 m of global sea level equivalent (Fretwell  
533 et al., 2013; Rignot et al., 2011; Tinto et al., 2019). Compared to many other  
534 ice shelves, the Ross Ice Shelf is currently relatively stable (Moholdt et al., 2014;  
535 Rignot et al., 2013). However, geologic evidence from throughout the Ross Sea and  
536 the Siple Coast shows that in the past  $\sim 7,000$  years the shelf has experienced rapid  
537 destabilization, disintegration, and large-scale grounding line retreat (e.g., Naish  
538 et al., 2009; Venturelli et al., 2020). This major Holocene retreat is thought to  
539 have been primarily caused by ocean forcings (Lowry et al., 2019), as bathymetric  
540 troughs guided in the inflow of melt-inducing ocean circulations (Tinto et al., 2019).  
541 Once destabilized, the grounding line retreat from the outer continental shelf to the  
542 present-day location was controlled primarily by the physiography and geology of  
543 the bed (Anderson et al., 2019; Halberstadt et al., 2016). This shows the importance  
544 of the underlying Earth's influence on the dynamics of the Ross Ice Shelf.

### 545 1.3.1 Past investigations

546 By examining various influences on ice dynamics, we identified some key data needed  
547 to understand these influences. This data included onshore bed topography, off-  
548 shore bathymetry, the distribution of sediment, and upper crustal structures such

as faults and the topography of the basement. Here, we summarize the history of data collection in the Ross Ice Shelf region specific to these geologic and physiographic features. Geological and geophysical exploration has occurred in the Ross Embayment for over a century. The earliest of these include the 1901-1904 *Discovery* expedition, the 1907-1909 *Nimrod* expedition, and the 1910-1913 *Terra Nova* expedition. These expeditions laid the groundwork of interest in the Ross Embayment from a scientific perspective. The first major survey of the Ross Ice Shelf was part of the 1957-1959 International Geophysics Year traverses. The three over-snow traverses all included a portion of the ice shelf and collected radar, gravity, and seismic data to determine ice thickness, surface elevation, and bed elevation (Crary, 1959). These surveys produced early evidence of the extensive below-sea-level bed, thin crust, and distinct geologic provinces throughout West Antarctica (Bentley et al., 1960). In the 1970s the Ross Ice Shelf Geophysical and Glaciological Survey (RIGGS, Bentley, 1984) consisted of a systematic grid of seismic surveys over the entire ice shelf with an average spacing between survey points of 55 km. After the RIGGS survey, there were a total of  $\sim 223$  point-source seismic surveys across the ice shelf, all yielding single-point sub-ice shelf bathymetry depths. Of these, eight reported sediment thicknesses beneath. Several faults were hypothesized, based on 2D gravity profiles conducted at many of the stations (Greischar et al., 1992). Since the 1970s, there have been many additional local surveys on the ice shelf, but these have been focused along the grounding zones (e.g., Horgan et al., 2017; Muto et al., 2013b; Patterson et al., 2022; Stern et al., 1994; ten Brink et al., 1993; Wannamaker et al., 2017). The next, and most recent major data-collection campaign on the Ross Ice Shelf was the ROSETTA-ice project.

The Ross Ocean and ice Shelf Environment, and Tectonic setting Through Aerogeophysical surveys and modelling project (ROSETTA-ice, Tinto et al., 2019), was a 3-season (2015-2017) airborne geophysical survey of the Ross Ice Shelf. It flew a regular grid of flight lines, with nominal N-S and E-W line spacings of 10 and 55 km, respectively. During each flight, various geophysical data was collected, including ice-penetrating radar, gravity, magnetics and laser altimetry. So far, these ROSETTA-ice data have been used to begin characterizing the geologic nature of the crust (Tinto et al., 2019), to model the depths to the sea floor (Tinto et al., 2019), and to quantify basal melt (Das et al., 2020).

Following 60 years of surveying and exploration of the Ross Ice Shelf, our fundamental understanding of the subglacial geology and physiography is still lacking. For an area almost twice the size of New Zealand, we have approximately 8 locations of reported sediment thickness, several hypothesized locations of faults, gaps of over 100 km without bathymetric depths, and limited understanding of our uncertainty in the bathymetry where it has been modelled/interpolated. We propose several research questions which we aim to answer in this thesis.

## 1.4 Research questions

The aim of this thesis is to improve our knowledge of boundary conditions beneath the Ross Ice Shelf in order to better understand the past, present, and future interactions between the ice, ocean, and underlying earth. We aim to accomplish this by answering the following questions:

- 596     1. What is the geologic structure of the upper crust beneath the Ross Ice Shelf?  
597       If there are sediments, what is their thickness and distribution? Where are  
598       the major faults likely located?
- 599     2. How can bathymetry beneath an ice shelf best be modelled? Are there further  
600       improvements that can be made to the currently employed gravity-inversion  
601       process? What are the predominant sources of uncertainty, and how can these  
602       be limited?
- 603     3. How deep is the bathymetry beneath the Ross Ice Shelf and where are we most  
604       and least certain about it?
- 605     4. What are the geologic controls on the Ross Ice Shelf's stability?

606     

## 1.5 Outline

607     This thesis is comprised of five chapters.

608

609     This chapter, Chapter 1, establishes the context behind the research, introduces  
610     the study region, proposes a series of research questions, and contains an outline of  
611     this thesis.

612

613     Chapter 2 is adapted from a journal article published in Geophysical Research  
614     Letters (Tankersley et al., 2022), reformatted to be included in this thesis. It presents  
615     a model of the basement topography, and overlying sediment distribution, beneath  
616     the Ross Ice Shelf. We use airborne magnetic data from the ROSETTA-ice project,  
617     and a depth-to-magnetic source technique to model the sediment-basement contact.  
618     This reveals large-scale, fault-controlled extensional basins throughout the sub-Ross  
619     Ice Shelf crust. From this, we are able to draw a wide range of inferences on the  
620     likely influence of this basement topography on the past, present, and future ice  
621     sheet, as well as some tectonic implications. These results provide the first holistic  
622     view of the upper crust beneath the Ross Ice Shelf.

623

624     Chapter 3 details our development of a method to model the depth to the sea floor  
625     beneath a floating ice shelf. This method is a gravity inversion, where observations  
626     of Earth's gravitational field are used to model bathymetry beneath an ice shelf. We  
627     develop open-source Python code with the aim for other researchers to utilize the  
628     inversion. We test the inversion against a suite of synthetic and semi-realistic data.  
629     This confirms the feasibility of using gravity data to attain bathymetry depths in an  
630     Antarctic setting. Additionally, these synthetic tests reveal the relative importance  
631     of various aspects of a gravity inversion. These include the importance of *a priori*  
632     constraints on the bathymetry, the large errors which can be introduced during the  
633     removal of the regional component of gravity, and several suggestions for optimal  
634     survey design to minimize error in the resulting bathymetry model. Our use of  
635     Monte Carlo simulation provides both a spatially variable estimation of uncertainty  
636     in the resulting bathymetry and an estimate of the various sources of this uncertainty.

637

638     Chapter 4 uses the inversion algorithm developed in Chapter 3 to create a new  
639     bathymetry model and associated uncertainties beneath the Ross Ice Shelf. Our

model shows some major differences with past bathymetry models, highlighting areas of the ice shelf that should be carefully considered in future surveys. These include a deeper bathymetric trench along the Transantarctic Mountains, a thicker ocean cavity along a portion of the ice front which may allow the incursion of warm ocean waters and a thicker ocean cavity proximal to the Siple Coast grounding line. Our uncertainty analysis shows the region of highest uncertainties is along the Transantarctic Mountain Front. Within this chapter, we perform a comprehensive review of past bathymetry-gravity inversions, for all Antarctic studies, and several Greenland studies. This highlighted some key differences, which we believe we have improved on.

650

Chapter 5 presents a synthesis of the 3 research chapters, and provides a discussion of the research questions. Various future works are suggested and the main conclusions of this thesis are presented. The research chapters in this thesis were written with the intent to publish, including Chapter 2 which is already published. Therefore, I have chosen to keep the style of writing consistent throughout the thesis, with the use of plural possessive pronouns ("we") instead of singular ("I").

## 1.6 Data and Code Availability Statement

In an effort to adhere to the principles of FAIR scientific investigations, Findability, Accessibility, Interoperability, and Reusability (Wilkinson et al., 2016), we have used only open-access data and published all code<sup>1</sup> used in this thesis. Here we describe where this code and data can be found. All data used from other studies has been cited within each chapter and can be accessed through their respective DOIs. However, most of these datasets were downloaded using the Python package Antarctic-Plots (Tankersley, 2023). I developed this package during this PhD to help with several aspects of conducting research related to Antarctica. See Appendix D for an overview of the capabilities of Antarctic-Plots. Analysis in this study was executed on a computer with an x86\_64 processor with a maximum clock frequency of 2600 MHz with 56 physical cores, 112 logical cores, and 1TB of RAM, using the Operating System Linux-Ubuntu.

### Chapter 2

All of the Python code used to perform the analysis and create the figures of Chapter 2 is available from the following GitHub repository; [https://github.com/mdtanker/RIS\\_basement\\_sediment](https://github.com/mdtanker/RIS_basement_sediment), and the version of the repository used in the published paper is archived at <https://doi.org/10.5281/zenodo.6499863> (Tankersley, 2022).

### Chapters 3 & 4

The gravity inversion Python code, the workflow conducted within Jupyter Notebooks, and the creation of all the figures is available from the following GitHub repository; [https://github.com/mdtanker/RIS\\_gravity\\_inversion](https://github.com/mdtanker/RIS_gravity_inversion) and the version of the repository used in this thesis is archived at <https://doi.org/10.5281/zenodo.8084469> (Tankersley et al., 2023).

The code for creating the figures in the remainder of this thesis, and the latex files of the thesis itself are available at the following GitHub repository; <https://>

<sup>1</sup>This excludes one component of Chapter 2 which was performed with proprietary software.

<sup>683</sup> github.com/mdtanker/phdthesis and is citable with the following DOI; <https://doi.org/10.5281/zenodo.8084606>.

# 685 Chapter 2

## 686 Airborne magnetic analysis: 687 Basement depths and sediment 688 thickness

### 689 Abstract

690 New geophysical data from Antarctica's Ross Embayment reveal the structure and  
691 subglacial geology of extended continental crust beneath the Ross Ice Shelf. We use  
692 airborne magnetic data from the ROSETTA-Ice Project to locate the contact be-  
693 tween magnetic basement and overlying sediments. We delineate a broad, segmented  
694 basement high with thin (0-500 m) non-magnetic sedimentary cover which trends  
695 northward into the Ross Sea's Central High. Before subsiding in the Oligocene, this  
696 feature likely facilitated early glaciation in the region and subsequently acted as a  
697 pinning point and ice flow divide. Flanking the high are wide sedimentary basins,  
698 up to 3700 m deep, which parallel the Ross Sea basins and likely formed during  
699 Cretaceous-Neogene intracontinental extension. NW-SE basins beneath the Siple  
700 Coast grounding zone, by contrast, are narrow, deep, and elongate. They suggest  
701 tectonic divergence upon active faults that may localize geothermal heat and/or  
702 groundwater flow, both important components of the subglacial system.

### 703 Plain Language Summary

704 The bedrock geology of Antarctica's southern Ross Embayment is concealed by  
705 100s-1000s of meters of sedimentary deposits, seawater, and the floating Ross Ice  
706 Shelf (RIS). Our research strips away those layers to discover the shape of the  
707 consolidated bedrock below, which we refer to as the basement. To do this, we use  
708 the contrast between non-magnetic sediments and magnetic basement rocks to map  
709 out the depth of the basement surface under the RIS. Our primary data source is  
710 airborne measurements of the variation in Earth's magnetic field across the ice shelf,  
711 from flight lines spaced 10 km apart. We use the resulting basement topography  
712 to highlight sites of possible influence upon the Antarctic Ice Sheet and to further  
713 understand the tectonic history of the region. We discover contrasting basement  
714 characteristics on either side of the ice shelf, separated by an N-S trending basement  
715 high. The West Antarctic side displays evidence of active faults, which may localize  
716 geothermal heat, accommodate movements of the solid earth caused by changes in

717 the size of the Antarctic Ice Sheet, and control the flow of groundwater between the  
718 ice base and aquifers. This work addresses critical interactions between ice and the  
719 solid earth.

720 **Key Points:**

- 721 1. Aeromagnetic analysis reveals basement surface and evidence of fault-controlled  
722 extensional basins beneath Antarctica's Ross Ice Shelf (RIS).
- 723 2. Active faults at Siple Coast likely influence ice streams through control of  
724 geothermal heat, groundwater, and glacioisostatic adjustments.
- 725 3. A basement high beneath RIS spatially coincides with a lithospheric boundary,  
726 with contrasting sedimentary basins on either side.

727 

## 2.1 Introduction

728 The southern sector of Antarctica's Ross Embayment beneath the Ross Ice Shelf  
729 (RIS; area  $\sim 480,000 \text{ km}^2$ ) is poorly resolved because the region is not accessible  
730 to conventional seismic or geophysical surveying. Rock exposures on land sug-  
731 gest that Ross Ice Shelf (RIS) crust consists of early Paleozoic post-orogenic sed-  
732 iments, intruded in places by mid-Paleozoic and Cretaceous granitoids (Goodge,  
733 2020; Luyendyk et al., 2003). Following the onset of extension in the mid-Cretaceous,  
734 grabens formed and filled with terrestrial and marine deposits, continuing into the  
735 Cenozoic (e.g. Coenen et al., 2019; Sorlien et al., 2007), as the Ross Embayment  
736 underwent thermal subsidence (Karner et al., 2005; Wilson & Luyendyk, 2009).  
737 The physiography of this region then responded to the onset of glaciation in the  
738 Oligocene (Paxman et al., 2019), coinciding with localized extension in the west-  
739 ern Ross Sea until 11 Ma (Granot & Dyment, 2018). The Oligocene-early-Miocene  
740 paleo-landscape of the Ross Sea sector was revealed by marine seismic data (e.g.  
741 Brancolini et al., 1995; Pérez et al., 2021) and offshore drilling that penetrated crys-  
742 talline basement (DSDP Site 270; Ford & Barrett, 1975) (Figure 2.1). Recognition  
743 of the role of elevated topography in Oligocene formation of the Antarctic Ice Sheet  
744 (DeConto & Pollard, 2003; Wilson et al., 2013) and the likely influence of subglacial  
745 topography upon ice sheet processes during some climate states (Austermann et al.,  
746 2015; Colleoni et al., 2018) motivated our effort to determine basement topography  
747 beneath the Ross Ice Shelf.

748

749 Ice sheet dynamics are of high interest in the RIS region because its grounding  
750 zone (GZ) and pinning points (Still et al., 2019) buttress Antarctica's second-largest  
751 drainage basin (Tinto et al., 2019). Our work in this sensitive region seeks to delimit  
752 the extent and geometry of competent basement because the margins of basement  
753 highs are sites of strong contrasts in permeability that influence the circulation of  
754 subglacial waters. A spectacular example of the confinement of subglacial water  
755 between the ice sheet and basement exists in ice radar profiles for the continental  
756 interior (Bell et al., 2011), but little is known about the subglacial hydrology of  
757 deep groundwater reservoirs within sediment-filled marine basins that receive ter-  
758 restrial freshwater influx (Gustafson et al., 2022; Siegert et al., 2018). These basins  
759 may contain up to 50% of total subglacial freshwater (Christoffersen et al., 2014),  
760 where the discharge and recharge along fault-damage zones (Jolie et al., 2021) is

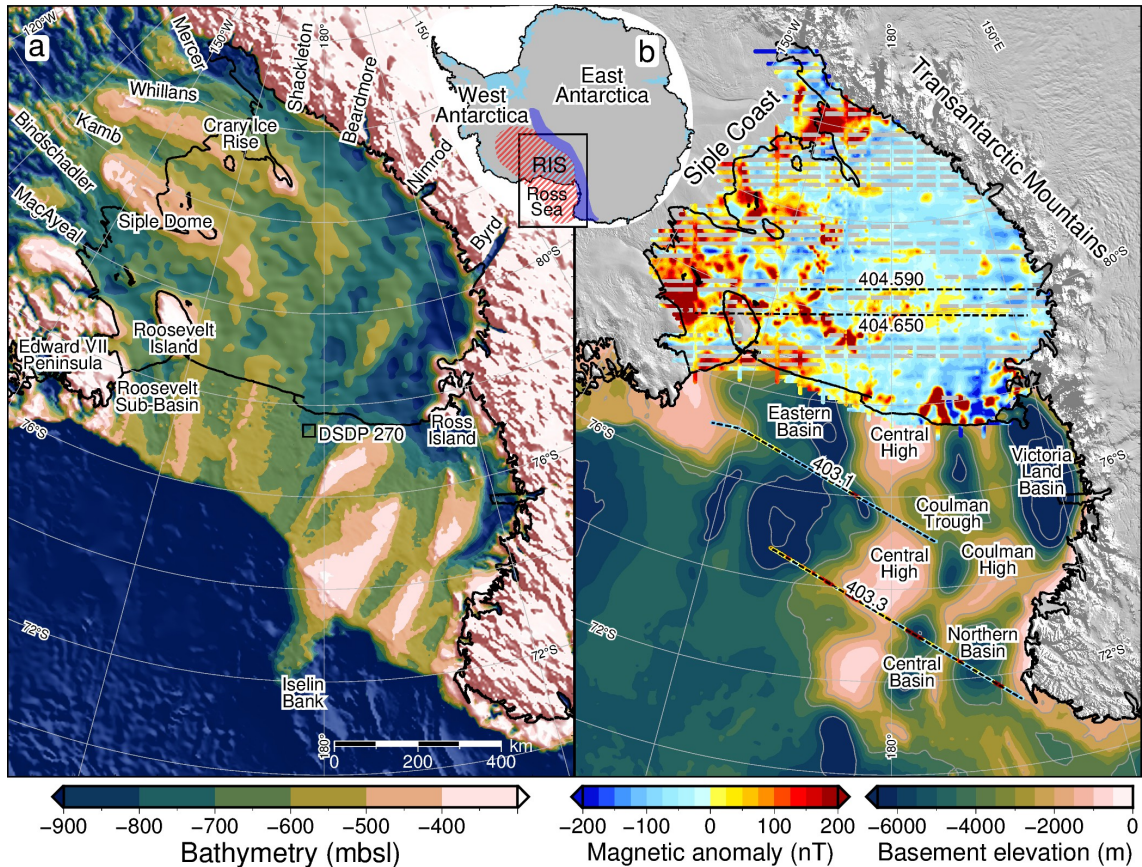


**Figure 2.1:** (a) Bathymetry and sub-ice bed elevations (Morlighem et al., 2020) including ROSETTA-Ice gravity-derived bathymetry (Tinto et al., 2019) beneath the Ross Ice Shelf (RIS). Labels include ice streams and outlet glaciers. (b) Basement elevation from Antarctic Offshore Stratigraphy project marine seismic compilation in the Ross Sea Brancolini et al. (1995) and air-borne magnetic data from ROSETTA-Ice (over RIS) and Operation IceBridge (black dashed lines). Inset map shows figure location, West Antarctic Rift System (hatched red), Transantarctic Mountains (dark blue), and ice shelves (light blue). Shelf edge, grounding line, and coastlines in black (Rignot et al., 2013). MODIS imagery from Scambos et al. (2007).

761 controlled by pressure from the overriding ice sheet (Gooch et al., 2016). Possible  
762 evidence that RIS basement margins localize basinal waters, causing the advection  
763 of geothermal heat, comes from elevated values and significant spatial variability of  
764 measured geothermal heat flux (GHF) at points around the Ross Embayment (Bege-  
765 man et al., 2017). Here we present the first map of magnetic basement topography  
766 and thickness of overlying non-magnetic sediments for the southern Ross Embay-  
767 ment, developed using ROSETTA-Ice (2015-2019) airborne magnetic data (Figure  
768 2.1b, Tinto et al., 2019). Our work reveals three major sedimentary basins and a  
769 broad basement ridge that separates crust of contrasting basement characteristics.

## 770 2.2 Data and Methods

771 We use ROSETTA-Ice aeromagnetic data to image the shallowest magnetic signals  
772 in the crust. Assuming that the overlying sediments and sedimentary rocks produce  
773 smaller magnetic anomalies than the crystalline basement, we treat the resulting  
774 solutions as the depth to the magnetic basement (Section A.2). To do this, we  
775 implemented Werner deconvolution (Werner, 1953) on 2D moving and expanding  
776 windows of line data, isolating anomalies and solving for their source parameters  
777 (Section A.3, location, depth, susceptibility, body type). The resulting solutions are  
778 non-unique; each observed magnetic anomaly can be solved by bodies at multiple  
779 locations and depths by varying the source's magnetic susceptibility and width. The  
780 result is a depth scatter of solutions (Figures 2.2 & A.2), which tend to vertically  
781 cluster beneath the true source. This magnetic basement approach has been used  
782 to map sedimentary basins throughout Antarctica (i.e. Bell et al., 2006; Frederick  
783 et al., 2016; Karner et al., 2005; Studinger et al., 2004a) where typically, the tops  
784 of solution clusters are manually selected to represent the basement depth. Our ap-  
785 proach expands on this method by utilizing a reliable, automated method of draping  
786 a surface over these depth-scattered solutions to produce a continuous basement sur-  
787 face (Section A.4 & A.5).

788

789 We implemented a 2-step tuning process that ties our RIS magnetic basement  
790 to well-constrained seismic basement in the Ross Sea, from the Antarctic Off-  
791 shore Stratigraphy project (ANTOSTRAT) (Figure 2.1b, Brancolini et al., 1995).  
792 This involved using Operation IceBridge (OIB) airborne magnetic data (Cochran  
793 et al., 2014a) collected over the RIS and Ross Sea. Minimizing misfits between  
794 OIB magnetic basement and ANTOSTRAT basement, as well as between OIB and  
795 ROSETTA-Ice magnetic basements, enabled tuning of our method to optimal base-  
796 ment depths (Figures 2.2, A.2, A.3e&f, Section A.4 & A.5).

797

798 Our RIS results (Figure A.4) were merged with offshore ANTOSTRAT data  
799 (Brancolini et al., 1995) and smoothed with an 80 km Gaussian filter to match the  
800 characteristic wavelengths of the Ross Sea basement (Section A.6). The combined  
801 grid (Figure 2.3a) was then subtracted from BedMachine bathymetry (Figure 2.1a,  
802 Section A.7, Morlighem et al., 2020), to obtain the sediment thickness distribution  
803 for the Ross Embayment (Figure 2.3b).

804

805 These sub-RIS results together with free-air gravity data allowed us to infer the  
806 locations of regional scale faults beneath the RIS. Criteria used to locate faults in-  
807 clude 1) high relief on the magnetic basement surface, 2) linear trends that cross

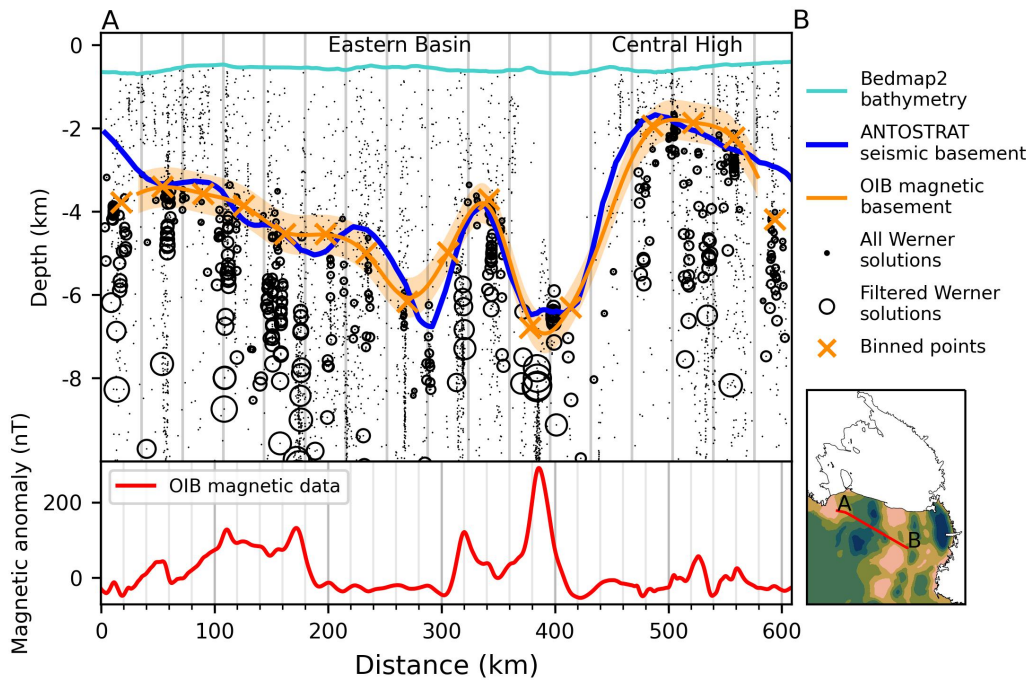


**Figure 2.2:** Ross Sea magnetic and seismic basement comparison. Operation IceBridge airborne magnetic data (lower panel) from segment 403.1 used in Werner deconvolution to produce magnetic anomaly source solutions (black dots). Filtering removed shallow solutions, and remaining solutions (circles scaled to magnetic susceptibility) were binned and interpolated to produce the magnetic basement (orange line with uncertainty band).

808 zones of shallow basement, 3) high gradient gravity anomalies (Figure A.1a, ROSETTA-  
 809 Ice) and 4) large contrasts in sediment thickness. Narrow, deep, linear basins are  
 810 likely to be controlled by active faults (e.g. Drenth et al., 2019; Finn, 2002). We  
 811 display the inferred faults upon a base map of crustal stretching factors ( $\beta$ -factor;  
 812 the ratio of crustal thickness before and after extension, Figure 2.4a), using an initial  
 813 crustal thickness of 38 km (Müller et al., 2007), a continent-wide Moho model (An  
 814 et al., 2015), and our basement surface as the top of the crust (Section A.7).

## 815 2.3 Results

816 We find that an almost continuous drape of sediment covers the RIS region (Figure  
 817 2.3b), with only  $\sim$ 3% of the area having  $<$ 200 m of sedimentary cover. Prominent  
 818 beneath the midline of the RIS is a broad NNW-SSE trending basement ridge  
 819 (Figure 2.3a, Mid-Shelf High; MSH), which comprises most of the shallowest ( $<$ 700  
 820 meters below sea level (mbsl)) sub-RIS basement, with several regions with as little  
 821 as 100 m of sedimentary cover. Basement is deeper on the East Antarctic side of  
 822 the MSH, where it averages  $\sim$ 2400 mbsl, compared to an average depth of  $\sim$ 1900  
 823 mbsl on the West Antarctic side (Figure 2.3a histogram). Sedimentary fill is  $\sim$ 400  
 824 m greater and more uniformly distributed on the East Antarctic side than the West  
 825 Antarctic side (Figure 2.3b histogram).

826 To estimate our uncertainty (Section A.8), we examined the misfit between OIB  
 827 and ANTOSTRAT basement (Figures 2.2 & A.2) and between our basement and

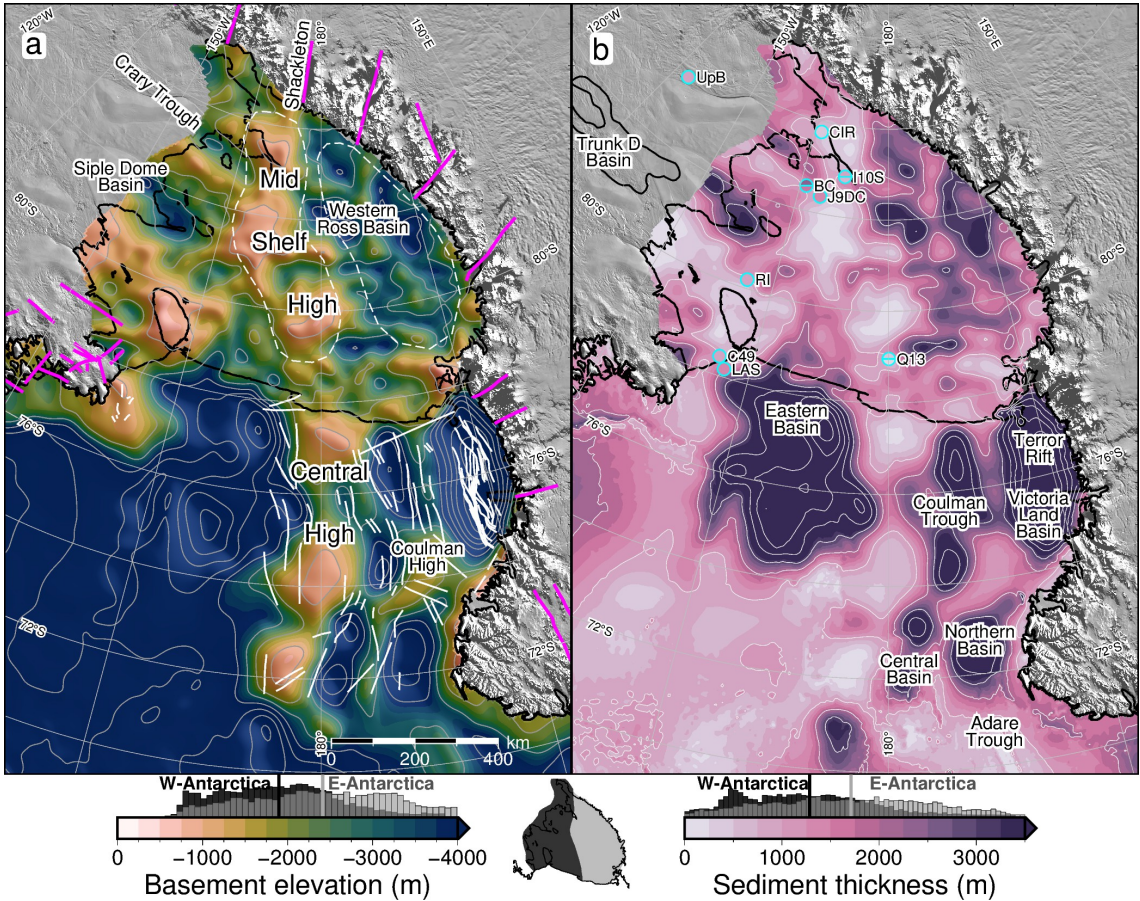


**Figure 2.3:** (a) Basement elevation (magnetic for Ross Ice Shelf (RIS), seismic elsewhere) contoured at 1 km intervals. Pink lines are onshore mapped and inferred faults (Ferraccioli et al., 2002; Goodge, 2020; Siddoway, 2008). White lines are offshore faults (Chiappini et al., 2002; Luyendyk et al., 2001; Salvini et al., 1997; Sauli et al., 2021). Dashed white lines show Mid Shelf High and Western Ross Basin extents. (b) Sediment thickness contoured at 1km intervals. Previous basement-imaging RIS seismic surveys (cyan circles, Table A.1) are plotted on same color scale, with upper and lower uncertainty ranges as circle halves, where reported. Trunk D Basin outlined in West Antarctica (Bell et al., 2006). Color scales for both a) and b) are set to sub-RIS data range. Colorbar histograms show data distribution for East vs West Antarctic sides of the sub-RIS, separated by the Mid-Shelf High. Inset map shows East vs West divide. Vertical lines on histograms denote average values of each side.

829 OIB basement (Figures A.3e&f). There is a median misfit of 480 m (22% of average  
 830 RIS depth) for basement (Figures A.5 & A.6). A similar 470 m median basement  
 831 misfit is estimated by comparing our results to eight active source seismic surveys  
 832 (Figure 2.3b, Table A.1). Incorporating the ~70 m uncertainty in the bathymetry  
 833 model (Tinto et al., 2019), our representative sediment thickness uncertainty is 550  
 834 m (37% of average RIS thickness, Figure A.5).

835 A single broad and deep basin (300 x 600 km) separates the MSH and the  
 836 Transantarctic Mountains (TAM) (Figure 2.3a, Western Ross Basin). The Western  
 837 Ross Basin parallels the TAM and has the deepest-observed sub-RIS basement  
 838 depths of 4500 mbsl, accommodating sediments up to 3800 m thick (Figure 2.3b).  
 839 It contains a long, narrow NW-SE trending ridge with ~1500 m structural relief  
 840 above the basement sub-basins on either side. Bordering the MSH on the east, an  
 841 elongate NW-SE trending basin runs from the RIS calving front to the Siple Coast  
 842 GZ (Figure 2.3a), where beneath Siple Dome we discover a 100 x 200 km depocenter  
 843 reaching basement depths up to 4000 mbsl, with sediments up to 3700m thick. We

refer to this depocenter as Siple Dome Basin, a feature bounded on the east by a basement high that trends southward from Roosevelt Island. This high rises to its shallowest point at the GZ, where its sedimentary cover is less than 100 m. A second deep, narrow basin (50 x 200 km in dimension) is found along the north margin of Crary Ice Rise, separated from the Siple Dome Basin by an NW-SE ridge underlying Kamb Ice Stream. The basin, labelled Crary Trough in Figure 2.3a, reaches basement depths of 3200 mbsl, with sediments 1800-2700 m thick. The southernmost RIS has an additional depocenter with up to 2000 m of fill beneath Whillans Ice Stream (location in Figure 2.1a).

853

Inferred active sub-RIS faults (Figures 2.4a & A.1) correspond to narrow, linear basement basins with high-gradient gravity anomalies, prevalent on the West Antarctic side (Figure A.1a). Inactive normal and strike-slip faults are inferred along lineaments that segment the shallow MSH into blocks and are oriented parallel to TAM outlet glacier faults.  $\beta$ -factors are indicative of thinned crust and are different on either side of the MSH. The TAM side shows higher  $\beta$ -factors (average 1.99) with low variability. The West Antarctic side has lower  $\beta$ -factors overall (average 1.82), but with some higher values up to 2.1 (Figure 2.4a).

## 2.4 Discussion

Sub-RIS sedimentary basins align with and show lateral continuity with the Ross Sea's Roosevelt Sub-Basin, Eastern Basin, Coulman Trough, and Victoria Land Basin (Figure 2.3, e.g. Cooper et al., 1995). The MSH passes northward into the Ross Sea's prominent Central High (CH). At the southern RIS margin, the narrow Siple Dome Basin has continuity with the previously identified Trunk D Basin (Figure 2.3a, Bell et al., 2006). The throughgoing trends imply regional continuity of crustal structure and a common tectonic development of the Ross Sea and RIS regions. Our sediment thicknesses are compatible with those determined by a) eight active-source seismic surveys (Figure 2.3b), for which the median misfit is 470 m (Table A.1), and b) surface wave dispersion indicating 2-4 km of sediment under the RIS, similar to our range, with the maximum beneath Crary Ice Rise (Zhou et al., 2022). Three additional western RIS seismic profiles report up to several kilometers of sediment, in general accordance with our results (Beaudoin et al., 1992; Stern et al., 1991; ten Brink et al., 1993). Additionally, machine learning applied to geophysical datasets predicts a high likelihood of sedimentary basins at the locations of Siple Dome Basin and Crary Trough (Li et al., 2022).

### 2.4.1 West Antarctic Rift System extensional basins

The Western Ross Basin has a configuration similar to the western Ross Sea rift basins (e.g. Salvini et al., 1997) with a broad and deep basin, separated into distinct depocenters by a linear, low relief ridge. The deeper of the depocenters, on the TAM side of the ridge, coincides with alternating high and low free-air gravity anomalies (Figure A.1a). These similarities suggest the sub-RIS continuations of Coulman Trough and Victoria Land Basin (Figure 2.3b) likely share a common tectonic origin as fault-controlled basins (Figures 2.3a & 2.4a) formed through Cretaceous distributed continental extension across the WARS (Jordan et al., 2020a). These sub-RIS basins terminate against the southern segment of the MSH (Figure

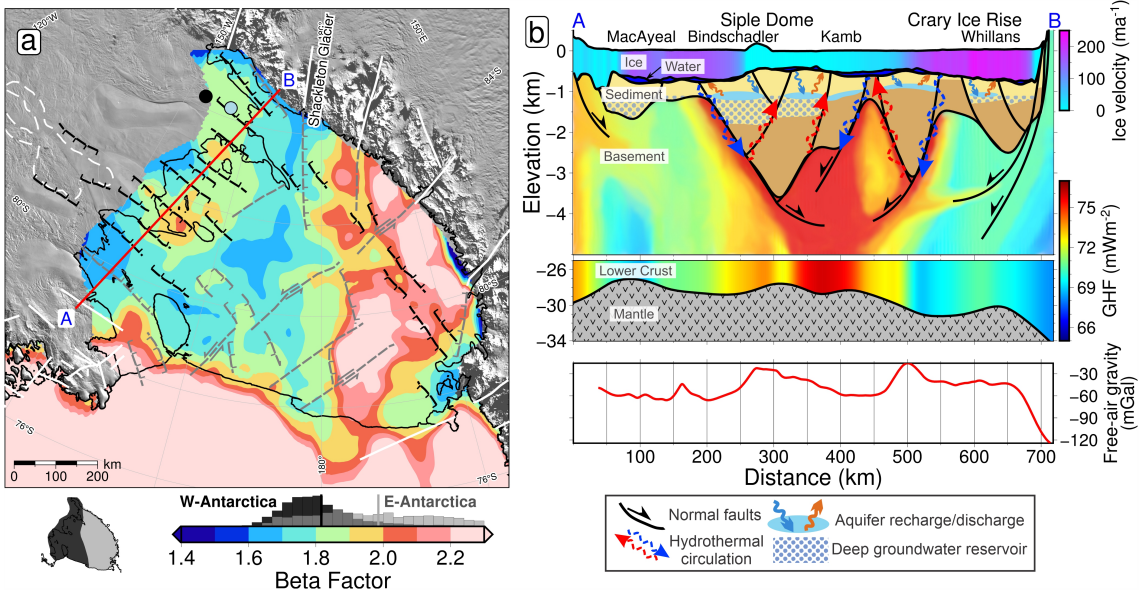


**Figure 2.4:** Tectonic interpretation of the sub-Ross Ice Shelf (RIS). **(a)**  $\beta$  stretching factors (Section A.7). Colorbar histogram shows data distribution of West vs. East Antarctic sides, same as Figure 2.3. Black and grey lines indicate inferred active and inactive faults, respectively, with kinematics shown with half-arrows (strike or oblique-slip) and hachures (normal-sense). White lines show previously reported faults, same as Figure 2.3a. Dashed-white outline is Trunk D Basin (Bell et al., 2006). Black and blue dots show Subglacial Lake Whillans and sedimentary basin from Gustafson et al. (2022), respectively. Cross-section A-B in red. **(b)** Siple Coast cross-section from A-B, showing basin sediments bounded by faults, with geothermal heat flux (GHF) through the crust (lower panel from Burton-Johnson et al. (2020), upper panel interpreted). Ice surface, ice base, and bathymetry from Morlighem et al. (2020). Ice streams coloured by velocity (Mouginot et al., 2019; Venturelli et al., 2020). Moho is from Shen et al. (2018a). Lower panel shows ROSETTA-Ice gravity. Named features are labelled on top.

889 2.3a).

890

891 The linear ridge within the Western Ross Basin (Figure 2.3a) may be an ex-  
892 pression of normal or oblique faults linked to the southward-narrowing Terror Rift  
893 (Sauli et al., 2021), formed due to Cenozoic oceanic spreading in the Adare Trough  
894 (Figure 2.3b, Granot & Dyment, 2018). The Western Ross Basin, with up to 3800  
895 m of fill, terminates along the prominent edge of the MSH that lines up with the  
896 fault-controlled trough and crustal boundary that passes southward beneath Shack-  
897 leton Glacier (Borg et al., 1990). We interpret the basement lineament (Figure 2.4a)  
898 as a transfer fault separating sectors of crust extended to different degrees.

899

900 The southeastern RIS margin is distinguished by linear ridges and narrow, deep  
901 basins. The prominent NW-SE basement trends coincide with high-gradient gravity  
902 anomalies (Figure A.1a, Tinto et al., 2019) and thick sediments, suggesting normal  
903 fault control and active divergent tectonics beneath the GZ. Our Siple Coast cross-  
904 section (Figure 2.4b) displays dramatic basement relief, exceeding 2 km, in the Siple  
905 Dome Basin and Crary Trough, which we attribute to displacement upon high angle  
906 faults. Portions of basin-bounding faults were previously detected by ground-based  
907 gravity surveys upon the Whillans Ice Stream flank (Figure 2.4a, Muto et al., 2013b)  
908 and site J9DC (Figure 2.3b), where large variations in sediment thickness indicate  
909 up to 600 m of fault throw (Grieschar et al., 1992). The continuity between the  
910 narrow Siple Dome Basin (this study) and the Trunk D Basin (Figure 2.3a, Bell et

911 al., 2006) suggests that the active tectonic domain continues southward past the GZ.  
 912 The fault-controlled tectonic basins may reflect a crustal response to the lithospheric  
 913 foundering hypothesized beneath the South Pole region (Shen et al., 2018b) or be a  
 914 broader regional expression of Neogene extension that formed the Bentley Subglacial  
 915 Trench (Lloyd et al., 2015).

### 916 2.4.2 Consequences for ice sheet dynamics

917 Our basement topography and suggested crustal faults likely exert a strong influence  
 918 on the overriding ice, especially along the Siple Coast. Here, we show deep and thick  
 919 sedimentary basins which likely contain voluminous basinal aquifers (Figure 2.4b; cf.  
 920 Gustafson et al., 2022). Where these aquifers discharge along fault-damage zones,  
 921 they can enhance GHF and promote basal melting (Gooch et al., 2016), as depicted  
 922 in Figure 2.4a. The elevated GHF seen at Subglacial Lake Whillans (285 mW/m<sup>2</sup>,  
 923 Fisher et al., 2015) may arise from fault localization (Figure 2.4a). Confinement  
 924 of the aquifers between the ice bed and low-permeability basement may promote  
 925 fluid overpressure, enabling ice streaming (e.g. Ravier & Buoncristiani, 2018). Ad-  
 926 ditionally, the Siple Coast faults likely accommodate the solid Earth's response to  
 927 fluctuating ice volume. A matter receiving considerable debate (Lowry et al., 2019;  
 928 Neuhaus et al., 2021; Venturelli et al., 2020), is Kingslake et al.'s 2018 finding of  
 929 rapid re-advance of the Siple Coast GZ following Holocene deglaciation. The re-  
 930 advance was in part due to swift glacioisostatic rebound (cf. Coulon et al., 2021;  
 931 Lowry et al., 2020), a process aided by the region's low-viscosity mantle (White-  
 932 house et al., 2019) and likely to be accommodated upon pre-existing crustal faults,  
 933 as observed in the Lambert Graben (Phillips & Läufer, 2009). Our proposed graben-  
 934 bounding faults would provide a tectonic control on the glacioisostatic adjustment  
 935 of the Siple Coast region.

### 936 2.4.3 Mid-Shelf High - Central High

937 The 650-km-long Mid-Shelf High features three shallow, blocky segments >150 km  
 938 in breadth, which have only thin sediment cover (<200 m). At their shallowest  
 939 points, the top of basement lies within ~30 0m of the ice shelf base, at a depth  
 940 comparable to the basement high at Roosevelt Island. Roosevelt Island is a modern  
 941 pinning point (Still et al., 2019) owing to the thicker sediment, there (Figure 2.3b).  
 942 We introduce the MSH as a prominent pinning point at times of advance and greater  
 943 extent of the Antarctic Ice Sheet, in keeping with evidence from subglacial sediment  
 944 records that indicate a major ice flow divide between East and West Antarctic ice  
 945 during and since Last Glacial Maximum (Coenen et al., 2019; Li et al., 2020; Licht  
 946 et al., 2014).

947  
 948 The prominence of the MSH is due in part to the contrasting geologic proper-  
 949 ties of the East versus West Antarctic type crust and their respective responses to  
 950 WARS extension. We distinguished  $\beta$ -factors on the TAM-side that are high and  
 951 uniform, indicating distributed crustal extension. The West Antarctic side displays  
 952 lower  $\beta$ -factors overall, but with localized extreme thinning beneath Siple Coast  
 953 (Figure 2.4a). The greater amount of extension on the East Antarctic side coincides  
 954 with the deeper bathymetry (Figure 2.1a), deeper basement, and thicker sediments  
 955 (Figure 2.3). The contrasting properties are also evident in ROSETTA-Ice magnetic

and gravity anomalies, used by Tinto et al. (2019) to identify a north-south trending tectonic boundary along the midline of Ross Embayment. The MSH in the magnetic basement coincides with and spans this boundary, which has been further substantiated by passive-seismic studies that show a lithospheric-scale boundary (Cheng et al., 2021; White-Gaynor et al., 2019). To the north, the features continue into the Ross Sea’s Central High. Southward, the MSH basement feature trends into the TAM, where its western edge aligns with Shackleton Glacier, occupying a major fault separating the distinct geologic domains of the central and southern TAM (Borg et al., 1990; Paulsen et al., 2004), which also parallels a prominent magnetic lineament at the South Pole (Studinger et al., 2006). The structure may be an expression of the East Antarctic craton margin or a major intracontinental transform (Figure 2.4a, Studinger et al., 2006).

968

At the time of Oligocene initiation of the Antarctic Ice sheet, paleotopographic reconstructions of the proto-Ross Embayment depict a long, broad range, emergent above sea level (Paxman et al., 2019; Wilson et al., 2012), that we equate to the MSH-CH that divides the Embayment. The CH hosted small ice caps with alpine glaciers formed during the initial glacial stage in the region (De Santis et al., 1995), and continental ice expanded to the outer Ross Sea continental shelf from those centres (Bart & De Santis, 2012). Between the late Oligocene and mid-Miocene, the CH subsided by up to 500 m (Kulhanek et al., 2019; Leckie, 1983), receiving 100’s of meters of sediment cover ( $\sim$ 400 m at DSDP 270; De Santis et al., 1995). The geophysical similarities and continuity between the Ross Sea’s CH and the RIS’s MSH imply a similar glaciation and subsidence history for the MSH. A terrestrial/alpine stage for the MSH helps to explain the region’s potential to hold the late Oligocene’s larger-than-modern ice volumes (Pekar et al., 2006; Wilson et al., 2013), with the MSH-CH having a central role in Oligocene ice sheet development and the subsequent evolution of the ice sheet and ice shelf, as is documented in the Ross Sea (Halberstadt et al., 2016).

#### 2.4.4 Thermal subsidence and sedimentation

Incorporating the updated basement basin extents and geometries into post-rift thermal subsidence modelling will enable better-constrained paleotopographic reconstructions. For the sub-RIS, these reconstructions (Paxman et al., 2019; Wilson et al., 2012) use a post-Eocene subsidence model based on gravity-derived basin geometries and uniform  $\beta$ -factors (Wilson & Luyendyk, 2009). This model predicts uniform stretching of the eastern sub-RIS from the ice front to the Siple Coast, while our  $\beta$ -factors show increasing stretching from the ice front to the Siple Coast. This observed additional thinning likely has resulted in more subsidence for Siple Dome and the north flank of Crary Ice Rise, which can now be accounted for in reconstructions. Our sediment thickness comparison with past models (Section A.7, Wilson & Luyendyk, 2009) shows the majority of the sub-RIS, especially the Siple Coast, contains more total sediment than previously estimated (Figure A.1f). Depending on the age of this sediment, reconstructions may need to account for the additional sediment deposition and loading.

## 1000 2.5 Conclusions

1001 Here we present a depth to magnetic basement map for the Ross Ice Shelf (RIS)  
 1002 from Werner deconvolution of airborne magnetic data. The RIS magnetic basement  
 1003 is tied to Ross Sea seismic basement, providing the first synthetic view of Ross  
 1004 Embayment crustal structure. Using a bathymetry model, we obtain the sediment  
 1005 thickness distribution and calculate crustal extension factors for the sub-RIS. The  
 1006 extensional features we image, resulting from West Antarctic Rift System extension,  
 1007 have continuity with Ross Sea basement structures to the north, and the prominent  
 1008 Mid-Shelf High trends northward into the Ross Sea's Central High. This combined  
 1009 high separates East and West Antarctic type crust, affected by different degrees  
 1010 of continental extension. The Mid-Shelf High was likely subaerial in the Oligocene,  
 1011 able to support alpine ice caps in early Antarctic glaciation. Subsequently, it formed  
 1012 a prominent pinning point and ice flow divide between the East and West Antarctic  
 1013 Ice Sheets.

1014  
 1015 Newly identified narrow, linear, deep sedimentary basins provide evidence of  
 1016 active faults beneath the Siple Coast grounding zone, where thinned crust overlying  
 1017 anomalous mantle (Shen et al., 2018a) likely experiences elevated geothermal heat  
 1018 flow promoting the formation of subglacial water. Faults that control basement  
 1019 margins may accommodate motion caused by the glacioisostatic response to ice sheet  
 1020 volume changes. Subglacial sedimentary basins in this setting likely contain confined  
 1021 aquifers within permeable basin fill. Here, ice overburden pressure would control  
 1022 flow both between and within the subglacial and groundwater systems, possibly  
 1023 localizing geothermal heat. Updated sediment thickness and basin extents should be  
 1024 incorporated into new paleotopographic reconstructions of time intervals of interest  
 1025 for paleo-ice sheet modelling. Our work contributes critical information about Ross  
 1026 Embayment basement topography and subglacial boundary conditions that arise  
 1027 from an interplay of geology, tectonics, and glaciation.

## 1028 2.6 Open Research

1029 ROSETTA-Ice and Operation IceBridge magnetics data are available through <https://www.usap-dc.org/view/project/p0010035> and <https://nsidc.org/data/IMCS31b>,  
 1030 respectively. Results from this study are available to download from <https://doi.pangaea.de/10.1594/PANGAEA.941238> and a Jupyter notebook documenting our  
 1031 workflow and figure creation is available at <https://zenodo.org/badge/latestdoi/470814953>.  
 1032  
 1033

## 1035 2.7 Acknowledgements

1036 Funding support from the New Zealand Ministry of Business and Innovation and  
 1037 Employment through the Antarctic Science Platform contract (ANTA1801) Antarctic  
 1038 Ice Dynamics Project (ASP-021-01) and the National Science Foundation (1443497  
 1039 and 1443534), and Antarctica New Zealand. We are grateful to Robin Bell, Isabel  
 1040 Cordero, Alec Lockett, Joel Wilner, Zoe Krauss, and the entire ROSETTA-Ice team  
 1041 for undertaking the ambitious data acquisition and processing effort. We thank

1042 Katharina Hochmuth and Guy Paxman for thoughtful reviews which greatly im-  
1043 proved the manuscript, as well as Chris Sorlien, Tim Stern, Simon Lamb, Lara  
1044 Pérez, Ryan Venturelli, Wei Ji Leong, and Dan Lowry for valuable input. Figures  
1045 used GMT6/PyGMT (Uieda et al., 2021; Wessel et al., 2019), with a script adapted  
1046 from Venturelli et al. (2020). Geosoft Oasis Montaj™ was used for magnetics pro-  
1047 cessing and Werner deconvolution. Open access publishing facilitated by Victoria  
1048 University of Wellington, as part of the Wiley - Victoria University of Wellington  
1049 agreement via the Council of Australian University Librarians.

1050

1051 Chapter 2, in full, is a reprint of material as it appears in *Geophysical Re-*  
1052 *search Letters*: Tankersley, M. D., Horgan, H. J., Siddoway, C. S., Caratori Tontini,  
1053 F., & Tinto, K. J. (2022). Basement topography and sediment thickness beneath  
1054 Antarctica's Ross Ice Shelf. *Geophysical Research Letters*, 49, e2021GL097371.  
1055 <https://doi.org/10.1029/2021GL097371>. The only changes made from the published  
1056 version include formatting and replacing preprint citations with accepted paper cita-  
1057 tions. I conceived the study with my co-authors, undertook the study and analysis,  
1058 and wrote the manuscript myself.

1059 **Chapter 3**

1060 **Gravity inversion: a tool for  
1061 bathymetry modelling**

1062 **Abstract**

1063 Sub-ice-shelf bathymetry exerts a primary control on the stability of many Antarctic  
1064 ice shelves through the geometry of pinning points and the guiding of melt-inducing  
1065 water masses. Collecting sub-ice-shelf bathymetry data using typical polar sur-  
1066 veying methods (e.g. seismic surveying or direct observations) can be inefficient,  
1067 expensive or unfeasible. Gravity inversions provide a more practical alternative,  
1068 in which observed variations in Earth's gravitational field are used to predict the  
1069 bathymetry. This chapter describes a gravity inversion algorithm developed specifi-  
1070 cally for modelling bathymetry. The inversion is tested on a suite of models, created  
1071 with a combination of synthetic and real bathymetric data. These tests provide the  
1072 ability to 1) determine the best practices for conducting bathymetric inversions, 2)  
1073 recognize the limitations of the inversions, and 3) identify where community efforts  
1074 should be focused for the future of modelling Antarctica's sub-ice-shelf bathymetry.  
1075 We find that estimating and removing the regional component of gravity prior to  
1076 the inversion is the largest source of error in the resulting bathymetry model. To  
1077 address this, we propose procedures to limit this error and provide recommendations  
1078 on the minimum spatial density of bathymetry constraint points. Additionally, for  
1079 common airborne gravity survey designs, we find minimizing noise in the data is  
1080 more important than collecting closer-spaced data.

1081 **Plain Language Summary**

1082 The shape of the seafloor beneath the floating extensions of the Antarctic Ice Sheet  
1083 exerts important controls on the ice. Controls include how the seafloor topography  
1084 (bathymetry) directs the flow of warm water masses which causes melting at the  
1085 base of the ice, and determines where ice is anchored to the bedrock. Conventional  
1086 methods of collecting data on bathymetry are ineffective, impractical, or expensive  
1087 when applied to ice shelves. One alternative method of acquiring sea floor depths  
1088 is a method called gravity inversion. Variations in bathymetry can be detected by  
1089 measurements of Earth's gravity over an ice shelf as a result of the difference in  
1090 density between seawater and the seafloor. Here, we develop a refined technique for  
1091 performing a gravity inversion and test the method on artificial data to examine its

effectiveness and learn which parts of the inversion are most prone to errors. We find that removing the portion of the gravity data that results from deep geologic structures is the largest source of error. To limit the impact of this and other sources of error in the inversion, we suggest researchers focus on collecting as many point measurements of bathymetry depth (from seismic surveys) and attempt to limit the noise in the gravity data as much as possible.

**Key Points:**

1. We present a new constrained geometric gravity inversion algorithm for recovering density contrasts.
2. Synthetic models show the regional-residual separation of the gravity data prior to inversion is the dominant source of error.
3. Quality over quantity for gravity data; efforts should be focused on reducing noise not increasing coverage.

## 3.1 Introduction

In the last two decades, the Antarctic Ice Sheet has experienced significant ice mass loss, averaging 118 billion tons per year, contributing 5.2mm to sea-level rise (Smith et al., 2020a). This mass loss has been concentrated along the coast, where ocean currents are able to bring warm waters in contact with the ice (Rignot et al., 2019). Much of Antarctica is fringed with floating extensions of the ice sheet, known as ice shelves (Figure 3.1). These ice shelves provide a critical buttressing effect on the upstream ice, slowing the flow of ice from the continent into the oceans (Dupont & Alley, 2005). This buttressing results from lateral drag along the margins of the ice shelf and friction between the ice and the bed at pinning points. Thinning of the ice shelves lowers these resistive forces. Due to the cold climate and lack of surface melt, the majority of Antarctic ice shelves' thinning occurs as basal melt. This basal melt (Figure 3.1b) occurs from contact with relatively warm ocean waters, such as circumpolar deep water and high-salinity shelf water (CDW and HSSW) (Jenkins et al., 2010; Rignot et al., 2019).

These deep-lying warm masses of water originate offshore from the ice shelves and thus can only induce basal melting if they circulate under the shelves. A large enough ocean draft, the distance between the ice base and the bathymetry (Figure 3.1a), is required for this circulation to be possible. This connection between ocean draft and basal melting is shown by generally low ice shelf basal melt rates for shelves, or sections of shelves, with shallow ocean drafts (e.g. Pritchard et al., 2012; Tinto et al., 2019). Additionally, deep bathymetric troughs in regions of otherwise thin drafts, or conversely, bathymetry ridges in regions of thick drafts, can control the incursion of these water masses (St-Laurent et al., 2013; Yang et al., 2021).

While the elevation of the ice base for many of Antarctica's ice shelves is relatively well-constrained, the water depth is poorly known. The relatively good understanding of the ice base comes from a combination of airborne radar surveys (e.g. Das et al., 2020) and satellite altimetry measurements (e.g. Griggs & Bamber, 2011), in conjunction with the hydrostatic equilibrium assumption (Bamber & Bentley, 1994). Conversely, there is no equivalent fast and cheap technique to directly survey the bathymetry beneath floating ice shelves. Radar (ground or airborne)

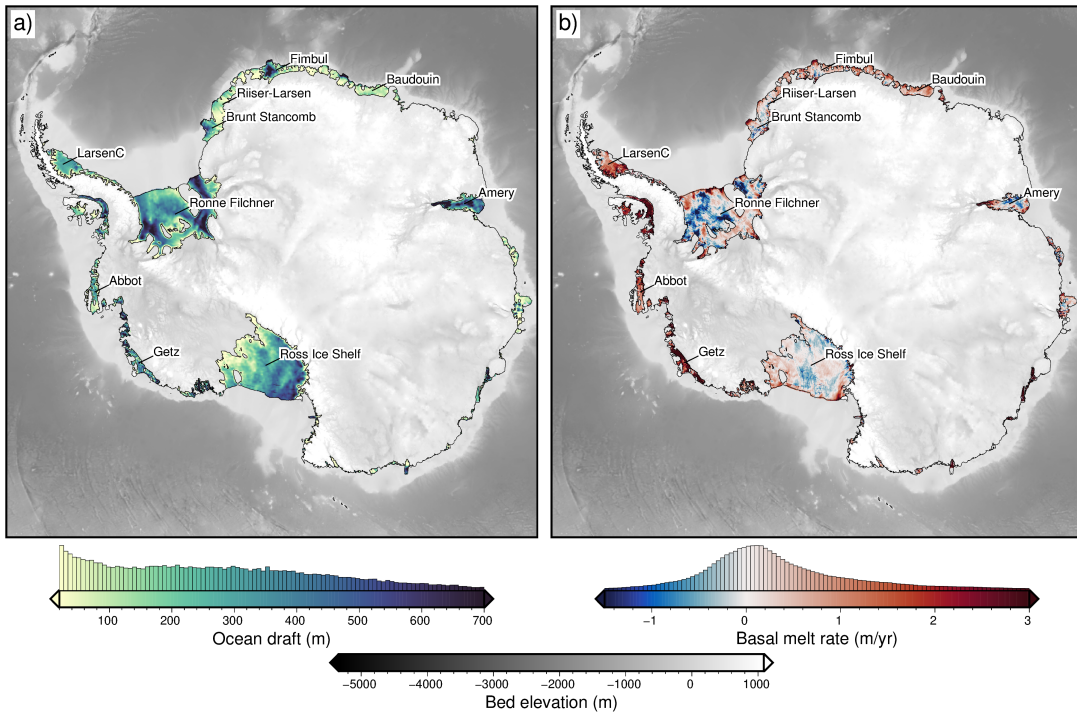


**Figure 3.1:** Ice shelves of Antarctica. **a)** Water column thickness beneath the ice shelves from Bedmachine data (Morlighem, 2022; Morlighem et al., 2020). **b)** Basal melt rate for the ice shelves from Adusumilli et al. (2020). Both plots show bed elevations in the gray colormap. The 10 largest ice shelves are labelled.

cannot image through the thick water, over-ice seismic surveys are slow and expensive, and numerous direct observations through drill holes are impractical. Due to the density contrast between the water and the sediment, the bathymetry surface produces a measurable gravity signal. This signal can be observed from airborne or ground-based gravity surveys, which provides a method, if used correctly, to model sub-shelf bathymetry. This method is a gravity inversion; a geophysical technique to take measurements of an energy source and estimate the physical properties responsible for these measurements (e.g., Menke, 2012; Oldenburg & Li, 2005; Tarantola, 2005). In this case, the energy source is Earth's gravitational field and the physical Earth property is the depth of the density contrast between the ocean and seafloor. This chapter will first introduce the gravity inversion technique in general, followed by the specific style of gravity inversion, a geometric inversion, which is used here. Next, a suite of synthetic models will be used to assess the performance and limitations of the inversion. The suite of models includes:

1. a simple synthetic topography.
2. a synthetic topography with a regional component of the gravity signal.
3. a semi-realistic model, using real Antarctic bathymetry and basement topographies to create the synthetic observed gravity.

With this suite of models, we will test the effects of various levels of noise, the data spacing of the observed gravity, the number of prior constraints, and various inversion methods and parameters. Finally, we will discuss the general limitations of using gravity inversions to recover bathymetry and will provide guidance for conducting gravity inversion for sub-ice-shelf bathymetry.

## 1159 3.2 Methods

1160 There are two fundamental types of geophysical modelling, forward modelling, and  
 1161 inverse modelling. Forward modelling is the process of simulating observed data  
 1162 from a model of physical properties. For a gravity application, this may be calcu-  
 1163 lating the gravitational field resulting from a sedimentary basin of a given geometry  
 1164 and/or density model. In general, forward problems are well-posed, meaning there  
 1165 is a unique answer (Oldenburg & Li, 2005). In contrast, inverse modelling, or in-  
 1166 version, is the process of determining physical properties from observed data. For  
 1167 the previous example, this would entail using observed gravity data to predict the  
 1168 sediment thickness of a basin. Inverse problems are generally ill-posed. For a given  
 1169 set of gravity observations, there is a multitude of sedimentary basin configurations  
 1170 which reproduce the observed data with the same degree of accuracy. This is re-  
 1171 ferred to as non-uniqueness and makes geophysical inversions a difficult procedure  
 1172 compared to forward modelling.

### 1173 3.2.1 Geophysical inversion

1174 In general, inversions consist of three components;

- 1175 1. Forward operator ( $f$ ): This is a mathematical means of linking a physical  
 1176 Earth property to the expected geophysical response. It accomplishes the task  
 1177 of forward modelling, as described above.
- 1178 2. Physical property model ( $p$ ): This is a representation of the physical Earth  
 1179 property of interest. While real-world properties are continuous (i.e. a smoothly  
 1180 varying topography), computation often necessitates discretization (i.e. a  
 1181 DEM (digital elevation model), see section 3.2.2.1). The starting model ( $p_0$ )  
 1182 typically will include the prior geologic knowledge of the region. To discretize  
 1183 the topography we use a layer of adjacent, vertical right-rectangular prisms.
- 1184 3. Fit function ( $\phi$ ): This function describes the similarity between the observed  
 1185 data and the predicted data (resulting from the forward calculation of the  
 1186 property model ( $f(p)$ )). The goal of the inversion is to minimize this function  
 1187 so that  $f(p)$  is as close to the observed data as possible.

1188 Here, a mathematical derivation of a generalized discrete inversion problem is  
 1189 shown, following closely to the derivation of Oliveira and Uieda (2014). The inversion  
 1190 problem can be framed as finding the set of physical parameters ( $\vec{p}$ ) which when  
 1191 modelled with the forward operator ( $f$ ) produce predicted data ( $\vec{d}^{pred}$ ) as close  
 1192 to the observed data ( $\vec{d}^{obs}$ ), as possible. This inversion is discrete because the  
 1193 topography is represented with a series of grid cells, instead of a continuous function.  
 1194 The difference between the observed and predicted data gives the misfit  $\vec{m}$ , where

$$\vec{m} = \vec{d}^{obs} - \vec{d}^{pred} = \vec{d}^{obs} - \vec{f}(\vec{p}). \quad (3.1)$$

1195 Here, the squared  $\ell^2$ -norm (mean squared error) of the misfit is the metric used  
 1196 to define the *closeness* between the predicted and observed data, where

$$||\vec{m}||_2^2 = \sum_{i=1}^N [d_i^{obs} - \vec{f}_i(\vec{p})]^2, \quad (3.2)$$

1197 where  $N$  is the number of observed data points.

1198 This is defined as the *fit function*,  $\phi(\vec{p})$ . The fit function can also be expressed

1199 as

$$\phi(\vec{p}) = \vec{m} \cdot \vec{m} = [\vec{d}^{obs} - \vec{f}(\vec{p})] \cdot [\vec{d}^{obs} - \vec{f}(\vec{p})]. \quad (3.3)$$

1200 In this context, the inversion problem is to determine a vector of parameters  $\tilde{\vec{p}}$   
 1201 of length  $M$  which minimizes  $\phi(\vec{p})$ . This minimum occurs where the gradient of  
 1202  $\phi(\vec{p})$  at the vector  $\tilde{\vec{p}}$  has zero length. The gradient of  $\phi(\vec{p})$  evaluated at any  $\vec{p}$  is  
 1203 an  $M$ -dimensional vector is defined as

$$\nabla \phi(\vec{p}) = \begin{bmatrix} \frac{\partial \phi(\vec{p})}{\partial p_1} \\ \frac{\partial \phi(\vec{p})}{\partial p_2} \\ \vdots \\ \frac{\partial \phi(\vec{p})}{\partial p_M} \end{bmatrix}. \quad (3.4)$$

1204 Evaluating the gradient at the  $i^{\text{th}}$  element, using Equation 3.3 gives

$$\begin{aligned} \frac{\partial \phi(\vec{p})}{\partial p_i} &= \frac{\partial}{\partial p_i} \sum_j [d_j^{obs} - f_j(\vec{p})] \cdot [d_j^{obs} - f_j(\vec{p})] \\ &= \sum_j \frac{\partial}{\partial p_i} [d_j^{obs} - f_j(\vec{p})] \cdot [d_j^{obs} - f_j(\vec{p})] \\ &= -2 \sum_j \frac{\partial f_j(\vec{p})}{\partial p_i} \cdot [d_j^{obs} - f_j(\vec{p})] \end{aligned} \quad (3.5)$$

1205 Substituting Equation 3.5 into the elements of Equation 3.4 gives

$$\nabla \phi(\vec{p}) = -2 \mathbb{J}(\vec{p}) [\vec{d}^{obs} - \vec{f}(\vec{p})], \quad (3.6)$$

1206 where  $\vec{p}$  is the parameter vector of dimension  $M$ ,  $\vec{d}^{obs}$  is the observed data  
 1207 vector of dimension  $N$  and  $\mathbb{J}$  is the Jacobian matrix of dimension  $M \times N$ , and is  
 1208 given by

$$\mathbb{J}(\vec{p}) = \begin{bmatrix} \frac{\partial f_1(\vec{p})}{\partial p_1} & \cdots & \frac{\partial f_N(\vec{p})}{\partial p_1} \\ \vdots & \ddots & \vdots \\ \frac{\partial f_1(\vec{p})}{\partial p_M} & \cdots & \frac{\partial f_N(\vec{p})}{\partial p_M} \end{bmatrix} \quad (3.7)$$

1209 Each element of the Jacobian matrix is given by

$$\mathbb{J}_{ij} = \frac{\partial f_j(\vec{p})}{\partial p_i}, \quad (3.8)$$

1210 which is the partial derivative of the  $j^{\text{th}}$  predicted data with respect to the  $i^{\text{th}}$   
 1211 physical parameter. The *Jacobian* ( $\mathbb{J}$ ) is a sensitivity matrix that describes how  
 1212 much the predicted data changes for an infinitesimal change in the physical parame-  
 1213 ter. For example, let's consider the case of a gravity inversion attempting to recover  
 1214 the density of subsurface cubes. The model consists of 100 cubes, and there are 10

1215 observation points. The Jacobian would be a  $100 \times 10$  matrix where  $\mathbb{J}_{1,1}$  (the first  
1216 entry) would be the 1st cube's gravitational derivative with respect to density at the  
1217 first observation point. The Jacobian, therefore, describes how sensitive each pair  
1218 of cubes and observations are to a change in density.

1219

1220 Once the Jacobian is created, a matrix equation of the form  $Ax = b$  is set up,  
1221 where  $A$  is the Jacobian,  $x$  is the unknown variable, and  $b$  is the data misfit.

$$\mathbb{J}\vec{x} = \vec{m} \quad (3.9)$$

1222 A solution to this linear equation can be found directly, by finding the inverse  
1223 or pseudo-inverse matrix of the Jacobian, or iteratively via a least-squares solver  
1224 (Jacoby & Smilde, 2009). The solution gives the correction which when applied to  
1225 the physical parameters of interest minimizes the misfit between the observed data  
1226 and the starting model.

### 1227 3.2.1.1 Non-Linear inversions

1228 The derivative of the forward operator with respect to the parameter of interest  
1229 determines the linearity of an inversion. For a gravity inversion attempting to recover  
1230 rock density, the derivative of gravity with respect to density is constant, and thus  
1231 the inversion is considered linear (Aster et al., 2018). Conversely, a gravity inversion  
1232 attempting to recover the depth to a surface, or the thickness of a layer, is non-linear  
1233 since the vertical derivative of gravity (derivative with respect to depth) is dependent  
1234 on the depth. Non-linear inversion cannot be solved directly, with matrix inversion  
1235 (Jacoby & Smilde, 2009). They must be linearized; which is the purpose of the  
1236 Jacobian matrix. The Jacobian enables a minimum-norm solution to be found with  
1237 an iterative solver, where at each iteration, the calculated corrections ( $\vec{x}$ ) are applied  
1238 to the starting model, the residuals ( $\vec{m}$ ) are recalculated, the Jacobian is updated,  
1239 and Equation 3.9 is solved again, giving a new set of corrections. This is repeated  
1240 until  $\phi(\vec{p})$  is suitably low.

### 1241 3.2.1.2 Geometric inversions

1242 Most gravity inversions aim to recover the distributions of densities in the subsurface.  
1243 For this technique, the model domain is discretized into a series of polygons (for  
1244 2D) or polyhedrons (for 3D), and the inversion aims to predict the density of each  
1245 polygon. This is widely used due to its relevance in mineral exploration (Oldenburg  
1246 & Pratt, 2007). Less commonly used are gravity inversions which aim to recover  
1247 the depth, shape, or volume of features. This style of gravity inversions are referred  
1248 to as geometric inversions. They are typically used to estimate relief of the Moho  
1249 (e.g Borghi, 2022; Uieda & Barbosa, 2017) or the sediment-basement contact (e.g.  
1250 Barbosa et al., 2007; Santos et al., 2015). In this chapter, geometric inversions  
1251 are used to recover the bathymetry. This use case of gravity inversion is unique  
1252 to studying the cryosphere. In locations without ice cover, bathymetry data is  
1253 typically collected with shipborne multi-beam echo sounding, airborne LiDAR, or  
1254 satellite altimetry.

### 3.2.2 Forward modelling

To perform a geometric gravity inversion, first, the gravitational field produced by a topographic surface must be able to be calculated. This topography is approximated as a constant density contrast between the overlying and underlying materials. The topography is often modelled as a series of adjacent vertical right-rectangular prisms. For a certain observation point, the gravitational field produced by this layer of prisms is the sum of the forward gravity of each prism. This forward gravity calculation of a prism is accomplished with the analytical solutions given by Nagy et al. (2000), as implemented in the Python package Harmonica (Fatiando a Terra Project et al., 2023).

#### 3.2.2.1 Discretization

There are several options for discretizing a density contrast as a series of prisms (Figure 3.2). The most conceptually simple method is for the prisms to represent the true density and geometry of the material on either side of the surface (Figure 3.2b). In this method, the topography is represented by the base of the above prisms, and by the tops of the lower prisms. Alternatively, the contrast can be represented by a layer of prisms either above or below the surface, ending at an arbitrary reference, typically the minimum or maximum value of the surface (Figure 3.2c-d). For this, the prism's density values are relative to the medium on the other side of the surface (i.e. if prisms are below the surface, their densities are  $\rho_{below} - \rho_{above}$ ). The last option is to choose a flat reference surface (typically the mean value of the surface or sea level) and create prisms between this and the surface (Figure 3.2e). Prisms above the reference are assigned a positive density contrast ( $\Delta\rho = \rho_{below} - \rho_{above}$ ), and prisms below the surface a negative density contrast ( $\Delta\rho = \rho_{above} - \rho_{below}$ ). All of these methods result in similar forward gravity calculations. Note that the absolute density option (Figure 3.2b) has twice as many prisms as the other options, significantly increasing its computational expense, regardless of whether or not a buffer zone is used.

#### 3.2.2.2 Gravity edge effects

Any forward gravity calculation of a surface will include gravitational edge effects. These effects are typically a decay in the gravitational field towards the edges of the prism model due to the void space (density of 0) beyond the edge of the model. The magnitude of decay is dependent on the average thickness and density of prisms near the edge. Larger or denser prisms create a large contrast with the void space, resulting in a greater amount of decay. Therefore, the absolute density method of discretization (Figure 3.2b) produces the largest edge effects due to the high-density values and large total thickness of the prisms. The relative density methods (Figure 3.2c-d) produce a smaller edge effect, since the prisms are only above or below the surface, reducing their total thickness. The density values are also less than in the absolute density method. The reference surface method (Figure 3.2e) produces the smallest edge effects due to both a) the mean prism thickness being smaller, and b) positive and negative density prisms having opposite edge effects, partially cancelling each other out. This is only applicable if the reference level is located within the range of the values of the surface. Note that with a reference level completely above or below the surface, the reference method becomes identical to methods c)

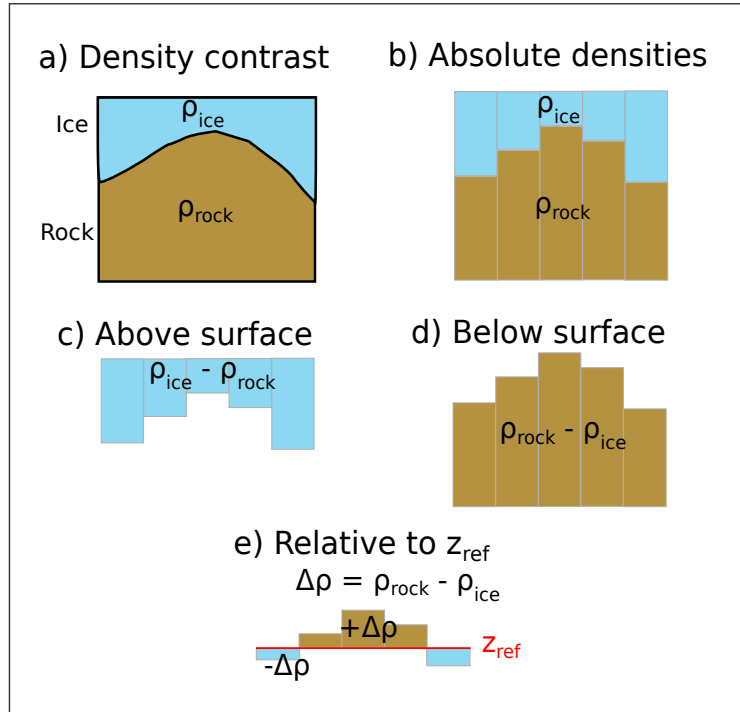


**Figure 3.2:** Equivalent methods of discretizing a density contrast (a) across a surface. b) Use absolute densities of the mediums above and below the reference, with prisms on either side. c-d) Use the density contrast across the surface, with prisms either above or below, and the sign of the density contrast reflecting whether they are above or below. e) Use a reference surface, with prisms above having a positive density contrast and prisms below a negative contrast.

1300 and d) of Figure 3.2.

1301

1302 A buffer zone can be used to reduce the impact of these edge effects by calculating  
 1303 forward gravity confined to an inner region, while the prism model extends beyond.  
 1304 This limits the majority of the edge effects to outside the region of calculation.  
 1305 Too large of a buffer zone will add an unnecessary amount of computation (more  
 1306 prisms), while too small of a zone will introduce unacceptably large edge effects to  
 1307 the calculations.

### 1308 3.2.3 Isolating anomalies

1309 For a successful geometric gravity inversion, the component of the observed grav-  
 1310 ity field resulting from the density contrast of interest must be isolated from all  
 1311 other gravity signals. This section describes the process of isolating the required  
 1312 anomaly. Since this section consists of synthetic gravity, the discussion of correcting  
 1313 raw gravity measurements and deriving the various gravity anomalies is omitted. See  
 1314 Chapter 4 for further discussion of gravity data processing. Here, *synthetic observed*  
 1315 *gravity* is taken to mean the gravity effect resulting solely from deviations between  
 1316 the true synthetic model, and a simple reference model, defined by a flat surface  
 1317 with a constant density above and a constant density below. This is considered a  
 1318 partial topo-corrected gravity disturbance, since the gravity effect of other layers,  
 1319 such as ice and water, if present, is assumed to have been corrected for. The misfit,  
 1320  $\vec{m}$ , in Equation 3.1, is defined as this synthetic observed gravity minus the forward  
 1321 gravity effect of the starting bathymetry.

1322

### 3.2.4 Regional vs. Residual gravity

The topography-free gravity disturbance is often simplified as consisting of two components, the regional and residual fields. The regional field typically dominates the signal and is often the result of deeper and broader structures, such as Moho variations. Superimposed on this signal is the residual field, which is typically the result of shallower structures. The terms residual and regional are relative; here, they are taken to mean the gravity effect of the bathymetry versus that of all deeper structures, respectively. In this inversion, the residual, regional, and misfit are related by

$$\vec{m} = \vec{m}_{res} + \vec{m}_{reg}, \quad (3.10)$$

where  $\vec{m}$  is the overall data misfit, from Equation 3.1. The residual misfit,  $\vec{m}_{res}$ , is the desired input into the inversion, and thus the regional component,  $\vec{m}_{reg}$ , must be removed prior to the inversion. This step proves to be one of the most challenging steps of a bathymetric inversion, especially in areas of limited constraints (Brisbourne et al., 2014). Removing an incorrect regional field, whether it is too much or too little, will directly impact the resulting bathymetry results. Regional-residual separation is also highly non-unique and benefits greatly from *a priori* constraints. Many methods of regional separation rely on the simplifying assumption that the regional field consists of longer-wavelength anomalies, while the residual field dominates the short-wavelength components. Here, four methods of estimating the regional component of gravity are described.

1. Low-pass filter: With the assumption outlined above, a low-pass filter can be used to isolate the regional gravity. For this, a Gaussian wavelength filter is used and the filter width can be varied based on the expected regional anomaly wavelengths. This method requires the data to be gridded over the entire domain, which may be a problem for sparse surveys, or irregularly shaped domains. The choice of wavelength is subjective and needs to be carefully considered. See Eisermann et al. (2020) for a bathymetry inversion utilizing this method of regional separation.
2. Trend removal: Similar to the low-pass filter method, a trend can be fit to the misfit data, representing the regional field. The order of the polynomial trend is subjective and can be varied to suit the data. Again, this parameter choice requires care.
3. Equivalent source prediction: The equivalent sources technique is a method commonly used to grid, smooth, or upward-continue gravity data. It creates a set of point sources with densities, which when forward-modelled, reproduce the measured gravity data. These sources are then used to predict the gravity anomaly at any desired point. The source depths can be varied to achieve the desired regional component. This technique is beneficial over low-pass filter and trend removal in that it does not require the data to be gridded and can thus accommodate sparse surveys, or compilations of surveys at varying altitudes. It is computationally expensive compared to the above methods. Additionally, source depths are a subjective parameter, which needs to be carefully chosen. Past bathymetry inversions have used upward continuation as a means to define the regional field (e.g., Tinto et al., 2015).

1367     4. Constraint point minimization: The last method makes use of constraint points  
 1368     where the bathymetry depths are known. This inversion defines the residual  
 1369     component of the misfit as the gravity effect from deviations of the true  
 1370     bathymetry with respect to the starting bathymetry. At constraints, there is  
 1371     no deviation between the starting and true bathymetries, and thus the residual  
 1372     component of the misfit should be zero at the constraints. This means the total  
 1373     misfit value at the constraints is equal to the regional component (Equation  
 1374     3.10). By sampling the misfit at each constraint, and fitting a surface to these  
 1375     values, a regional component is estimated. This technique has a few advan-  
 1376     tages. It imposes a form of smallness regularization, where the inversion won't  
 1377     significantly alter the depth of the constraint points since the input residual  
 1378     at the points is  $\sim 0$  mGal. Additionally, except for the gridding technique,  
 1379     this method doesn't require a subjective parameter, unlike the other methods.  
 1380     Similar to the low-pass filter and trend removal, this method requires gridded  
 1381     data. If this data is sparse, or the constraints are not located near gravity  
 1382     observation points, some inaccuracies will be introduced. This technique has  
 1383     been used in several bathymetry inversions (An et al., 2019a; Millan et al.,  
 1384     2020; Yang et al., 2021).

1385     Other methods used to approximate the regional component include using high-  
 1386     altitude (satellite) gravity data (Muto et al., 2016; Tinto et al., 2015), the forward  
 1387     modelling of a geologic model, either inferred from 1) other geophysical data (Hodg-  
 1388     son et al., 2019), 2) *a priori* geologic knowledge (Tinto & Bell, 2011), or 3) from an  
 1389     approximated crustal density distribution (Cochran et al., 2020; Tinto et al., 2019).  
 1390     Once estimated, the regional component is then removed from the total misfit, giv-  
 1391     ing the residual misfit. This residual misfit ideally results solely from discrepancies  
 1392     between the starting and true bathymetries.

### 1393     3.2.5 Running the inversion

1394     Here, the necessary steps for running an inversion are explained. First, the Jacobian  
 1395     matrix is calculated (Equation 3.7). Next, the matrix equation (Equation 3.9) is  
 1396     solved, giving the necessary corrections to apply to the bathymetry. Additionally,  
 1397     this solution needs to be constrained to account for the inherent non-uniqueness  
 1398     of the inversion. This is accomplished with various forms of regularization; i.e., a  
 1399     unique solution is determined subject to minimize an additional objective function.

#### 1400     3.2.5.1 Jacobian matrix

1401     The first step of the inversion is to calculate the sensitivity matrix, the Jacobian  
 1402     (Equation 3.7). Each entry of the Jacobian (Equation 3.8) is the vertical derivative  
 1403     of gravity of a prism relative to a single observation point. While a solution exists to  
 1404     the analytical vertical gravity derivative of a prism, we use an approximation to limit  
 1405     the computational expense (Nagy et al., 2000). Here two methods are derived for  
 1406     approximating the vertical gravity derivative resulting from a prism; 1) an annular  
 1407     approximation and 2) a finite differences approach.

#### 1408     Annulus approximation

1409     A vertical prism can be approximated as a sector of an annulus (a cylindrical shell),  
 1410     as in Figure 3.3. This approximation greatly simplifies the calculation of the vertical

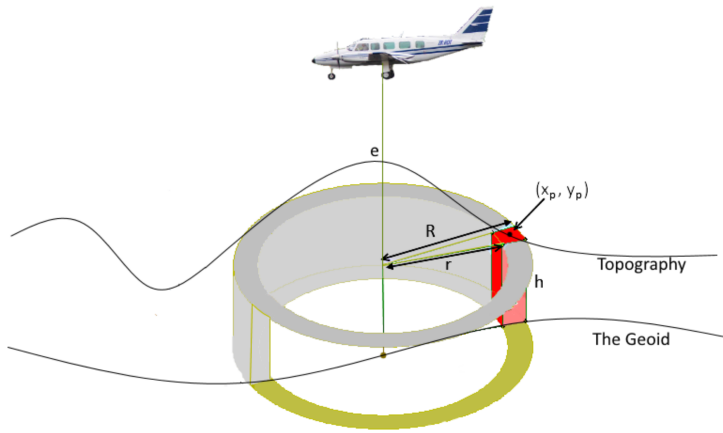


**Figure 3.3:** An illustration of an annulus of topography as an approximation for a vertical prism. From McCubbine (2016).

derivative of the prisms' gravity. The vertical component of gravity of an entire annulus (grey hollow cylinder in Figure 3.3) is defined by

$$\delta g = 2\pi G\rho(R - r + \sqrt{r^2 + h^2} - \sqrt{R^2 + h^2}) \quad (3.11)$$

where  $\rho$  is the density,  $G$  is the gravitational constant,  $r$  and  $R$  are the inner and outer radii, respectively, and  $h$  is the average height of the cylinder (Hammer, 1939).  $r$ ,  $R$ , and  $h$  are relative to the observation point, located in the centre bottom of the annulus. McCubbine (2016) provides an adaption of Equation 3.11 which isolates the gravity of just a portion of this annulus (red section in Figure 3.3). This is accomplished by adding an additional factor  $f$ , relating the area of the annulus to the area of a sector of it:

$$f = \frac{\alpha^2}{\pi(R^2 - r^2)} \quad (3.12)$$

where

$$r = \sqrt{x^2 + y^2} - \sqrt{\frac{\alpha^2}{2}} \quad (3.13)$$

$$R = \sqrt{x^2 + y^2} + \sqrt{\frac{\alpha^2}{2}} \quad (3.14)$$

where  $\alpha$  is the prism width,  $x$ ,  $y$ , and  $z$  are coordinates of the prism centre, relative to the observation point. This factor  $f$  is then multiplied by Equation 3.11 to give the vertical component of gravity for a section of an annulus,  $\delta g_{annulus} = f\delta g$ .

Taking the derivative of this with respect to  $h$  gives

$$\frac{\partial g}{\partial h} = 2f\pi G\rho h \left( \frac{1}{\sqrt{r^2 + h^2}} - \frac{1}{\sqrt{R^2 + h^2}} \right). \quad (3.15)$$

While the approximation of a prism as a section of an annulus introduces some errors, the calculation is efficient and simple to implement.

**1427 Finite differences approximation**

**1428** Another option to calculate the vertical derivative for the Jacobian matrix is with  
**1429** numerical differentiation. For this, a small prism is added above each existing prism,  
**1430** its forward gravity is calculated and the result is divided by the small prism's height.  
**1431** This approximates the vertical derivative of gravity at the surface of the prism, rel-  
**1432** ative to the observation point.

**1433** Both methods adequately determine the Jacobian. The annulus method is a  
**1434** more simple calculation and is thus faster, but is likely less accurate and introduces  
**1435** singularities. These singularities occur if the prism is directly beneath the observa-  
**1436** tion point, so that either the inner or outer radii are negative (Figure 3.3). These  
**1437** singularities are resolved by shifting the observation point to a prism edge. Con-  
**1438** versely, the finite differences method, while it is a numerical approximation, uses  
**1439** analytical solutions for calculating the forward gravity (Fatiando a Terra Project  
**1440** et al., 2023; Nagy et al., 2000), and thus is valid in the entire domain, with no sin-  
**1441** gularities. This increased robustness makes the computation slower. Section 3.3.1.3  
**1442** compares the effectiveness and computation time of both of these methods.

**1444 3.2.5.2 Least-squares solver**

**1445** With the Jacobian matrix and the vector of gravity residuals, Equation 3.9 can be  
**1446** solved to find the set of surface correction values that minimize the fit function.  
**1447** Here, the matrix equation  $\mathbb{J}\vec{x} = \vec{r}$  is solved with an iterative damped least squares  
**1448** algorithm (LSQR Paige & Saunders, 1982). The algorithm gives the minimum-norm  
**1449** solution, where for a set of solutions that each fit the data with the same accuracy,  
**1450** the solution with the minimum  $\|p\|^2$  is chosen. LSQR accepts a damping parameter,  
**1451** which helps regularize the problem, preventing the solution from becoming too large.  
**1452** The choice of the damping value is important as it directly affects the inverted  
**1453** results. The optimal value can be chosen with a cross-validation routine following  
**1454** that of Uieda and Barbosa (2017), as described below.

**1455 3.2.5.3 Regularization**

**1456** Regularization is a series of techniques used to help constrain ill-posed inversion  
**1457** problems (Aster et al., 2018). Most potential field inversions, due to their inher-  
**1458** ent non-uniqueness, are ill-posed, containing many solutions which equally satisfy  
**1459** the data. Here regularization is split into *smallness* and *smoothness*. *Smallness*  
**1460** deals with adhering to *a priori* constraints, i.e. having the inverted surface eleva-  
**1461** tion match the previous bathymetry measurements (constraint points). *Smoothness*  
**1462** helps to achieve realistic topographic results, without major jumps or excessively  
**1463** steep slopes.

**1464 Smoothness**

**1465** To achieve a form of smoothness regularization, damping is applied at each iteration  
**1466** to the solver of the matrix equation. One method to choose an optimal damping  
**1467** value is cross-validation of the input gravity data (Uieda & Barbosa, 2017). An  
**1468** effective inversion should produce a topography that, when forward-modelled, accu-  
**1469** rately recreates observed gravity data that weren't included in the inversion. This  
**1470** idea is the basis of the cross-validation routine. The observed gravity data is split

1471 into two sets, a *training* and a *testing* set. For an individual damping value, the  
 1472 inversion is run using only the training set. The final inverted bathymetry is then  
 1473 forward-modelled onto the observation points of the testing set. The difference be-  
 1474 tween the observed and forward gravity at these testing points is calculated. The  
 1475 root mean square (RMS) of the differences provides a metric for the effectiveness  
 1476 of the damping; this is referred to as the *score*. This process is then repeated for a  
 1477 suite of damping values, and the value which produces the lowest score is used as the  
 1478 optimal damping value. In this inversion, the gravity data, whether it is airborne  
 1479 flight lines or scattered ground stations, are interpolated onto a regular grid (see  
 1480 Section 3.3.1.5). To create the testing set of observed gravity data, the original data  
 1481 is interpolated onto a grid at half the desired grid spacing. This leaves the training  
 1482 set with the desired amount of points. This grid spacing configuration is shown in  
 1483 Figure 3.4.

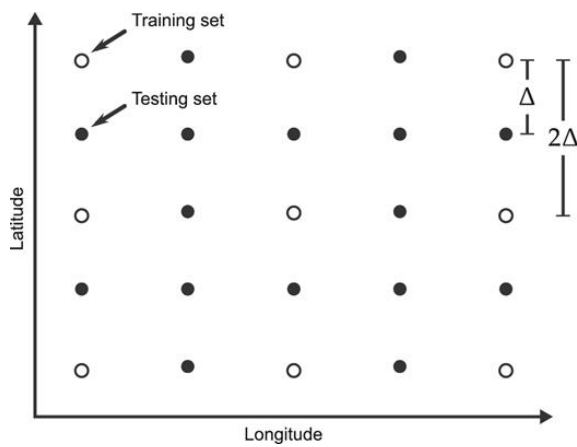


**Figure 3.4:** Configuration of observed gravity data observation points, split into training and testing sets. Reprinted from Uieda and Barbosa (2017).

#### 1484 Smallness

1485 A form of smallness regularization is applied here to ensure the inversion results ad-  
 1486 here to any *a priori* bathymetry constraints. A portion of this smallness regulariza-  
 1487 tion is already accounted for when using the constraint point minimization method  
 1488 of regional-residual separation. This method minimizes the residual component of  
 1489 the gravity misfit at the constraint points by assigning the majority of the misfit to  
 1490 the regional component. However, non-zero residual values near the constraints will  
 1491 result in a non-zero correction of the prisms immediately surrounding the constraint.  
 1492 For further smallness regularization, a weighting grid (Figure 3.5) is used to ensure  
 1493 the surface correction values at each iteration are 0 at constraint points. If only  
 1494 the prism immediately at the constraint point is fixed, a *pedestal* effect commonly  
 1495 develops. This is where the nearby prisms' surfaces freely move during the inversion,  
 1496 yet the constrained prism is fixed, resulting in either a pedestal or a hole. To avoid  
 1497 this, the weighting grid smoothly decays from a value of 0 at the constraints, to a  
 1498 value of 1 at a distance. To create this grid, the minimum distance between each  
 1499 grid cell (prism) and the nearest constraint point is calculated. These values are  
 1500 then normalized from 0 to 1 (Figure 3.5). At each iteration, the least squares solver  
 1501 yields a grid of surface correction values. Before being added to the prism layer, the  
 1502 grid is multiplied by this weighting grid. This results in surface corrections of 0 for  
 1503 prisms located at constraint points, unmodified surface correction values far from

1504 constraint points, and a smooth taper between these two endmembers.

1505

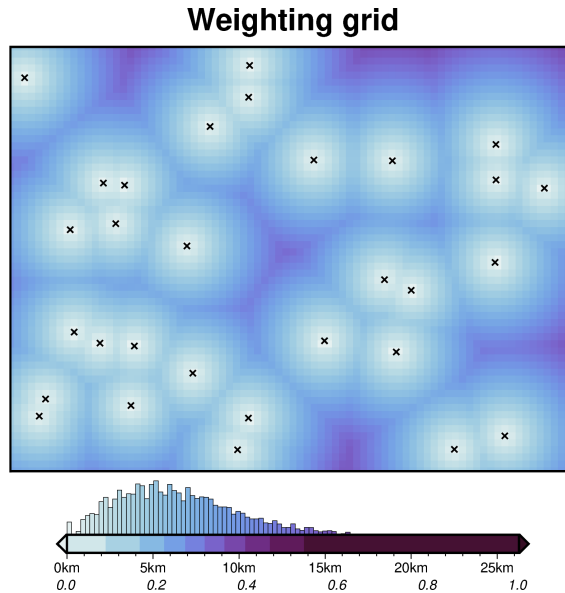


**Figure 3.5:** Weighting grid for the simple synthetic inversion, created from the minimum distance between each grid cell and the nearest constraint (black crosses). Grid values are normalized from 0 to 1 to produce the weighting grid (lower colourmap annotations).

1506 The above sections outline a single iteration of the inversion. Once the surface  
 1507 correction is calculated and the weights are applied, these values are added to the  
 1508 starting bathymetry (or the last iterations inverted bathymetry). This is then re-  
 1509 discretized into prisms. The updated prisms are then forward modelled to create a  
 1510 new predicted gravity,  $\vec{d}^{pred}$ . This is subtracted from the observed gravity,  $\vec{d}^{obs}$ ,  
 1511 to get a new misfit,  $\vec{m}$ . Using the same original regional component, the updated  
 1512 residual gravity misfit,  $\vec{m}_{res}$ , is calculated. This is now the input into the second iter-  
 1513 ation of the inversion. This process is repeated until a user-determined termination.  
 1514 Next, we outline the four criteria for ending the inversion.

### 1515 3.2.6 Stopping Criteria

1516 The inversion is terminated on one of four stopping criteria:

- 1517 1. when the inversion reaches a maximum number of iterations ( $N$ )
- 1518 2. when the  $\ell^2$ -norm of the residual ( $\|\vec{m}\|_2$ , Equation 3.1) is less than a set  $\ell^2$ -  
 1519 norm tolerance
- 1520 3. if there is no significant variation in the  $\ell^2$ -norm between iterations (i.e. the  
 1521  $\Delta\|\vec{m}\|_2$  is less than a set tolerance)
- 1522 4. if the  $\ell^2$ -norm increases above a certain threshold of the starting  $\ell^2$ -norm.

1523 The maximum number of iterations is set as a safety margin to avoid excessively  
 1524 long-running inversions. The  $\ell^2$ -norm tolerance is used to end the inversion before  
 1525 excessive over-fitting of noise in the data. This should be set to the square root  
 1526 of the assumed noise level of the gravity data. The  $\Delta\ell^2$ -norm tolerance is used to

end inversions that have reached their limit of reducing the  $\ell^2$ -norm, Finally, the upper limit of  $\ell^2$ -norm terminates run-away inversions, which occurred during the development of the inversion due to coding errors but is retained here as a fail-safe.

### 3.2.7 Software implementation

The inversion algorithm described here is implemented within the Python programming language. The algorithm uses many open-source scientific libraries. These include Harmonica for the forward gravity modelling of prisms and equivalent sources calculations (Fatiando a Terra Project et al., 2023; Soler & Uieda, 2021), Verde for various spatial operations (Uieda, 2018), PyGMT and Antarctic-Plots for figure creation (Tankersley, 2023; Uieda et al., 2021), Scipy for least squares regression (Virtanen et al., 2020), and Optuna for hyperparameter optimization (Akiba et al., 2019). The majority of the experiments were run in Jupyter notebooks (Pérez & Granger, 2007), which are documented to explain the details of using the software. All source code, results, and figures involved in this chapter are made available in an online GitHub repository ([https://github.com/mdtanker/RIS\\_gravity\\_inversion](https://github.com/mdtanker/RIS_gravity_inversion)). See Section 1.6 for the hardware used in this study.

## 3.3 Synthetic models

To assess the performance of the inversion and showcase its use, it is applied to a suite of synthetic test models. Each model has three components; 1) the ‘true’ bathymetry surface, which the inversion is expected to model, 2) the ‘observed’ gravity data, and 3) the ‘starting’ bathymetry model, which is a low-resolution version of the true surface. The only inputs into the inversions are the observed gravity data and the starting bathymetry. The true bathymetry is only used to evaluate the performance of each inversion. The observed gravity data contains the forward gravity calculated from the true bathymetry, plus, in some cases, additional noise and other gravity signals such as a regional field. The starting bathymetry is created by sampling the true bathymetry at a set of points. These values are then used to re-grid the data for the entire region using a bi-harmonic spline interpolator (Uieda, 2018). This simulates the bathymetric knowledge of many ice shelves, where few direct measurements of bathymetry exist, such as drill holes, or single-point seismic surveys. These points are referred to as the constraints. The models tested here include:

1. A simple model (Section 3.3.1): This model sets a baseline performance expectation of the inversion, with no noise, dense gravity observation points, and no additional components included in the observed gravity. The synthetic bathymetry is created with Gaussian functions of various amplitudes and wavelengths. With this same simple model, the observed gravity data is re-gridded at a lower resolution, and random noise is added, to better simulate a gravity survey.
2. A simple model with a regional field (Section 3.4): Using the same model as above, a ‘regional’ component of the gravity field is added to the observed data.

1569     3. A semi-realistic model (Section 3.5): This last model is created from real  
 1570     bathymetry data from Antarctica's Ross Sea. This model tests the inversion's  
 1571     capabilities with more realistic bathymetric features expected for sub-ice-shelf  
 1572     environments.

1573     **3.3.1 Simple model**

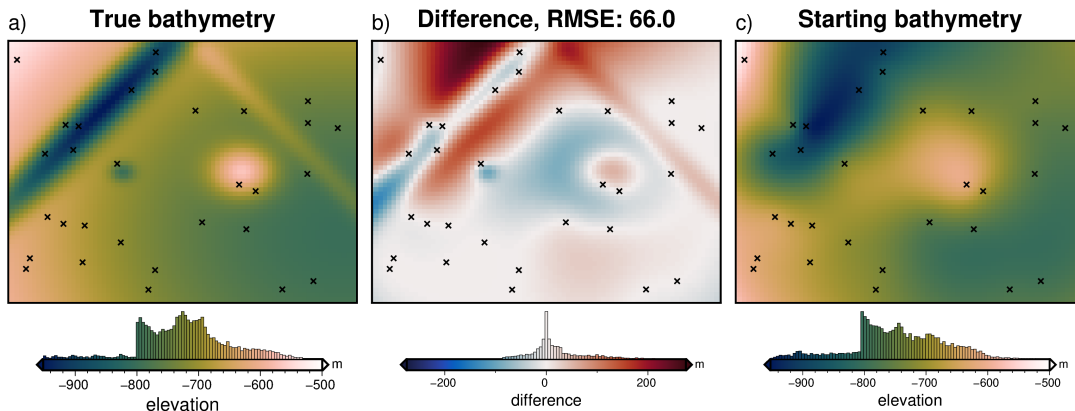


**Figure 3.6:** Simple synthetic model bathymetry. **a)** True bathymetry created from Gaussian functions, **b)** difference between a and c, and **c)** starting bathymetry, created from the sampling and re-gridding of the true bathymetry at 30 points (black crosses).

1574     **3.3.1.1 Model setup**

1575     Simulating typical sub-ice-shelf bathymetry, this model (Figure 3.6a) has an average  
 1576     elevation of  $\sim -700$  m and ranges between  $\sim -400$  m and  $\sim -1000$  m. It contains  
 1577     features of various wavelengths, amplitudes, and shapes; namely two circular fea-  
 1578     tures and two linear features. Overall, the grid is eastward deepening and contains  
 1579     a shallow and wide E-W trough through the centre. The model domain is 80 km x  
 1580     60 km, with 1 km grid cells (4800 cells). A 6 km buffer zone in all directions was  
 1581     included to limit gravitational edge effects. 30 randomly located constraint points  
 1582     were used to create the starting bathymetry (Figure 3.6c). The starting bathymetry  
 1583     has an RMS difference with the true bathymetry of 66 m.

1584

1585     To forward model the gravity of the true bathymetry, a layer of adjacent verti-  
 1586     cal right-rectangular prisms was created using the reference discretization method  
 1587     (Figure 3.2e) with the mean elevation as the reference level. A density contrast of  
 1588      $\Delta\rho = 1276 \text{ kg m}^{-3}$  (contrast between seawater ( $1024 \text{ kg m}^{-3}$ ) and sediment ( $2300 \text{ kg}$   
 1589      $\text{m}^{-3}$ )), was used, with  $+\Delta\rho$  for prisms above the reference, and  $-\Delta\rho$  for prisms below  
 1590     the reference. The forward gravity of this prism layer was calculated at a constant  
 1591     height of 1000 m (roughly 1700 m above the bathymetry) on a regular grid at half  
 1592     the grid spacing (500 m) of the bathymetry. This represents the observed gravity  
 1593     data (Figure 3.7a) and consists of both the training and testing data sets used for  
 1594     the cross-validation (Section 3.2.5.3, Figure 3.4).

1595

1596     The low-resolution starting layer was discretized in the same method, and the  
 1597     same density contrast was used. The forward gravity of these starting layer prisms  
 1598     results in the predicted gravity (Figure 3.7c). To account for any offset between

the observed and predicted data, the observed data is DC-shifted to minimize the differences at the constraint points. The difference between the shifted observed and the predicted data gives the gravity misfit (Figure 3.7b). Since there is no regional component in this synthetic model, the input into the inversion, the residual misfit, is equal to this total misfit (Equation 3.10). This residual misfit describes the ability of the starting model to predict the observed data.

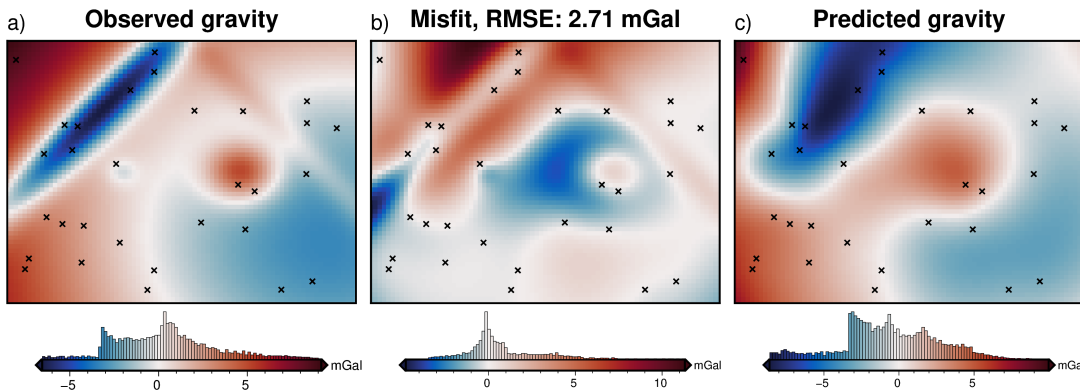


**Figure 3.7:** a) Synthetic gravity data generated from the true bathymetry, b) the residual anomaly, defined as the difference between a and c, and c) the predicted gravity from the starting bathymetry (Figure 3.6c).

### 3.3.1.2 Cross validation

To find the optimal value for the regularization damping parameter, the cross-validation method of Uieda and Barbosa (2017) is used (Section 3.2.5.3). The full set of observed data with a 500 m spacing ( $N = 19481$ ), was separated into the training ( $N = 4941$ ) and testing set ( $N = 14540$ ). With the grid configuration from Figure 3.4, the resulting training data was on a regular 1 km grid, which matches the grid of the bathymetry. This training data set was used as the input to 10 inversions. Each inversion used a different damping value between  $10^{-4}$  and  $10^{-1}$ . The resulting inverted bathymetry of each inversion was then forward-modelled on the observation points of the testing data set (not used in the inversion). The RMS difference between the forward-modelled gravity value and the initial residual misfit values was calculated, giving the cross-validation score (Figure 3.9a). Of the 10 inverted bathymetry models, the model with the lowest score is retained.

This model is shown in Figure 3.8c, and resulted from a damping value of  $10^{-2}$ . This inverted bathymetry has an RMS difference with the true bathymetry of 8 m and an RMS difference at the constraint points of 1 m. Figure 3.9b shows a profile across the model. The overlap of the true (red) and inverted (blue) bathymetry in the first panel shows the effectiveness of the inversion at recovering the true bathymetry. The lower panel shows the inversion's ability to minimize the misfit between the observed gravity (red) and the forward response of the inverted bathymetry (blue). The inversion was able to recover all the features of the true bathymetry, with only minor errors along the edges of the domain, and adjacent to constraint points. For this simple model, the inversion converged in 37 iterations, with a total computation time of 30 seconds and a final RMS residual misfit of 0.022 mGal. It terminated due to the  $\ell^2$ -norm decreasing between the set threshold of 0.15 (0.0225 mGal).

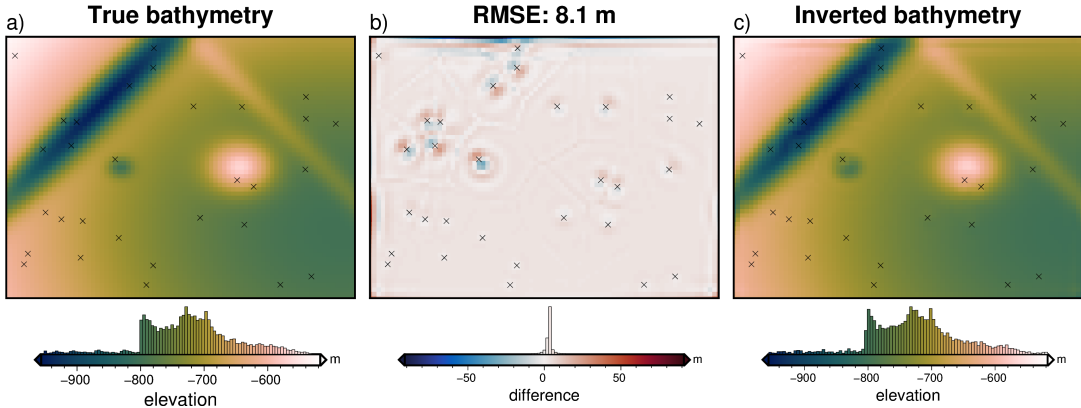


**Figure 3.8:** Inverted results with optimized parameters, using the annulus approximation method of calculating the Jacobian matrix. **a)** True bathymetry, **b)** difference between a and c, and **c)** final inverted bathymetry. Black crosses are constraint points. The RMS difference with the true bathymetry at these constraints is 1 m

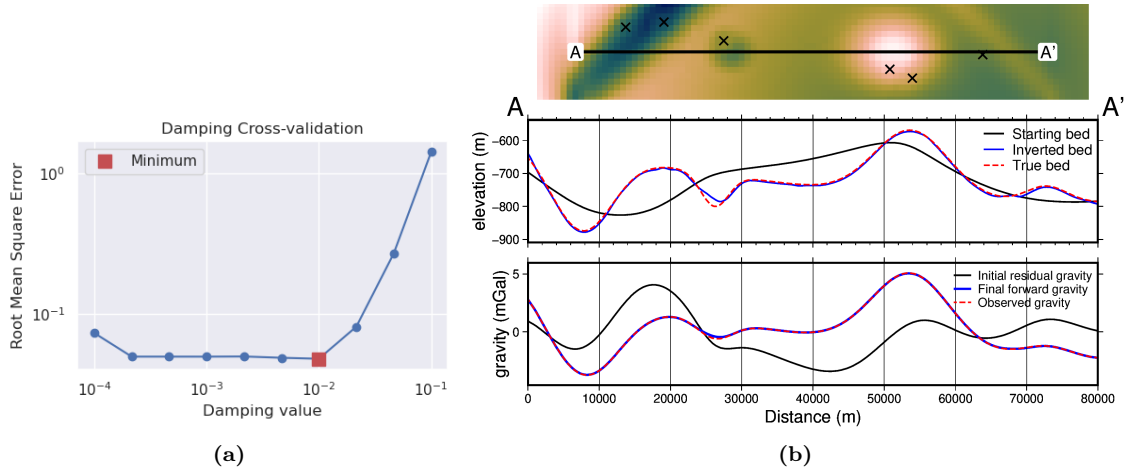


**Figure 3.9:** Cross-validation and profiles for the simple synthetic inversion. **a)** Cross-validation curve showing the optimal damping parameter (red square). Both axes are on a logarithmic scale. **b)** 2D profile of the inversion results. The top panel shows profile location and constraint points (black crosses). The middle panel contains topographic profiles of the starting, inverted, and true bathymetries. The bottom panel contains gravity anomaly profiles.

### 1630 3.3.1.3 Comparing vertical derivative methods

1631 Section 3.2.5.1 presented two methods for calculating the vertical derivative of grav-  
 1632 ity of a prism. This vertical derivative is used to create the Jacobian matrix (Equa-  
 1633 tion 3.9) and needs to be calculated at each iteration of the inversion. The above  
 1634 cross-validation and inversion were performed using the *annulus approximation* of  
 1635 the vertical derivative. Here, this process is repeated with the *finite differences*  
 1636 method of the vertical derivative. Figure 3.10 shows the results of this inversion.  
 1637 The optimal damping parameter was  $10^{-2}$ , and the inversion resulted in an RMS  
 1638 difference with the true bathymetry of 9 m, compared to 8 m for the annulus ap-  
 1639 proximation. Figure 3.11 shows the inversion convergence curves for the inversion of  
 1640 the annulus approximation and the finite differences methods. The inversion with  
 1641 the annulus approximation was  $\sim 500\%$  faster to converge than the finite differences  
 1642 method (30 sec vs 169 sec). Because these vertical derivatives need to be recalcul-  
 1643 ated at each iteration, a large portion of the inversion time is spent performing  
 1644 these calculations. This comparison shows the annulus approximation is not only

significantly faster, but results in comparable, or slightly more accurate, inversion results. For the remainder of this chapter, only the annulus approximation will be used.

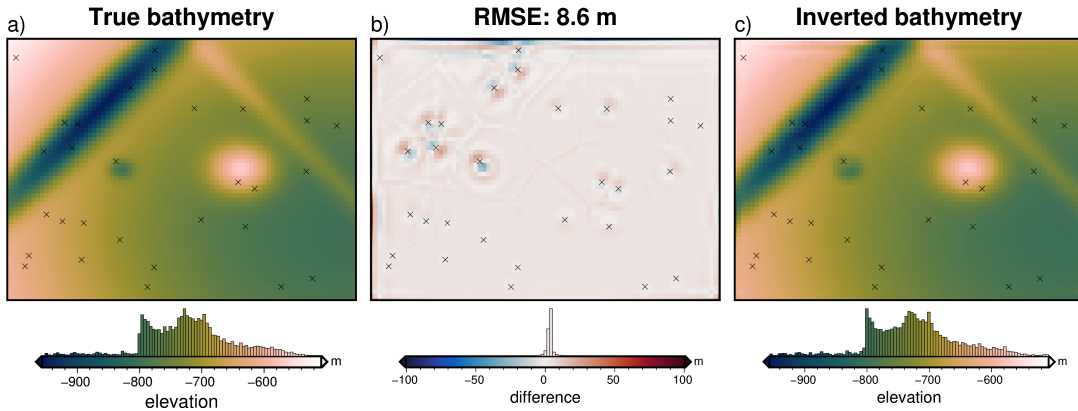


**Figure 3.10:** Inversion results with optimized parameters using the finite differences method. **a)** True bathymetry, **b)** difference between a and c, and **c)** final inverted bathymetry. Black crosses are constraint points. The RMS difference with the true bathymetry at these constraints is 1 m

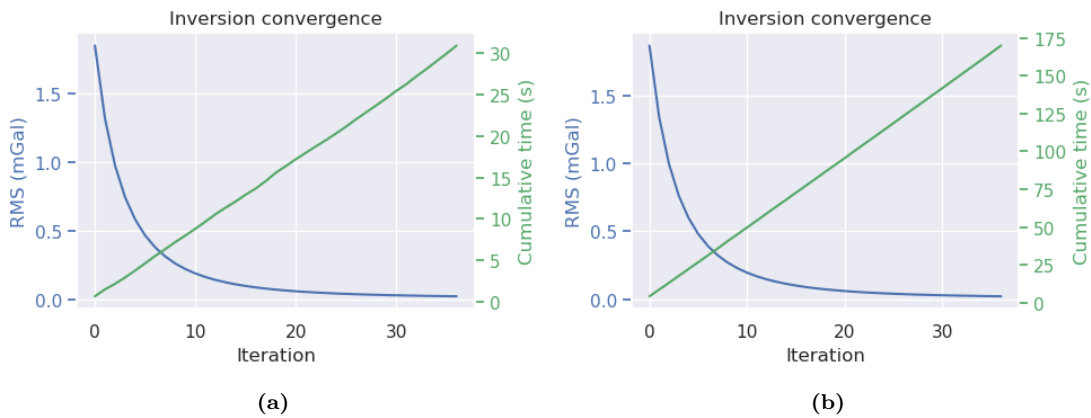


**Figure 3.11:** Inversion convergence curves for the two methods of creating the Jacobian matrix. Blue line (left y-axis) shows the RMS of the residual misfit at each iteration of the inversion. Green line (right y-axis) shows the cumulative time to complete the inversion. **a)** Results for the annulus approximation method of finding the vertical derivative. **b)** Results for the finite differences method.

#### 3.3.1.4 Added noise

To test the effect of noise in the gravity data, which is inevitable in data collection, especially so in airborne surveying, the observed gravity was contaminated with noise. The noise has a Gaussian distribution with a mean of 0 mGal and a standard deviation of 2% of the max absolute value of the data ( $\sim .16$  mGal). Similarly, Rashidifard et al. (2021) used 5% noise in their synthetic gravity inversion while Uieda and Barbosa (2017) use 5 mGal of noise, which for their synthetic application equated to  $\sim 1\%$  of the max absolute value. Using this noise-corrupted gravity data, the same damping parameter cross-validation was run as previously (Figure 3.13a), and the lowest score was achieved with a damping value of  $10^{-2}$ . Figure 3.12 shows the inversion results of this noise-contaminated model. The inversion converged in 18 iterations, with a total computation time of 13 seconds and a final RMS residual

misfit of 0.16 mGal. It terminated after the  $\ell^2$ -norm became lower than the set tolerance of 0.4 (0.16 mGal). This tolerance was set to match the known level of noise. The inverted bathymetry had an RMS difference of 12 m with the true bathymetry and an RMS difference of < 1 m at the constraint points. Figure 3.13b shows the inversion is still able to reproduce the observed gravity (lower panel), but a component of the noise was introduced into the final bathymetry (upper panel). All major features of the true bathymetry are recovered, albeit not as accurately as the no-noise model (Figure 3.8).

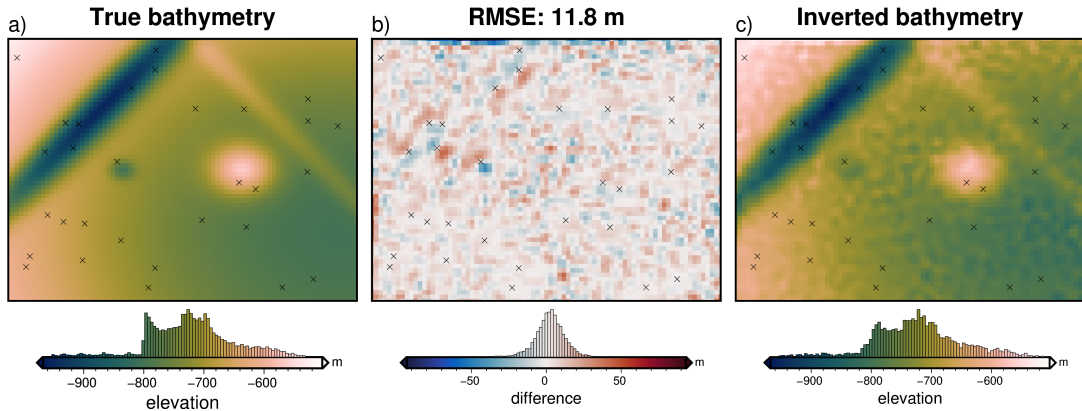


**Figure 3.12:** Simple synthetic model inversion results with 2% added noise (0.16 mGal). **a)** True bathymetry, **b)** difference between a and c, **c)** final inverted bathymetry. Black crosses are constraint points. The RMS difference with the true bathymetry at these constraints is < 1 m.

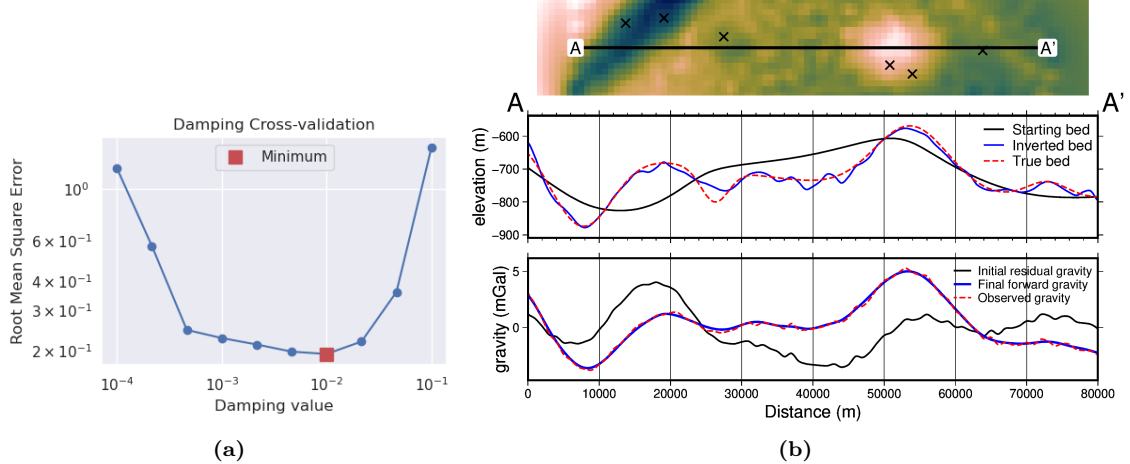


**Figure 3.13:** Cross-validation and profiles for the inversion with noise. **a)** Cross-validation curve showing the optimal damping parameter (red square). **b)** 2D profile of the inversion results. The top panel shows profile location and constraint points (black crosses). The middle panel contains topographic profiles of the starting, inverted, and true bathymetries. The bottom panel contains gravity anomaly profiles.

### 3.3.1.5 Down-sampled data

The previous two models used observed gravity data collected on a grid of observation points at the same grid spacing as the prism layer (1 km). This represents a very dense gravity survey. Gravity surveys are often relatively sparse compared to the resolution of the surface they are attempting to recover in an inversion. This section tests the effect of changing the resolution of the gravity data, to simulate

a coarser gravity survey. Simply sampling the gravity data at a coarser resolution leads to a checker-boarding effect, where the inversion alters prisms nearby the gravity observations, but not prisms further away. For this reason, it is recommended here to re-grid the observed gravity data at a similar grid spacing to the prism layer. This can be accomplished with standard gridding techniques, such as minimum curvature or bi-harmonic splines (see section 3.4.2). However, these techniques aren't well suited for potential field data since they don't account for the variation in observation heights (Soler & Uieda, 2021). An alternative method of interpolating the gravity data onto a finer resolution grid is the equivalent sources technique (Dampney, 1969)<sup>1</sup>.

1684

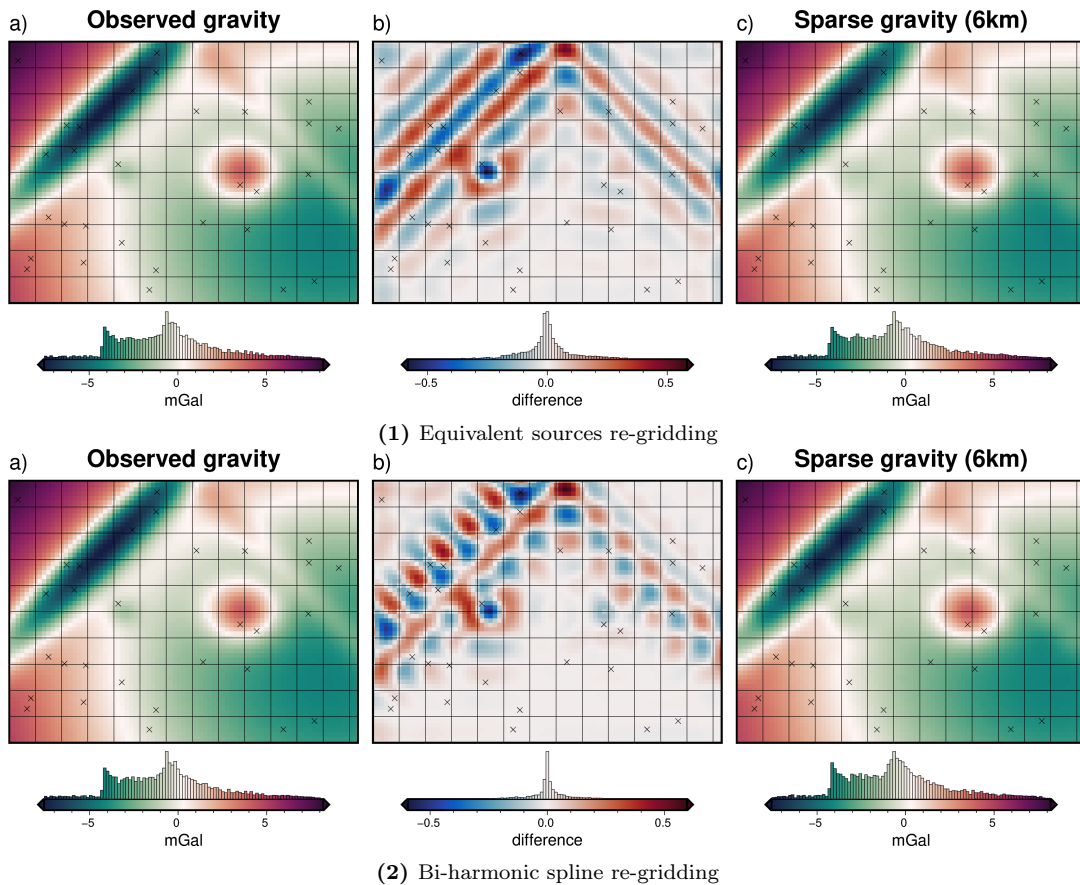


**Figure 3.14:** Creating a low-resolution observed gravity survey. **Top panel** shows results using the equivalent source technique of gridding gravity data. **Bottom panel** shows simple gridding using a bi-harmonic spline. **a)** Original observed data on a 1 km grid, **b)** gravity signal lost due to sampling and re-gridding, **c)** the low-resolution observed gravity (6 km spacing) re-gridded at 1 km with either equivalent sources (top) or a regular gridding algorithm (bottom). Black crosses show constraint points and black lines show 6 km grid.

1685 Here, the original gravity data, on a 1 km grid, is sampled at a 6 km spaced grid  
 1686 to represent a low-resolution survey with observations every 6 km. A series of point  
 1687 sources are created at depth, and their densities are altered to best reproduce the  
 1688 observed gravity data. Once this process of fitting the source parameters to the data  
 1689 is accomplished, the gravity field can be predicted anywhere. For this application,  
 1690 the equivalent sources are predicted onto an even 1 km grid, to match the spacing

<sup>1</sup>The equivalent sources technique is also used in this study as a means of regional separation (see section 3.2.4, this is a similar application but for different purposes).

of the bathymetry. Figure 3.14 shows the results of this process (top panel) and the results using simple gridding without equivalent sources (bottom panel). *Subplot a* shows the original observed gravity data (just training points) on a 1 km grid. This grid is sampled onto a 6 km grid (black grid lines) and re-gridded at 1 km (*subplot c*). *Subplot b* shows the difference, which represents the lost data resulting from the sparse survey. Typically the equivalent sources gridding technique is most beneficial to account for variations in observation heights. Here, even with constant elevations, there are noticeable differences between equivalent source gridding and simple gridding with bi-harmonic splines.

1700

The equivalent-source resampled grid is used, with no added noise, in the same inversion procedure as the previous sections. The cross-validation (Figure 3.16a) resulted in an optimal damping value of  $10^{-2}$ . The inverted bathymetry with this damping value is shown in Figure 3.15. The inversion was completed in 29 seconds and 38 iterations with a final RMS residual misfit of 0.019 mGal. The inversion was terminated due to the  $\ell^2$ -norm decreasing below the set threshold of 0.15 mGal $^{1/2}$ . The inverted bathymetry had an RMS difference of 11 m with the true bathymetry and an RMS difference of 1 m at the constraint points. While the overall difference from the true bathymetry is low, this inversion failed to fully recover the small circular depression. Figure 3.14 shows that the nearest observation point (intersection of gridlines) was on either side of this anomaly, and thus the sparse gravity survey used here failed to image the true magnitude of the feature. Figure 3.15b shows the absence of this feature in the inverted bathymetry.

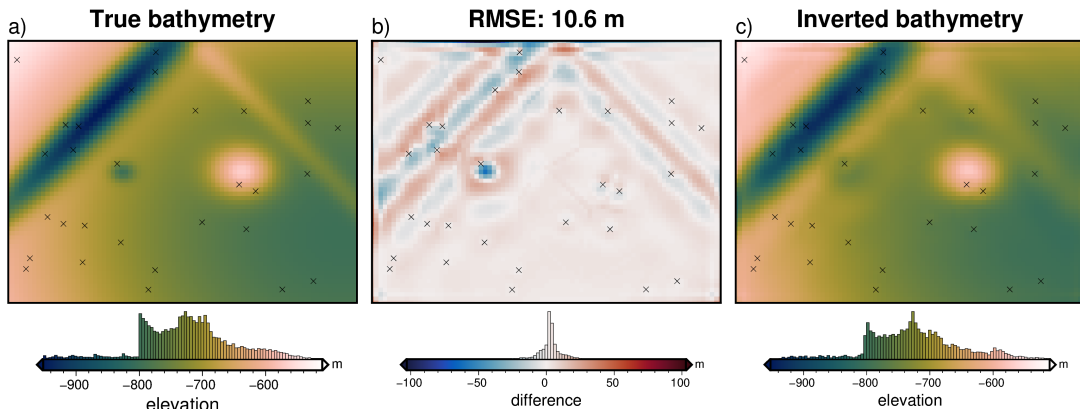


**Figure 3.15:** Simple synthetic model inversion results with input data resampled at 6x the bathymetry grid spacing (6 km). **a)** True bathymetry, **b)** difference between a and c, and **c)** final inverted bathymetry. Black crosses show constraint points. The RMS difference with the true bathymetry at these constraints is 1 m.

### 3.3.2 Ensemble of Noise and Sampling values

To test the relative importance of the level of noise and the resolution of the gravity data (i.e. station/flight line spacing), an ensemble of 100 inversions was run, with 10 noise levels between 0 and 9%, and 10 gravity resolutions between 1 and 10 km. The noise level percentages are of the maximum absolute value of the data, equating to 10 levels between 0 and 0.85 mGal. The differing gravity resolutions were created with the sampling and re-gridding of equivalent sources outlined in the above section. For each set of noise and spacing values, the cross-validation routine was used to

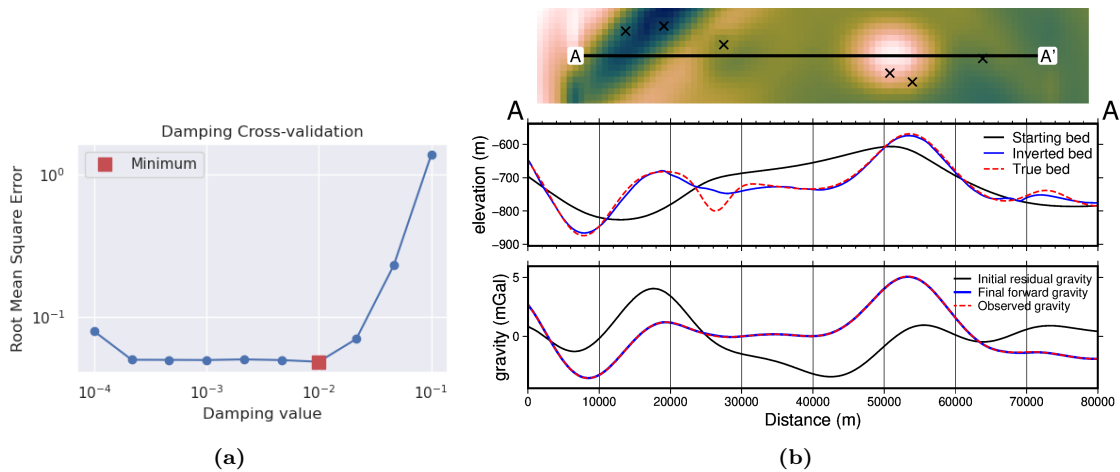


**Figure 3.16:** Cross-validation and profiles for the 6 km resampled inversion. **a)** Cross-validation curve showing the optimal damping parameter. **b)** 2D profile of the inversion results. The top panel shows profile location and constraint points (black crosses). The middle panel contains topographic profiles of the starting, inverted, and true bathymetries. The bottom panel contains gravity anomaly profiles.

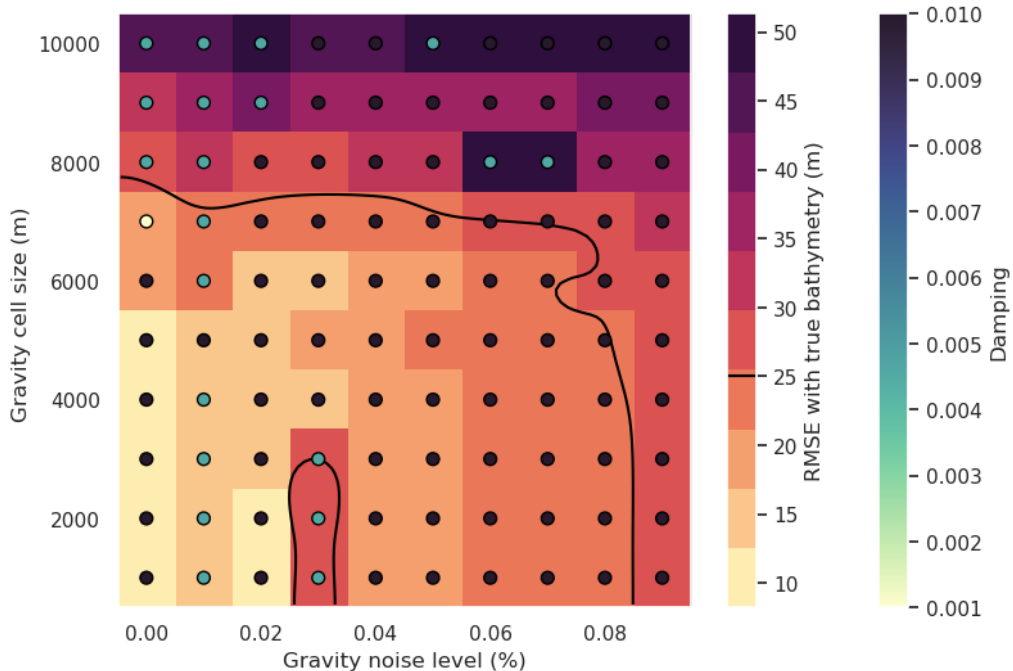


**Figure 3.17:** Ensemble of noise levels and gravity spacing for the simple synthetic model. Grid cell colour indicates each inversion's RMS difference with the true bathymetry. The circles' colour indicates the optimal damping value found for each inversion's cross-validation. Black line shows the 25 m RMSE contour, indicative of the amplitude of the smallest amplitude features.

1722 find the optimal damping parameters and associated inverted bathymetries. Each  
1723 of these 100 inversions were then compared to the true bathymetry yielding an RMS  
1724 difference for each.

1725 Figure 3.17 shows the results of this ensemble of inversion. Each grid cell  
1726 represents a single inversion, with the level of noise and gravity resolution for  
1727 the inversion indicated by the x and y axis, respectively. The background colour  
1728 (warm colours) indicates each inversion's resulting RMS difference with the true  
1729 bathymetry. Coloured circles show the optimal damping value for each inversion

1730 found through cross-validation. This shows a general decrease in the inversion's ac-  
 1731 curacy with either more noise or lower-resolution gravity data. The smallest bathy-  
 1732 metric features which this inversion ideally should recover have amplitudes of tens  
 1733 of meters (small circular depression and narrow ridge). The RMSE here indicates a  
 1734 base-level of error in the inversions, while the error in the vicinity of the short wave-  
 1735 length bathymetry features is likely higher (Figure 3.15b). Inversions with RMSEs  
 1736 of 10's of meters will likely fail to resolve these small features. For this inversion, an  
 1737 RMSE of 25 m (black contour in Figure 3.17) approximately equates to a gravity  
 1738 observation spacing greater than 8 times the prism layer spacing, and a noise level  
 1739 higher than 8% of the survey's max absolute value.

## 1740 3.4 Adding a regional component

1741 Now that the inversion has been demonstrated to adequately recover bathymetry  
 1742 with various levels of noise and resolutions of the input gravity data, an additional  
 1743 complexity is added. This complexity is a regional component of the observed  
 1744 gravity field. To account for this, the inversion remains the same, but the regional  
 1745 component of the gravity misfit must be removed beforehand (Equation 3.10). In  
 1746 this section, first, the four methods of regional separation laid out in 3.2.4 are  
 1747 compared. Next, one of these methods, constraint point minimization, is further  
 1748 investigated. Lastly, the effects of noise and gravity survey spacing are explored.

1749 This model uses the same starting bathymetry (Figure 3.6) as the previous sec-  
 1750 tion, but the observed gravity includes a regional field, which represents the portion  
 1751 of observed gravity signal resulting from unknown crustal sources, such as anomalous  
 1752 bodies or crustal thickness variations. This component (Figure 3.18b) is calculated  
 1753 from a synthetic topography with a median elevation of -4300 m and a density con-  
 1754 trast of  $700 \text{ kg m}^{-3}$ . Its range of gravity values is set to be the dominant signal in the  
 1755 observed gravity, but not large enough to fully mask the signal of the bathymetry  
 1756 signal. Figure 3.18 shows the various components of the gravity and resulting misfit  
 1757 for this model.

### 1758 3.4.1 Regional separation methods

1759 The four methods of regional separation discussed in section 3.2.4 each have at least  
 1760 one hyper-parameter which affects their calculation of the regional field. For each  
 1761 method these include

- 1762 1. Low-pass filter: the distance width of the Gaussian filter.
- 1763 2. Trend removal: the degree of the polynomial trend fit to the misfit.
- 1764 3. Equivalent source prediction: the depth and damping parameters of fitting  
 1765 sources to the data (Soler & Uieda, 2021).
- 1766 4. Constraint point minimization: parameters for the associated gridding method,  
 1767 such as the tension factor for minimum curvature gridding (Smith & Wessel,  
 1768 1990) or the minimum distance and damping parameter for bi-harmonic spline  
 1769 gridding (Uieda, 2018).

1770 Since for this synthetic model, the true regional field is known (Figure 3.18b), the  
 1771 effect of the parameters associated with each of the four methods can be explored.

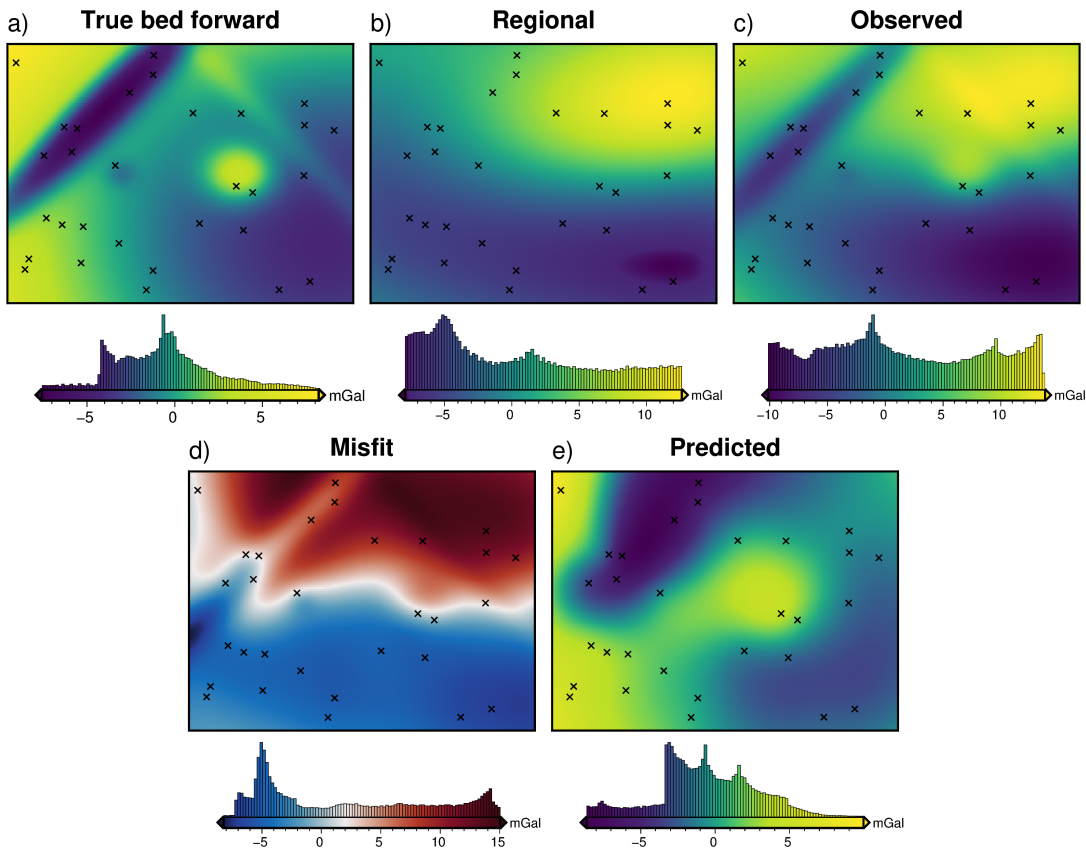


**Figure 3.18:** Gravity components and anomalies for the simple synthetic model with the addition of a regional field. **a)** the forward gravity of the true bathymetry, **b)** the regional component of gravity, **c)** the observed gravity from the combination of a and b, **d)** the gravity misfit from the difference between c and e, and **e)** the predicted gravity from the forward calculation of the starting bathymetry.

Excluding the constraint point minimization method, an optimization is run for each method, with the goal of finding the parameter values which minimize the RMS difference between the true and calculated regional gravity. Each optimization has 20 trials. The constraint point minimization doesn't require optimization because the various gridding parameters won't significantly affect the RMS difference between the resulting regional field and the true field. However, the gridding parameters will affect the inversion itself; this is explored in the next section. For this comparison of the regional removal method, the constraint point minimization method uses bi-harmonic spline gridding, and the gridding damping parameter is chosen with a cross-validation (Uieda, 2018). The best regional field (lowest RMS with the true regional field) of each method was found with the following parameters:

1. a 30 km filter width for the low pass filter method
2. a 3<sup>rd</sup> order trend for the trend removal method
3. source depth of 89 km and a damping value of 1.72 for the equivalent source technique
4. an interpolator damping of  $1.27 \times 10^{-8}$  for the bi-harmonic spline interpolator of the constraint point minimization method.

Each of these regional fields was then removed from the gravity misfit, producing the residual anomalies (Figure 3.19a-d). These resulting residuals were then input

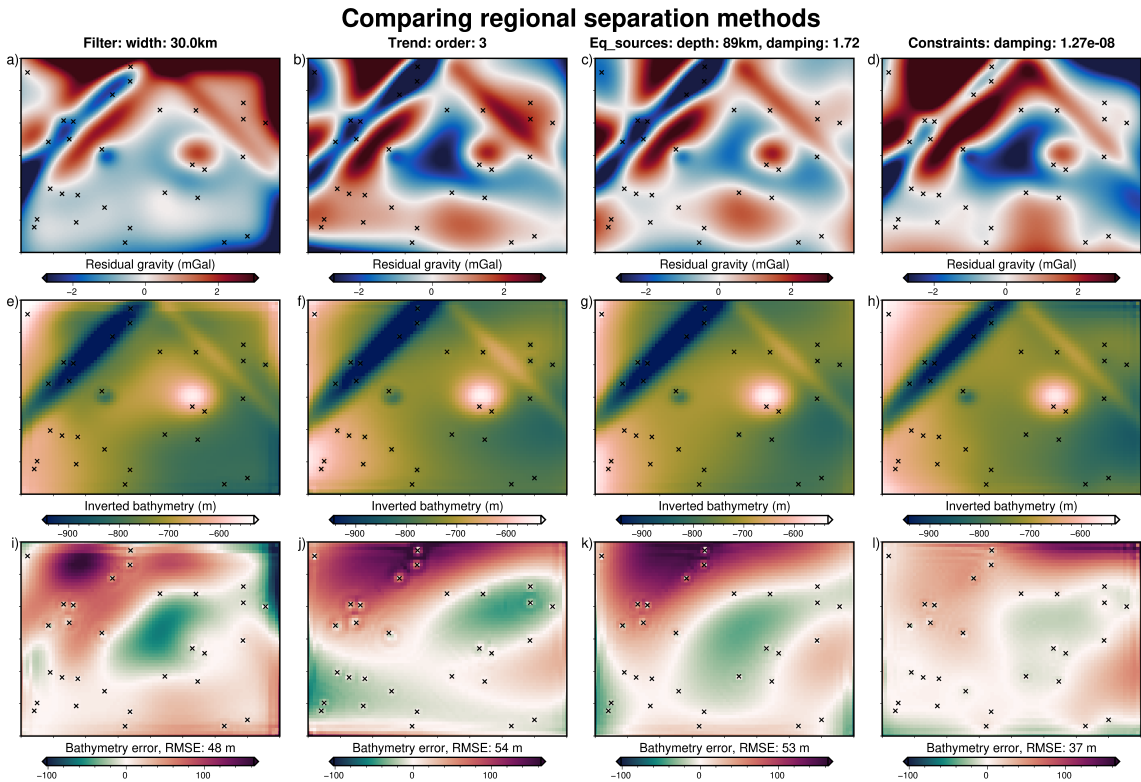


**Figure 3.19:** Comparison of inversions with 4 regional separation methods. First row (**a-d**) shows residual gravity misfit after regional separation. Second row (**e-h**) shows the inverted bathymetry for each method. Third row (**i-l**) shows the error of the inverted bathymetries with the true bathymetry. Constraint points are shown as black crosses. Colourmaps are identical for each row. Profiles of these data are shown in Figure B.1 of Appendix B.

1791 into an inversion, resulting in the inverted bathymetries of d-h of Figure 3.19, and the  
 1792 bathymetry error relative to the true bathymetry was found (Figure 3.19i-l). For  
 1793 these inversions, the same damping parameter cross-validation was conducted, as  
 1794 described in Section 3.3.1.2. This comparison of regional separation methods shows  
 1795 that the constraint point minimization method (Figure 3.19l) produces the best  
 1796 inverted bathymetry, both visually (Figure 3.19h), and based on the RMS difference  
 1797 with the true bathymetry (37 m). Figure B.1 in Appendix B shows a profile of  
 1798 the resulting regional fields and inverted bathymetries of these various methods of  
 1799 regional separation. The remainder of this section further examines the constraint  
 1800 point minimization method of regional separation.

### 1801 3.4.2 Constraint point minimization

1802 The constraint point minimization method assumes that at locations of known  
 1803 bathymetry, there is no residual component of gravity misfit, and the regional com-  
 1804 ponent entirely equals the misfit. To implement this, misfit values at the constraints  
 1805 are sampled and used to create a region-wide grid of regional values. This grid is  
 1806 then removed from the misfit to get the residual misfit (Equation 3.10). This grid-  
 1807 ding can be accomplished by many techniques, which at an initial inspection appear  
 1808 to produce similar results. Here, two methods of gridding and their gridding par-  
 1809 meters are compared, and the impact on the inverted bathymetry are shown. These  
 1810 gridding methods are tensioned minimum curvature (Smith & Wessel, 1990) and  
 1811 bi-harmonic splines (Sandwell, 1987).

**3.4.2.1 Tensioned minimum curvature**

Tensioned minimum curvature gridding is a commonly used technique for gridding sparse data which fits the smoothest possible surface while still matching the data (Wessel & Bercovici, 1998). It allows variation in the location of maximum curvature through the tension factor parameter. A tension factor of 0 results in the minimum curvature solution (maxima and minima allowed anywhere), while a value of 1 localizes the curvature at the data points (maxima or minima only allowed at the data points) (Smith & Wessel, 1990). A tension of 0.25 is suggested for potential field data (Wessel et al., 2019). Tensioned minimum curvature has been used in several bathymetric inversions for constraint point minimization (An et al., 2019a; Millan et al., 2020; Yang et al., 2021).

**3.4.2.2 Bi-harmonic splines**

The second method of gridding the sampled gravity misfit values uses bi-harmonic splines. This method uses Green's functions and the least squares fit to the data (Sandwell, 1987). Computation time for this technique is approximately proportional to the cube of the number of data, making it computationally expensive for large datasets (Deng & Tang, 2011). There is a damping parameter value that can be adjusted, to smooth the resulting interpolation. As implemented in the *SplineCV* class of the Python package Verde (Uieda, 2018), automated cross-validation of the data can be used to identify the damping value which best predicts the data. Once the parameter is determined, and the data is interpolated, the interpolation can be predicted at any location, such as on the nodes of a uniform grid.

Despite its slow run time with large datasets, bi-harmonic spline gridding has several advantages over tensioned minimum curvature gridding. It allows the incorporation of data uncertainties into the fitting via a weighting parameter. With the use of cross-validation, there are no subjective parameters that can significantly alter the results. Lastly, the predicted data don't need to be on a regular grid, which is useful for irregularly shaped domains that don't adhere to a rectangular region. In their bathymetry inversion, Millan et al. (2020) point out features in their inverted bathymetry which likely result from the minimum curvature gridding technique. Apart from this, there appears to be little work related to the how the gridding procedure affects this aspect of a bathymetry inversion.

**3.4.2.3 Gridding comparison**

In this section, the effect which the gridding process has on the inverted bathymetry is analyzed. Four sets of regional separations were conducted, three using the tensioned minimum curvature technique, and one using the bi-harmonic spline technique. For the three minimum curvature separations, the tension factors used were the end members, 0 and 1, and the suggested value for geopotential data, 0.25. For the bi-harmonic spline, a cross-validation with 20 varying damping values was conducted, and the best resulting damping value was used. For each of the four calculated regional fields, the resulting residual fields (Figure 3.20a-d) were used as inputs to an inversion. All four residual anomaly data were included in an inversion damping parameter cross-validation, as described in Section 3.3.1.2. The difference between the resulting inverted bathymetry and the true bathymetry of each model

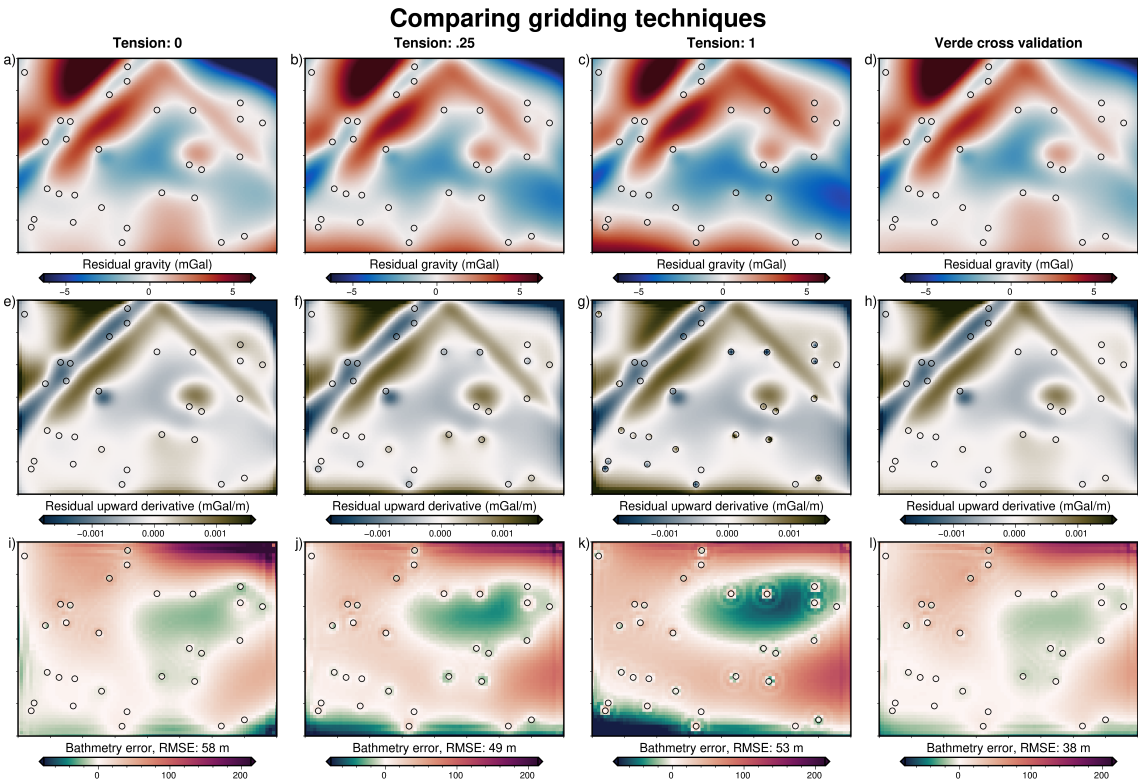


**Figure 3.20:** Comparison of gridding techniques for the constraint point minimization method of regional-residual separation. By sampling the misfit at constraints, and re-gridding over the entire domain, the regional component of the misfit is estimated. Gridding methods include minimum curvature gridding with tension factors of 0 (**column 1**), 0.25 (**column 2**), 1 (**column 3**), and cross-validated bi-harmonic spline gridding (**column 4**). Resulting gridded regional components were removed from the misfit grids to produce the residual grids (**a-d**). Second row (**e-h**) shows the vertical derivative of the residual, to highlight the gridding variations. Third row (**i-l**) shows the error of the inverted bathymetries with the true bathymetry. Constraint points are shown as open circles. Colourmaps are identical across all columns. Profiles of these data are shown in Figure B.2 of Appendix B.

is shown in Figure 3.20i-l. To help visualize the difference in the resulting residual grids, 3.20e-h shows the vertical derivative of the residual fields. This highlights that while the residual values at the constraints are all similar, the slope of the residual in the vicinity of the grids is strongly dependent on the gridding method <sup>2</sup>. Additionally, the minimum curvature gridding is shown, in subplots a-c, to create large artificial anomalies away from constraint points (low values in upper right corners). These gridding artifacts result in large errors in the resulting bathymetry 3.20i-k. The bi-harmonic spline interpolator (last column in 3.20) is shown to produce a residual field that adheres to the constraints, has smooth curvature near constraints, and doesn't create large artificial anomalies. The effectiveness of this interpolator is confirmed by the low RMS difference between the inverted and true bathymetry (38 m). Figure B.2 in Appendix B shows a profile of the resulting regional fields and inverted bathymetries of these various gridding methods. With the bi-harmonic spline gridding techniques shown to be the most effective, the remainder of this chapter uses this gridding technique for the constraint point minimization method of regional separation.

<sup>2</sup>Note that the gridding process creates the regional field (not shown in Figure 3.20), which when subtracted from the total misfit gives the residual field. The residual grid is affected by these gridding effects through the removal of the regional field.

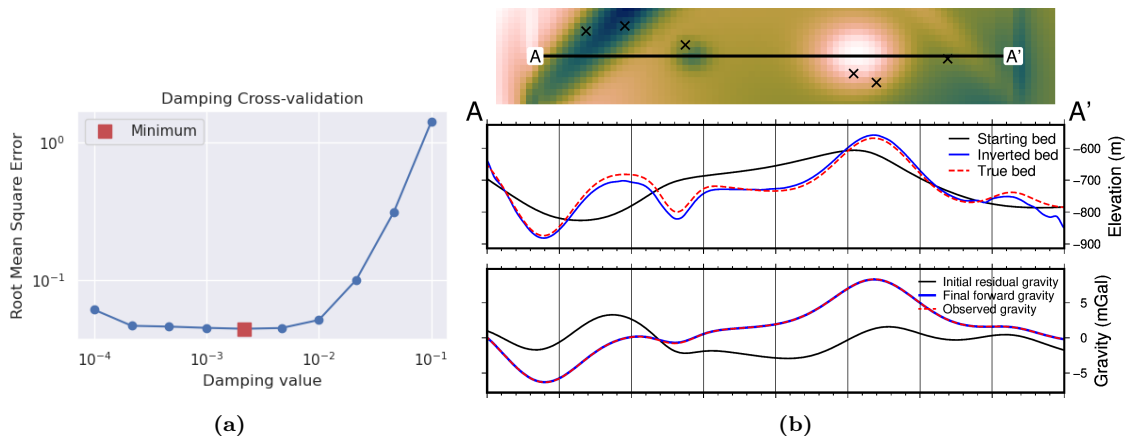


**Figure 3.21:** Cross-validation and profiles for the simple synthetic inversion with a regional component removed. **a)** Cross-validation curve showing the optimal damping parameter (red square). **b)** 2D profile of the inversion results. The top panel shows profile location and constraint points (black crosses). The middle panel contains topographic profiles of the starting, inverted, and true bathymetries. The bottom panel contains gravity anomaly profiles.

### 3.4.3 Inversion results

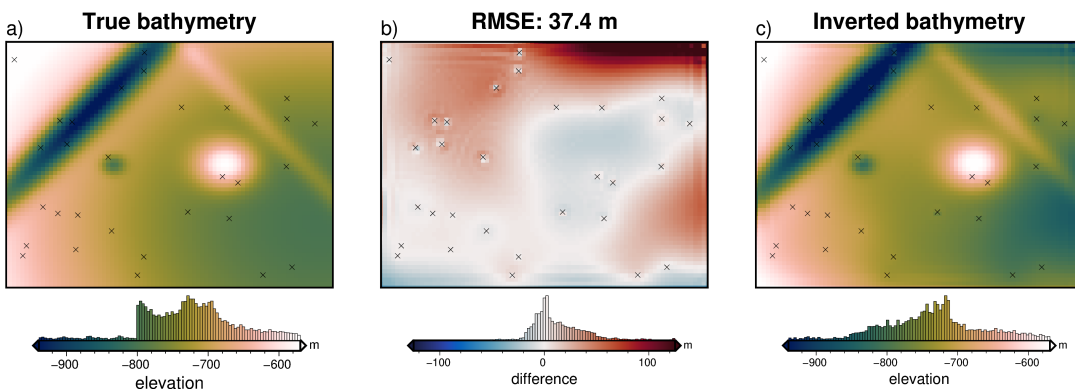


**Figure 3.22:** Simple synthetic model inversion with a removed regional component. **a)** True bathymetry, **b)** difference between a and c, **c)** final inverted bathymetry. Black crosses are constraint points. The RMS difference with the true bathymetry at these constraints is 2 m.

Using the cross-validated bi-harmonic gridding method to separate the regional component of the gravity misfit, the resulting residual misfit was used in an inversion. The same gravity data cross-validation method of determining the optimal damping parameter is used (Figure 3.21). The optimal damping parameter was found to be  $\sim 10^{-2.6}$ . The resulting inversion is shown in Figure 3.22. The inverted bathymetry had an RMS difference with the true bathymetry of 37 m and an RMS difference at the constraints of 2 m. The inversion was completed in 66 seconds, with 39 iterations and a final RMS residual of 0.022 mGal. The inversion was terminated due to the  $\ell^2$ -norm decreasing below the set threshold of  $0.15 \text{ mGal}^{1/2}$ . All four bathymetric features were recovered, but a lack of constraints in a few regions (the upper-right corner) lead to a miscalculation of the regional field and a subsequent over-deepening of the bathymetry.

The regional separation, parameter cross-validation, and inversion were repeated with additive noise and re-sampling of the gravity data to a coarser resolution (Appendix B.1). As in section 3.3.2, this above workflow was also repeated for an ensemble of noise levels and gravity data grid spacings, as discussed next.

### 1890 3.4.4 Ensemble of Noise and Sampling values

1891 Following the method outlined in Section 3.3.2, an ensemble of 100 inversions with  
 1892 varying levels of noise and gravity observation spacings was conducted. The noise  
 1893 and gravity spacing changes were applied to the original observed data, and the  
 1894 forward calculation of the starting model, initial misfit calculation, and regional field  
 1895 removal were all repeated. Each model was then inverted with a cross-validation,  
 1896 and the resulting RMS differences with the true bathymetry are shown in Figure  
 1897 3.23.

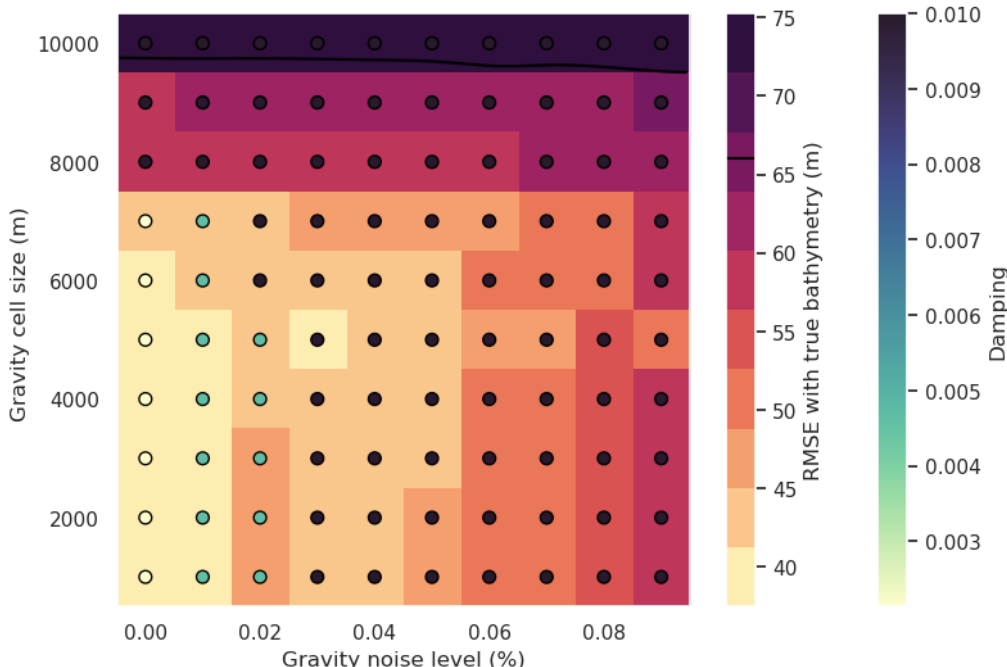


**Figure 3.23:** Ensemble of noise levels and gravity spacing for the simple synthetic model with a regional field. Grid cell colour indicates each inversion's RMSE with the true bathymetry. The circles' colour indicates the optimal damping value found for each inversion's cross-validation. Black line shows the 66 m contour, representing the RMS difference between the true and starting bathymetry.

### 1898 3.4.5 Simple model comparison

1899 Table 3.1 compares the performance of each of the above inversions. The four  
 1900 inversions without a regional component of the gravity data (annulus approximation,  
 1901 prism approximation, with noise, and resampled), all recovered the bathymetry with  
 1902 an RMSE of  $\sim 10$  m. With the regional component, the lowest RMS was raised to  
 1903 37 m. The constraint point minimization method of regional separation produced  
 1904 significantly more accurate bathymetry models than the other methods. With these  
 1905 optimal methods and baseline performance standards, a new synthetic model is  
 1906 introduced which was created to emulate the expected bathymetry features and  
 1907 gravity anomalies associated with a sub-ice-shelf environment.

	RMS (m)	RMS at constraints (m)	Total time (hr:min:sec)	# iterations	Final residual RMS (mGal)
<b>No regional component</b>					
Starting bathymetry	66	0.04	—	—	2.7
annulus	8	1	00:00:30	37	0.022
finite differences	9	1	00:02:49	37	0.022
2% noise	12	< 1	00:00:13	18	0.16
6 km re-grid	11	1	00:00:29	38	0.019
<b>With regional component</b>					
Starting bathymetry	66	0.04	—	—	7.4
filter	48	—	—	—	—
trend	54	—	—	—	—
equivalent sources	53	—	—	—	—
constraint point minimization	37	2	00:01:06	39	0.022
2% noise	45	2	00:00:12	13	0.23
4 km re-grid	38	2	00:00:51	38	0.022

**Table 3.1:** Summary of the simple synthetic model inversion results.

## 3.5 Ross Sea model

Here a semi-realistic model is introduced. In the past section, two synthetic topographies (bathymetry and a crustal layer) were used in forward modelling to create synthetic gravity data. Here, real topographic data is used to create the synthetic gravity. This model is termed semi-realistic since the gravity is synthetically calculated, but it results from geologically real surfaces. This model uses data from Antarctica's Ross Sea (Figure 3.1, north of Ross Ice Shelf). The bathymetry data is from the IBCSO v2 data compilation (Dorschel et al., 2022), resampled at a 5 km resolution (Figure 3.24a). This data is mostly from shipborne multi-beam echo sounding. To create the regional component of gravity, basement depths from the ANTOSTRAT compilation of shipborne seismic data have been used (Brancolini et al., 1995), at a 5 km resolution (Figure 3.24b). The inversion domain is  $320 \times 420$  km and a buffer zone of 40 km was included in all directions, resulting in 8000 grid cells per surface.

### 3.5.1 Observed gravity

The bathymetric and crustal surfaces were discretized with the reference discretization method (Figure 3.2e) with the mean elevation of each surface as its reference level. A density contrast of  $\Delta\rho = 1276 \text{ kg m}^{-3}$  (contrast between seawater( $1024 \text{ kg m}^{-3}$ ) and sediment ( $2300 \text{ kg m}^{-3}$ )), was used, with  $+\Delta\rho$  for prisms above the reference, and  $-\Delta\rho$  for prisms below the reference. For the basement, a density contrast of  $\Delta\rho = 200 \text{ kg m}^{-3}$  was used, representing the contrast between sediment ( $2300 \text{ kg m}^{-3}$ ) and low-density basement rock ( $2500 \text{ kg m}^{-3}$ ). This contrast was set so that the resulting forward gravity of the basement was slightly greater in magnitude than that of the bathymetry. The forward gravity of each layer was calculated at a regular grid of observation points with a 5 km spacing, at a constant elevation of 1 km (Figure 3.24c-d). This created the full-resolution synthetic observed gravity dataset. To represent an airborne gravity survey, this grid is sampled along synthetic flight lines.

This synthetic survey (Figure 3.25b) consisted of five N-S and 24 E-W flight lines. Spacing between lines was 50 km for the N-S lines and 15 km for the E-W lines. One

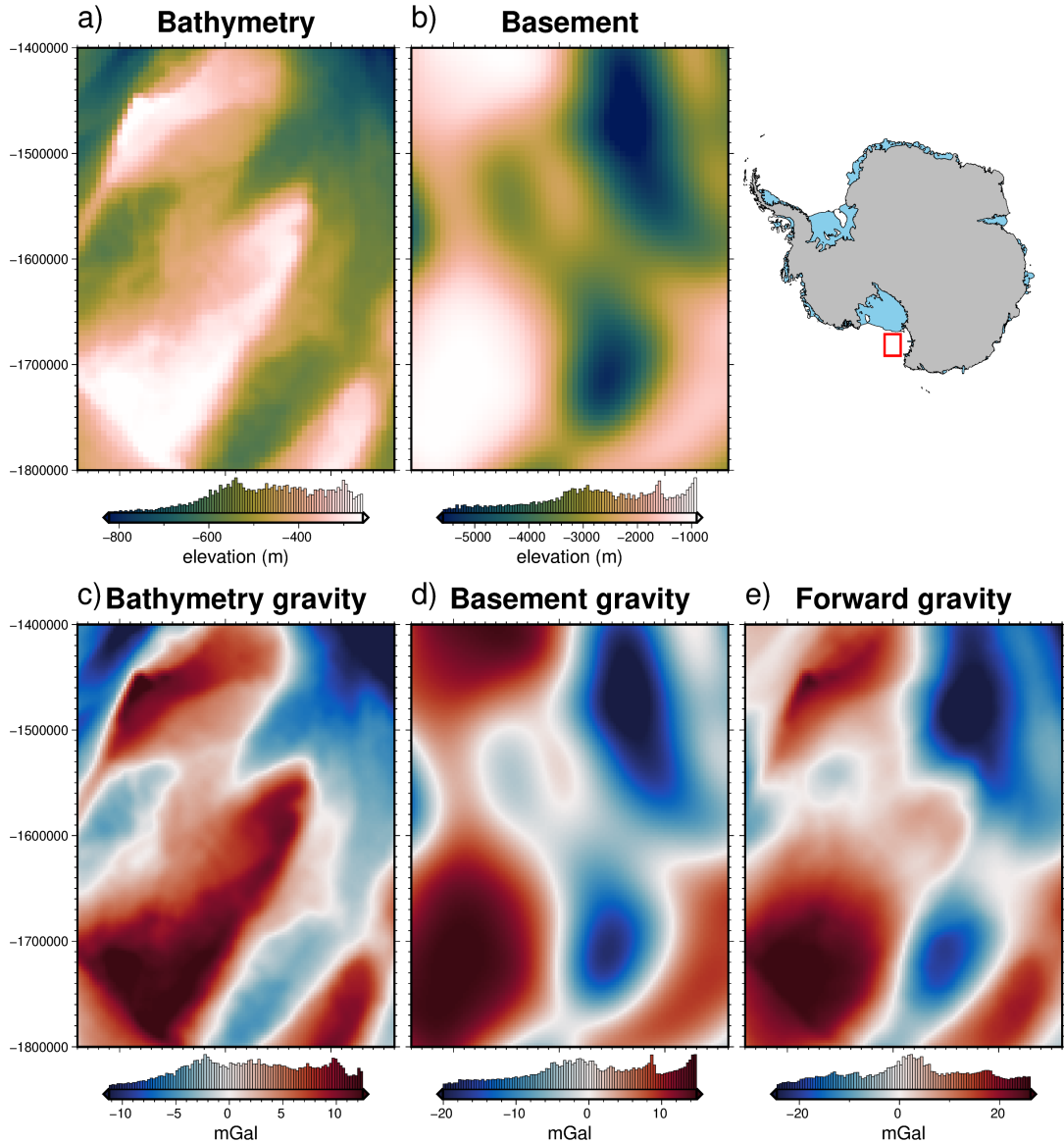


**Figure 3.24:** Ross Sea semi-synthetic model. **a)** Bathymetry data at 5 km resolution from IBCSO v2 (Dorschel et al., 2022), **b)** basement topography from the ANTOSTRAT project at 5 km resolution (Brancolini et al., 1995), **c)** forward gravity calculated at a regular 5 km grid at 1 km altitude for the bathymetry and **d)** for the basement. **e)** Total forward gravity from the combinations of c and d. Location of Ross Sea inversion domain shown as red box.

1939 N-S line and 3 E-W were omitted to represent missed flights. Along line spacing  
 1940 of data was 5 km. This survey configuration is similar to other Antarctic airborne  
 1941 surveys (Tinto et al., 2019). The full resolution gravity (Figure 3.25a) was sampled  
 1942 at these flight line locations, and the resulting values were fitted with equivalent  
 1943 sources. Gravity observations were then predicted from these sources on an even 5  
 1944 km grid<sup>3</sup> over the whole domain (Figure 3.25c). Lastly, the survey data was con-  
 1945 taminated with noise from a Gaussian distribution, with a mean of 0 and a standard  
 1946 deviation of 0.6 mGal (2% of the max absolute value of the full-resolution data).  
 1947 The difference between the true gravity and this noise-contaminated synthetic sur-  
 1948 vey (Figure 3.25b) represents the typical loss of data resulting from a sparse airborne  
 1949 survey. The RMS difference is 0.75 mGal. The largest differences are located within

<sup>3</sup>The gravity observations were actually interpolated onto a 2.5 km grid to account for the testing data.

1950 the flight line data gaps.

1951

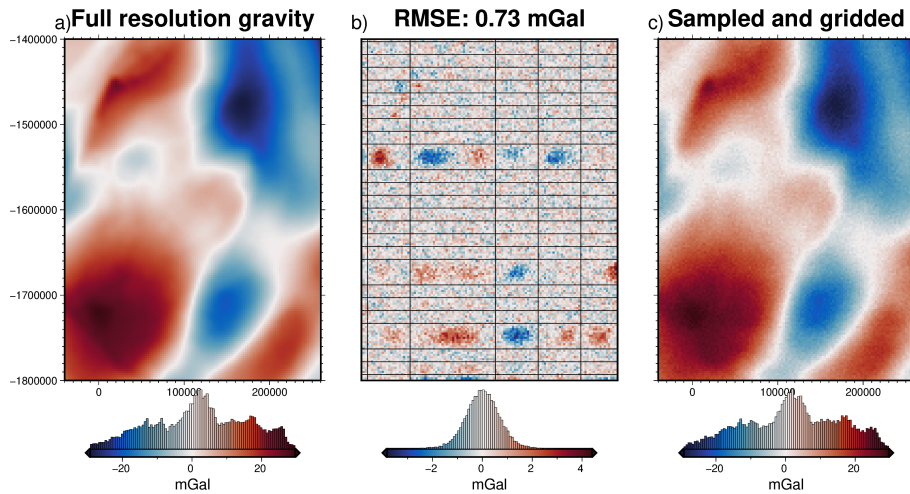


**Figure 3.25:** Ross Sea synthetic airborne survey. **a)** Full-resolution gravity data from the forward calculation of the bathymetry and basement. **b)** Difference between a and b, with black lines showing the synthetic airborne survey points. **c)** Gravity data from sampling along flight lines and re-gridded with equivalent sources.

### 1952 3.5.2 Starting bathymetry

1953 The bed elevations around the borders of ice shelves are generally well-constrained.  
 1954 Bathymetry depths from the open ocean portion of the ice shelf border can be  
 1955 found through satellite altimetry or multi-beam sonar surveys. The remainder of  
 1956 the ice shelf border consists of grounded ice. Bed elevations beneath grounded ice  
 1957 can be efficiently imaged or modelled with methods such as airborne radar or mass-  
 1958 conservation modelling (Morlighem et al., 2020). Many Antarctic ice shelves also  
 1959 contain sparse direct measurements of bathymetry from seismic surveying. This re-  
 1960 sulting configuration for many ice shelves is generalized by a very well-constrained  
 1961 border with sparse constraints located within. Here, this configuration is mimicked  
 1962 for a hypothetical ice shelf in the Ross Sea.

1963

1964 Within the model domain, a polygon is created to represent the ice shelf border  
 1965 (Figure 3.26). Outside this border, constraint points are placed in each grid  
 1966 cell of the model ( $N = 3503$ , small black dots in Figure 3.26). Within the border,  
 1967 constraints are placed on a semi-regular grid. To represent a spatial constraint den-  
 1968 sity similar to other Antarctic ice shelves<sup>4</sup>, 1 constraint per  $2500 \text{ km}^2$  is used. This  
 1969 equates to 39 constraints. In the previous models, the true bathymetry was sampled  
 1970 at the constraints and the resulting values were gridded for the entire domain. Here,  
 1971 to represent measurement uncertainties for attaining the constraint point depths, af-  
 1972 ter each point is sampled, Gaussian noise is added to the values before gridding.

1973

1974 Points outside of the ice shelf are contaminated with noise from a Gaussian  
 1975 distribution with a standard deviation of 5 m. This represents the well-constrained  
 1976 methods associated with bed observations on either grounded ice or in the open  
 1977 ocean. Points within the shelf are contaminated with noise based on their depth.

<sup>4</sup>The Ross Ice Shelf has  $\sim 1$  constraint per  $2200 \text{ km}^2$

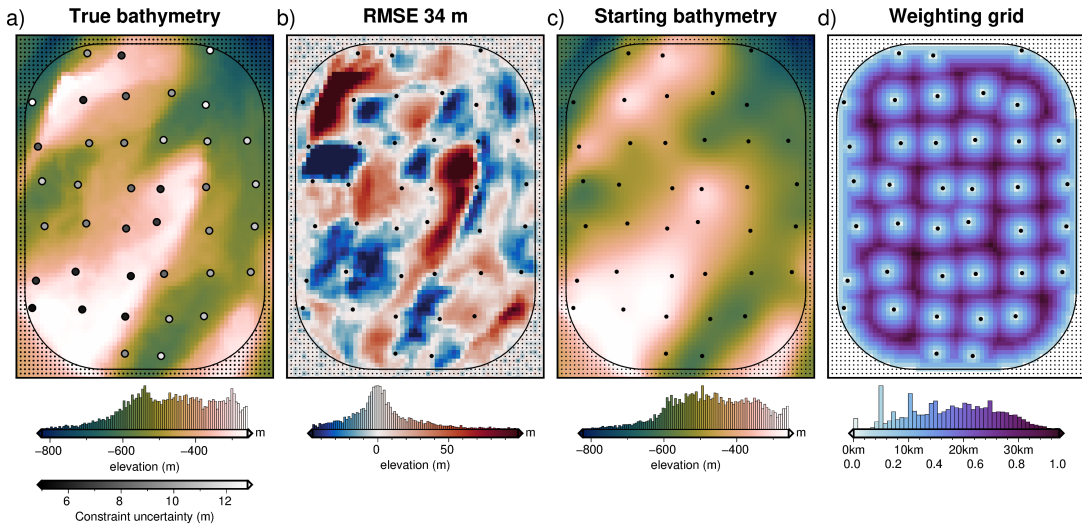


**Figure 3.26:** Gridding of the Ross Sea starting bathymetry. **a)** True bathymetry at 5 km resolution from the IBCSO v2 compilation (Dorschel et al., 2022). Constraint points (coloured dots), show the uncertainty values of each point. These uncertainties were used as the standard deviations of the Gaussian function for contaminating the sampled data with noise before regridding. **b)** Difference between a and b, **c)** starting bathymetry from the sampling and gridding of the constraint points with added noise. **d)** Weighting grid used in the inversion. Grid colours show both the distance between each grid cell and the nearest constraint point and the weight values (0 - 1) from the normalization of these distances. Small black dots and large black dots indicate constraints outside and inside of the ice shelf border, respectively. Semi-rounded black line shows the outline of the synthetic ice shelf.

1978 The Gaussian distribution used has a standard deviation of 2% of each point's depth.  
 1979 This simulates increasing measurement uncertainty with depth. Brisbourne et al.  
 1980 (2020) provide depth uncertainties for seismically imaged bathymetry beneath the  
 1981 Larsen C ice shelf, which have an average uncertainty as the percentage of depth  
 1982 from the surface of  $\sim 2\%$ . For our points, this equates to an RMS noise value of  $\sim$   
 1983 10 m for the ice shelf constraints. The uncertainty (the standard deviation of the  
 1984 Gaussian function used, not the actual value of the noise) of each point is shown  
 1985 in Figure 3.26a. This noise-contaminated sparse data is then gridded with a cross-  
 1986 validated bi-harmonic spline yielding the starting bathymetry. This interpolator  
 1987 takes the uncertainties of each point into account so that highly uncertain points  
 1988 don't introduce a bias into the interpolation (Uieda, 2018). The difference between  
 1989 the true and starting bathymetries had an RMS of 34 m over the whole grid, and  
 1990 an RMS at the constraint points of 10 m.

### 1991 3.5.3 Gravity misfit

1992 The starting bathymetry was discretized and forward modelled at the observation  
 1993 points with a density contrast of  $1276 \text{ kg m}^{-3}$ . This forward gravity was then sub-  
 1994 tracted from the observed gravity to get the gravity misfit (Figure 3.27a). Using  
 1995 the constraint point minimization method, the regional field was estimated with a  
 1996 bi-harmonic spline interpolator (Figure 3.27b), which was subsequently removed,  
 1997 leaving the residual misfit (Figure 3.27c). As in the above section, the interpolator  
 1998 takes the uncertainty of each constraint point into account to avoid overfitting the  
 1999 regional field to highly-uncertain constraint points.

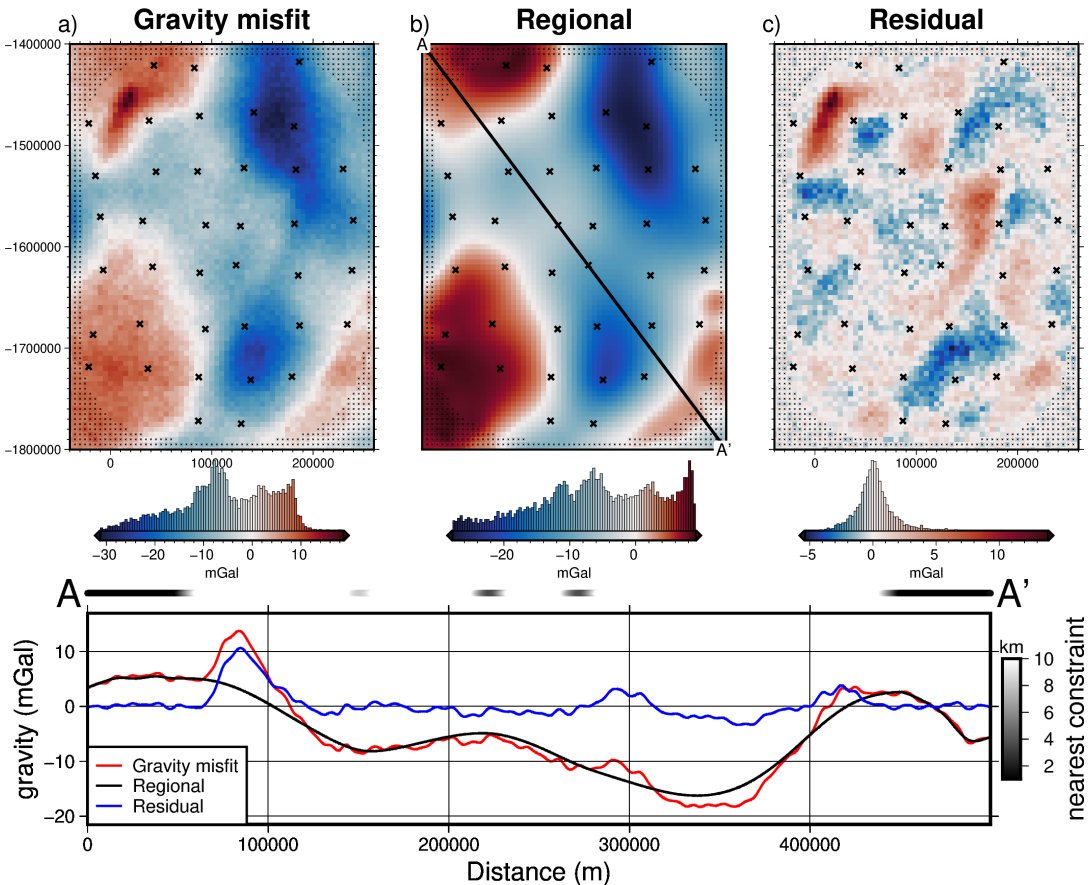


**Figure 3.27:** Ross Sea synthetic gravity anomalies. **a)** total gravity misfit, **b)** the estimated regional component using the constraint point minimization method, and **c)**, the residual misfit, as the difference between the total misfit and the regional component. Black crosses, large and small, show constraints inside and outside the ice shelf, respectively. **Lower panel** shows profile A to A' of gravity misfit and the regional and residual components. Distance to the nearest constraint at each point along the profile shown in black to white colours at top of profile.

### 3.5.4 Inversion

This residual misfit was then used in a cross-validation of 16 damping parameter values (Figure 3.28a). The inversion with the lowest cross-validation score was then chosen as the best model. During the inversions, a weighting grid was used to constrain the bathymetry at the points of known depths(Section 3.2.5.3). This grid (Figure 3.26d) is a normalized (0-1) grid of the minimum distance between each grid cell and the nearest constraint point. The inversion result and the difference from the true bathymetry are shown in Figure 3.29. The inversion had an RMS difference with the true Ross Sea bathymetry of 21 m and an RMS at the constraints of < 1 m. The inversion converged in 12 seconds at 15 iterations and had a final residual misfit of 0.43 mGal (Figure 3.28b).

### 3.5.5 Uncertainty analysis

Since the true Ross Sea bathymetry for this inversion is known, a direct measurement of the spatial uncertainty of the resulting bathymetry is simple to calculate (Figure 3.29b). This spatial uncertainty is useful to provide alongside the bathymetry results. It informs ocean modellers where results can be confidently interpreted and

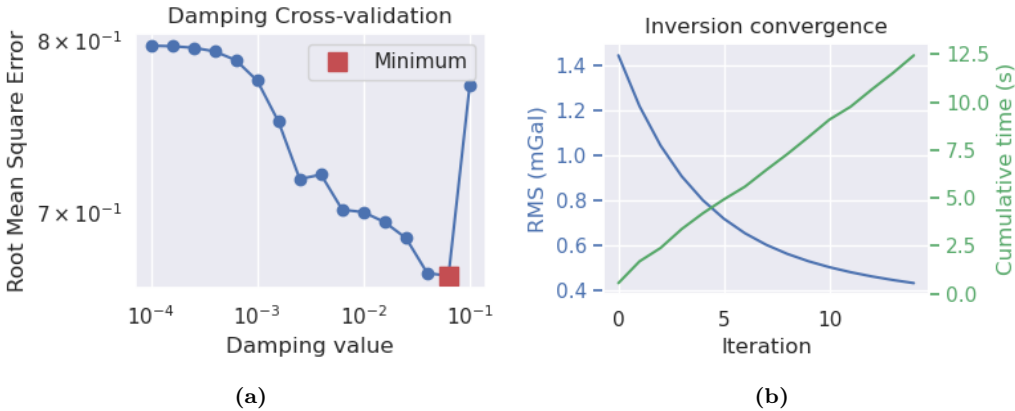


**Figure 3.28:** a) Cross-validation curve showing the optimal damping parameter (red square). b) Convergence of the inversion misfit. Blue line (left y-axis) shows the RMS of the residual misfit at each iteration of the inversion. Green line (right y-axis) shows the cumulative time to complete the inversion.

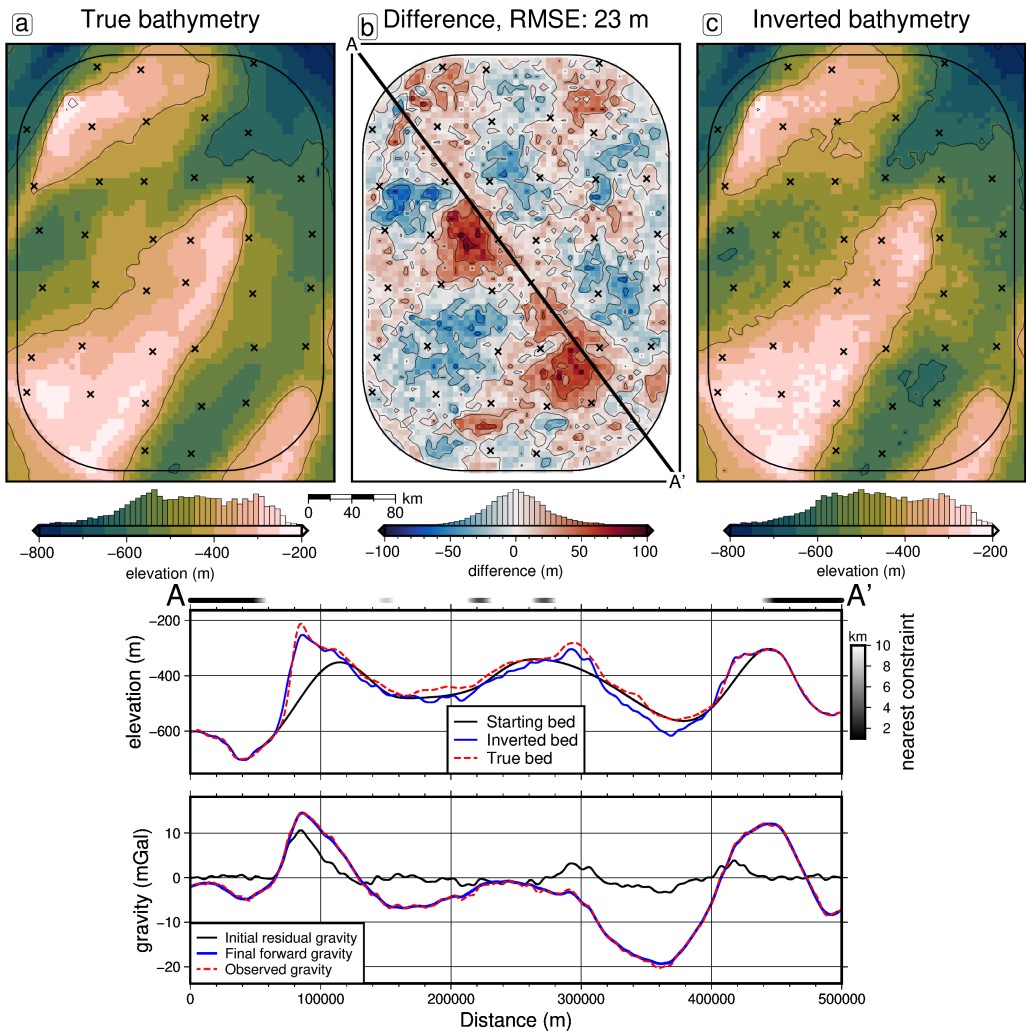


**Figure 3.29:** Ross Sea synthetic model inversion results. a) True bathymetry, b) difference between a and c, and c) final inverted bathymetry. Black crosses are constraint points. The RMS difference with the true bathymetry at these constraints is < 1 m. Lower panel) Profile from A to A'. The top panel contains topographic profiles of the starting, inverted, and true bathymetries. The bottom panel contains gravity anomaly profiles. Distance to the nearest constraint at each point along the profile shown in black to white colours at top of profile.

2018 highlights regions to focus future data collection. Here, a method of uncertainty  
 2019 analysis for this inversion is proposed, and the resulting uncertainty is compared to  
 2020 the inversion error to get a sense of the accuracy of our calculation of uncertainty.  
 2021 This uncertainty analysis is accomplished with Monte Carlo simulations (Helton et  
 2022 al., 2006; Jansen et al., 1994).

2023  
 2024 Here, 20 inversions are run with the same damping parameter cross-validation  
 2025 as conducted previously. For each inversion, the input parameters are sampled from  
 2026 distributions of their possible values. These prior distributions represent all plau-  
 2027 sible parameter values and thus the resulting inverted bathymetries should cover  
 2028 the range of plausible inversion outcomes. For each grid cell, the weighted standard  
 2029 deviation of the 20 inverted bathymetry values of that grid cell was calculated. The  
 2030 weighting came from the inverse square of each inversion's RMS difference between  
 2031 the inverted grid values and the constraint point depths. This reduces the bias from  
 2032 inversions with large misfits to the actual constraint points (Schnaadt & Heinson,  
 2033 2015). Chapter 4 Section 4.2.4 contains a detailed description of this uncertainty  
 2034 analysis methodology.

2035  
 2036 The parameters included in the Monte Carlo sampling are:

- 2037 1. the observed gravity data, sampled from a normal distribution with a mean  
 2038 equal to the observed values and a standard deviation of 0.6 mGal (2% of the  
 2039 maximum absolute value).
- 2040 2. the constraint point depths, sampled from a uniform distribution with a centre  
 2041 as the measured point depth and bounds of  $\pm 5$  m for the points outside the  
 2042 ice shelf, and  $\pm 2\%$  depth for points within the shelf.
- 2043 3. the bathymetry density contrast. This is defined as the difference between the  
 2044 densities of water and sediment. The mean value was taken to be  $1276 \text{ kg m}^{-3}$   
 2045 ( $2300 - 1024 \text{ kg m}^{-3}$ ). A standard deviation of  $400 \text{ kg m}^{-3}$  was used.

2046 Four suites of Monte Carlo simulations were run and are shown in 3.30. Each  
 2047 of the above parameters; gravity, constraints, and densities, were included in their  
 2048 own Monte Carlo simulations, and the fourth simulation included all parameters  
 2049 together. Simulations that included the sampling of the constraint depths required  
 2050 the re-calculation of the starting bathymetry, the starting forward gravity, gravity  
 2051 misfit, regional separation, and finally running the inversion. Simulations that in-  
 2052 cluded sampling the density values required recalculating the forward gravity, misfit,  
 2053 regional separation, and running the inversion. Simulations that included the sam-  
 2054 pling of gravity values only required recalculating the regional field and running the  
 2055 inversion. These values were sampled from their respective distributions using Latin  
 2056 hypercube sampling (Jansen et al., 1994). This allows an adequate coverage of the  
 2057 parameter space with only 20 inversions. See Chapter 4 Section 4.2.4 for further  
 2058 details.

### 2059 3.5.6 Effects of constraint spacing

2060 Here we test the effects of the number and spacing of constraint points on the  
 2061 accuracy of the inversion. The constraints outside the ice shelf are kept as they have  
 2062 been in the previous section, at the same grid spacing as the bathymetry (5 km).

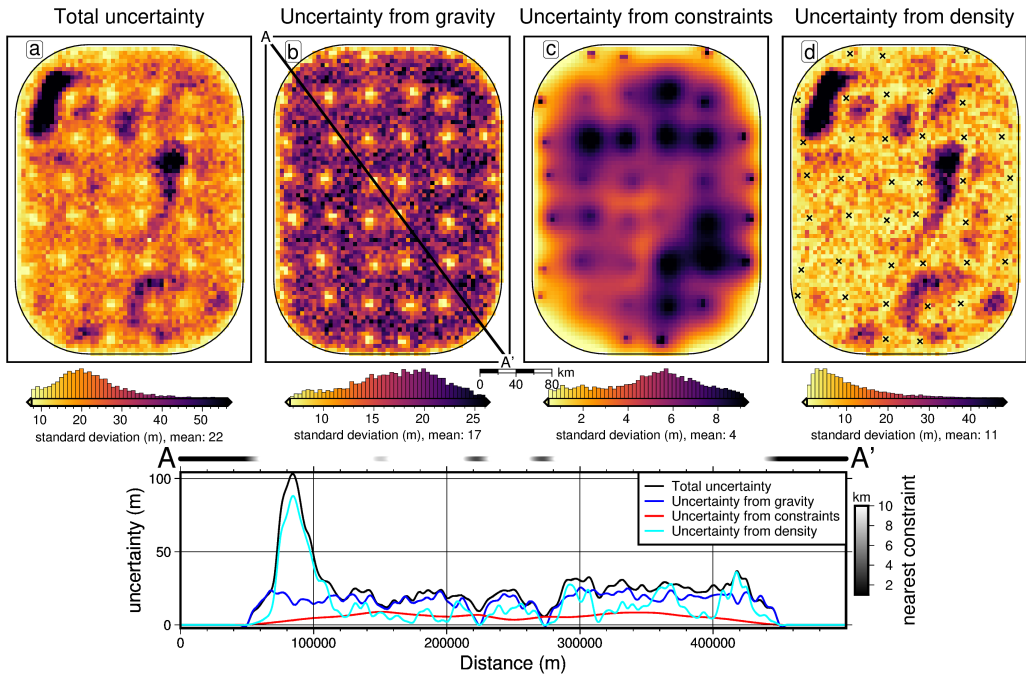


**Figure 3.30:** Monte Carlo simulation results for the Ross Sea synthetic inversion. Cell-wise weighted standard deviations of all inversions in each simulation. **a)** Total uncertainty from the sampling of gravity data, constraint depths, and density contrast value. **b)** Sampling of only the gravity data values. **c)** Sampling of only the constraint point depths. **d)** Sampling of only the density contrast. To aid in interpretation, locations outside of the ice shelf have been masked. Constraints within the ice shelf are shown as black crosses in **d**. **Lower panel**) Profile from A to A' of the total uncertainty and individual components. Distance to the nearest constraint at each point along the profile shown in black to white colours at top of profile.

2063 Constraints within the ice shelf are re-created on a regular grid, where the spacing of  
 2064 the grid, and thus the number of constraints, is varied from 10 km (959 constraints)  
 2065 to 100 km (9 constraints). The depth of the true bathymetry is sampled at each  
 2066 constraint. As in the previous section, points outside the shelf are contaminated with  
 2067 Gaussian noise with a standard deviation of 5 m. Noise for constraints within the  
 2068 ice shelf is relative to each point's depth (to simulate seismic survey uncertainties).  
 2069 These noise-contaminated constraint point depths are used in a bi-harmonic spline  
 2070 gridding to create the starting bed for each of the 10 constraint sets. The RMS  
 2071 difference between each of the starting beds and the true bed is shown as green dots  
 2072 in Figure 3.31a. From these starting beds the inversion workflow was conducted, as  
 2073 below:

- 2074 1. The forward gravity of the starting beds were calculated.
- 2075 2. The misfits with the observed gravity (Figure 3.25a) were calculated<sup>5</sup>.
- 2076 3. The regional component of the misfit was estimated and removed with the  
 2077 constraint point minimization method.
- 2078 4. The residual misfit was inverted with the cross-validation routine.
- 2079 5. The difference between each inverted bed and the true bed was found.

<sup>5</sup>To isolate the effects of changing the constraint density, the full resolution observed gravity with no added noise was used here, instead of the synthetic survey gravity.

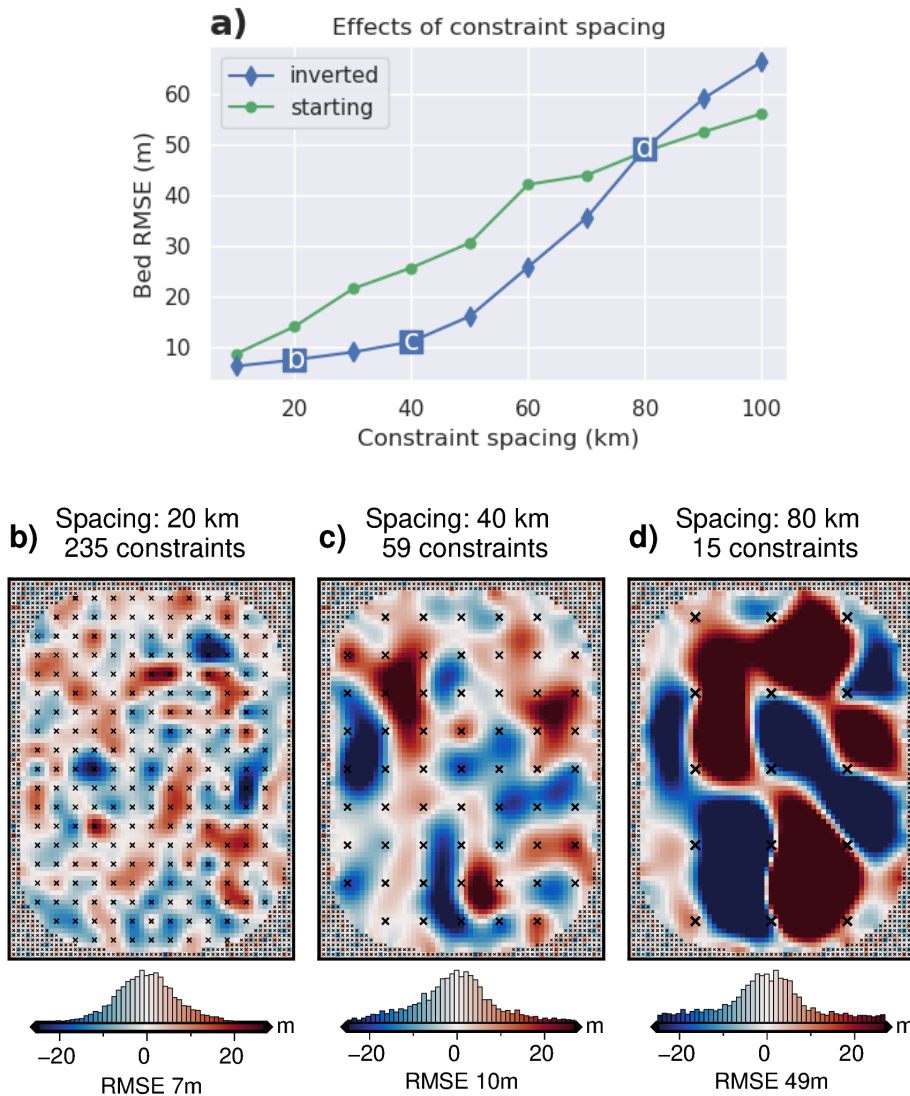


**Figure 3.31:** Effects of constraint spacing on inversion accuracy. **a)** Bathymetry error (RMSE) relative to the true bathymetry for 10 different constraint spacing. Green (circles) shows the starting error and blue (diamonds) shows the error after inversion. Labels b, c, and d refer to the three inversion error results shown as subplots. **b-d)** Inversion error grids for three of the ten configurations of constraints (labelled on a)). Note b-d use the same colour map. Small black crosses show constraints outside the ice shelf, and larger black crosses show inside constraints with the corresponding constraint spacing.

2080     Figure 3.31 shows the results of this analysis. Subplot a) shows the relationship  
 2081     between constraints spacing and the RMSE with the true bed of the starting bed  
 2082     (green circles) and the final inverted bed (blue diamonds). Three of the inverted  
 2083     bed errors are shown in subplots b-d. See Appendix B.2 for plots of the regional  
 2084     separation errors for these three inversions.

### 2085     3.5.7 Effects of gravity data

2086     As the above section analyzed the impact of the number of constraint points on  
 2087     the inversion's accuracy, here we investigate the impact of the quality and quantity  
 2088     of input gravity data. Following the methods of the two ensembles presented in  
 2089     the simple synthetic inversion (Figure 3.3.2 & 3.23), an ensemble of 100 inversions

with varying levels of noise and gravity observation spacing's are conducted with this Ross Sea model. The observed gravity data was contaminated with noise as described in the past sections, with 10 levels between 0 and 9% of the max absolute value. To simulate a more spare gravity survey, the previous two ensembles sampled the full-resolution gravity data onto a coarser evenly spaced grid and then re-gridded the sparse data with equivalent sources back to the full resolution of the bathymetry. Here instead of evenly spaced grids, we use airborne flight lines.

2097

We use a constant along-line observation spacing of 5 km but vary the spacing between flight lines. The N-S and E-W lines both use the same between-line spacing. The full-resolution gravity is then sampled at these points, and the sparse data is re-gridded to the full resolution (5 km) with equivalent sources. The noise and line spacing changes were applied to the original observed data, and the forward calculation of the starting model, initial misfit calculation, and regional field removal were all repeated. Each model was then inverted with a cross-validation, and the resulting RMS differences with the true bathymetry are shown in Figure 3.32.

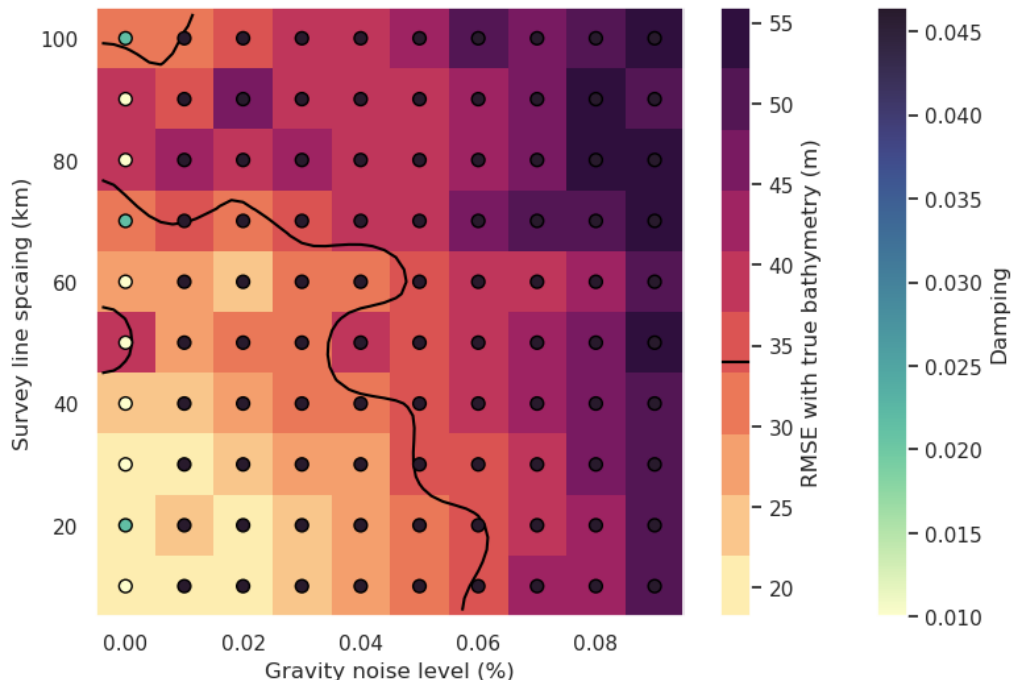


**Figure 3.32:** Ensemble of noise levels and airborne gravity line spacing for the Ross Sea synthetic model. Grid cell colour indicates each inversion's RMSE with the true bathymetry. Circles' colour indicates the optimal damping value found for each inversion's cross-validation. Black line shows the 34 m contour which represents the RMS difference between the true and starting bathymetry (Figure 3.26b).

## 3.6 Discussion

### 3.6.1 Simple synthetic model

The simple synthetic model of Section 3.3.1 was introduced to 1) present the basic workflow of the inversion, 2) determine the best options for various components of the inversion and 3) demonstrate the capabilities and limitations of the inversion.

2111 The starting bathymetry had an RMS difference with the true bathymetry of 66 m  
 2112 (Figure 3.6). This error demonstrates the limitations of gridding sparse data. Even  
 2113 with a very high spatial constraint density (1 constraint per 160 km<sup>2</sup>) compared to  
 2114 most ice shelves (Fretwell et al., 2013), simply gridding the constraints greatly misin-  
 2115 terpreted the true bathymetry. To reduce this bathymetric error, we presented three  
 2116 inversions, a noise-free full-resolution inversion, a noise-contaminated full-resolution  
 2117 inversion, and a noise-free lower-resolution inversion.

### 2118 3.6.1.1 Inversion results

2119 All of these inversions (without a regional component) were able to reduce this  
 2120 RMS difference with the true bathymetry to  $\sim 10$  m and recover all bathymetric  
 2121 features of interest. We demonstrated that the two methods of calculating the verti-  
 2122 cal derivative of gravity produced similar results, but the annulus approximation was  
 2123 significantly faster ( $\sim 5\times$ ). Additionally, for each of these inversions, the weighting  
 2124 grid, based on the distance to the nearest constraints (Figure 3.5), successfully con-  
 2125 strained the resulting inverted bathymetry at the points of prior bathymetry obser-  
 2126 vations. Each inversion's constraint point RMS difference with the true bathymetry  
 2127 was  $<\sim 2$  m, and the technique avoided any pedestal effect around the constraints in  
 2128 the resulting bathymetries. Interestingly, the inversion with low-resolution (6 km)  
 2129 gravity data yielded a very similar RMSE compared to the inversion with the full-  
 2130 resolution (1 km) data. This demonstrates that for recovering bathymetric features  
 2131 of wavelengths similar to those found in our synthetic model, high-resolution gravity  
 2132 surveys may not be necessary to achieve adequate results from an inversion.

### 2133 3.6.1.2 Ensemble results

2134 To test this theory further, we conducted an ensemble of 100 inversions with 10  
 2135 levels of noise contamination and 10 gravity survey resolutions. The resulting RMS  
 2136 difference of each inversion with the true bathymetry is shown in Figure 3.17. All  
 2137 inversions in this ensemble, including the worst-case scenario of 9% noise and a  
 2138 gravity observation grid of  $10\times$  the bathymetry spacing, still resulted in an RMS  
 2139 difference lower than that of the starting bathymetry (66 m). It is worth noting  
 2140 that this metric for the accuracy of the inversion, the root mean squared (RMS)  
 2141 difference with the true bathymetry, is used to give extra weighting to the outlier  
 2142 errors, as opposed to using a mean average error (MAE). These outliers typically  
 2143 include the features of interest in a bathymetry inversion. Figure 3.33a shows these  
 2144 ensemble results grouped by cell size. For each cell size value (colour of lines), the  
 2145 inverted bed RMSE for the range of noise levels is shown. This shows a roughly  
 2146 linear relationship between noise and RMSE, regardless of cell size. This means  
 2147 there is a continuous improvement in the inversion's accuracy with lower levels of  
 2148 noise. Conversely, figure 3.33b shows these ensemble results grouped by the noise  
 2149 level. For each noise level (colour of lines), the inverted bed RMSE for the range of  
 2150 cell sizes is shown. This shows an exponential relationship between gravity survey  
 2151 resolution and RMSE. This exponential relationship is strongest for low noise levels.  
 2152 This means inversion accuracy greatly benefits from increasing the survey resolution  
 2153 (decreasing the cell size), but this benefit diminishes once the survey resolution is at  
 2154 a certain point. Here, surveys at or below  $\sim 6$  km resolutions result in a diminish-  
 2155 ing improvement in RMSE. The linear relationship between noise and RMSE, and  
 2156 the exponential relationship between resolution and RMSE can also be seen by the

spacing of lines in either figure. The close spacing of the low-cell-size lines (purples) in Figure 3.33a show the diminishing improvements at small cell size surveys, while the continuous spacing of lines in Figure 3.33b shows the linear relationship.

2160

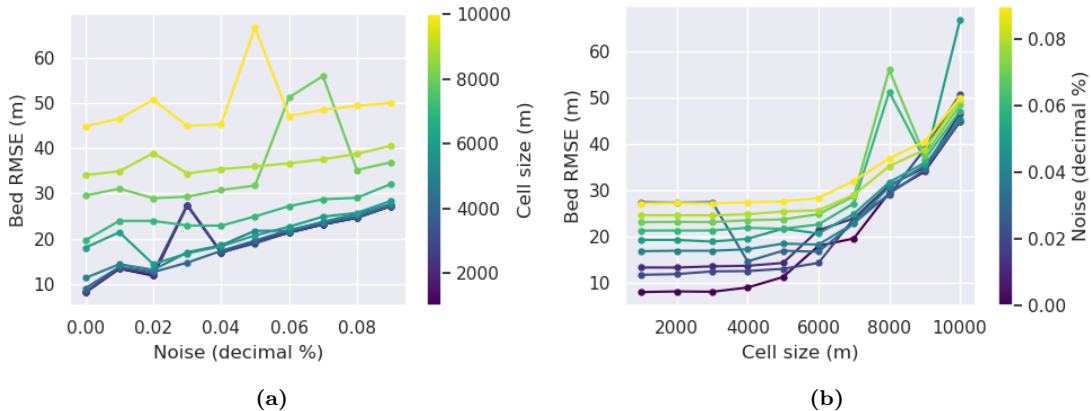


**Figure 3.33:** Ensemble results for the simple synthetic inversion, grouped by **a)** gravity survey cell size, and by **b)** noise level. Each line in a) corresponds to a row of Figure 3.17 and each line in b) corresponds to a column.

2161 In a typical gravity survey, there is often a trade-off between the number of  
 2162 observations made and the quality (noise) of the data. This is due to the time re-  
 2163 strictions of both the total data collection period (i.e. the length of a field season  
 2164 in Antarctica), and the necessity to repeat base-station measurements to account  
 2165 for instrument drift. Collecting more data in the same time period inevitably re-  
 2166 sults in increased noise. At a certain point, this increased noise will have a greater  
 2167 negative effect on the inversion results, than will be counteracted by the increased  
 2168 amount of data. These are important considerations for survey design. Figure 3.33b  
 2169 shows that for a given noise level, there is little benefit in increasing the gravity  
 2170 survey resolution from  $\sim 6$  km to 1 km. For this survey domain ( $60 \times 80$  km),  
 2171 a 6 km resolution results in  $\sim 130$  gravity station, while with a 1 km resolution,  
 2172 this increases to 4800 observation points. Simplistically speaking, if keeping total  
 2173 survey time constant, this means at 6 km spacing as opposed to 1 km spacing, ei-  
 2174 ther  $\sim 36\times$  more area could be surveyed, or higher quality data could be collected,  
 2175 with shorter base station loops, more repeated ties, and more careful measurements.  
 2176

2177 The results from the noise-contaminated inversion (Figure 3.12 & 3.9b) show  
 2178 that this gravity noise is directly reflected in the inversion results. For this reason,  
 2179 data, either the observed data or the residual misfit, is typically low-pass filtered  
 2180 prior to inversion (i.e. Boghosian et al., 2015; Yang et al., 2020a). This is typically  
 2181 done with either a time-based filter for airborne surveys, or a spatial filter (Jordan  
 2182 et al., 2010). With this filtering, there is a trade-off between removing the noise and  
 2183 removing the true signal. Due to this, we have chosen to omit the filtering in these  
 2184 synthetic examples.

**3.6.2 Simple model with a regional component****3.6.2.1 Regional separation methods**

The addition of a regional component to the observed gravity data adds a major complexity to the inversion workflow. The actual inversion remains the same, but this regional component must be estimated and removed beforehand. We tested four methods of regional estimation; 1) a low-pass filter, 2) fitting a polynomial trend to the data, 3) predicting the data with a set of deep point sources, and 4) attributing the entire misfit value to the regional field at constraint points and interpolating between these values. Figure 3.19 compares the inversion results of each of these methods. While each method recovered the short wavelength bathymetry features, the misestimation of the true regional field for each method introduced long-wavelength errors in the inversion results. We show that the constrain point minimization method most accurately estimated the region, and thus produced the best inversion results. For the simple regional field used here, the filter and trend methods achieved reasonable results, but the effectiveness of these methods is expected to be reduced with more complex regional fields associated with real data.

While the constraint point minimization worked best for this model, each of these methods may work better in specific scenarios. All the methods except the equivalent source method require the gravity data to be gridded over the entire region of interest. For sparse gravity surveys the interpolation required may introduce large errors. For this scenario, the equivalent source technique is likely the most appropriate. In scenarios with few bathymetry constraints and where the regional field is expected to be simple, the trend and low-pass filter methods are efficient and can be effective. However, if there are distributed bathymetry constraints, such as in this synthetic scenario, constraint point minimization is likely the best choice. This technique will only effectively remove regional anomalies with a wavelength equal to or greater than the average constraint spacing. If the constraints are sparse relative to the expected regional anomaly wavelengths, this method will underestimate the regional component. Lastly, if the bathymetry contains long-wavelength features which would result in long-wavelength anomalies, the trend, filter, and equivalent source techniques may include these in the regional removal. Therefore, the inverted bathymetry, while recovering the super-imposed short-wavelength bathymetry features, will underestimate the long-wavelength features. It is for these reasons that regional separation is perhaps the most important aspect of a bathymetry inversion.

**3.6.2.2 Constraint point minimization**

This constraint point minimization technique requires the gridding of sparse measurements of the regional field. We explored the impact of this gridding process on the resulting inversion. Figure 3.20 shows the results of four different gridding processes. Minimum curvature gridding without tension (tension of 0, Figure 3.20a) produces a smoothly varying surface at the constraints but introduces artificial minima and maximum at points far from any constraints. This erroneous effect is minimized with a higher tension factor. Using a tension factor of 1, figure 3.20c shows the limited erroneous minima and maxima, but this added tension results in high gradients in the surface immediately near the constraint points (Figure 3.20g). These high gradients in the resulting residual anomalies create a *ringing* effect in

the inverted bathymetry (Figure 3.20k). For these reasons, an intermediate tension factor of 0.25 is suggested for potential field data. While this limits the negative effects of both low and high tension, there are still false minima and maxima (Figure 3.20b), and high gradients at the constraints (Figure 3.20f). The last gridding technique uses bi-harmonic splines. The optimal damping parameter associated with this technique is chosen from a cross-validation of the constraint points. This technique, while being more computationally expensive, solves both issues of tensioned minimum curvature.

### 3.6.2.3 Inversion results

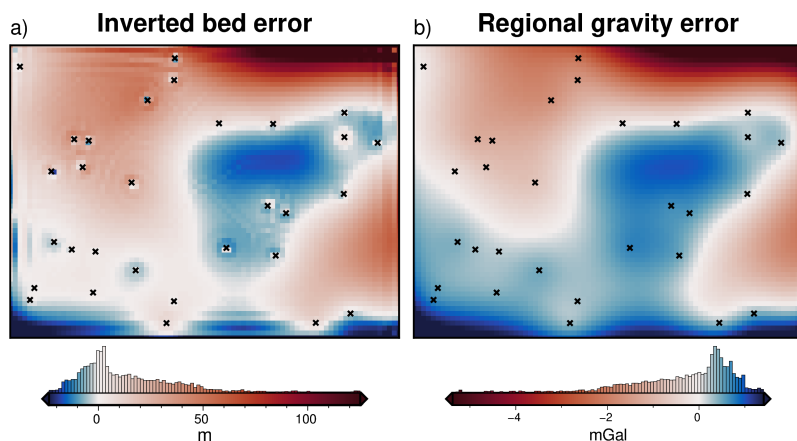


**Figure 3.34:** Source of inverted bathymetry error for the simple synthetic model with a regional field. **a)** Inverted bathymetry error from Figure 3.22b. **b)** Error in the estimation of the regional component of gravity from comparison with the true regional component (Figure 3.18b). Black crosses show constraint points. Colourmaps are inverted to highlight the similarities and the median has been removed from the regional error.

With both the optimal regional separation method and the optimal gridding method determined, we performed a cross-validated inversion with the remaining residual misfit. This inversion was able to recover all the short-wavelength bathymetry features but introduced some long-wavelength errors. Figure 3.34 shows the inverted bathymetry error alongside the error in estimating the regional component of gravity. Comparing these shows that almost all of the inverted bathymetry error is tied to the inaccuracies of determining the regional component. the remaining error is all minor short-wavelength features, mostly around constraint points. They appear to result from the weighting grid implementation of regularization. Since the errors in the regional estimation are the dominant source of error in most inversions, as shown above, and by other Antarctic bathymetry inversions (Brisbourne et al., 2014), we have shown these details of the gridding process are a vital and often overlooked step in many studies.

### 3.6.2.4 Ensemble results

As with the simple model, an ensemble of noise and gravity survey spacing experiments were performed with this model containing a regional component. The lowest resulting RMS difference with the true bathymetry was raised from values of  $\sim 10$  m for the inversion without the regional component, to the lowest value of  $\sim 40$  m with the additional regional component. The black line in Figure 3.23 shows

the 66 m contour, which represents the RMS difference between the true and starting bathymetries. Inversions that fall outside (above) this line resulted in a worse bathymetry than the starting model. This shows that for this model, inversion is only worth conducting if the gravity survey has a spacing less than  $\sim 9$  km ( $\sim 9 \times$  the spacing of the desired bathymetry resolution). Figure 3.35 show these ensemble results grouped by cell size and noise level. There is a linear relationship between gravity noise and the resulting bathymetry RMSE, for all gravity survey spacings. There is an approximately exponential relationship between gravity survey resolution (cell size) and resulting bathymetry RMSE. The degree of this exponential relation decreases with increased noise.

2269

For this model, the *elbow* of the exponential curves in Figure 3.35b is at  $\sim 6 - 8$  km survey resolutions ( $6-8 \times$  bathymetry resolution). This suggests that for a survey resolution finer than  $\sim 8$  km, there is little benefit in collecting more data. This is supported by the close spacing of low-cell-size lines (purples) in Figure 3.35a. The effort would be better spent collecting data over a wider region, reducing noise in the data, or if possible collecting more bathymetric constraints.

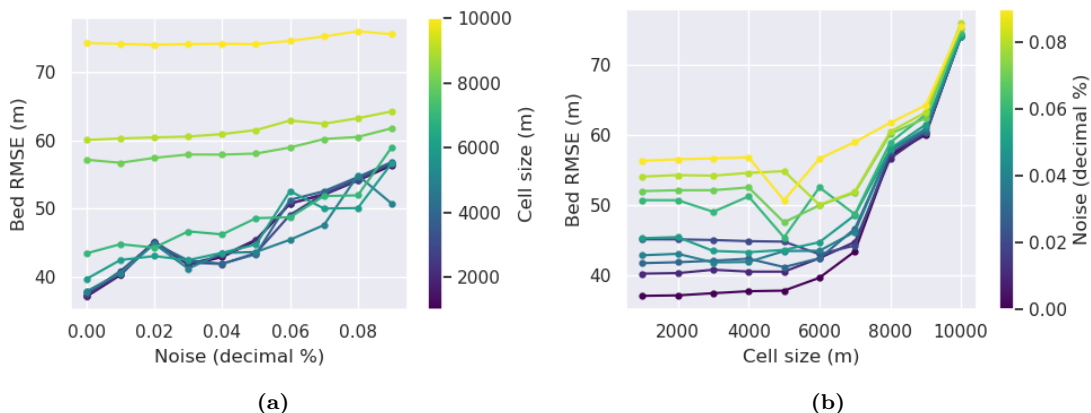


**Figure 3.35:** Ensemble results for the synthetic inversion with a regional component, grouped by **a)** gravity survey cell size, and by **b)** noise level. Each line in a) corresponds to a row of Figure 3.23 and each line in b) corresponds to a column.

### 3.6.3 Ross Sea model

The Ross Sea semi-realistic model was created to better emulate the gravity and bathymetries expected for ice shelves. A few extra complexities were added to this model compared to the purely synthetic models. An ice shelf border was included, with a high density of constraints outside of the border, and sparse constraints within. All the constraints had an associated uncertainty, instead of directly sampling the true bathymetry depths. The observed gravity was calculated along the flight paths of a typical airborne survey, instead of along a uniform grid. The main inversion in this section had 2% noise added and had flight lines with 50 km N-S spacing and 15 km E-W spacing. The inversion successfully reduced the starting bathymetry error from an RMSE of 34 m to 23 m. The resulting bathymetry shows a recovery of most of the lost bathymetry features, but some noise from the gravity data has been introduced into the bathymetry. Sharp bathymetry features (upper left corner) and smooth features were both recovered. The constraint points were

2290 relatively evenly distributed (Figure 3.26d), resulting in a relatively even distribution  
 2291 of bathymetry misfits.

2292

2293 Of these errors, the largest were located at the gaps in the synthetic survey  
 2294 where there were missing flight lines (Figure 3.25b). To understand the cause of  
 2295 the remaining errors, we compare the inverted bathymetry error with the regional  
 2296 separation error (Figure 3.36). The strong correlation between these two grids shows  
 2297 that the majority of errors in the inversion are tied to the miscalculation of the  
 2298 regional field, as was seen in the simple synthetic inversion with a regional field.  
 2299 The remaining errors appear to be from the flight line gaps and noise in the gravity  
 2300 data.

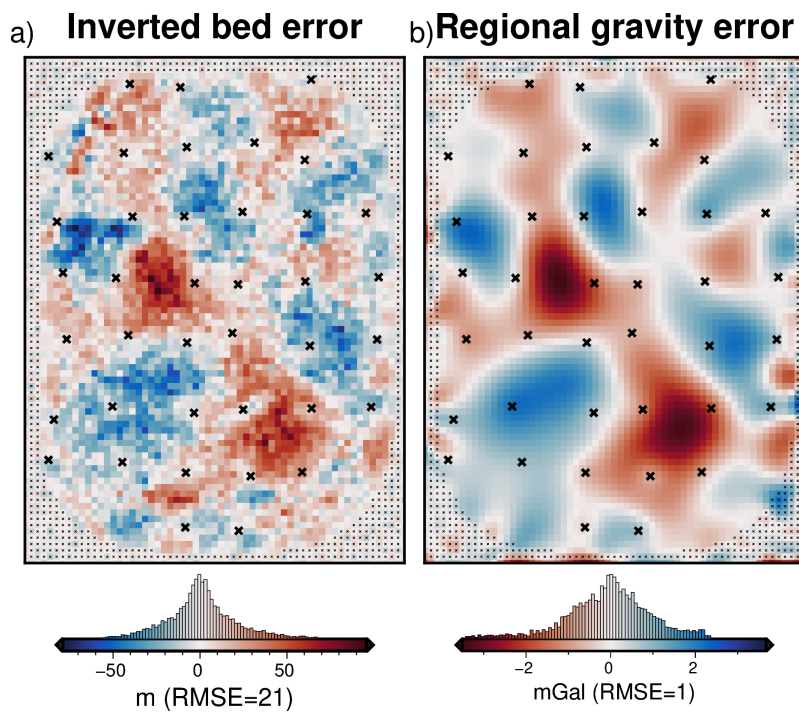


**Figure 3.36:** Comparison of the inverted bathymetry error and the error in the regional field estimation. **a)** Inverted bathymetry error from Figure 3.29b. **b)** Error in the estimation of the regional component of gravity from comparison with the true regional component (Figure 3.24d). Black crosses show constraint points. Colourmaps are opposed to highlight the similarities and the median has been removed from the regional error.

### 2301 3.6.3.1 Effects of the gravity data

2302 The ensemble of gravity data noise levels and flight line spacings from Section 3.5.7  
 2303 shows the relative importance of these two aspects of a gravity survey. As for the  
 2304 previous ensembles, Figure 3.37 shows these results grouped by line spacing and by  
 2305 the noise level. For the Ross Sea model, both factors have a roughly linear relation-  
 2306 ship with inverted bathymetry error. The slopes for the lines of best fit for Figure  
 2307 3.37a and b means the inversion RMSE increases by  $\sim 10$  m for either a 4% increase  
 2308 in the noise level or a 60 km increase in the average flight line spacing. The inversions  
 2309 with a small line-spacing (purple lines) of Figure 3.5.7a are closely grouped, relative  
 2310 to the higher line spacings. This shows that at already low line spacings (40 km)  
 2311 there may be little benefit to reducing the line spacing further. Conversely, there  
 2312 is a larger spread for the low noise inversions (purple lines) in Figure 3.5.7b. This

2313 shows that even at low noise levels, further decreases may still provide important  
 2314 improvements to the inversion outcome. As in the previous ensemble results, for  
 2315 a field application, this demonstrates the important tradeoff between quantity and  
 2316 quality of gravity data.

2317

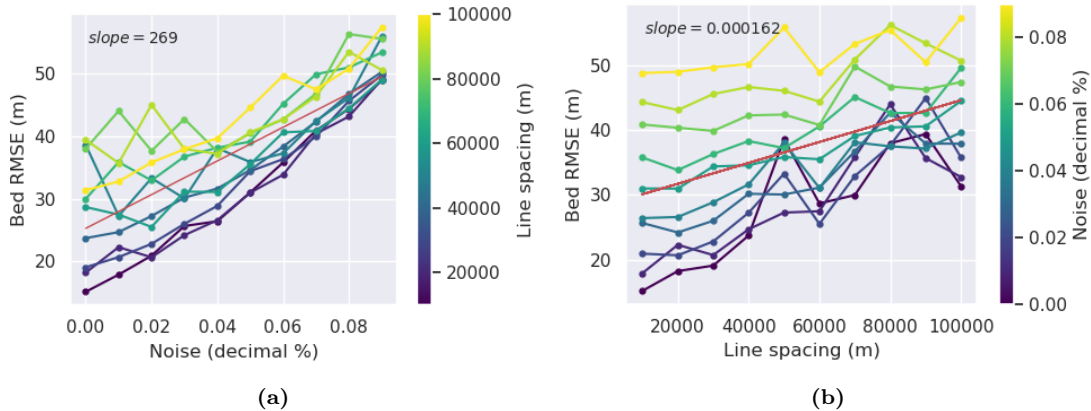


**Figure 3.37:** Ensemble results for the Ross Sea inversion, grouped by **a)** gravity survey line spacing, and by **b)** noise level. Each line in a corresponds to a row of Figure 3.32 and each line in b corresponds to a column. Red lines show the line of best fit, with their slopes shown in the upper left corners.

2318 These specific relationships between noise, line spacing, and inversion error, while  
 2319 not applicable to all survey configurations, show the importance of choosing an  
 2320 appropriate survey design. This analysis with synthetic data could be included in a  
 2321 pre-survey plan, to explore the effects of differing survey configurations.

### 2322 3.6.3.2 Effects of the constraints

2323 These synthetic inversions have shown that the removal of the regional field presents  
 2324 the biggest challenge for gravity inversions for bathymetry. The most robust tech-  
 2325 nique for removing the regional field requires a distribution of points of known  
 2326 bathymetry across the inversion region. Since the largest errors in the inverted  
 2327 bathymetries occur at the largest distance to constraints, an even distribution of  
 2328 constraints will best be able to estimate the regional field. Section 3.5.6 explored  
 2329 the effects of varying the numbers of constraints, while keeping the remaining com-  
 2330 ponents of the inversion constant. Figure 3.31a shows the bathymetry RMSE with  
 2331 the true bathymetry both before (green) and after (blue) the inversion is conducted.  
 2332

2333 Figure 3.31a shows for this synthetic model that for average constraint spacing's  
 2334 less than  $\sim 20$  km there is little improvement made by running an inversion. This  
 2335 is due to the starting bathymetry model already being relatively accurate, with the  
 2336 inversion only producing minor adjustments between constraint points. At the other  
 2337 end of the spectrum, with constraint densities greater than  $\sim 70$  km, the inverted  
 2338 bathymetry has an error similar to or higher to the un-inverted bathymetry. This is  
 2339 due to the inaccuracies in calculating the regional field with only very sparse con-  
 2340 straints. For these scenarios, the errors introduced by the inversion are greater than  
 2341 the errors of simply interpolating the constraint points. The inverted bathymetry  
 2342 error curve (Figure 3.31a) shows that for this survey, once below a certain constraint  
 2343 spacing ( $\sim 30$  km) there is little benefit to having additional constraints.

**3.6.3.3 Uncertainties**

We have demonstrated that the majority of the inverted bathymetry error is related to the estimation of the regional component of gravity. Without knowing the true regional component, as we do in these synthetic examples, estimating the uncertainty in the interpolation between constraint points of the regional field is difficult. The uncertainty of each grid cell is likely strongly dependant on the distance to the nearest constraint, as well as the depth uncertainties of these nearby constraints. While we show this to be true with our synthetic models, a quantitative method of predicting this uncertainty has yet to be implemented here. The field of conventional bathymetry surveying has developed uncertainty analysis tools that may be applicable to this (Bourgeois et al., 2016).

2355

These tools are able to account for both the depth uncertainty of each measurement, and the distance of each grid cell to the nearest measurement. Future work will benefit from a quantitative assessment of the uncertainty of gridding the regional field from the constraint point values. While the uncertainty of the regional removal accounts for the majority of the uncertainty of the inverted bathymetry, it is technically completed before the inversion and is thus not a component of the inversion uncertainty. To address the uncertainty resulting from the inversion process, we introduced a suite of Monte-Carlo simulations in Section 3.5.5. The results in figure 3.30 show a mean uncertainty for the entire region of 22 m. The majority of this uncertainty is attributed to the uncertainty in the gravity data, as shown by histograms of Figure 3.30. Here we discuss the significance of each component of the uncertainty analysis:

2368

**1. Gravity uncertainty:** The uncertainties in the gravity data result in a relatively uniform bathymetry uncertainty across the region of 17 m. A simple calculation with the Bouguer slab formula with a density contrast of 1276 kg m<sup>-3</sup> and our assumed gravity uncertainty of 0.612 mGal (%2 max absolute value) gives a value of 11.5 m ( $\Delta g_{boug} = 4.18e-5\rho h$ ). This may show the conventionally used Bouguer slab approximation is underestimate the true uncertainty in inversions resulting from gravity data uncertainty. This uncertainty is lowest at the constraints, due to the use of the weighting grid in the inversion.

2377

**2. Constraint depth uncertainty:** The contribution to the bathymetry uncertainty from the depth uncertainty of the constraint points is small, with a mean of ~4 m. This uncertainty resulting from the constraints is also concentrated around the constraint points. This shows improving the constraint point uncertainties will not greatly improve the inversion, and will only improve it in the immediate vicinity of constraints.

2383

**3. Density uncertainty:** The bathymetry uncertainty component resulting from the prism densities is heterogeneous, with some spatially limited, but large values. The mean value is ~11 m, but some areas are up to 50 m. These high uncertainties are strongly correlated with the error in the starting bathymetry (Figure 3.26b). This is due to the change in density contrast resulting in a change in the total bathymetry correction calculated in the inversion. In other words, the residual misfit can be minimized by a large surface

2390 correction with a low-density contrast or a small surface correction with a  
 2391 large-density contrast.

2392 The combined Monte-Carlo simulation (Figure 3.30a) shows the expected fea-  
 2393 tures of an uncertainty map. It has a base level uncertainty similar to the Bouguer  
 2394 slab thickness from the assumed gravity uncertainty, it is generally lowest at the con-  
 2395 straints and highest in the large constraint gaps, and it is high where the inversion  
 2396 has produced a large change from the starting model.

## 2397 3.7 Future work

2398 Running this inversion with the various synthetic models gave us the ability to  
 2399 assess the inversion performance. From this assessment, we have determined several  
 2400 components which would benefit from additional investigation.

- 2401 1. Implement an additional cross-validation routine to estimate the optimal den-  
 2402 sity contrast, as in Uieda and Barbosa (2017). Here, we have used the same  
 2403 density contrasts for the creation of the observed gravity data and for the  
 2404 inversion itself. In a non-synthetic scenario, this contrast would need to be  
 2405 estimated.
- 2406 2. Test the effects of flight line orientation relative to the dominant trend of  
 2407 geologic structures.
- 2408 3. Implement a more robust method of enforcing the constraint points. This  
 2409 may likely be in the form of a bounded least squares solver or some form of  
 2410 manipulation of the Jacobian matrix.
- 2411 4. Quantify the uncertainty of the regional separation process. This will likely  
 2412 include techniques used in conventional bathymetry surveying (Bourgeois et  
 2413 al., 2016; Calder & Elmore, 2017), or a sequential Gaussian simulation (Perozzi  
 2414 et al., 2021).
- 2415 5. Testing the effects of pre-filtering the gravity data, either spatially or tempo-  
 2416 rally, to remove the effects of noise (Jordan et al., 2010).

## 2417 3.8 Conclusion

2418 With the goal of modelling the bathymetry beneath a floating ice shelf, we present  
 2419 a geometric gravity inversion that 1) adheres to prior bathymetry point measure-  
 2420 ments, within their uncertainties, 2) produces a smooth and realistic bathymetry,  
 2421 3) accounts for the regional gravity field and 4) is computationally efficient and  
 2422 fully-open source. To demonstrate the effectiveness, as well as the limitations, we  
 2423 conducted a series of inversions using synthetic and semi-realistic data. These in-  
 2424 versions showed the importance of accurately estimating and removing the regional  
 2425 component of gravity prior to the inversion. We showed that for the constraint ar-  
 2426 rangement for many Antarctic ice shelves, the optimal method for estimating this  
 2427 regional field is with a constraint-point minimization. In addition, we further ex-  
 2428 plored this method by testing various gridding (interpolation) techniques and found

2429 a clear increase in performance when using a cross-validated bi-harmonic spline in-  
2430 stead of the typically used tensioned minimum curvature.

2431

2432 Here we reiterate a few of the key findings from this chapter:

2433

- 2434 1. Estimating and removing the regional component of gravity for typically in-  
2435 version scenarios is the most important aspect of the inversion procedure. For  
2436 typical bathymetry inversions, the optimal method for estimating the regional  
2437 field is constraint point minimization.
- 2438 2. When collecting data for an inversion, it is best to aim for quality over quanti-  
2439 ties for the gravity data, and conversely, quantity over quality for bathymetry  
2440 constraint measurements.
- 2441 3. We provide general guidelines on the optimal ranges of constraint density, grav-  
2442 ity survey line spacing, and gravity noise, for which conducting an inversion is  
2443 suitable.

2444

2445 Testing the various models with differing levels of gravity noise and numbers  
2446 of gravity observation points highlights an important factor in planning a grav-  
2447 ity survey. We show for the Ross Sea synthetic model, which likely emulates the  
2448 scenario expected from many Antarctic ice shelves, **there are diminishing re-**  
2449 **turns for average flight line spacings smaller than  $\sim 40$  km** if the goal is  
2450 to recover bathymetry features typical of the Ross Sea. **However, the inverted**  
2451 **bathymetry's accuracy is strongly affected by noise in the gravity data.**  
2452 With this, the typically airborne survey focus on quantity of quality may need to be  
2453 reassessed. If 40 km spaced flight lines produce similar results to 20 km lines, flying  
2454 half the number of lines will save a significant amount of time. This time could  
2455 be used to either expand the area of the survey or reduce the noise in the data.  
2456 Reducing the data noise for an airborne survey may not always be feasible, but a  
2457 few measures may be taken to attempt this, all of which are aided by the increased  
2458 survey time allowed by reducing the number of flight lines. These include repeating  
2459 lines or sections which are noisy, limiting flights to good weather windows, increasing  
2460 the number of tie-lines, making shorter loops for base-station ties, or flying at  
2461 lower altitudes and or ground speeds.

2462

2463 **The previous measurements of bathymetry, referred to as the con-**  
2464 **straints, are a vital part of an inversion for bathymetry.** Due to the non-  
2465 uniqueness of an inversion, there are an infinite number of inverted bathymetry  
2466 models which will equally match the observed data. These constraints provide the  
2467 ground truth necessary to confidently chose a model out of these infinite choices.  
2468 Additionally, if not more importantly, they provide the primary method of account-  
2469 ing for the regional component of gravity. Since this is shown to be the largest  
2470 source of uncertainty, the constraints are the most important aspect of the inver-  
2471 sion. We tested the effects of varying the spatial density of the constraint points.  
2472 The results (Figure 3.31) show the range of constraint point spacings for the Ross  
2473 Sea synthetic model which justifies conducting a gravity inversion if the goal is to  
2474 recover bathymetry with a 5 km resolution.

2475

**The optimal constraint spacing is between  $\sim 20\text{-}70$  km.** Smaller spacing  
2476 values already have an adequate amount of information and little is gained over a

simple interpolation of the data. At spacings larger than  $\sim 70$  km, the errors in estimating the regional field are larger than the improvements made by the inversion. These values, while specific to the Ross Sea scenario, provide an important context for the feasibility of conducting bathymetry inversions. Taken together with the above assessment of the relative importance of gravity data noise and density, some general guidelines are provided.

2482

As long as the gravity data is on the order of magnitude of  $2\text{-}4 \times$  the spacing of the desired bathymetry resolution, and the noise levels are low, **efforts should be focused on collecting more bathymetry measurements**. The uncertainty of these depth measurements is relatively unimportant (Figure 3.30c), meaning quantity over quality is acceptable here. The final spatial uncertainty of the inverted bathymetry is strongly tied to the distance to the nearest constraint. This suggests that an even distribution of the constraints is important. However, if specific regions of the survey are expected to have larger amplitude regional anomalies, an increased spatial density of constraints over this region would be beneficial. With these recommendations, future planning for Antarctic fieldwork should be able to collect data that prioritizes the accurate assessment of sub-ice-shelf bathymetry.

2484

Chapter 4 applies the inversion presented here to model the bathymetry beneath Antarctica's Ross Ice Shelf.

2485

2486

2487

2488

2489

2490

2491

2492

2493

2494

2495

2496



2497 **Chapter 4**

2498 **Ross Ice Shelf bathymetry inversion**

2499 **Abstract**

2500 Antarctica's Ross Ice Shelf buttresses large catchments of ice from both the East and  
2501 West Antarctic Ice Sheets. Changes to the current stability of the ice shelf, likely  
2502 through basal melt of the sensitive grounding zones or pinning points, will reduce this  
2503 buttressing and accelerate the Antarctic Ice Sheet's contribution to global sea level  
2504 rise. The distribution of basal melt is predominantly controlled by the ocean cavity  
2505 thickness and the channelling of ocean waters by bathymetric features. Bathymetry  
2506 is, however, poorly known for the Ross Ice Shelf. Here we use airborne gravity  
2507 data and distributed seismic constraints across the ice shelf to create an updated  
2508 sub-ice shelf bathymetry model. We accomplish this with a non-linear geometric  
2509 gravity inversion, available as open-source Python code. Monte Carlo sampling  
2510 of the inversion inputs provides a robust means of addressing spatial uncertainty  
2511 and the relative significance of each component of the inversion. The resulting  
2512 bathymetry closely matches the seismic constraints and reveals significant changes  
2513 compared to past bathymetry models. We find several likely locations of past pinning  
2514 points, locations where enhanced basal melting is likely, and sites of possible tectonic  
2515 significance.

2516 **Plain Language Summary**

2517 The floating Ross Ice Shelf slows the flow of a large amount of ice into the ocean.  
2518 Melting at the base impacts the ice shelf's ability to slow down this upstream ice.  
2519 The shape of the seafloor beneath the ice shelf (bathymetry), acts to guide ocean cur-  
2520 rents which cause this melting. Our knowledge of the bathymetry beneath the Ross  
2521 Ice Shelf comes from a series of point measurements with an average distance be-  
2522 tween points of over 40 km. Here, we use measurements of Earth's gravity collected  
2523 over the ice shelf to estimate the shape of the bathymetry beneath. This technique  
2524 provides an increased resolution of the bathymetry and informs us about where we  
2525 are most and least confident of the bathymetry depth. With this new model of  
2526 sub-ice-shelf bathymetry, we highlight locations where melt-inducing ocean currents  
2527 are likely directed, and several places with the seafloor is very close to the base of  
2528 the ice. These results will better inform ocean circulation models beneath the ice  
2529 shelf, and therefore the likely future contributions of the Ross Ice Shelf to sea level  
2530 rise.

**2531 Key Points**

- 2532 1. We present a new bathymetry model beneath Antarctica's Ross Ice Shelf from  
2533 a gravity inversion.
- 2534 2. A Monte Carlo simulation provides a detailed spatial uncertainty analysis.
- 2535 3. Results highlight locations where the updated bathymetry may impact ocean  
2536 circulation models or where the shelf may have been recently grounded.

**2537 4.1 Introduction**

2538 Much of Antarctica's coastline is fringed by floating extensions of the Antarctic Ice  
2539 Sheet. These floating masses of ice, referred to as ice shelves, are connected to the  
2540 grounded ice. Over 80% of Antarctica's grounded ice drains to the oceans through  
2541 these ice shelves (Rignot et al., 2013). While they are floating, and thus already  
2542 displace their mass equivalent of seawater, they are vital to the current and future  
2543 contribution of the Antarctic Ice Sheet to global sea level rise (Fürst et al., 2016;  
2544 Jacobs et al., 1992). The ice shelves slow the flow of upstream ice into the ocean  
2545 by imparting a resistive force, known as buttressing. This buttressing occurs from  
2546 lateral drag along the sides of the ice shelves and resistive stresses incurred where  
2547 they flow over pinning points (localized areas of grounded ice) (Dupont & Alley,  
2548 2005; Matsuoka et al., 2015). Changes to the geometry of the ice shelves can reduce  
2549 their restraining effect on the flow of grounded ice, leading to an increased mass  
2550 flux of ice across the grounding zone, thus increasing the ice sheet's contribution to  
2551 global sea level rise (e.g., Pritchard et al., 2012; Scambos et al., 2004).

2552  
2553 The largest ice shelf is the Ross Ice Shelf (Figure 4.1, Fretwell et al., 2013). Situated  
2554 in West Antarctica, along the boundary with East Antarctica, the Ross Ice  
2555 Shelf comprises ice from both the East and West Antarctic Ice Sheets; a combined  
2556 catchment totalling 11.6 meters of potential global sea level rise (Tinto et al., 2019).  
2557 While the Ross Ice Shelf is in approximate steady-state, that is a near net-zero mass  
2558 change (e.g., Moholdt et al., 2014; Rignot et al., 2013), geologic evidence shows rapid  
2559 disintegration (Naish et al., 2009; Yokoyama et al., 2016) and extensive grounding  
2560 line retreat (Spector et al., 2017; Venturelli et al., 2020) may have occurred as re-  
2561 cently as the mid-Holocene ( $\sim 7$  kyr B.P.). Ocean forcing, specifically basal melting  
2562 along the grounding zone, is thought to drive these rapid grounding line retreats  
2563 (Lowry et al., 2019). The current stability of the ice shelf is in part attributed to  
2564 the lack of warm Circumpolar Deep Water penetrating into the cavity (Dinniman  
2565 et al., 2011; Tinto et al., 2019). Ocean waters that do penetrate the cavity, such as  
2566 High Salinity Shelf Water, are dense and relatively cold. Despite their temperature,  
2567 they are responsible for significant melting at the large depths of the grounding zone  
2568 (Adusumilli et al., 2020) due to the pressure suppression of the freezing temperature  
2569 of ice (Tinto et al., 2019).

2570  
2571 This High Salinity Shelf Water is formed on the continental shelf from the cre-  
2572 ation of sea ice. Due to their density and the reverse slope of the continental shelf,  
2573 they flow into the cavity, guided by bathymetric troughs (Jacobs et al., 1992; Tinto  
2574 et al., 2019). There are many examples of bathymetric features controlling the  
2575 routing of these sub-shelf waters (e.g., De Rydt et al., 2014; Dutrieux et al., 2014;

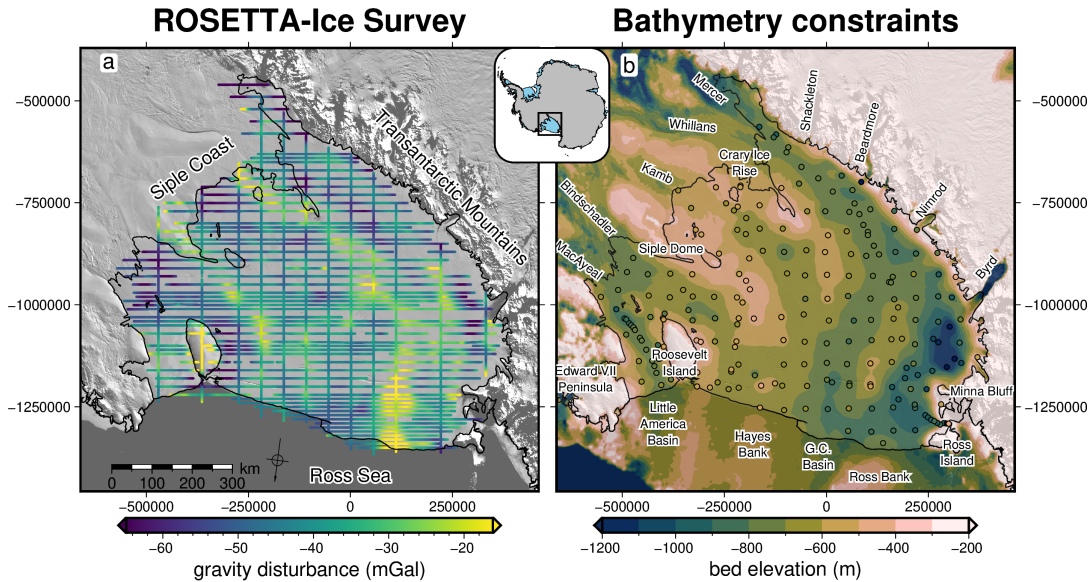


**Figure 4.1:** Input datasets for the Ross Ice Shelf bathymetry inversion. **a)** ROSETTA-Ice airborne gravity disturbance data (cleaned and re-levelled). **b)** Bedmap2 bed elevations in background, with individual constraint points within the ice shelf boundary (dots) on the same colour scale. Black line in both figures shows the grounding line and ice front from Mouginot et al. (2017). Background imagery is from MODIS-MOA (Scambos et al., 2007). Regional names shown in **a** and specific location names shown in **b**, which include ice streams along the Siple Coast, outlet glaciers along the Transantarctic Mountains, and bathymetry features in the Ross Sea. The RMS difference between the constraint point values and the BedMap2 gridded values is 138 m.

2576 Gladish et al., 2015; Zhao et al., 2019). Additionally, ocean modelling sensitivity  
 2577 testing highlights the importance of bathymetric features to sub-shelf circulations  
 2578 and melt (De Rydt et al., 2014; Goldberg et al., 2020). Bathymetry, therefore, plays  
 2579 a key role in the stability of the Ross Ice Shelf through its likely control on the basal  
 2580 melt magnitude and distribution (Goldberg et al., 2019) and through the buttressing  
 2581 effect of bathymetric pinning points (Still et al., 2019).

2582  
 2583 Direct observations of the sea floor beneath the Ross Ice Shelf (excluding along  
 2584 its periphery) are limited to two drill holes. The first was the 1977 J9 drill hole north  
 2585 of Crary Ice Rise as part of the Ross Ice Shelf Project (Clough & Hansen, 1979). The  
 2586 second was the 2017 HWD2 drill hole near the centre of the ice shelf (Stevens et al.,  
 2587 2020). Apart from these two drill holes, all other inferences of sub-shelf bathymetry  
 2588 depths have been from seismic surveying, or the gravity inversion of Tinto et al.  
 2589 (2019). The majority of seismic surveys on the Ross Ice Shelf were accomplished  
 2590 during two projects, the International Geophysics Year traverses of the late 1950s  
 2591 and early 1960s (Crary et al., 1962; Crary, 1959; Crary & Robinson, 1962), and the  
 2592 Ross Ice Shelf Geophysical and Glaciological Survey (RIGGS, 1973-1974 Bentley,  
 2593 1984). These extensive surveys systematically covered the entire ice shelf, collecting  
 2594 223 observations of bathymetry with a mean spacing of approximately 40 km be-  
 2595 tween points (Figure 4.1b).

2596  
 2597 These seismic and drill hole depths have been included in various Antarctic bed  
 2598 and bathymetry products (Fretwell et al., 2013; Le Brocq et al., 2010; Timmermann  
 2599 et al., 2010). As discussed later, Tinto et al. (2019) conducted a gravity inver-  
 2600 sion over the entirety of the ice shelf with data from the Ross Ocean and ice Shelf  
 2601 Environment, and Tectonic setting Through Aerogeophysical surveys and modelling

project (ROSETTA-Ice). This provided a significantly improved resolution over just the interpolation of the sparse seismic data. This gravity-inverted bathymetry was later incorporated in the BedMachine bed compilation (Morlighem, 2022; Morlighem et al., 2020). This chapter focuses on once again improving the sub-Ross Ice Shelf Bathymetry model. Following Tinto et al. (2019), we also use a gravity inversion of the ROSETTA-ice data to model the bathymetry. However, we conduct additional processing of the gravity data, and apply an entirely new gravity inversion algorithm, as described in Chapter 3. Additionally, our method provides an assessment of the spatial uncertainty of the resulting model, a useful component needed for the ocean modelling community (Goldberg et al., 2020).

2612

## 2613 4.2 Methods

2614 Here we describe the three main methodologies of this chapter; 1) the gravity reduction process (Figure 4.2a), 2) the bathymetric inversion process (Figure 4.2b), which  
 2615 is explained in detail in Chapter 3 and briefly re-introduced here, and 3) the use of a  
 2616 Monte Carlo simulation to quantify spatial uncertainty in the resulting bathymetry.

### 2618 4.2.1 Gravity reduction

2619 A common task in geophysics is the removal of predictable noise to help amplify the  
 2620 signal of interest. This is the basis of gravity reduction; the process of isolating the  
 2621 desired gravity signal from the raw measurements of the Earth's gravitational field.  
 2622 The magnitude of Earth's gravitational acceleration, which we will refer to as *gravity*  
 2623 from here-on, ranges from  $\sim 978,000$  to  $\sim 983,000$  mGal, from the equator to the  
 2624 poles, respectively (Hofmann-Wellenhof & Moritz, 2006). The range in these values,  
 2625 approximately 5000 mGal, vastly outweighs the typical values of gravity anomalies  
 2626 resulting from geologic features of interest. These anomalies of interest are typically  
 2627 on the order of magnitude of 10's of mGal. This exemplifies the issue of removing  
 2628 *noise* which has a significantly greater magnitude than the *signal* of interest.

2629

2630 Here, we start the gravity reduction process with observed gravity. We take ob-  
 2631 served gravity to be the signal which is produced by 1) the gravitational attraction  
 2632 of all massive bodies in Earth and 2) the rotation of the Earth. This means non-  
 2633 geological and time-dependent effects such as machine drift, tidal changes, aircraft  
 2634 manoeuvres and the effect of measuring gravity on a moving platform (Eötvös cor-  
 2635 rection) have already been removed from the observed gravity (Hinze et al., 2005;  
 2636 Hinze et al., 2013). With this, observed gravity is defined as;

$$g_{obs}(p) = \gamma(p) + g_{geology}(p) \quad (4.1)$$

2637 where, for an observation point  $p$ ,  $g_{obs}(p)$  is the observed gravity,  $\gamma(p)$  is the  
 2638 attraction of the *normal* Earth and  $g_{geology}(p)$  encompasses the gravity effects of all  
 2639 deviations between the *normal* Earth and the real Earth. This *normal* Earth is  
 2640 often taken as a single surface (here the reference ellipsoid) with a constant density  
 2641 above ( $\rho_{air}$ ) and a constant density below ( $\rho_{crust}$ ). Therefore, deviations between  
 2642 the *normal* and real Earth include 1) any masses above the ellipsoid which don't  
 2643 have the uniform density of air or 2) any masses below the ellipsoid which don't

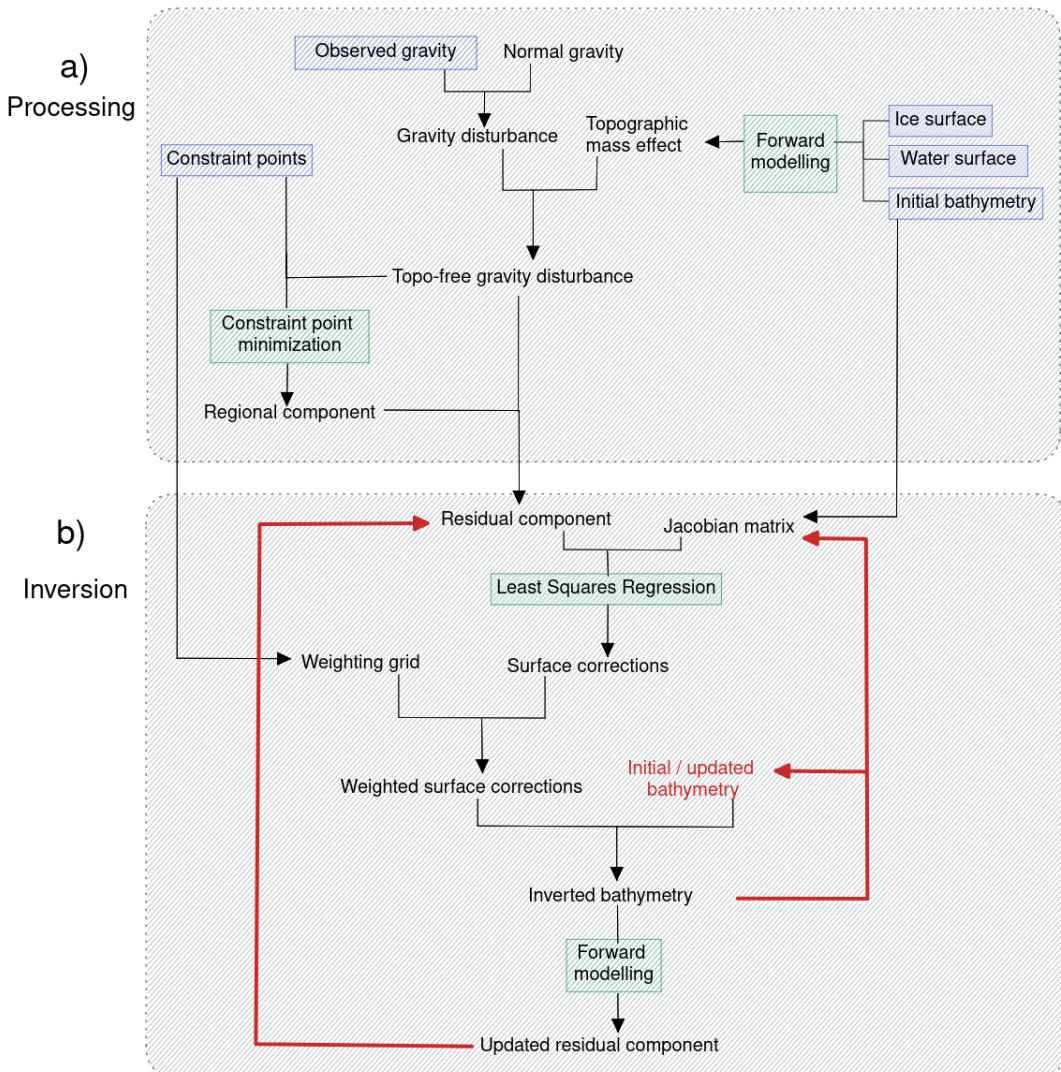


**Figure 4.2:** Schematic workflow diagram for **a)** gravity processing steps and **b)** running the inversion. Blue boxes show the input datasets, green boxes show the key processes and red lines signify iterative components of the inversion.

2644 have the uniform density of crust. For a bathymetry inversion, the gravity signal of  
 2645 interest is a component of  $g_{\text{geology}}$ , which we must separate from  $\gamma$ .

#### 2646 4.2.1.1 Attraction of normal Earth

2647 Observed gravity varies greatly due to the observation point's position, both based  
 2648 on latitude and elevation. Due to the oblate shape of the Earth, gravity is generally  
 2649 lower at low latitudes due to 1) increased distance from the centre of Earth's mass,  
 2650 and 2) more importantly, the increased tangential velocity (Jacoby & Smilde, 2009).  
 2651 Additionally, there is a decay of gravity with increased elevation, due to an increased  
 2652 distance from the centre of Earth's mass. These effects aren't related to the geologic  
 2653 variations of interest and thus should be removed. Historically, these effects of  
 2654 latitude and elevation were approximated separately, using the International Gravity  
 2655 Formula (*Latitude correction*) and the *Free-air correction*, respectively (Hinze et al.,  
 2656 2005). Alternatively, Li and Götze (2001) derived an analytical solution to the

2657 gravity effects of an ellipsoid, at any point on or above its surface<sup>1</sup>. With this,  
 2658 the Latitude and Free-air corrections are combined, and their approximations are  
 2659 replaced with closed-form solutions. By subtracting the normal gravity from the  
 2660 observed gravity at each observation point the gravity disturbance is found, where

$$\delta g(p) = g_{obs}(p) - \gamma(p), \quad (4.2)$$

2661 where for an observation point  $p$ ,  $\delta g(p)$  is the gravity disturbance,  $g_{obs}(p)$  is the  
 2662 observed gravity, and  $\gamma(p)$  is the normal gravity (Pašteka et al., 2017).

2663  
 2664 The observation point,  $p$ , is defined by three coordinates; latitude, longitude, and  
 2665 geometric height (ellipsoidal height). It is a common mistake in geophysical studies  
 2666 for the normal gravity calculation to use the point  $p$ 's orthometric height (geoidal  
 2667 height or mean sea level), instead of its geometric height (Oliveira et al., 2018). This  
 2668 results in the calculation of normal gravity at a different point in 3D space relative  
 2669 to the observation. This calculation, while truly determining the gravity anomaly  
 2670 (a.k.a. free-air anomaly), is not well-suited for geological interests because the grav-  
 2671 ity anomaly contains signal from centrifugal acceleration effects due to the different  
 2672 locations of the points. Conversely, the gravity disturbance is defined as the differ-  
 2673 ence between gravity and normal gravity at the same point, and thus only contains  
 2674 signal resulting from geologic sources (Hofmann-Wellenhof & Moritz, 2006). The dif-  
 2675 ference between the gravity anomaly and the disturbance for Antarctica ranges from  
 2676 -20 to +20 mGal (See Figure C.1 in appendix C for a comparison). It is common  
 2677 for studies to correctly use the gravity disturbance while referring to it as the free-  
 2678 air anomaly to adhere to tradition. Combining Equations 4.1 and 4.2, shows that  
 2679 the gravity disturbance,  $\delta g$ , results solely from deviations between the theoretical  
 2680 model of the Earth (the *normal* Earth) and the true density variations and topog-  
 2681 raphy of the Earth (Vajda et al., 2004). Figure 4.3 compares the observed gravity,  
 2682 the normal gravity, the gravity disturbance, and the gravity anomaly for Antarctica.  
 2683

#### 2684 4.2.1.2 Topographic mass effects

2685 Typically, geophysical studies are interested in interpreting or inverting gravity sig-  
 2686 nals resulting from subsurface features. To accommodate this, all other gravity  
 2687 effects must be computed and removed from the gravity disturbance. These other  
 2688 effects include the gravity resulting from masses bound by known surfaces, referred  
 2689 to as *topographic* or *terrain masses*. These surfaces include, but are not limited to,  
 2690 the rock surface (topography), the ocean surface (geoid), the seafloor (bathymetry),  
 2691 and the ice surface. Together, the gravity resulting from these masses is referred to  
 2692 as the *topographic mass effect*. Correcting the gravity disturbance for these topo-  
 2693 graphic masses yields the *topo-free gravity disturbance*  $\delta g_{TC}$ , where

$$\delta g_{TC}(p) = \delta g(p) - g_{topo}(p). \quad (4.3)$$

---

<sup>1</sup>Note that the normal gravity calculation with this analytical solution is not valid below the ellipsoid. While this is irrelevant for most locations on Earth, West Antarctic has negative geoid elevations, meaning observations near sea level are likely below the reference ellipsoid, invalidating the normal gravity calculation. For these situations, the use of a quasi-ellipsoid is recommended (Pašteka et al., 2017; Vajda et al., 2008b)

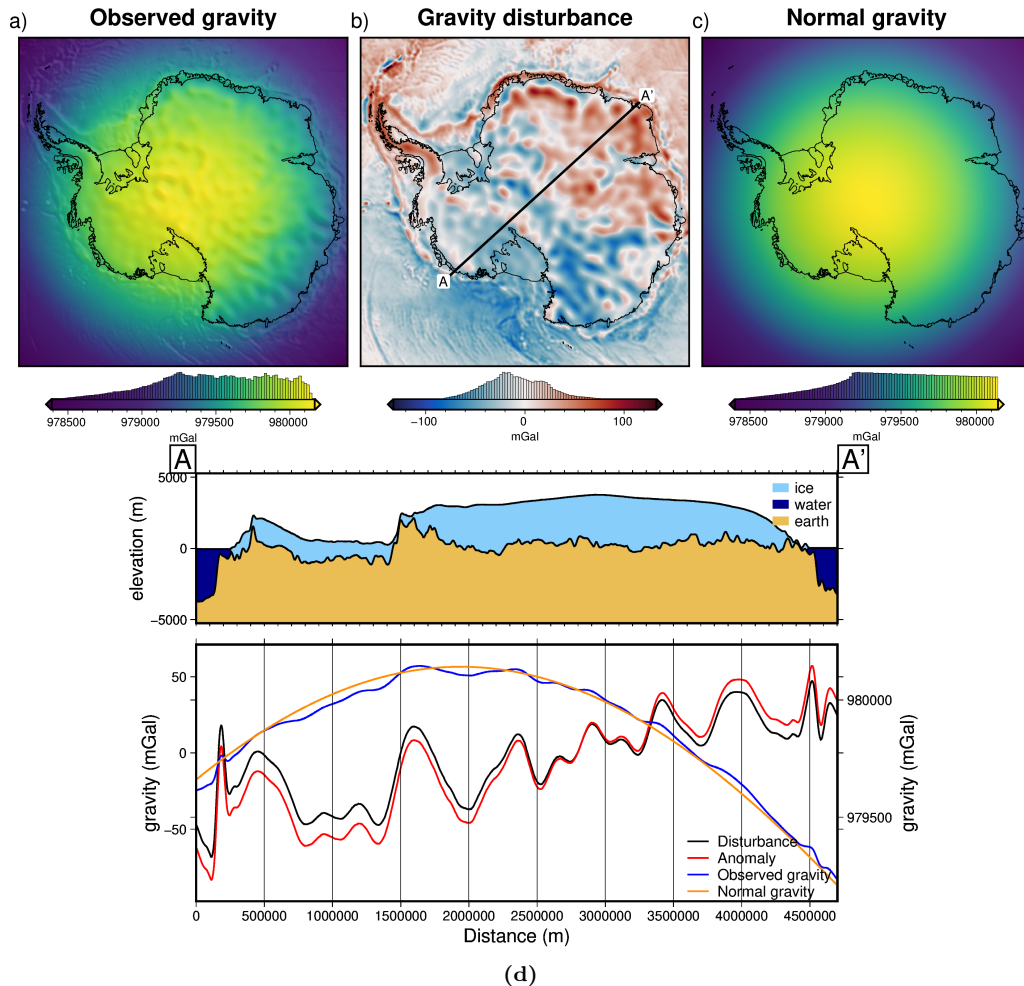


**Figure 4.3:** Observed gravity data reduction for Antarctica. **a)** Observed gravity data from Förste et al. (2014) at a geodetic observation height of 10 km. **b)** The gravity disturbance at 10 km height, defined as **a-c.** **c)** The normal gravity calculated at the same observation points as **a** using the closed-form equations of Li and Götze (2001). **d)** Profile A-B across Antarctica, location shown in **b.** Gravity disturbance (black) and anomaly (red) values are on the left y-axis, while observed (blue) and normal (orange) gravity values are on the right y-axis.

2694      $g_{topo}(p)$  represents the summed topographic mass effect.  $\delta g_{TC}$  is sometimes referred to as the *Bouguer disturbance*, owing to the historic use of the *Bouguer anomaly*. In accordance with Vajda et al. (2007), we refer to it as the *topo-free gravity disturbance* to clarify that the ellipsoid has been used instead of the geoid in all reduction steps. In the past, the topographic mass effect has been split into the Bouguer slab correction and the terrain correction. The Bouguer slab correction approximates the topographic masses as laterally infinite flat slabs, while the terrain correction accounts for the overestimation of the Bouguer slab resulting from the assumption of the flat slab. With modern computing able to efficiently calculate the gravity resulting directly from a topographic surface (Fatiando a Terra Project et al., 2023), there is no need for the separate two-step correction.

2705     The topographic mass effect reflects all topographic deviations (including topography of the ice, water, and seafloor) between the *normal* Earth and the real Earth. The *normal* Earth model is shown in Figure 4.4a, as defined by air above the ellipsoid and crust below. A simplified model of the true Earth is shown in Figure 4.4b, and contains air, ice, water, crust, and various geologic bodies within the crust. These

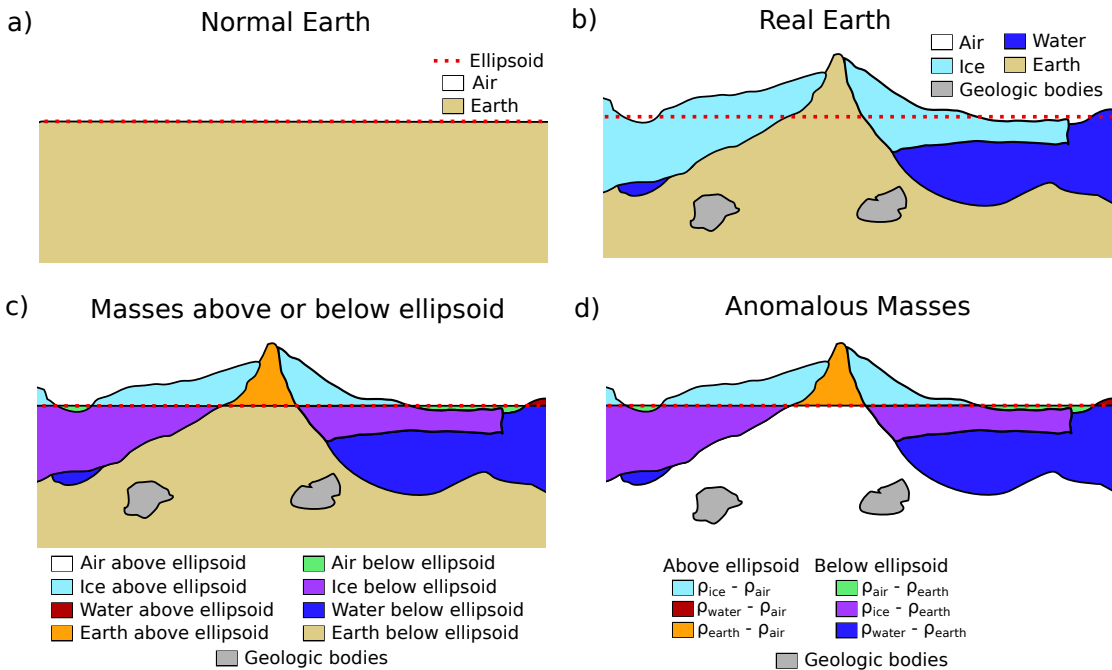


**Figure 4.4:** Components of the topographic mass effect and resulting topo-free gravity disturbance, or Bouguer disturbance. **a)** The normal Earth model, **b)** a simplified real Earth model. **c)** Topographic masses separated into components above and below the ellipsoid. **d)** Real Earth topographic masses which are anomalous with respect to the normal Earth. Note if the reference level (red dashed line) is switched from the ellipsoid to the geoid, this would result in a Bouguer anomaly.

masses are separated in Figure 4.4c into components above and below the ellipsoid. From this, the masses which are anomalous with respect to the *normal* Earth can be distinguished, as shown in Figure 4.4d. These anomalous masses include water, ice, and crust above the ellipsoid, and air, ice, water, and geologic bodies below the ellipsoid. The gravitational effect of these anomalous masses can be approximated by assuming each mass's density and setting it relative to the density of the component of the *normal* Earth which the mass is replacing. These relative densities are shown in the key of Figure 4.4d. Calculating and summing the gravity effect of each of the components of Figure 4.4d (excluding the geologic bodies) gives the topographic mass effect. Subtracting this from the gravity disturbance gives the topo-free gravity disturbance<sup>2</sup>.

To compute the topographic mass effect, the anomalous masses from Figure 4.4d are discretized into a series of vertical right-rectangular prisms. To achieve the geometry and density configuration of Figure 4.4d, three sets of prisms are used, as shown in Figure 4.5c-e.

1. Prisms between the ice surface and the ellipsoid are assigned densities of  $\rho_{ice} - \rho_{air}$  for prisms above the ellipsoid, and  $\rho_{air} - \rho_{ice}$  for prisms below the ellipsoid.
2. Prisms between the water surface (ice base) and the ellipsoid are assigned densities of  $\rho_{water} - \rho_{ice}$  for prisms above the ellipsoid, and  $\rho_{ice} - \rho_{water}$  for prisms below the ellipsoid.

<sup>2</sup>The use of the reference ellipsoid as the bounding surface of the topographic mass effect calculations results in a topo-free gravity disturbance while using the geoid as the bounding surface would result in a Bouguer anomaly (Vajda et al., 2006).

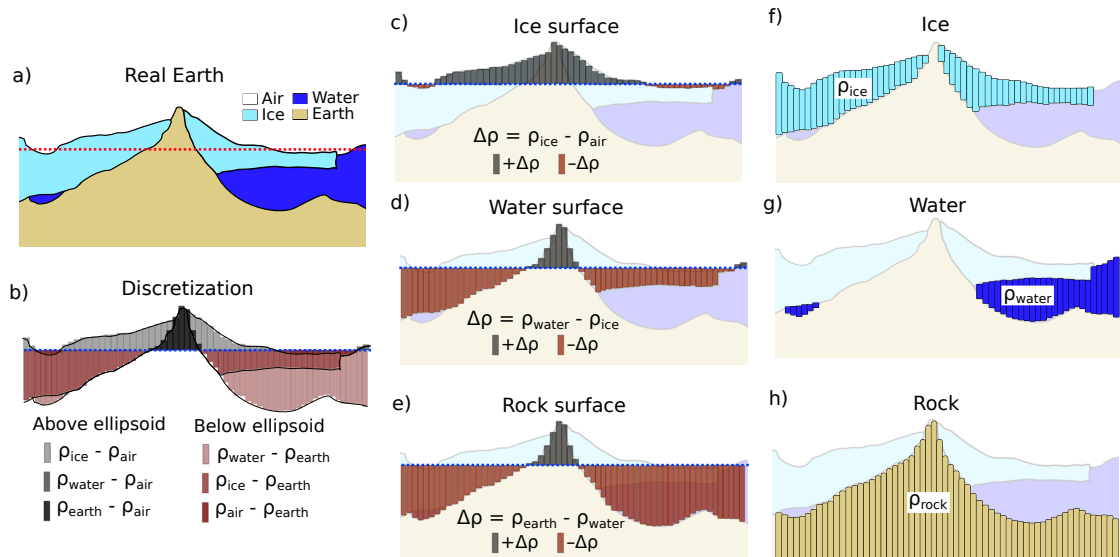


**Figure 4.5:** Discretizing the topographic mass effect. **a)** The simplified real Earth model, with air, ice, water, and earth. **b)** the resulting anomalous masses relative to the *normal* Earth, as shown in Figure 4.4d. **c)** Prisms between the ellipsoid and the ice surface, **d)** prisms between the ellipsoid and the water surface (ice base), and **e)** prisms between the ellipsoid and the rock surface (topography onshore and bathymetry offshore). Overlap of prisms from **c-e** creates the different shades shown in **b**. The alternative discretization approach, commonly used, is shown in **f-h** where the prism layers are bound both above and below by topographic layers, or arbitrary references (bottom of prisms in **h**), instead of by the normal Earth reference surface (ellipsoid). Additionally, density values of the prisms are related to the material they discretize and are not relative to the expected density of the normal Earth.

- 2732     3. Prisms between the rock surface (topography onshore and bathymetry off-  
2733       shore) and the ellipsoid are assigned densities of  $\rho_{rock} - \rho_{water}$  for prisms above  
2734       the ellipsoid, and  $\rho_{water} - \rho_{rock}$  for prisms below the ellipsoid.

2735     This configuration of prisms correctly discretizes the topographic mass effect be-  
2736     cause the ice surface is equal to the water surface in areas of no ice thickness, and  
2737     the water surface is equal to the rock surface in areas of no water thickness. Due  
2738     to this, the overlap between the three sets of prisms, shown in Figure 4.5b gives the  
2739     appropriate densities, as defined in Figure 4.4d. From these three sets of prisms, the  
2740     topographic mass effect can be calculated at the gravity observation points using the  
2741     analytical solutions of Nagy et al. (2000). As a demonstration, the topographic mass  
2742     effect for Antarctica is calculated using topographic data from Bedmap2 (Fretwell  
2743     et al., 2013), referenced to the WGS-84 ellipsoid. The observed satellite gravity data  
2744     has a low spatial resolution, so the lower resolution of Bedmap2 over BedMachine  
2745     v3 is insignificant. The calculated topographic mass effect, the gravity disturbance,  
2746     the resulting topo-free gravity disturbance, and the topographic mass effect from  
2747     the alternative method of discretization (Figure 4.5f-h) are shown in Figure 4.6.

2748     The theoretical topo-free gravity disturbance is the gravity effect caused by and  
2749     only by anomalous subsurface bodies, which have a density different from the as-  
2750     sumed constant density of the crust. In reality, there are additional components of  
2751     the topo-free gravity disturbance resulting from 1) noise in the observed data, 2)  
2752     non-uniform densities used in the topographic mass effect calculation, and 3) inac-  
2753     curate topographic data used for the topographic mass effect calculation. In most  
2754     geophysical applications, the uncertainty of the topographic data is small compared

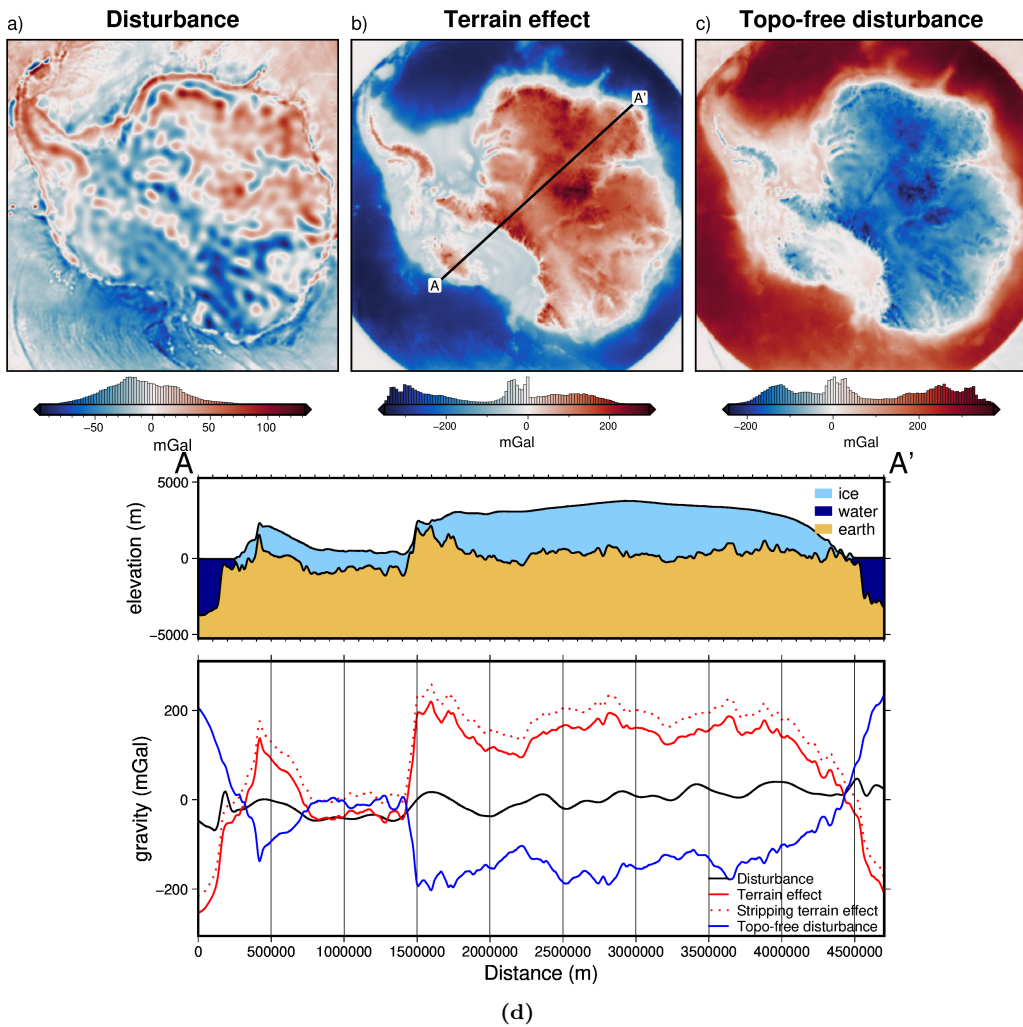


**Figure 4.6:** Topographic mass effect at 10 km height for Antarctica, from Bedmap2 topographic data (Fretwell et al., 2013). **a)** Gravity disturbance at a geodetic observation height of 10 km, from Figure 4.3b. **b)** The combined gravity effect of the anomalous masses defined in Figure 4.4d and discretized following 4.5b. **c)** The topo-free gravity disturbance, calculated as **a** - **b**. **d)** Profile A-A' across Antarctica, location shown in **b**. The dotted red line shows the terrain mass effect results of the alternative discretization method shown in Figure 4.5f-h. A DC shift was applied to attempt to remove the offset.

2756 to other uncertainties in the analysis, and thus component #3 is assumed to be zero.  
 2757 Conversely, for the case of a bathymetry inversion, this component of the topo-free  
 2758 disturbance resulting from the inaccuracies of the topography (bathymetry) data is  
 2759 the signal of interest. Next, we will isolate this component from the remainder of  
 2760 the topo-free gravity disturbance.

2761

#### 2762 4.2.1.3 Regional separation

2763 Here, we separate the topo-free gravity disturbance into components resulting from  
 2764 1) subsurface geologic variations and 2) inaccuracies between the true bathymetry  
 2765 and the low-resolution bathymetry data used for the terrain mass effect. These  
 2766 are referred to as the regional and residual components, respectively. Chapter 3  
 2767 highlighted the importance of accurately estimating and separating this regional  
 2768 component from the residual. The regional estimation was found to be the largest

source of uncertainty in several synthetic bathymetry inversions, as well as other Antarctic bathymetry inversions (Brisbourne et al., 2014). While there are many techniques to estimate the regional component, we will use constraint point minimization due to its demonstrated effectiveness over the other methods (Section 3.2.4). This technique samples the topo-free gravity disturbance at points of known bathymetry depth, referred to as the constraint points. Since the depth is known here, the residual component of gravity should be near zero, and thus the regional component should entirely equal the topo-free gravity disturbance. Using these sampled values, the entire model domain is gridded with an interpolation, using either bi-harmonic splines (Uieda, 2018) or minimum curvature (Smith & Wessel, 1990). The resulting grid makes up the regional component, and when subtracted from the topo-free gravity disturbance gives the residual component. This residual component is the input into the inversion.

2782

## 2783 4.2.2 Bathymetry inversion

2784 Here we start by briefly summarising the bathymetry inversion workflow described  
 2785 in Chapter 3, and shown schematically in Figure 4.2b. Then we compare our method  
 2786 to several other commonly used bathymetry inversion algorithms. The basis of mod-  
 2787 ellling bathymetry with a gravity inversion is that the bathymetry surface, which is  
 2788 a contrast between lower-density material (seawater) and higher-density material  
 2789 (sediment) creates a measurable effect on Earth’s gravity. Our inversion begins by  
 2790 computing the Jacobian matrix (Equation 3.7), which is a quantitative means of  
 2791 describing the sensitivity of the residual gravity data to changes in the height of  
 2792 each grid cell of bathymetry. In other words, the Jacobian quantifies the ratio be-  
 2793 tween the amplitude of bathymetric features and the gravity anomaly resulting from  
 2794 them. From this Jacobian matrix, the optimal change to apply to each bathymetry  
 2795 grid cell to minimize the residual gravity data is estimated. This is in the form of  
 2796 a surface correction grid, with a value for each grid cell of bathymetry. Since there  
 2797 are locations of already known bathymetry depths (constraint points), this surface  
 2798 correction grid should be zero at these points. To achieve this, a weighting grid is  
 2799 calculated, which is based on the minimum distance between each grid cell and the  
 2800 nearest constraint point. These distance values are then normalized from 0 to 1,  
 2801 with 0 being the cells closest to the constraints, and 1 being the cells furthest. The  
 2802 surface correction grid is multiplied by this weighting grid, to achieve a correction  
 2803 value of 0 m at the constraints, smoothly tapering off to the full estimated correction  
 2804 values at a distance.

2805

2806 With this weighted surface correction grid, the original bathymetry depths are  
 2807 updated. To ensure the updated bathymetry doesn’t intersect the ice base, the ice  
 2808 base topography is set as an upper-bounding surface. The forward gravity of this  
 2809 updated bathymetry is then re-calculated, with the prism configuration and densi-  
 2810 ties shown in Figure 4.5e. The updated forward gravity is used to recalculate the  
 2811 topo-free gravity disturbance. Using the same regional component as calculated be-  
 2812 fore the inversion (Section 4.2.1.3), an updated residual gravity is computed. This  
 2813 is then input into the next iteration of the inversion (red lines in Figure 4.2b). Iter-  
 2814 ations continue until a set of user-defined stopping criteria are met; 1) a maximum  
 2815 number of iterations is reached, 2) a minimum value of the  $\ell^2$ -norm of the residual

2816 is reached, or 3) there is no significant variation in the  $\ell^2$ -norm in two consecutive  
2817 iterations.

2818

2819 This process describes a single *inversion*. The critical step in this inversion, deter-  
2820 mining the surface correction values from the sensitivity matrix, includes a damping  
2821 parameter that controls the smoothness of the resulting inverted bathymetry. This  
2822 damping parameter value directly affects the resulting bathymetry model and needs  
2823 to be carefully chosen. For this, we follow the cross-validation routine described in  
2824 Chapter 3 from Uieda and Barbosa (2017). This involves running the entire inver-  
2825 sion for a suite of different damping parameter values. The input gravity data to  
2826 these inversions is split into a *testing* set and a *training* set. The inversion only  
2827 uses the *training* set. After each inversion, the forward gravity effect of the updated  
2828 bathymetry model is calculated at the points of the *testing* set. The root mean  
2829 squared difference between the testing gravity values and the forward gravity values  
2830 gives the *score* of each cross-validation. The damping parameter which produces  
2831 the lowest score is chosen as the optimal value.

2832

### 2833 4.2.3 Starting bathymetry

2834 An initial bathymetry model for the inversion is needed to compute the topographic  
2835 mass effect and to run the inversion. The weighting grid constrains the inversion  
2836 from changing the starting grid values at the constraint points. For this reason,  
2837 the starting model should be carefully created. As discussed in the previous chap-  
2838 ter (Chapter 3, Section 3.4.2), there are several methods of creating the starting  
2839 model from the sparse measurements at the constraint points. Here, we use and  
2840 compare two techniques for interpolating these constraint point values over the en-  
2841 tire domain; tensioned minimum curvature (Smith & Wessel, 1990) and bi-harmonic  
2842 splines (Sandwell, 1987). See Chapter 3 Section 3.4.2 for the details of these gridding  
2843 techniques. Figure 4.1b

2844

### 2845 4.2.4 Uncertainty quantification

2846 A major component missing from many bathymetry inversions is assessing the spa-  
2847 tially variable uncertainty in the resulting bathymetry depths. This uncertainty  
2848 arises from a multitude of sources, including uncertainty in 1) the gravity data mea-  
2849 surements, 2) constraint point depths, 3) user-defined variables, such as ice, water,  
2850 or sediment density, and 4) uncertainties associated with the various methodologies  
2851 of the inversion. Here we use a sampling-based approach to estimate the uncertainty,  
2852 where the uncertainty of the *inputs* is used to assess the uncertainty of the *output*,  
2853 in this case, the inverted bathymetry. This general method of uncertainty analysis  
2854 is referred to as Monte Carlo sampling (Jansen et al., 1994).

2855

2856 For a generalized problem of inputs  $\mathbf{x}$  and a function  $\mathbf{y}(\mathbf{x})$ , Monte Carlo sim-  
2857 ulation provides a means to answer the two following questions; 1) what is the  
2858 uncertainty in  $\mathbf{y}(\mathbf{x})$  given the uncertainty in  $\mathbf{x}$ ? and 2) what are the relative im-  
2859 portance of the various components of  $\mathbf{x}$  with respect to  $\mathbf{y}(\mathbf{x})$  (Helton et al., 2006)?  
2860 While there are many components that contribute to the overall inversion uncer-

tainty, here we will examine 1) uncertainty in the gravity data values, 2) depth uncertainty of the constraint points, 3) uncertainty in the chosen density values used for ice, water, and earth, and 4) uncertainties related to user-chosen parameter values in the inversion. Uncertainties that are not covered here are those which relate to processes of the inversion which don't have associated measurable input uncertainties. This includes the use of spatially non-variable density values for ice, water, or earth, or the effects of discretizing a real topographic surface as a series of prisms.

2868

The Monte Carlo simulation consists of sampling the input parameters  $N$  times from their respective distributions (Figure 4.7b) and running the entire inversion workflow for each of the  $N$  parameter sets (Figure 4.7c). For each bathymetry grid cell, the weighted standard deviation of the  $N$  resulting inverted bathymetries is found (Figure 4.7d). This grid of cell-specific standard deviations show where the input parameters have a large effect on the bathymetry results. This grid is used as our estimate of the spatial uncertainty in the inversion. The grid of cell-specific weighted median values is then taken to be the optimal inversion result. These cell-specific statistics are weighted by the inverse square of each inverted bathymetry's RMS difference with the constraint point depths (Figure 4.7d). This reduces the bias of inversions in the ensemble which performed poorly, as defined by not adhering to the constraints (Schnaidt & Heinson, 2015). To assess the relative importance of the input parameters, in addition to the complete Monte Carlo simulation, additional simulations are run where each parameter's effect is isolated. For these, only a singular parameter is sampled from its distribution, so that the resulting spatial standard deviation is due solely to the uncertainty of that parameter.

2885

The parameters included in the Monte Carlo sampling are; 1) the gravity disturbance data, 2) the constraints point depths, 3) the gridding parameters to create the starting bathymetry, 4) the density of ice, 5) the density of water, 6) the density of sediment, and 7) gridding parameters for the constraint point minimization technique of regional gravity estimation (Figure 4.7b). For the full Monte Carlo simulation, with all the above inputs sampled from their respective distributions, the entire inversion workflow needs to be repeated with each of the  $N$  parameter sets. This includes 1) creating the starting bathymetry model from the constraint points (Section 4.2.3), 2) calculating the terrain mass effect to get the topo-free gravity disturbance (Section 4.2.1.2), 3) estimating the regional component of the disturbance and removing it (Section 4.2.1.3), and 4) running the damping parameter value cross-validation (Section 4.2.2) to obtain the inverted bathymetry (Figure 4.7). For the individual Monte Carlo simulations, only portions of this workflow need to be repeated. For example, if only the gravity disturbance is sampled, only the regional field and inversion need to be re-run. The starting bed and topographic mass effect calculated during the baseline inversion are re-used.

2902

Due to the computational demand of a full inversion workflow, the total number of inversions in each Monte Carlo simulation is limited. To ensure the uncertainty distributions of the inputs are adequately sampled with this limited number of possible runs, we have used Latin hypercube sampling where possible (Jansen et al., 1994). This sampling technique is well suited for computationally demanding tasks since it ensures proper coverage of the uncertainty distributions of the sampled values, despite a low number of samples Helton et al., 2006. To accomplish this, for a

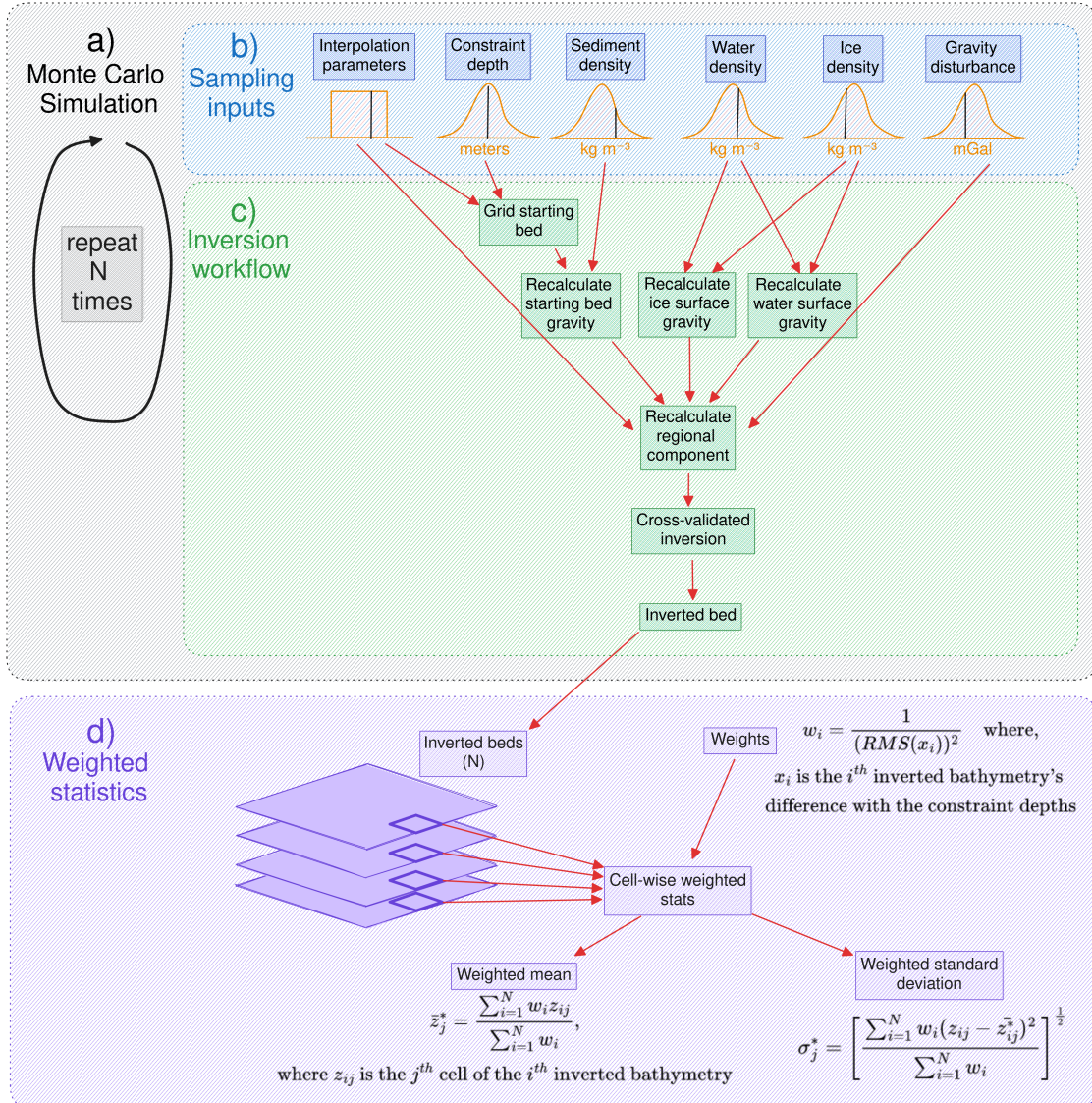


**Figure 4.7:** Schematic workflow diagram for the Monte Carlo uncertainty analysis. **a)** The Monte Carlo simulation, consisting of **b)** sampling the inputs from their respective distributions, and **c)** implementing the various components of the workflow, depending on which inputs have been sampled. This process is repeated  $N$  times, yielding  $N$  inverted bathymetry grids. **d)** Weighted cell-specific statistics are computed. Each inverted bathymetry grid (large purple boxes) is weighted by the respective inversion's constraint depth RMSE. These weights are used to compute the weighted mean and weighted standard deviation of each grid cell (bold purple square).

2910 Monte Carlo simulation of  $N$  runs, the given distributions are split into  $N$  intervals  
 2911 of equal probability and one value is chosen from each interval. The  $N$  values for  
 2912 each parameter are then randomly paired to get  $N$  sets of sampled input parameter  
 2913 values (Helton et al., 2006). Since the gravity data and constraint points are each  
 2914 sampled on a point-by-point basis, Latin hypercube sampling is unnecessary and  
 2915 random sampling is used. Figure 4.8 shows a  $N = 9$  comparison of random sam-  
 2916 pling and Latin hypercube sampling for a two-parameter simulation.

2917

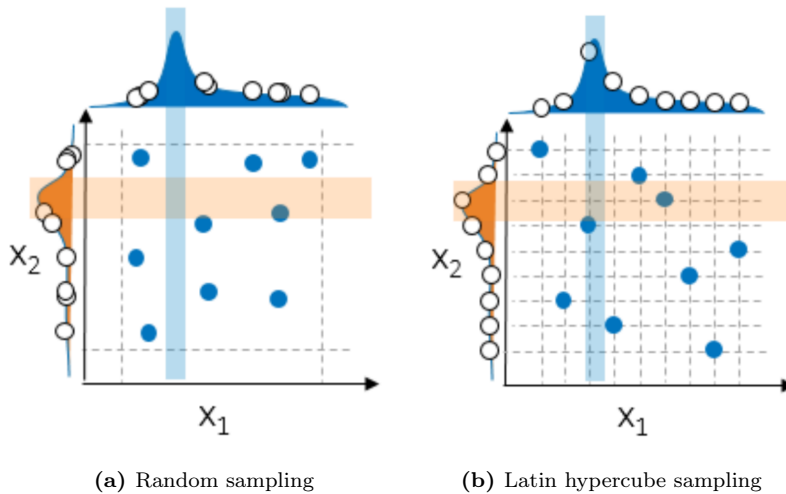


**Figure 4.8:** Comparison of sampling methods for a Monte Carlo simulation of two variables ( $X_1$  and  $X_2$ ) with 9 samples drawn from each. **a)** Random sampling, where values are drawn at random from each variable's distribution, and **b)** Latin hypercube sampling, where values are drawn from equal-probability intervals. Note the effective coverage of the distributions in **b** relative to **a**. The figure is adapted from Koch et al. (2017).

### **4.3 Relation to past bathymetry inversions**

The fundamental theory in all bathymetry inversions is based on the fact that the density contrast across the bathymetry surface produces a measurable gravity effect. This phenomenon gives rise to several techniques to convert observed gravity data into bathymetric depths. This by definition is a geophysical inverse problem (Oldenburg & Li, 2005), but the methods chosen to solve it vary from 3D rigorous inversions to iterative 2D forward modelling. Our inversion method follows a classical least-squares approach to solving the inverse problem, while our uncertainty and sensitivity analysis follows a Bayesian approach (Aster et al., 2018). Here, we compare our inversion method and workflow to other bathymetry inversions. We attempt to include all past studies related to Antarctica, as well as several from Greenland. We start by comparing our technique for the gravity reduction process, followed by differences in the actual inversion, and finally by differences in our assessment of uncertainty.

### 4.3.1 Gravity reduction comparison

One of the largest differences between our method and past studies is the gravity reduction process. We employ a rigorous terrain mass effect calculation to obtain a topo-free gravity disturbance, often referred to as a Complete Bouguer Anomaly (Vajda et al., 2007). Theoretically, this gravity signal contains only effects due to subsurface density anomalies and inaccuracies in calculating the terrain mass effect. Our method isolates the gravity effect of this inaccuracy since it is due to the deviations between the starting model of bathymetry and the true bathymetry. This is referred to as our residual component of the topo-free gravity disturbance. While most other bathymetry inversion studies achieve a similar residual anomaly, they complete this procedure in a theoretically different way, which may be introducing unnecessary errors. The differences arise from other studies ignoring the reference

2945 surface (the ellipsoid) for all calculations after the normal gravity correction.

2946

2947 The sign of a gravity disturbance value informs the interpreter as to whether  
2948 the true Earth has either excess or deficient mass at that location with respect to  
2949 the normal Earth. Therefore, the absolute level of gravity disturbance data should  
2950 be retained, even though direct offsets (DC shifts) don't alter the amplitude of  
2951 the gravity anomalies. For this reason, the reference surface used in the normal  
2952 gravity calculation (here the ellipsoid) should be continued to be used in all further  
2953 calculations of topographic masses, including in the forward calculation made during  
2954 the inversion, as shown in Figure 4.5 b. Many studies instead have discretized the  
2955 ice, water, and starting bathymetry surfaces into prism layers which either have  
2956 arbitrary references or density values not relative to the normal Earth model. This  
2957 alternative discretization is shown in Figure 4.5f-h. For example, the gravity effect of  
2958 ice, if not just ignored (e.g., Cochran & Bell, 2012; Jordan et al., 2020b; Millan et al.,  
2959 2017; Yang et al., 2020b), is typically removed via a "stripping" technique (Vajda  
2960 et al., 2008a), (e.g., Greenbaum et al., 2015; Millan et al., 2020; Muto et al., 2013a;  
2961 Yang et al., 2021). This stripping involves calculating the forward gravity of prisms  
2962 with tops defined by the ice surface, bottoms defined by the ice base, and densities  
2963 defined by the assumed density of ice (Figure 4.5f). Additionally, the prisms which  
2964 comprise the starting bathymetry model for many inversions are bound above by  
2965 the starting bathymetry, and below by an arbitrary constant depth (Figure 4.5h)  
2966 (e.g., Muto et al., 2013a; Tinto et al., 2019). The forward gravity calculations of  
2967 this style of discretization can introduce several errors:

- 2968 1. The largest of these errors is an offset in the mean value of the forward gravity  
2969 relative to the observed gravity. This offset needs to be estimated and removed  
2970 prior to comparison with the observed data. The DC-shift used to remove the  
2971 offset is typically estimated by finding a value that minimizes the difference  
2972 between the observed and predicted data at locations of known bathymetry  
2973 (e.g., Boghosian et al., 2015; Cochran et al., 2020; Constantino et al., 2020;  
2974 Eisermann et al., 2020; Millan et al., 2017; Muto et al., 2013a). This additional  
2975 step, referred to as "pinning", is unnecessary in our implementation, due to  
2976 adhering to a rigorous determination of the terrain mass effect. If an incorrect  
2977 DC shift is applied, the significance of the zero level of the topo-free gravity  
2978 disturbance is lost. The value of 0 signifies that the simplified model of the  
2979 Earth (i.e. the starting bathymetry model) is equal to the true Earth density  
2980 distribution. Shifting this zero-level due to errors in estimating the DC-shift  
2981 may lead to a shift in the inverted bathymetry, especially if the inversion  
2982 domain isn't well constrained. The DC-shifted terrain mass effect and the  
2983 rigorous terrain mass effect for Antarctica are compared in Figure 4.6d.
- 2984 2. The forward gravity calculation with this style of discretization results in  
2985 slightly different amplitude anomalies compared to the true terrain mass ef-  
2986 fect. This difference is due to the different densities assigned to the prism layer  
2987 between the two techniques (Figure 4.5). While this difference is likely below  
2988 the range of uncertainties in the gravity error, it is an unnecessary addition of  
2989 error to the gravity reduction process.
- 2990 3. The last drawback to using this alternative discretization is an increased grav-  
2991 itational edge effect. As shown in Figure 4.5, the average densities and prism

heights are larger with this technique. This increases the overall decay of calculated gravity at the edges of the model space, due to the contrast with the void-space beyond the model domain. To account for this, a larger buffer zone is needed, which can significantly increase the computational requirements during forward modelling (see Chapter 3 Section 3.2.2.2).

#### 4.3.1.1 Regional separation

The last step in the gravity reduction process for bathymetry inversion is separating the regional and residual signals, where the residual signal should theoretically be entirely a result of the bathymetry surface. Some techniques commonly used for this are described in Chapter 3 Section 3.2.4. Past bathymetry inversions have used a variety of these techniques, as summarized below;

1. Zero or uniform adjustment; For small inversion domains the regional field is sometimes assumed to be minimal. In these scenarios, past studies have either limited the inversion domain to where the regional field is assumed small (Boghosian et al., 2015; Cochran & Bell, 2012), have used a uniform value for the regional component (Muto et al., 2013b), or have found a constant density value for the starting model which minimize the gravity misfit (An et al., 2017; Millan et al., 2018; Millan et al., 2017).
2. Low-pass filtering; for inversion domains with an expected regional field slightly larger than the above scenario, low-pass filtering of the gravity data can approximate the regional component (Eisermann et al., 2020; Hodgson et al., 2019).
3. Geologic modelling; To account for the regional field, some studies create geologic models of varying density to estimate the regional field. These models are typically informed from other geophysical data (Greenbaum et al., 2015; Hodgson et al., 2019), *a priori* geologic knowledge (Cochran et al., 2014b; Constantino et al., 2020; Tinto & Bell, 2011), or from an approximated crustal density distribution (Cochran et al., 2020; Eisermann et al., 2021; Tinto et al., 2019; Wei et al., 2020).
4. Upwards continuation / high altitude surveys; This technique estimates the long-wavelength regional component by either upward continuing the gravity data to large altitudes, using separate gravity data collect from high-altitude surveys (Muto et al., 2016), or a combination of both (Tinto et al., 2015)
5. Constraint point minimization; the last commonly used technique utilizes the assumption that the desired residual component is near-zero at points of known bathymetry. From this assumption, the regional component at these constraints is entirely equal to the gravity anomaly value. To estimate the regional field, the gravity values are sampled at the constraints and interpolated over the region. This technique has been used in several recent inversions where sparse constraints are available (An et al., 2019a; An et al., 2019b; Jordan et al., 2020b; Millan et al., 2020; Vaňková et al., 2023; Yang et al., 2021; Yang et al., 2020a). While implemented in a different method, this constraint point minimization follows the same concept as several studies which use the constrained locations to derive a spatially variable density model, accounting for the regional field (Eisermann et al., 2021; Tinto et al., 2019; Wei et al., 2020).

3037 Here, we use the constraint point minimization technique for estimating and  
 3038 removing the regional component of the topo-free gravity disturbance.

### 3039 4.3.2 Inversion comparison

3040 We have developed a conventional non-linear geometric gravity inversion algorithm,  
 3041 as often used in modelling density contrasts, such as sedimentary basins (e.g., Martins  
 3042 et al., 2010; Santos et al., 2015), or the Moho (e.g., Pappa et al., 2019; Uieda  
 3043 & Barbosa, 2017). This algorithm is similar in concept to inversions used in other  
 3044 bathymetric studies but differs in its implementation. Past inversion techniques  
 3045 used for bathymetry modelling can be grouped into several categories;

- 3046 1. algorithmic approaches. This method termed the "topographic shift method"  
 3047 (Hodgson et al., 2019; Jordan et al., 2020b), while not a formal inversion,  
 3048 calculates the equivalent rock thickness from the residual component of gravity,  
 3049 adds this to the starting bathymetry model, and constrains the results by the  
 3050 locations of known bathymetry.
- 3051 2. 2D profile inversions. Using the method of Talwani et al. (1959), and often  
 3052 implemented within the commercial software Geosoft Oasis Montaj, these in-  
 3053 verisions retain the 2D nature of the airborne flight lines and invert only along  
 3054 the path of the flight (Boghosian et al., 2015; Cochran et al., 2014b; Cochran  
 3055 et al., 2020; Constantino & Tinto, 2023; Tinto & Bell, 2011; Tinto et al., 2015;  
 3056 Wei et al., 2020).
- 3057 3. 3D frequency-based inversions. This category of inversion uses a Fourier trans-  
 3058 formation to calculate the forward gravity effect of a continuous topographic  
 3059 surface, forgoing the need to discretize the topography into vertical prisms  
 3060 (Oldenburg, 1974; Parker, 1972). This Fourier transform is then iteratively  
 3061 modified to minimize the misfit to the observed gravity. This method, par-  
 3062 ticularly its implementation within the commercial software Geosoft Oasis  
 3063 Montaj, is frequently used for bathymetry inversions (An et al., 2017; An et  
 3064 al., 2019a; An et al., 2019b; Cochran & Bell, 2012; Eisermann et al., 2020;  
 3065 Eisermann et al., 2021; Greenbaum et al., 2015; Millan et al., 2018; Millan  
 3066 et al., 2017; Millan et al., 2020; Studinger et al., 2004b).
- 3067 4. Simulated Annealing. This global optimization technique (Kirkpatrick et al.,  
 3068 1983) performs many forward calculations of possible bathymetry surfaces and  
 3069 slowly converges on a model which minimizes the misfit with the observations.  
 3070 This method, similar to our Monte Carlo uncertainty analysis, has the benefit  
 3071 of providing an uncertainty estimate of the resulting bathymetry based on the  
 3072 uncertainty in the inversion inputs. This has been used in several bathymetric  
 3073 inversions (Filina et al., 2008; Muto et al., 2013a; Muto et al., 2016; Roy et al.,  
 3074 2005; Yang et al., 2021; Yang et al., 2018; Yang et al., 2020a)
- 3075 5. Regularized least-squares inversions. This style of inversion is the conven-  
 3076 tional approach to solving non-unique inverse problems (Aster et al., 2018).  
 3077 While this method is commonly used for other geometric gravity inversions  
 3078 (e.g., Moho and basement), to our knowledge it is only applied to bathymetry  
 3079 inversions here, and in Vaňková et al. (2023).

### 4.3.3 Uncertainty comparison

Here we compare our uncertainty analysis to those from other bathymetry-gravity inversion studies. Most of these past studies provide an estimation of uncertainty, but only a few provide spatially variable uncertainties (e.g., An et al., 2019a; Muto et al., 2016). Typically, these inversion uncertainties are assumed to result from three sources.

1. Uncertainty in the gravity data. The uncertainties resulting from the gravity data uncertainty are typically estimated using a Bouguer slab approximation, with an assumed density of the contrast between rock and water ( $\sim 1600 \text{ kg m}^{-3}$ ), and a gravity uncertainty approximated from the RMS crossover values of the airborne gravity survey (e.g., Boghosian et al., 2015; Constantino et al., 2020; Tinto et al., 2019). Alternatively, a simple conversion factor has been proposed of 100 m of inversion uncertainty per 5 mGal of gravity uncertainty (An et al., 2019a; An et al., 2019b).
2. Assumptions of the geologic structure. The uncertainty resulting from assumptions of the geologic structure is typically simplified as uncertainties in the choice of the constant density contrast between sediment and seawater. This uncertainty is sometimes approximated as a ratio of change in density to change in inverted relief as a percentage (e.g.,  $\sim 3\%$  relief for  $50 \text{ kg m}^{-3}$  Tinto et al., 2019) or by altering the density and comparing the results (Boghosian et al., 2015).
3. Uncertainties in the past measurements of bathymetry (constraints). Lastly, constraint point measurement uncertainties are typically assumed to result in a 1:1 uncertainty in the inverted bathymetry (e.g., Boghosian et al., 2015; Tinto et al., 2019).

Our uncertainty analysis, through Monte Carlo simulation, provides robust spatial uncertainty estimates for each of these three sources of uncertainty. Similar to the above methods, Monte Carlo simulation only addresses uncertainties related to the uncertainty of the inputs to the inversion.

## 4.4 Results

Here we apply the above-described methods to recover a higher resolution bathymetry beneath Antarctica's Ross Ice Shelf. First, we show the results from an individual workflow, as depicted in Figure 4.2. This includes the starting bathymetry model, the topo-free gravity disturbance calculations, and the resulting inverted bathymetry. Next, we present the Monte Carlo simulation results, where this entire workflow is repeated many times with varying values of input data and parameters.

### 4.4.1 Starting bathymetry

Existing options for a starting bathymetry model for the sub-Ross Ice Shelf include Bedmap2 (Fretwell et al., 2013) or BedMachine v3 (Morlighem, 2022; Morlighem et al., 2020). BedMachine v3 for the Ross Ice Shelf contains the gravity-inverted

bathymetry results from Tinto et al. (2019). To avoid over-interpretation of the gravity data (starting an inversion with the results of a separate inversion) we opted to not use BedMachine for the starting model. Bedmap2 bed elevations for the Ross Ice Shelf were created through the interpolation of the point constraints (Fretwell et al., 2013). These point constraints within the ice shelf (Figure 4.1b) were compiled from several surveys, including the early traverses of the 1950s and 60s (Crary et al., 1962; Crary, 1959; Crary & Robinson, 1962)<sup>3</sup>, and the Ross Ice Shelf Geophysical and Glaciological Survey (RIGGS, 1973-1974 Bentley, 1984) ( $N = 223$ ). However, the gridding algorithm used (ArcGIS Topogrid), while producing smooth results for the Ross Ice Shelf, didn't strictly adhere to the constraint point depths. This can be seen through the comparison of constraint point depths and Bedmap2 grid values at the same location (Figure 4.1b). The RMS difference between the constraint depths and the grid depths within the ice shelf is 138 m. The largest differences are concentrated along the Transantarctic Mountain Front, where Bedmap2 grid values are much shallower than the constraint points. Due to this over-smoothing of the constraints, we have opted to create our own starting bathymetry model.

3137

Our starting model was created from the combination of various seismic survey constraint points on the ice shelf, and bed data from BedMachine v3 (Morlighem, 2022; Morlighem et al., 2020) outside of the ice shelf. To create this, the BedMachine v3 bed elevations, relative to the WGS-84 ellipsoid, were masked within the Ross Ice Shelf, based on the MEASUREs v2 Ross Ice Shelf boundary (Mouginot et al., 2017; Rignot et al., 2013). These data were converted from gridded data into point data and merged with the various bathymetry data within the ice shelf. A continuous grid of bathymetry depths at a 5 km cell size was then interpolated from the combined data inside and outside the shelf. The interpolation can be accomplished with two gridding methods, bi-harmonic splines (Sandwell, 1987), and minimum curvature (Smith & Wessel, 1990). While the bi-harmonic spline method appears to have several advantages over minimum curvature (Chapter 3 Section 3.4.2), such as the ability to apply weights to the data, interpolating the above Ross Ice Shelf data resulted in significant unconstrained minima and maxima. Initial inversion results showed these erroneous features carry through to the final inverted bathymetry. Due to this, we have opted to interpolate the data to create the starting bathymetry model using tensioned minimum curvature. This method resulted in less extreme un-constrained minima and maxima.

3156

To test the importance of the tension value used in the minimum curvature gridding, we performed 6 interpolations, with tension values of 0, 0.2, 0.4, 0.6, 0.8, and 1 (Figure 4.9a-f). From these six resulting bathymetry models, we calculated the standard deviation (Figure 4.9g) and the cell-specific mean (Figure 4.9h). These statistics were weighted, in the same method described in Figure 4.7d. The weight value used for each grid was the inverse square of the RMS difference between the constraint point depth values and the resulting grid values at the same points. These RMS values are shown in the figure titles of Figure 4.9a-f. This weighted mean starting model is compared to Bedmap2 bathymetry (Figure 4.9i). Note that while low tension factors result in models that closely match the constraints, they

---

<sup>3</sup>These surveys included the Ross Ice Shelf Traverse (1957-1958), the Little America Station Byrd Trail Traverse (1958), the Victoria Land Traverse (1958-1959), and the Discovery Deep Traverse (1960), see Bennett (1964) for the data and descriptions.

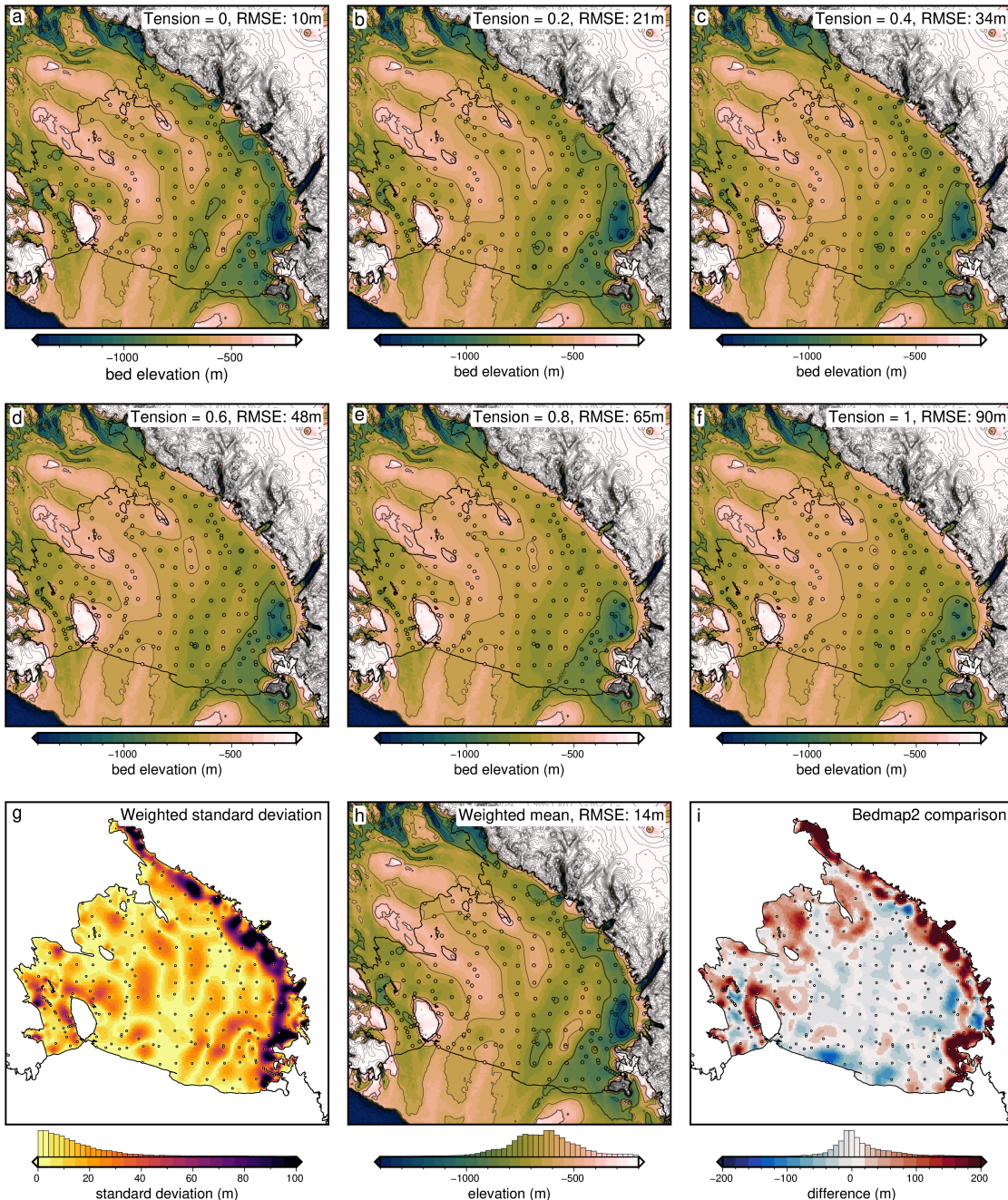


**Figure 4.9:** Starting bathymetry models from the interpolation of constraint points within the ice shelf and BedMachine v3 gridded data outside of the shelf (Morlighem, 2022; Morlighem et al., 2020). The ice shelf border, from Mouginot et al. (2017), is shown as the solid black line, representing the grounding line and the calving front. **a-f**) Bathymetry models resulting from 6 varying tension factor values of minimum curvature interpolation. Contours shown at 400m intervals. **g)** The cell-specific weighted standard deviation of the six models (**a-f**). **h)** The cell-specific weighted mean bed elevation from the six models. **i)** The difference between Bedmap2 bathymetry and the mean model (**h**). The RMS difference is 95 m. Blues show where the mean model is shallower than Bedmap2, while reds show where the mean model is deeper. Root mean square error (RMSE) values in the plot titles are between the constraint point depths and the values at those points on the interpolated grids.

3167 also produce local maxima and minima away from the data, which is not ideal since  
 3168 these features can be seen to carry through the inversion to the final bathymetry,  
 3169 as discussed later. Alternatively, higher tension values produce models that don't  
 3170 match the constraints as well (higher RMS values), but they don't have as many

3171 erroneous features. For this reason, we use the cell-specific mean of the six models  
3172 as our starting bathymetry (Figure 4.9h). This model has an RMS difference from  
3173 BedMap2 within the ice shelf of 95 m.

3174

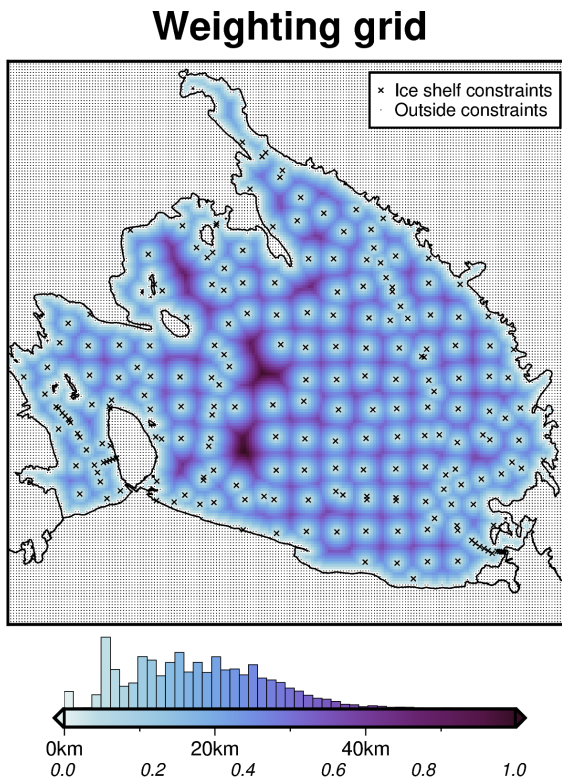


**Figure 4.10:** Weighting grid used in the Ross Ice Shelf bathymetry inversion. Grid colours show both the distance between each grid cell and the nearest constraint point and the weight values (0 - 1) from the normalization of these distances. Constraint points are defined as either direct measurements of bathymetry within the ice shelf (black crosses), or any grid cell outside of the ice shelf (small black dots). The ice shelf border, from Mouginot et al. (2017) is shown as the solid black line, representing the grounding line or the calving front.

3175 From these constraint points used to create the starting bathymetry, a weighting  
3176 grid was created (Figure 4.10). This grid was calculated from the distance between  
3177 each grid cell and the nearest constraint point. This minimum constraint distance  
3178 (top annotations of Figure 4.10 colorbar) was then normalized between 0 and 1 to  
3179 create the weighting grid (bottom annotations of Figure 4.10 colorbar). As all grid  
3180 cells outside of the ice shelf border are considered constraint points non-zero weights  
3181 and minimum constraint distances are confined to within the ice shelf border. The  
3182 colorbar histogram shows a mean minimum constraint distance within the ice shelf  
3183 of approximately 20 km, and an upper limit of approximately 60 km. Within the  
3184 shelf, there are 223 constraint points. Over an area of  $\sim 480,000 \text{ km}^2$  (Mouginot et  
3185 al., 2017), this equates to a constraint density of  $\sim 1$  constraint per  $46 \times 46 \text{ km}$  ( $2154 \text{ km}^2$ ).  
3186

3187

#### 3188 4.4.2 Gravity processing results

3189 We use airborne gravity data from the Ross Ocean and ice Shelf Environment, and  
3190 Tectonic setting Through Aerogeophysical surveys and modelling project (ROSETTA-

3191 Ice). This project was created with the goal of investigating the interactions between  
 3192 ice, ocean, and earth of Antarctica's Ross Ice Shelf (Tinto et al., 2019). The survey  
 3193 consisted of 3 field seasons (2015-2017) of airborne geophysical surveying with a  
 3194 survey design consisting of E-W flight lines, at a nominal spacing of 10 km, and  
 3195 N-S tie lines with a nominal spacing of 55 km (Figure 4.1a). Flights were flown  
 3196 at an average of 750 m above the ice surface and a speed of 180 knots ( $93 \text{ ms}^{-1}$ ).  
 3197 The survey was designed to maximize the overlap between the flight lines and the  
 3198 past bathymetry constraints across the ice shelf from the RIGGS seismic surveys  
 3199 (Bentley, 1984). The data collection and initial processing were performed by Tinto  
 3200 et al. (2019) and are briefly summarized here. The gravity data were collected with  
 3201 a combination of a LaCoste and Romberg gravimeter upgraded with a ZLS UltraSys  
 3202 control system, an iMAR inertial measurement unit, and a DgS gravimeter. The  
 3203 ZLS data was tied to an absolute gravity reference station at McMurdo Station.  
 3204 Poor-quality data from the ZLS was replaced with the iMAR or DgS values. The  
 3205 accelerations of the aircraft were calculated from GPS data and removed from the  
 3206 gravity signal. The Eötvös correction was applied, to account for measuring gravity  
 3207 on a moving platform (Harlan, 1968). At each observation point, the effects of the  
 3208 normal earth were calculated and removed, giving the gravity disturbance values  
 3209 (See Section 4.2.1.1). Levelling was then performed using the cross-over values be-  
 3210 tween E-W flight lines and N-S tie lines.

3211

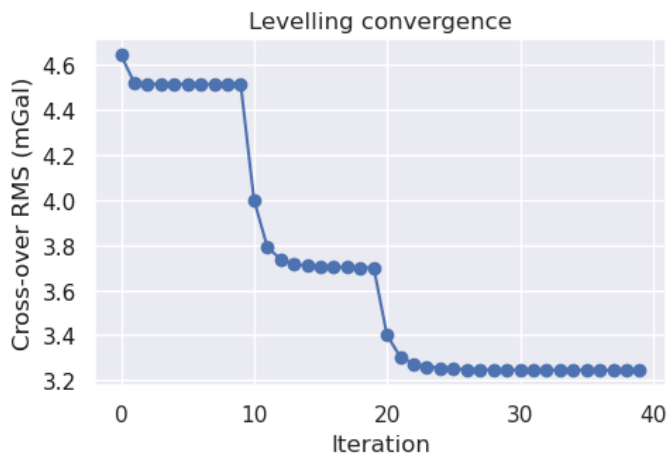


**Figure 4.11:** Re-leveelling of the ROSETTA-Ice gravity data. First, flight lines were individually upward continued, then cross-over point misties were found. These were used in 0<sup>th</sup>, 1<sup>st</sup>, and 2<sup>nd</sup> order iterative levelling, alternative between levelling flight lines to tie lines and vice versa at each iteration. The RMS cross-over errors at each iteration are shown. The major steps show the 0<sup>th</sup>, 1<sup>st</sup>, and 2<sup>nd</sup> order stages of levelling.

3212 Since this bathymetry inversion is strongly influenced by noise in the gravity  
 3213 data, as demonstrated in Chapter 3 Section 3.6.3.1, we have performed additional  
 3214 processing to the published ROSETTA-Ice dataset. Erroneous sections of flight line  
 3215 data were manually removed, and the dataset was re-levelled. The levelling proce-  
 3216 dure utilizes the gravity difference between E-W and N-S flight lines at cross-over  
 3217 points. While the flight paths intersect in 2-D space, their altitudes typically differ,  
 3218 meaning there is no true cross-over point in 3-D space. To account for this, the flight  
 3219 lines are individually upward continued to a constant elevation of 1 km (ellipsoidal  
 3220 height). The mean elevation of the cleaned data was  $\sim 790$  m, and 1 km was greater  
 3221 than 96% of the data. This limited the amount of downward continuation while

retaining a spatial resolution close to the original data. This continuation was calculated using the equivalent source technique (see Section 3.3.1.5 Dampney, 1969; Soler & Uieda, 2021). Since the cross-over points are now true 3-D intersections, the difference between E-W and N-S lines at these points (mis-ties) can be used to re-level the dataset. Here, we alternate between levelling the E-W lines to the N-S lines, and vice versa. We start with a 0-th order levelling, where only DC shifts are applied. Followed by a 1st and 2nd order levelling, where 1 and 2-degree polynomials, respectively, are fit to the mis-ties, and used to level the lines. The results of this levelling procedure are shown in Figure 4.11. For each order of levelling several iterations are performed. The step-wise convergence of the RMS mis-tie values shows the 0<sup>th</sup>, 1<sup>st</sup>, and 2<sup>nd</sup> order levelling stages. The re-levelling procedure brought the RMS mis-tie from  $\sim 4.8$  mGal to  $\sim 3.2$  mGal.

3234

Finally, this re-levelled gravity disturbance line data were gridded onto a regular grid at 2.5 km spacing, using equivalent sources. Since the inversion only affects the bathymetry within the ice shelf border, as implemented with the weighting grid (Figure 4.10), the interpolated gravity grid is masked beyond 10 km outside of the ice shelf border (Figure 4.11b). This 2.5 km gridded data ( $N = 85,914$ ) consists of both the *testing* ( $N = 64,435$ ) and *training* ( $N = 21,479$ ) sets used in the cross-validation. With the grid configuration shown in Chapter 3 Figure 3.4, the *training* data used in the actual inversion are on a regular 5 km grid.

3243

### 4.4.3 Gravity reduction results

The terrain mass effect was calculated at each of the gridded gravity data points. For this calculation, the three layers of prisms shown in Figure 4.5c-e were created from BedMachine v3 (Morlighem, 2022; Morlighem et al., 2020) ice surface and water surface data and the mean starting bathymetry from Figure 4.9h. All data are referenced to the WGS-84 ellipsoid. The ice surface elevations used from BedMachine v3 are in ice equivalent, meaning they have had a firn depth correction applied, making for a slightly lower surface elevation to account for spatially variable firn thickness (Morlighem et al., 2020). An ice equivalent surface is suitable for calculating the terrain mass effect since it gives the estimated thickness of the ice shelf with a density of ice, instead of the true ice shelf thickness, with a layer of low-density firn above. Comparing the forward gravity calculated from the true geometry of ice shelf thickness, the ice equivalent thickness, and a 2-layer model with firn and ice, show minimal differences, and thus we use the ice equivalent thickness in the terrain mass effect. The densities used in the terrain mass effect calculations were 1 kg m<sup>-3</sup> for air, 915 kg m<sup>-3</sup> for the density of ice, 1024 kg m<sup>-3</sup> for the density of seawater (Griggs & Bamber, 2011), and 2300 kg m<sup>-3</sup> for the density of the seafloor. Since we use a single value for the density of the seafloor, it should represent the expected average density of the seafloor over the entire region. Chapter 2 showed a continuous drape of sediment over the seafloor. We chose 2300 kg m<sup>-3</sup> to be in the middle between unconsolidated sediment ( $\sim 1900$  kg m<sup>-3</sup>) and low-density crystalline rock ( $\sim 2700$  kg m<sup>-3</sup>) (Schön, 2015). The inversion domain was 1 million km<sup>2</sup> (1000 km  $\times$  1000 km). To avoid gravitational edge effects in the forward calculations, the prism layers were extended in all directions by a 40 km buffer zone, resulting in 120,000 prisms. The resulting terrain mass effect was subtracted from the gravity distur-

3269 bance to get the topo-free gravity disturbance. These data are shown in Figure 4.12.

3270

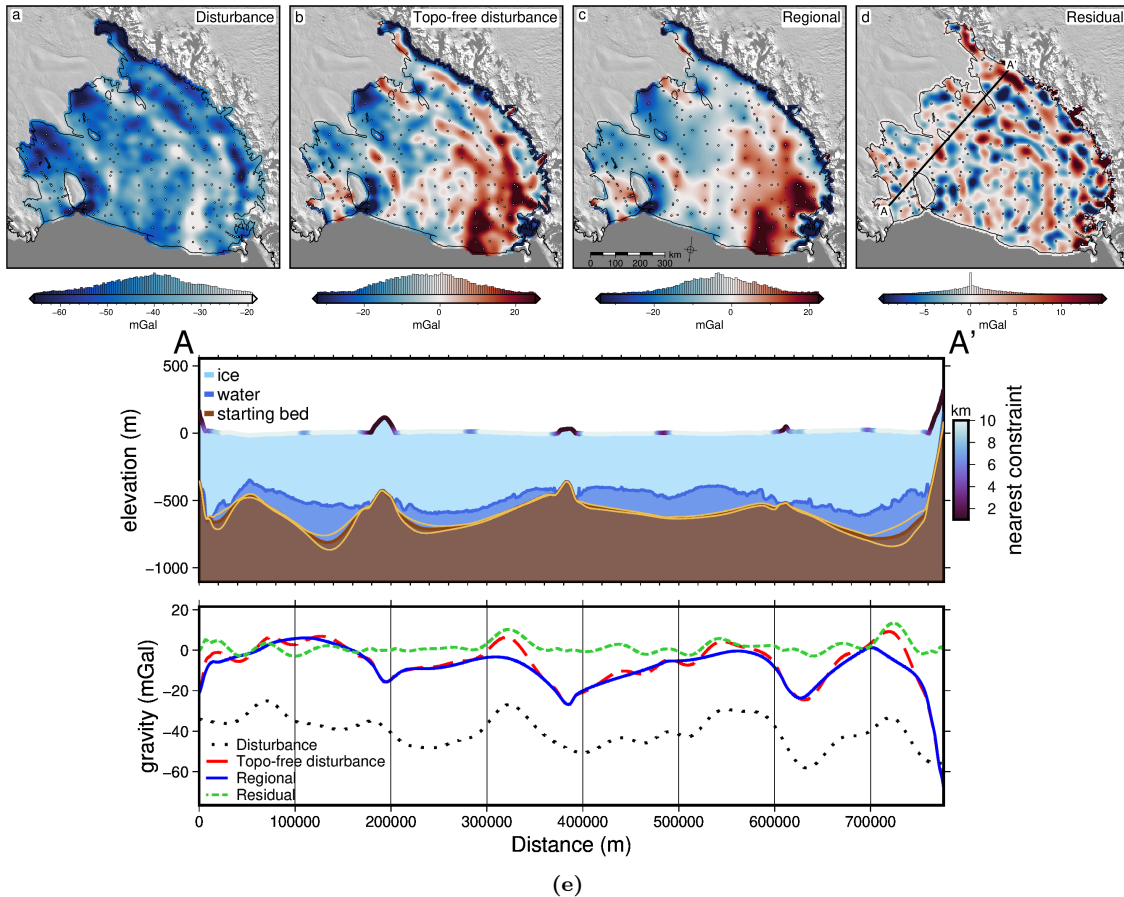


**Figure 4.12:** Gravity reduction results for the Ross Ice Shelf. **a)** Gravity disturbance, **b)** topo-free gravity disturbance, after the removal of the terrain mass effect, **c)** regional component of the topo-free disturbance, estimated with constraint point minimization, and **d)** residual component of the topo-free disturbance, as the difference between **b** and **c**. Background imagery is from MODIS-MOA (Scambos et al., 2007) and grounding line and coastlines are from (Morlighem, 2022). Constraint points within the ice shelf are shown as dots. **e)** Profile from A to A', location shown in **d**. **Upper panel** shows cross-section, with ice surface and ice base from BedMachine v3 (Morlighem, 2022; Morlighem et al., 2020). Brown layer shows the mean starting bed model with bounding uncertainty (light brown lines) from the standard deviation of the various starting bed models in Figure 4.9. The color of ice surface shows the distance to the nearest constraint point. **Lower panel** shows data from **a-d** along the profile.

3271 The topo-free gravity disturbance was subsequently separated into the regional  
 3272 and residual components. This was accomplished with constraint point minimization  
 3273 (Chapter 3 Section 3.2.4). While the synthetic data of the past chapter showed  
 3274 a clear benefit of using a bi-harmonic spline interpolation over a minimum curvature  
 3275 interpolation, we use minimum curvature here. As with the interpolation for the  
 3276 starting bathymetry model, bi-harmonic spline interpolation led to excessive uncon-  
 3277 strained maximum or minima. The resulting regional and residual components are  
 3278 shown in Figure 4.12.

3279

#### 3280 4.4.4 Inversion results

3281 With the residual component of the topo-free gravity disturbance as the inversion  
 3282 input (Figure 4.12d), we ran 10 inversions with varying levels of damping. Each in-  
 3283 version used a density of  $1024 \text{ kg m}^{-3}$  for ocean water and  $2300 \text{ kg m}^{-3}$  for the density  
 3284 of the seafloor. For each value of the damping parameter, the cross-validation score  
 3285 was calculated by forward modelling the gravity effect of the resulting bathymetry  
 3286 model onto the locations of the testing gravity data. The RMS difference between the  
 3287 residual component of the topo-free gravity disturbance and the forward-modelled  
 3288 results at these testing points gave the score. These scores are shown in Figure  
 3289 4.13a. The lowest score was achieved with a damping value of  $10^{-2}$ .

3290

3291 This inversion took 8 iterations and 135 seconds<sup>4</sup> and converged due to a lack of  
 3292 change in the  $\ell^2$ -norm between subsequent iterations (Figure 4.13b). The RMS of  
 3293 the residual gravity started at 6.1 mGal prior to the inversion and was reduced to  
 3294 4.0 mGal (Fig 4.13b).

3295

3296 The inverted bathymetry model for the sub-Ross Ice Shelf, at a 5km resolution,  
 3297 is shown in Figure 4.13c. Note that this is just the result of a single inversion. Our  
 3298 final inverted bathymetry model is achieved through the Monte Carlo simulation, as  
 3299 described below. The RMS difference between the inversion results and the starting  
 3300 model at the constraints is 16 m. The thickness of the water column, defined as the  
 3301 difference between BedMachine v3 ice base and the inverted bathymetry, is shown  
 3302 in Figure 4.13d.

3303

#### 3304 4.4.5 Uncertainty

3305 We used a series of Monte Carlo simulations (Figure 4.7) to assess both the spatial  
 3306 uncertainty of the resulting inverted bathymetry and the importance of the various  
 3307 components and parameters of the inversion. By varying the inputs of the inversion  
 3308 within their ranges of uncertainties, we can gather a range of the possible bathymetry  
 3309 results, which when compared shows where the inversion results are more or less  
 3310 certain. The inputs and their respective uncertainty distributions included in the  
 3311 sampling are:

- 3312 1. Gravity disturbance data; sampled from a normal distribution with a mean of  
 3313 the data point, and a standard deviation of the RMS mis-tie of the line data  
 3314 after levelling (3.3 mGal).
- 3315 2. Constraint point depths; sampled from a normal distribution with a mean of  
 3316 the measured depth, and a standard deviation of 10 m for points outside of  
 3317 the ice shelf, and 5% of depth from the ice surface for points within the ice  
 3318 shelf (mean of 36 m).
- 3319 3. The density of ice, water, and sediment; all sampled from normal distribu-  
 3320 tions with means of  $915 \text{ kg m}^{-3}$ ,  $1024 \text{ kg m}^{-3}$ , and  $2300 \text{ kg m}^{-3}$  respectively,  
 3321 and standard deviations of  $5 \text{ kg m}^{-3}$ ,  $5 \text{ kg m}^{-3}$ , and  $400 \text{ kg m}^{-3}$ . The small  
 3322 standard deviations of ice and water compared to sediment reflects the rela-  
 3323 tive certainty of the value and spatial heterogeneity of the density of ice and

---

<sup>4</sup>See Appendix 1.6 for a description of the hardware used.

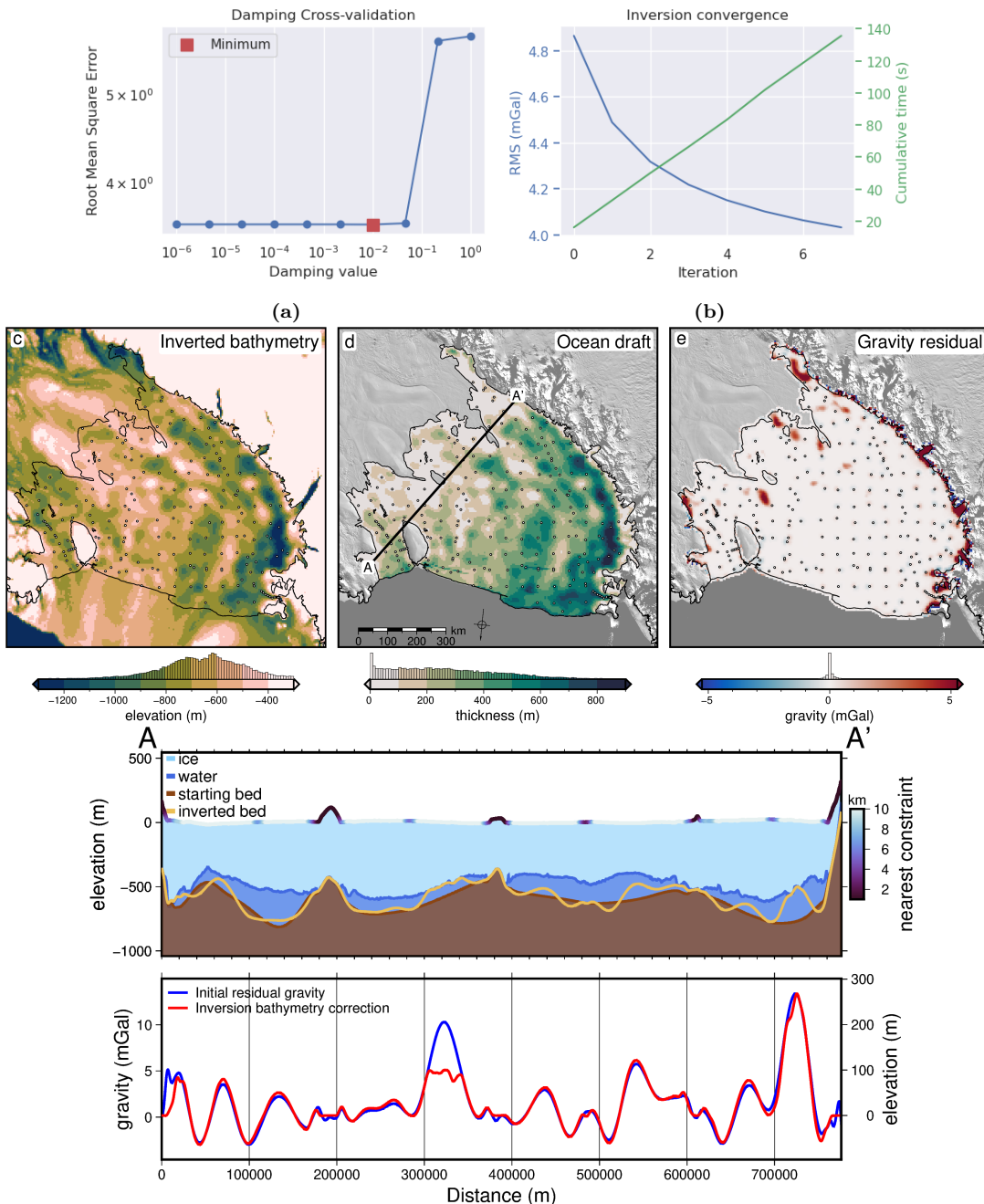


**Figure 4.13:** Ross Ice Shelf singular bathymetry inversion results. **a)** Damping parameter cross-validation with the lowest score shown in red. **b)** Convergence curve and cumulative inversion time for the optimal inversion. Blue line (left y-axis) shows consecutive iteration's RMS residual component of the topo-free gravity disturbance. Green line (right y-axis) shows cumulative time to run the inversion. **c)** Inverted bathymetry, **d)** water column thickness between the inverted bathymetry and Bedmachine v3 icebase (Morlighem, 2022; Morlighem et al., 2020), **e)** final residual component of the topo-free gravity disturbance. **Profile A to A'.** **Upper panel** shows ice surface and icebase from BedMachine v3, both the starting bathymetry (dark brown) and the inverted bathymetry (light brown). The colour of the ice surface shows the distance to the nearest constraint point. **Lower panel** shows the initial residual gravity used as input to the inversion (blue line, left y-axis), and the total correction (red line, right y-axis) applied to the starting bathymetry surface during the inversion to get the inverted bathymetry.

water, compared to those of the material comprising the sea floor. For the Ross Ice Shelf, the entire region is likely to be draped in at least 10's of meters of sediment (Chapter 2, Tankersley et al., 2022). With a mean of 2300 kg

3327         $\text{m}^{-3}$  and a standard deviation of  $400 \text{ kg m}^{-3}$ , these values span the range from  
 3328        unconsolidated sediment to low-density crystalline rock (Schön, 2015).

3329        4. The tension factor used in minimum curvature gridding for interpolating both  
 3330        the starting bathymetry model and the regional component of gravity. The  
 3331        tension factor values were sampled from a uniform distribution between 0 and  
 3332        1.

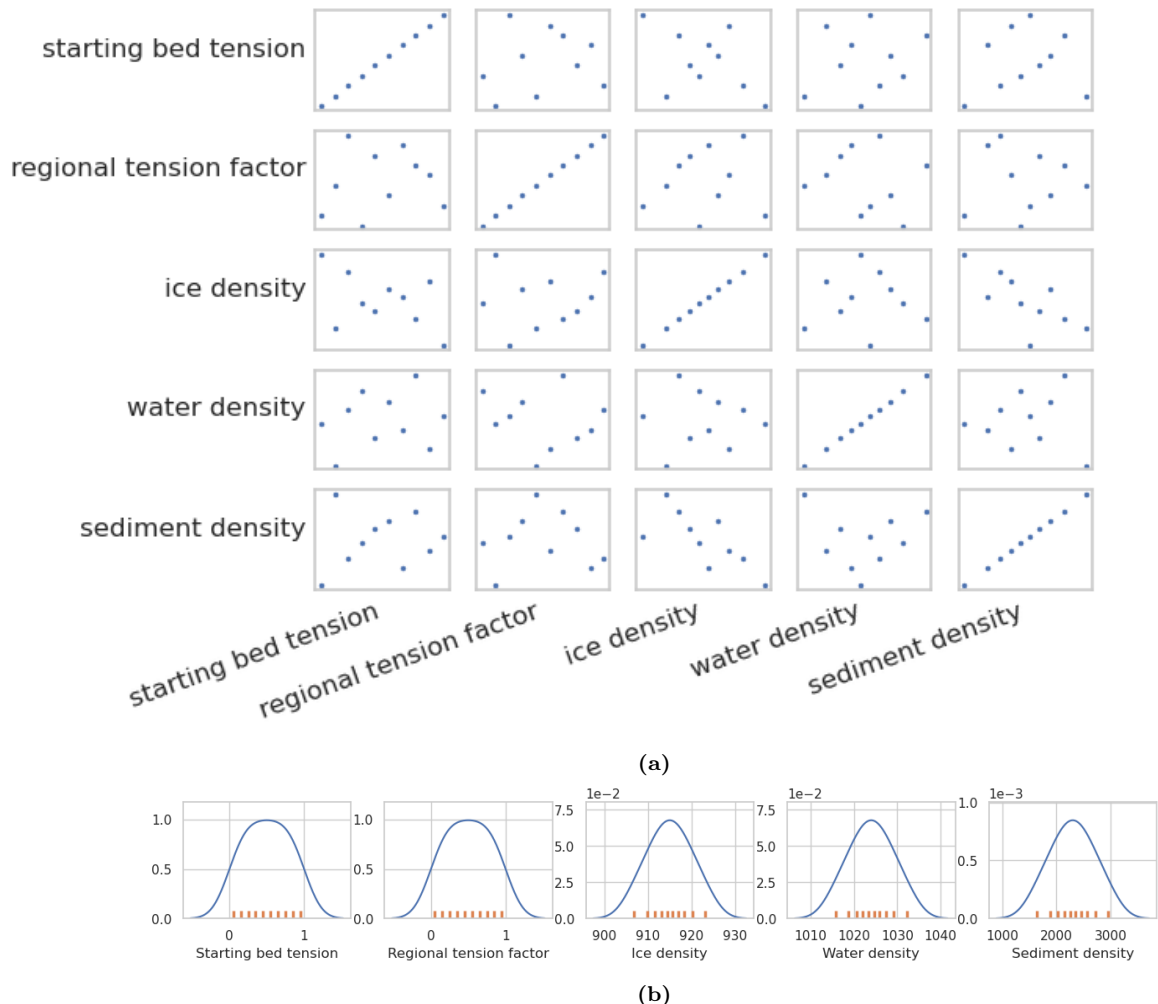


**Figure 4.14:** Latin hypercube sampling results for the 10 inversions of the full Monte Carlo simulation. **a)** Correlations between each pair of the 5 sampled input parameters. **b)** Resulting distributions of the 10 sampled values of each parameter. Blue line shows kernel density estimates fit to each set of sampled values, which are shown as orange ticks.

3333        Figure 4.14 shows the results of the Latin hypercube sampling of the 5 input  
 3334        variables (not including the gravity and constraints data). The correlations between  
 3335        each set of variables show that pairwise correlation was minimal. This is ideal since  
 3336        these inputs are unrelated, and therefore their sampled values should be uncorre-  
 3337        lated (Helton et al., 2006). This also shows that with only 10 samplings, the Latin  
 3338        hypercube sampling was able to provide adequate spatial coverage of the individual  
 3339        distributions (4.14b) as well as all the pairwise distributions combinations (4.14a).

3340        Each simulation consisted of 10 runs. We performed a *full* simulation, where  
 3341        each of the above inputs were sampled (Figure 4.15). We performed five additional  
 3342        simulations (Figure 4.16) where 1) only the gravity data was sampled, 2) only the

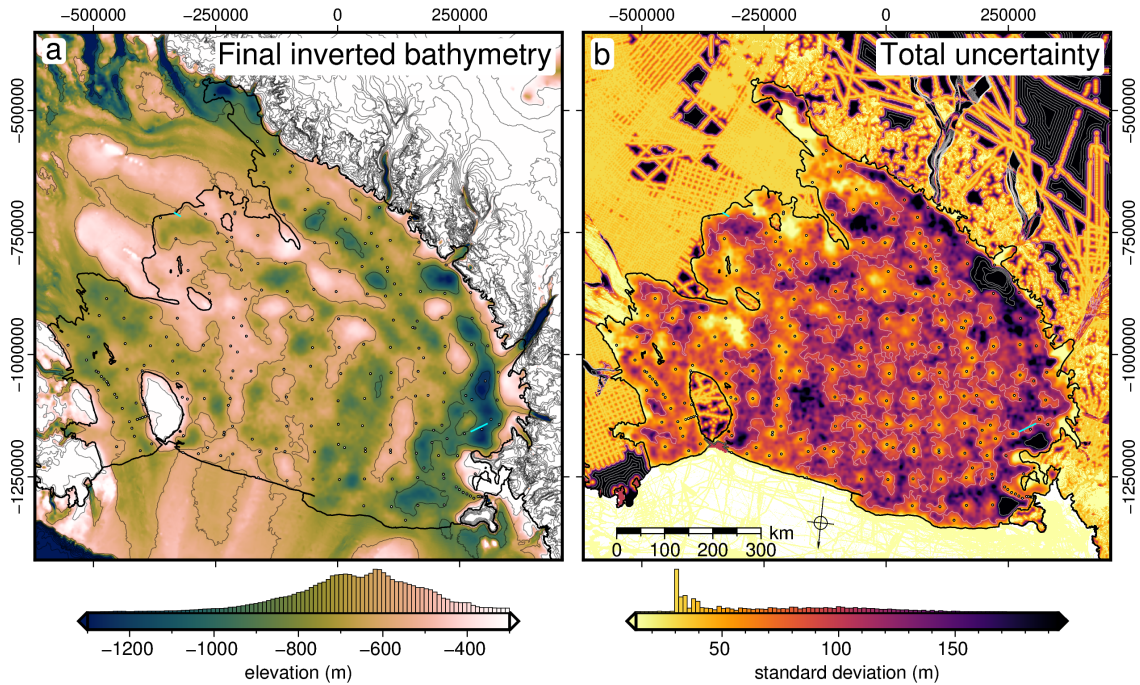


**Figure 4.15:** Final bathymetry depths and uncertainties from the full Monte Carlo simulation, merged with 500m resolution elevation and uncertainty data outside of the shelf from BedMachine v3 (Morlighem, 2022; Morlighem et al., 2020). **a)** Final inverted bathymetry model, calculated as the weighted mean of the full Monte Carlo simulation. Shown with 300 m contours. **b)** Uncertainty estimation of the inverted bathymetry from the cell-specific weighted standard deviation of the inverted bathymetry results from the full Monte Carlo simulation. Shown with 100 m contours. Constraints within the ice shelf are shown as dots in **a**. Grounding line and coastline are shown in black (Morlighem, 2022). Background imagery is from Scambos et al. (2007). Cyan lines show Discovery Deep and Kamb Ice Stream seismic surveys.

constraint point depths were sampled, 3) only the density values of ice, water, and sediment were sampled, 4) only the tension factor for interpolating the starting bathymetry model was sampled, and finally 5) only the tension factor for interpolating the regional component of gravity was sampled. Each simulation results in a series of inverted bathymetries. Finding the cell-specific weighted standard deviation of the bathymetry depths for each of these simulations gives an estimation of the uncertainty resulting from the associated parameter. The cell-specific statistics of these simulations were low-pass filtered to remove high-frequency noise induced by the random sampling. For the full simulation (Figure 4.15b) the weighted mean of the resulting bathymetries gives the final inverted bathymetry results of this study (Figure 4.15a). Note that this final bathymetry model resulting from the Monte Carlo simulation is similar, but distinct from the inverted bathymetry resulting from a single inversion without the Monte Carlo simulation, shown in Figure 4.13c.

3356

The final bathymetry and uncertainty grids were resampled to a resolution of 500 m, from their original 5 km resolutions, masked outside of the ice shelf, and merged to the 500 m resolution bed and uncertainty data of BedMachine v3. This final bathymetry has a mean elevation of  $\sim 700$  m within the ice shelf. The deepest point is  $\sim -1370 \pm 187$  m, located near the Byrd Glacier outlet (Figure 4.1b). Bathymetric features appear to have continuity with features from BedMachine v3 data outside of the ice shelf. The RMS difference between the bathymetry and the original constraint point depths is 44 m. Subtracting the bathymetry from the ice base

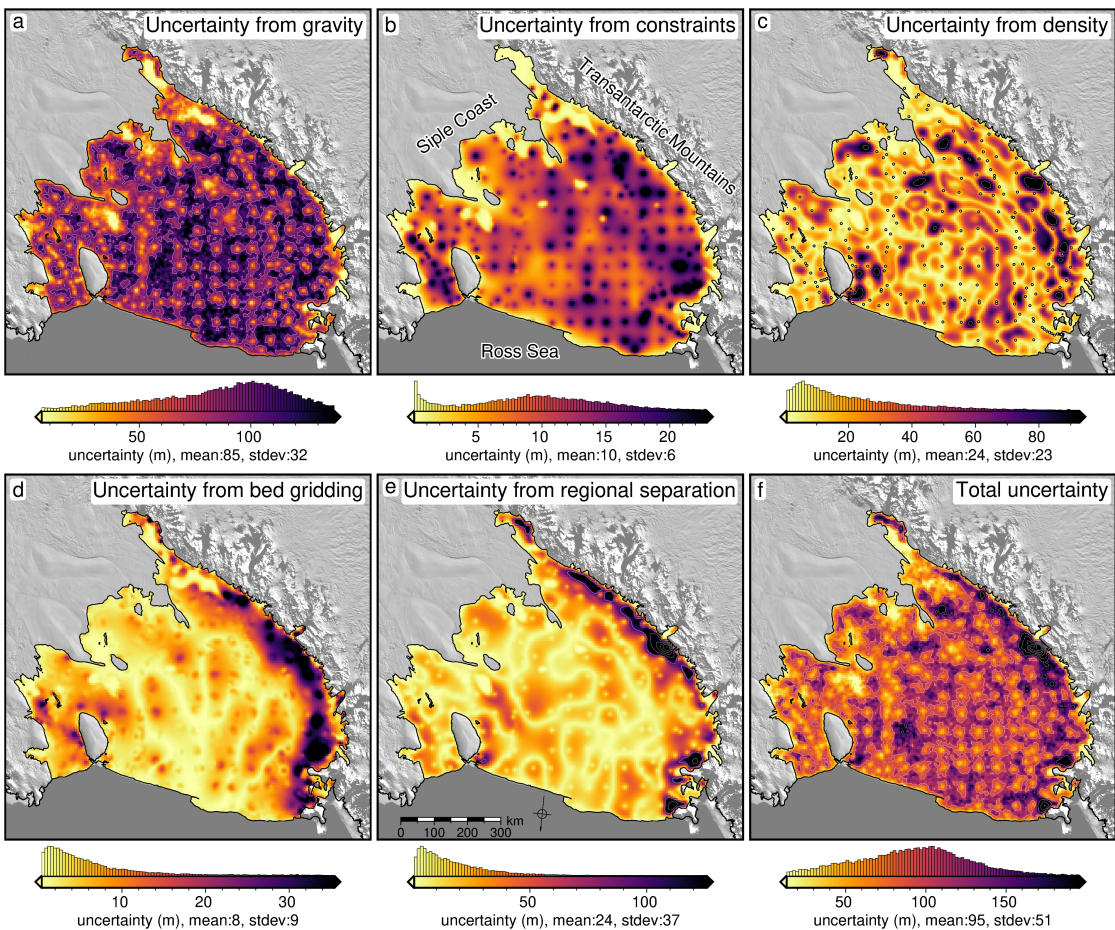


**Figure 4.16:** Sensitivity analysis for the inversion input data and parameters. Cell-specific weighted standard deviations of the inverted bathymetry results from Monte Carlo simulations with sampling the uncertainties of the **a)** gravity data, **b)** constraint points depths, **c)** ice, water, and sediment density values, **d)** starting bed interpolation tension factor, and **e)** tension factor for interpolating the regional gravity component. **f)** The total uncertainty from the full simulation. 100 m contours in white. Constraints within the ice shelf are shown as dots in **c)**. Grounding line and coastline shown in black (Morlighem, 2022). Background imagery is from Scambos et al. (2007).

3365 elevations of BedMachine v3 (Morlighem, 2022; Morlighem et al., 2020) gives the  
 3366 water column thickness, as shown in Figure 4.18b. Without ice base uncertainty es-  
 3367 timates from BedMachine v3, we use the bathymetry uncertainty as our uncertainty  
 3368 for the water column thickness, acknowledging that this is a minimum uncertainty.  
 3369 Within the ice shelf boundary, this water column thickness has a mean value of 260  
 3370 m and a maximum of 1000 m, located near the Nimrod Glacier outlet. Here, the  
 3371 bathymetry has an uncertainty of  $\pm 800$  m. Outside of this region, the thickest ocean  
 3372 cavity is  $\sim 940 \pm 180$  m, located at the Byrd Glacier outlet. The similarity between  
 3373 the bathymetry depth and the water column thickness shows that the ocean cavity is  
 3374 predominantly controlled by bathymetry and that the ice base topography is smooth  
 3375 compared to the bed. The uncertainty in the bed elevation ranges from  $\sim 10 - 850$  m,  
 3376 with a mean of 95 m (Figure 4.13b). It has an approximately normal distribution,  
 3377 with a slight skew to the higher values. In general, the uncertainty is lowest at the  
 3378 constraint points and highest far from constraints. There are elevated uncertain-  
 3379 ties in several spots, with the largest being along the Transantarctic mountain front.

3380

### 3381 4.4.5.1 Partitioning uncertainty

3382 The uncertainty in the inverted bathymetry which arises from the uncertainty in  
 3383 gravity data (Figure 4.16a) is relatively spatially uniform, with a mean of 85 m. It  
 3384 is lowest immediately at the constraints, and generally highest far from constraints.  
 3385 The uncertainty from the constraints point depths (Figure 4.16b) is also generally  
 3386 spatially uniform, with a mean of 10 m. Conversely, it is highest at the constraints,  
 3387 and lowest far from constraints. The uncertainty resulting from the choice of den-  
 3388 sity values (Figure 4.16c) displays a more heterogenous spatial distribution than the  
 3389 previous two uncertainties. It is lowest at the constraints and has a mean of 24 m.  
 3390 The largest values are located at the gaps between constraints. The uncertainty  
 3391 resulting from the interpolation of the starting bed (Figure 4.16d) has a distinct  
 3392 spatial distribution. It is highest along the Transantarctic mountain front, with val-  
 3393 ues up to 40 m, but it has an overall mean of 7 m. Lastly, the uncertainty resulting  
 3394 from the estimation and removal of the regional component of gravity, prior to the  
 3395 inversion, (Figure 4.16e), also shows highest values along the mountain front, with  
 3396 values over 200 m (up to 700 m at the Nimrod Glacier outlet). The mean value is  
 3397 24 m. The reported uncertainties and their components from a wide range of past  
 3398 studies are shown in Table 4.1.

3399

## 3400 4.5 Discussion

3401 Here we discuss the results of our Ross Ice Shelf bathymetry model from the in-  
 3402 version of airborne gravity data. First, we describe the results of the uncertainty  
 3403 and parameter sensitivity analysis. Then we compare our results with two past  
 3404 bathymetry models beneath the Ross Ice Shelf and discuss the differences. Lastly,  
 3405 we discuss various implications of this updated bathymetry model, including how  
 3406 the findings relate to geology, tectonics, and ice sheet dynamics.

### 3407 4.5.1 Uncertainties and parameter importance

3408 The results of our Monte Carlo simulations provide answers to several important  
 3409 questions; 1) how confident are we in the inverted bathymetry depths? 2) where  
 3410 are we most and least confident about the bathymetry depth? 3) what are the  
 3411 specific sources of this uncertainty? and finally, 4) what can be done to limit the  
 3412 uncertainty? Figures 4.15b and 4.16f show the resulting spatial uncertainty of the  
 3413 inverted bathymetry, providing an answer to the first two questions. To determine  
 3414 the sources of this uncertainty, the individual inputs to the inversion were isolated  
 3415 and their effects on the estimated uncertainty were found (Figure 4.16).

3416

#### 3417 4.5.1.1 Gravity component

3418 The largest contributor to the overall uncertainty of the inversion is the uncertainty  
 3419 of the gravity data (Figure 4.16a). This uncertainty resulting from the gravity data  
 3420 results in a base-level bathymetry uncertainty of  $\sim 85$  m and is relatively spatially  
 3421 uniform. This is because each gridded gravity data point is contaminated with  
 3422 independent noise of varying levels during the Monte Carlo sampling. It is this

Study	Inverted bathymetry uncertainty (m)			
	total	from gravity	from geology	from constraints
<b>This study (<math>\bar{x} \pm 1\sigma</math>)</b>	95±51	85±32	48±30	10±6
Eisermann et al. (2021)	220	84	116	20
Tinto et al. (2015)	160	26	124	10
Constantino et al. (2020)	133	34	90	5-10
Boghosian et al. (2015)	110	10-28	50-70	10
Tinto and Bell (2011)	70	34	10-15	20
Constantino and Tinto (2023)	69-123	32-39	27-74	10
Tinto et al. (2019)	68	48	10	10
Eisermann et al. (2020)	175-225	-	-	10
Jordan et al. (2020b)	100	23	-	-
An et al. (2019a)	60	60	-	-
Studinger et al. (2004b)	250	-	-	-
Wei et al. (2020)	246	-	-	-
Greenbaum et al. (2015)	190	-	-	-
Brisbourne et al. (2014)	160	-	-	-
Hodgson et al. (2019)	100	-	-	-
Yang et al. (2021)	68	-	-	-
An et al. (2017)	60	-	-	-
Millan et al. (2017)	50-65	-	-	-
Millan et al. (2018)	30-50	-	-	-
Millan et al. (2020)	45	-	-	-
Filina et al. (2008)	-	19	-	-
<b>Mean</b>	117 (N=25)	40 (N=13)	57 (N=11)	12 (N=10)

**Table 4.1:** Reported inverted bathymetry uncertainties and the various components. Our reported geologic uncertainty is the combination of uncertainties resulting from the density values and the tension factor used in grinding the regional field.

3423 point-by-point random noise that creates the noisy component in the final inverted  
 3424 bathymetry. In reality, the uncertainty of nearby gravity data is likely correlated,  
 3425 where entire lines, or sections of lines have similar uncertainty values, due to chang-  
 3426 ing data collection conditions, like turbulence, or mis-levelling, causing values of  
 3427 entire lines to be offset, or tilted. Here our estimate of gravity uncertainty is entirely  
 3428 dependent on cross-over mistakes; likely an oversimplified estimation of uncertainty  
 3429 for an entire survey. This suggests that the true uncertainty resulting from the  
 3430 gravity data likely has a different spatial distribution and may be larger than we re-  
 3431 port; a finding which is not surprising, since the entire method depends on this data.

3432

#### 3433 4.5.1.2 Constraints component

3434 The uncertainty in the other data input to the inversion, the constraint point depths,  
 3435 has only a small effect on the results (Figure 4.16b). It is worth noting that while  
 3436 the uncertainty resulting from the constraint point measurement uncertainty is low,  
 3437 the constraints themselves are fundamental to the inversion. These constraints feed  
 3438 into all the components of the inversion and thus affect the uncertainty of each  
 3439 component, including the uncertainty from the gravity data. This is shown by the  
 3440 correlation between uncertainty and the distance to the nearest constraint (Figure  
 3441 4.10) of all the components of Figure 4.16. Our Monte Carlo sensitivity analysis only  
 3442 tests the effects of estimated noise in the inputs, and not their overall importance for  
 3443 the inversion. Since the uncertainty in the constraints only impacts the inversion  
 3444 in the immediate vicinity of the constraint, for constraint data collection, efforts  
 3445 should be focused on quantity over quality, assuming the uncertainty can be limited  
 3446 to a reasonable amount. In practice, for over-ice seismic surveying, this may lead to  
 3447 the choice of fast and efficient systems as opposed to high-resolution systems. For  
 3448 example, towable snow streamers and sources such as surface detonations or vibro-  
 3449 seis (e.g., Hofstede et al., 2021; Smith et al., 2020b) can collect data very efficiently  
 3450 ( $\sim 20$  km/day), compared to higher-resolution surveys with buried geophone arrays  
 3451 and drill-emplaced explosives (e.g., Horgan et al., 2013). The remaining sources of  
 3452 uncertainty are related to user-defined inversion parameters.

3453

#### 3454 4.5.1.3 Density component

3455 The choice of density values for the ice, water, and sediment results in a mean un-  
 3456 certainty in the bathymetry model of 24 m (Figure 4.16c). The ranges of densities  
 3457 tested in the Monte Carlo simulation were  $\sim 905 - 925 \text{ kg m}^{-3}$  for ice<sup>5</sup>,  $\sim 1015 -$   
 3458  $1035 \text{ kg m}^{-3}$  for seawater, and  $\sim 1600 - 3000 \text{ kg m}^{-3}$  for the seafloor. We only test  
 3459 homogeneous changes in the density values.

3460

3461 The uncertainty arising from the choice in density values has a strong spatial cor-  
 3462 relation with the absolute value of the inversion's input gravity, the residual gravity  
 3463 (Figure 4.12d). This correlation can be explained by the inverse relation between  
 3464 the amplitude of the corrections applied to the bathymetry during the inversion,  
 3465 and the density contrasts used in the inversion. For the same gravity anomaly, a

---

<sup>5</sup>We note that the maximum density of meteoric ice is  $917 \text{ kg m}^{-3}$ , however, the inclusion of marine ice may raise this value (Fricker et al., 2001)

3466 smaller density contrast results in a larger amplitude correction while a larger den-  
3467 sity contrast results in a smaller correction. This means that changes in the density  
3468 values just affect the amplitude of the correction applied to the bathymetry. Often,  
3469 spatially variable density is used as a means to account for the regional component  
3470 of gravity (e.g., Constantino et al., 2020; Tinto et al., 2019). We note that there  
3471 is an additional benefit to incorporating spatially variable densities. If adequate  
3472 *a priori* information is known to justify a density distribution, this can be used  
3473 to allow differing amplitudes of corrections across the inversion domain. In other  
3474 words, if the seafloor truly is denser in one region of the inversion compared to the  
3475 seafloor elsewhere, for a similar gravity anomaly, the inversion correction should be  
3476 of smaller amplitude in the high-density region. However, due to a lack of geologic  
3477 knowledge beneath the ice shelf, we use constant density values. We propose Monte  
3478 Carlo sampling of a wide range of possible density values as a robust and feasible  
3479 method to avoid biasing the resulting bathymetry model to either too high or too  
3480 low correction amplitudes, to achieve both the most realistic results and an estima-  
3481 tion of the uncertainty.

3482

#### 3483 4.5.1.4 Interpolation component

3484 The final components of the overall uncertainty are related to interpolation con-  
3485 ducted during two stages of the inversion; 1) the interpolation of the starting model  
3486 from the sparse constraint point depths, and 2) the estimation of the regional field  
3487 from the interpolation of gravity values at the constraint points. Here, we have used  
3488 a minimum curvature gridding algorithm (Smith & Wessel, 1990), which accepts a  
3489 tension factor for the interpolation which can range from 0 to 1. Figure 4.9 shows  
3490 the results of six different values of this tension factor for creating the starting bed  
3491 model. These figures show that low values of tension are able to accurately reproduce  
3492 the data with a smooth interpolation, but can result in unconstrained local maxima  
3493 or minima. Conversely, high tension values produce smooth surfaces without false  
3494 oscillations but don't adhere to the data as well. For these issues associated with  
3495 the two end members, intermediate values of 0.25 and 0.35 are often suggested for  
3496 potential field data and topographic data, respectively. We suggest a more robust  
3497 alternative to using these suggested values is the Monte Carlo sampling approach  
3498 we have used. This runs the inversion with a variety of tension factors and uses  
3499 the standard deviation of the resulting bathymetry models as a means to estimate  
3500 the uncertainty associated with the choice of the tension factor. While tensioned  
3501 minimum curvature gridding has been used in several past inversions (e.g., An et al.,  
3502 2019a; Millan et al., 2020; Yang et al., 2021), the choice of the tension values has  
3503 not been discussed for these applications.

3504

3505 The uncertainties arising from the choice of tension factors are shown in Figure  
3506 4.16d and e. The tension factor for gridding the starting bed model results in a  
3507 relatively low uncertainty with a mean of 7 m. The resulting uncertainty for the  
3508 regional separation is comparatively high, with a mean of 24 m. Both of these re-  
3509 sults show large spatial heterogeneity, with significantly larger uncertainties along  
3510 the Transantarctic Mountain front. This is likely related to the poor performance  
3511 of this gridding algorithm for high-gradient data. This region along the mountain  
3512 front has both steep topography and high amplitude gravity anomalies.

3513

**3514 4.5.1.5 Reducing uncertainties**

3515 Of the various components of the uncertainty analysis, only some can feasibly be  
3516 reduced. Reducing the uncertainty resulting from the interpolation parameters may  
3517 be possible with future method development, but this is beyond the discussion of this  
3518 research. To our knowledge, there is no robust method of determining a spatially  
3519 variable density distribution to be used in the inversion, without the collection of in-  
3520 situ data. This leaves the data inputs, gravity and constraints, as viable components  
3521 of a bathymetry inversion where further reductions of uncertainties can occur. We  
3522 propose a favorability of quantity over quality for constraint data since typical bed  
3523 elevation uncertainty is already relatively low, and therefore more data of mediocre  
3524 quality should be prioritized over high-quality but spatially limited data. In order  
3525 to reduce the uncertainty component resulting from the gravity data, first we must  
3526 be able to estimate the realistic spatial uncertainty of the gravity data itself. A  
3527 simple cross-over analysis is too simple to cover the effects of turbulence, chang-  
3528 ing flight speed and altitude, and errors in processing steps, such as base station  
3529 ties and levelling. The areas of largest uncertainty are generally a function of 1)  
3530 distance to the nearest constraint point (Figure 4.10) and 2) proximity to steep gra-  
3531 dients of topography and/or gravity (Figure 4.16d and e). This highlights the entire  
3532 Transantarctic Mountain front of the Ross Ice Shelf and the two major constraint  
3533 gaps in the central-east portion of the ice shelf (Figure 4.10) as locations that would  
3534 greatly benefit from additional seismic surveying.

**3535 4.5.1.6 Past estimations of uncertainty**

3536 Our comprehensive uncertainty and sensitivity analysis is shown to be similar to the  
3537 approximated uncertainties reported for other ice shelves (Table 4.1). Some differ-  
3538 ences include; our reported uncertainty resulting from the gravity data uncertainty  
3539 is the highest reported, while our values resulting from other sources, and the total  
3540 uncertainty, were similar to those of other studies. Our larger reported uncertainty  
3541 resulting from the gravity data likely shows that the simple Bouguer slab approx-  
3542 imation used by the other studies underestimates the component of uncertainty  
3543 resulting from the gravity data uncertainty. We take the uncertainties resulting  
3544 from geologic variations to be the combination of our reported uncertainties from  
3545 the chosen density values (Figure 4.16c) and from the regional separation gridding  
3546 (Figure 4.16e) since these both affect the estimation of the regional component. The  
3547 uncertainty resulting from the constraint point measurement uncertainty was very  
3548 similar across all studies.

3549 From this, we propose future bathymetry inversions undertake similar uncer-  
3550 tainty analysis through the Monte Carlo sampling of the input parameters. This  
3551 technique not only provides similar uncertainty estimates to past studies, but it ac-  
3552 complishes it in a systematic and reproducible method. Additionally, this technique  
3553 provides a spatial distribution of the uncertainties, instead of a single value. Once  
3554 the inversion workflow is set up, the sampling and re-running of the inversion is a  
3555 simple procedure, and with the use of Latin hypercube sampling, we have shown  
3556 that with only 10 runs, the parameter space of all the inputs is adequately sampled  
3557 (Figure 4.8).

3559

### 3560 4.5.2 Past bathymetry models

3561 Our gravity-inverted bathymetry model for the sub-Ross Ice Shelf reveals significant  
3562 differences with previous bathymetry models. However, a portion of these differences  
3563 are not related to the inversion, but to the creation of the starting model. First,  
3564 we will discuss the differences between our starting bathymetry model and another  
3565 interpolation-based bathymetry model, then we will compare our inversion results  
3566 with two past models. These past models include Bedmap2 (Fretwell et al., 2013)  
3567 and BedMachine v3 (Morlighem, 2022; Morlighem et al., 2020). The Bedmap2  
3568 model for the Ross Ice Shelf region is created from the interpolation of the same  
3569 constraint points within the ice shelf as used in this study, as well as grounded ice  
3570 thickness measurements and limited rock outcrop elevation data (Fretwell et al.,  
3571 2013; Le Brocq et al., 2010; Timmermann et al., 2010). BedMachine v3 used these  
3572 point measurements and applied additional methods to increase the resolution of  
3573 the bed. For outside of the ice shelf, this included mass conservation for areas of  
3574 fast-moving ice (outlet glaciers and ice streams), streamline diffusion for regions of  
3575 slow-moving ice, as well as minimum curvature gridding to interpolate the remaining  
3576 gaps (Morlighem et al., 2020). Within the ice shelf, BedMachine used the gravity  
3577 inversion results of Tinto et al. (2019).

3578

#### 3579 4.5.2.1 Starting model comparison

3580 Figure 4.9 shows the series of six starting bed models we created from the interpolation  
3581 of the sparse constraints. These were created with six levels of tension applied  
3582 to a minimum curvature interpolation. The cell-specific standard deviation of these  
3583 six models shows the uncertainty associated with this interpolation (Figure 4.9g),  
3584 and the mean of the six grids is our chosen starting model (Figure 4.9h). This is  
3585 compared with the Bedmap2 model in (Figure 4.9i). The RMS difference between  
3586 the two grids, within the ice shelf, is 95 m. Our starting bed is deeper proximal to  
3587 the entire grounding zone, while it is shallower along the ice front and throughout  
3588 the centre of the ice shelf. However, these differences of up to 200 m do not suggest  
3589 our starting model is inaccurate. Sampling the grid values at the constraint points  
3590 and comparing them with the constraint depths shows that our model was signif-  
3591 icantly better at adhering to these constraints, compared to Bedmap2. The RMS  
3592 of the difference with our model was 14 m, while the RMS of Bedmap2 was 138 m  
3593 (Figure 4.1).

3594

3595 These large differences for Bedmap2 are concentrated along the Transantarctic  
3596 Mountain front, where the interpolation algorithm used in Bedmap2 resulted in ex-  
3597 cessively shallow bathymetry. This interpolation appears to have favoured smooth-  
3598 ness over accuracy for this location of steep terrain. This has resulted in a "leakage"  
3599 of the high elevations within the mountains into the bathymetry interpolation, as  
3600 pointed out in this region (Le Brocq et al., 2010), as well as for other ice shelves  
3601 (Brisbourne et al., 2020). This over-smoothing and "leakage", while strongest along  
3602 the mountain front, can be seen along the entire grounding zone. This is the reason  
3603 why Bedmap2 was more shallow than our starting model along the grounding line.  
3604 This shows that care needs to be taken when picking or creating a starting model for  
3605 an inversion, especially in regions of steep topography. The re-creation of the start-  
3606 ing model from the point data allows the choice of interpolation techniques better

3607 suited for the region of interest, compared to techniques determined most suitable  
 3608 for a continent-wide study.

3609

3610 **4.5.2.2 Inversion result comparisons**

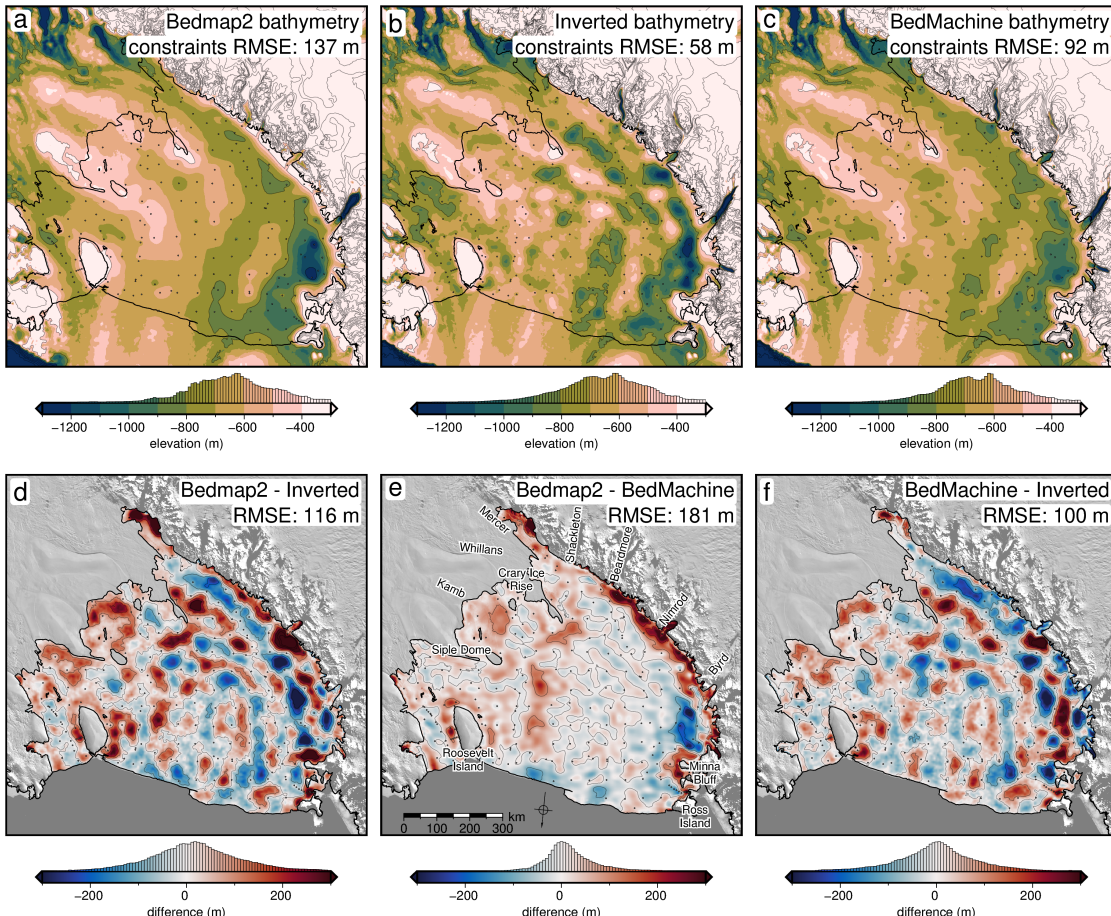


**Figure 4.17:** Comparison of our inverted bathymetry with past models. **a)** Bedmap2 bathymetry, **b)** our inversion results, from the weighted mean of the full Monte Carlo simulation, and **c)** BedMachine bathymetry. All three share the same colour scale and are contoured at 400 m intervals. RMS difference with the constraint points for each model is stated on the maps. **d)** Difference between our model and Bedmap2, **e)** difference between Bedmap2 and BedMachine v3, and **f)** difference between our model and BedMachine v3. Grids share a colour scale and are contoured at 100 m intervals. Blue regions in **d** and **f** indicate where our results are shallower, while red regions indicate where our results are deeper than the past models. Blue regions in **e** indicate where BedMachine is shallow, while red regions indicate where BedMachine is deeper than Bedmap2. RMS differences are stated on the maps. Grounding line and coastline are shown in black (Morlighem, 2022). Background imagery is from Scambos et al. (2007). Elevations are referenced to the WGS-84 ellipsoid.

3611 **Bedmap2 comparison**

3612 Figure 4.17 compares our final bathymetry results with the models of Bedmap2 and  
 3613 BedMachine v3. Additionally, several profiles across different regions are shown in  
 3614 Figure 4.18, comparing the various models. Interestingly, the inversion has raised  
 3615 the RMS difference with Bedmap2, compared to the starting model. But due to the  
 3616 issues with the Bedmap2 grid along the mountain front, this increased difference is

3617 expected. The differences between our inverted bed and Bedmap2 have a normal  
3618 distribution (Figure 4.17d). Our results introduce many small-scale features, as ex-  
3619 pected since Bedmap2 is an inherently smooth product. However, there are several  
3620 noticeable large-scale differences with Bedmap2. Proximal to the grounding line,  
3621 our results are generally deeper, as seen with the starting model comparison (Figure  
3622 4.18g). Many of the regions where our results are deeper are related to the issue of  
3623 over-shallow interpolation of Bedmap2. Portions of the grounding zone along the  
3624 Siple Coast are over 200 m deeper, including the Kamb (Figure 4.18c) and Mercer  
3625 ice stream grounding zones.

3626  
3627 Another notable difference is an NW-SE oriented trough which appears in our  
3628 results but is essentially absent in Bedmap2. This feature begins at the southern  
3629 end of the Crary Ice Rise grounding zone and continues  $\sim$  300 km, paralleling the  
3630 mountain front (Figure 4.18c). This feature is the southwestern-most of a series of  
3631 2 or 3 parallel troughs and ridges, as shown in Figure 4.18d. These features are  
3632 oriented at a high angle to both E-W and N-S flight lines, increasing their likelihood  
3633 as true features of the bathymetry and not flight line levelling artifacts. While they  
3634 are subtle, their presence alters the general *texture* in the region from a primary  
3635 N-S / NNE-SSW to an NW-SW orientation. This switches the general trend of  
3636 bathymetry features in the region to be aligned with Siple Coast ice flow, rather  
3637 than the Transantarctic outlet glacier ice flow. Whether these bedforms are tectonic  
3638 in nature, revealing the tectonic fabric, or are erosion/depositional, and thus reveal-  
3639 ing the past flow directions of the previously grounded ice sheet is unknown. The  
3640 last major difference with Bedmap2 is a significantly deeper bathymetry along the  
3641 western edge of Roosevelt Island (Figure 4.18a)

3642

### 3643 **Bedmachine comparison**

3644 Comparing our results to Bedmachine v3 provides a unique opportunity to evaluate  
3645 the differences resulting from different gravity inversion algorithms. The gravity  
3646 inversion results of Tinto et al. (2019), which comprise the Bedmachine v3 data be-  
3647 neath the ice shelf, used similar input datasets (gravity data and constraint points),  
3648 suggesting that differing inversion algorithms and workflows are likely responsible  
3649 for the majority of the differences shown in Figure 4.17f. However, some of the  
3650 differences may arise from re-processing the gravity data, and a different method of  
3651 gravity reduction applied here, as compared in Section 4.3.

3652

3653 To remove the regional component of gravity, Tinto et al. (2019) used a smoothly  
3654 varying density model in their inversion. To create this density model, they created  
3655 an initial prism layer with prisms extending from their starting bathymetry to a  
3656 depth of 60 km. With the gravity disturbance, they performed a density inver-  
3657 sion to recover the density of each prism. This spatially variable density was then  
3658 low-pass filtered, with a 50km cutoff. Incorporating this remaining long-wavelength  
3659 gravity signal within the density model removed the regional component from the  
3660 gravity input to the inversion. This technique is conceptually similar to high-pass  
3661 filtering the gravity data to remove the long-wavelength component. For the in-  
3662 version, Tinto et al. (2019) used the commercial software Geosoft Oasis Montaj.  
3663 Limited information is available from Geosoft as to the specifics of this inversion  
3664 procedure.

3665

3666 Comparing our bathymetry (Figure 4.17f), there is a normal distribution of dif-  
3667 ferences, centred on zero. The RMS difference between the two grids is  $\sim$ 100 m.  
3668 Comparing each grid to the constraint point depths, the BedMachine grid has an  
3669 RMS difference of 92 m, compared to our RMS of 44 m. Generally, our results  
3670 are approximately 50-100 m deeper proximal to most of the Siple Coast ground-  
3671 ing line. Conversely, our results are approximately 50-100 m shallower along the  
3672 Transantarctic Mountain front. This could be due to our inability to fully fix the  
3673 issue of overly-shallow interpolation of data along the mountain front in the creation  
3674 of our starting model, as discussed.

3675

3676 Alternatively, the differences could be a result of the different gravity reduction  
3677 steps. Figure 4.12b and e show that correcting the gravity disturbance for the terrain  
3678 mass effect results in a large negative topo-free disturbance along the Transantarctic  
3679 mountain front (dark blues in b). During the regional field estimation, fitting  
3680 a spline to these large negative values would bring down the nearby regional field,  
3681 resulting in an underestimation of the regional (more negative), and thus an over-  
3682 estimation of the residual (positive values). This is shown by the profile of Figure  
3683 4.12e. On the right side, along the mountain front, in an attempt to fit the negative  
3684 values of the topo-free disturbance (red dashed line), the regional field (blue) has  
3685 been underestimated, leaving a large positive residual anomaly (pink dashed). This  
3686 positive residual results in a shallowing of the inverted bathymetry.

3687

3688 These shallower depths along the mountain front, instead, could be revealing  
3689 a flaw in the constraint point minimization assumption of the residual being 0 at  
3690 constraints. While the constraint point itself doesn't contribute to the residual sig-  
3691 nal, since the actual bed is equal to the starting bed at those points, deviations  
3692 between the actual bed and the starting bed in the vicinity of the constraints may  
3693 lead to a non-zero residual at the constraint. In this case, the interpolation of the  
3694 regional field attempts to smoothly connect extremely negative values at the moun-  
3695 tain front, and high values at the nearby constraints. This high gradient leads to  
3696 poor interpolation. This can be seen in 4.12e where the regional (blue line) is force  
3697 exactly equal to the topo-free disturbance (red dashed line) at the constraint point  
3698 at 700 km along the profile. In reality, the residual gravity at that constraint is  
3699 likely non-zero. A non-zero value may allow the regional field to closer match the  
3700 large positive topo-free disturbance located at 720 km.

3701

3702 The remaining major differences between our results and BedMachine v3 in-  
3703 clude the same series of alternating NW-SE troughs and ridges as discussed above,  
3704 an  $\sim$ 100 m deeper region on the west side of Roosevelt Island, and a significantly  
3705 deeper ( $\sim$ 250 m) trough spanning from the south side of Minna Bluff to the outlet  
3706 of the Byrd Glacier. The deepest depths we model in this trough are  $\sim$  1350  $\pm$  100  
3707 m, located offshore of the Byrd Glacier Outlet. Preliminary results of a seismic  
3708 survey at Discovery Deep, just south of Minna Bluff (cyan line Figure 4.15), in the  
3709 2021/2022 field season report depths up to 1450 m (pers. comm. Prof. A. Gor-  
3710 man). These findings confirm the presence of depths of this magnitude. However,  
3711 our deepest location is approximately 100 km south of the Discovery Deep survey.  
3712 This seismic data was not included in this inversion. An additional comparison to  
3713 a seismic survey can be made proximal to the Kamb Ice Stream grounding zone

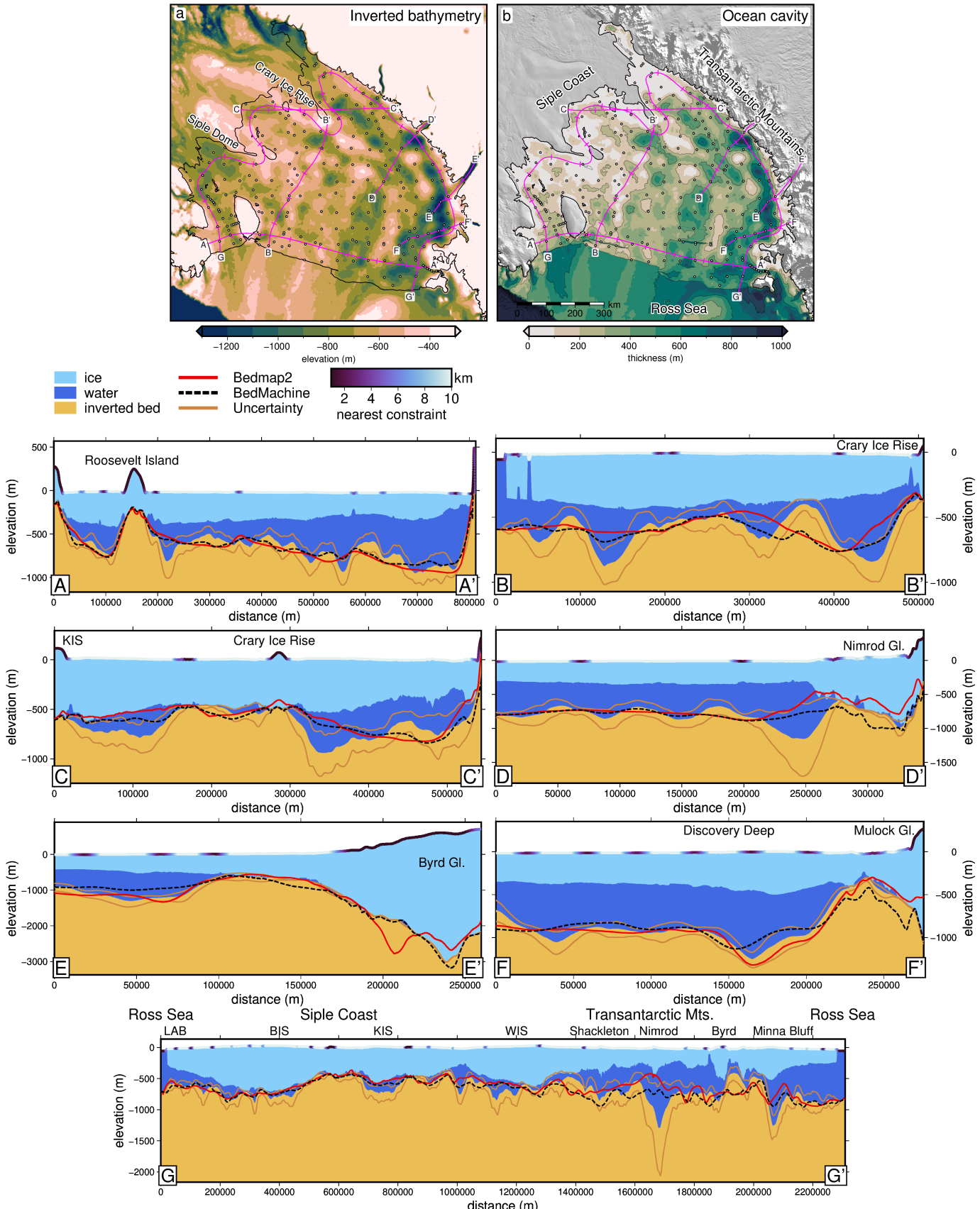


**Figure 4.18: Upper panel)** Ross Ice Shelf inverted bathymetry (left) and water column thickness (bed to ice base) relative to BedMachine v3 ice base (Morlighem, 2022). Pink lines show profile locations with ticks every ~100 km. Grounding line and coastline in black (Mouginot et al., 2017). Constraint points shown as dots. **Profiles A-G)** Various cross-sections showing the ice layer (light blue), water layer (darker blue), and bathymetry (yellow), with uncertainties (brown). Red and black lines show Bedmap2 and BedMachine v3 bathymetry, respectively. The colour of the ice surface indicates the distance to the nearest constraint. Legend and colourmap shown above profile A.

(cyan line Figure 4.15). Horgan et al. (2017) image bathymetry depths along a  $\sim 20$  km seismic survey with a mean depth of  $\sim 605$  m. Sampling our bathymetry and uncertainty along this profile yields a mean depth of  $\sim 608 \pm 45$  m, while sampling BedMachine v3 bathymetry and uncertainty yields a mean depth of  $\sim 572 \pm 79$  m.

Comparing the various difference maps of Figure 4.17 shows that our inversion has resulted in more varied topography across the ice shelf compared to Tinto et al. (2019). This increased amplitude is likely due to the differences in densities used between the inversions. Tinto et al. (2019) used a spatially variable density model, which ranged from  $\sim 2600 - 2800$  kg m $^{-3}$ , with a mean of  $\sim 2700$  kg m $^{-3}$ . While we used a spatially-constant density value, in the Monte Carlo analysis the density was varied between  $\sim 1800 - 3000$  kg m $^{-3}$ , with a mean of  $\sim 2400$  kg m $^{-3}$ . This  $\sim 300$  kg m $^{-3}$  difference between the mean density values would result in a more subdued inverted bathymetry from the (Tinto et al., 2019) model. While the Tinto et al. (2019) density model does a good job of removing the regional field prior to the inversion, whether or not the density values used are representative of the seafloor is questionable. The lowest values in their model of approximately 2600 kg m $^{-3}$  represent the upper end of sedimentary rock densities (Schön, 2015), and are significantly greater than expected densities of unconsolidated sediments. For a region with an expected continuous drape of seafloor sediments (Chapter 2, Tankersley et al., 2022), we believe the densities used in (Tinto et al., 2019) to be too high. This explanation for the differences between the inversion results is supported by the strong correlation between our bathymetry uncertainty resulting from the choice in density (Figure 4.16c) and the difference between the inversion results (Figure 4.17f). This shows the importance of picking a plausible density value, and the added benefit of testing many values to estimate the uncertainty related to the chosen density value.

3740

#### 3741 4.5.2.3 Ocean cavity comparison

3742 Due to the smoothness of the base of an ice shelf, relative to bathymetry, the water  
3743 column thickness beneath many ice shelves is predominately determined by the  
3744 bathymetry. We use BedMachine v3 ice base elevations and our updated bathymetry  
3745 to calculate the water column thickness beneath the Ross Ice Shelf and compare the  
3746 results to the water column thicknesses of Bedmap2 and BedMachine (Figure 4.19).  
3747 These differences are very similar to those described above, due to the smooth nature  
3748 of the ice base. Notable areas where our results show a thicker ocean cavity (within  
3749 uncertainty ranges) compared to past models include;

- 3750 1. Nearby the Kamb grounding zone ( $\sim 100 \pm 50$  m thicker, Figure 4.18c near  
3751 km 100).
- 3752 2. The west side of Crary Ice Rise ( $\sim 300 \pm 150$  m thicker, Figure 4.18c near km  
3753 350).
- 3754 3. The south side of Minna Bluff ( $\sim 300 \pm 200$  m thicker, Figure 4.18g near km  
3755 2100).
- 3756 4. The west side of Roosevelt Island ( $\sim 200 \pm 100$  m thicker, Figure 4.18a near  
3757 km 220)).

3758 Notable areas where our results show a thinner cavity include;

- 3759 1. The mountain front north of Byrd Glacier ( $\sim 300 \pm 50$  m thinner, Figure 4.18g  
 3760 near km 2000)).
- 3761 2. Three 50 km wide regions in the central ice shelf, which are up to  $200 \pm 50$  m  
 3762 thinner.
- 3763 3. Several points approximately 50 km off of the Transantarctic Mountain front  
 3764 which are up to  $400 \pm 50$  m thinner (Figure 4.18c near km 450).

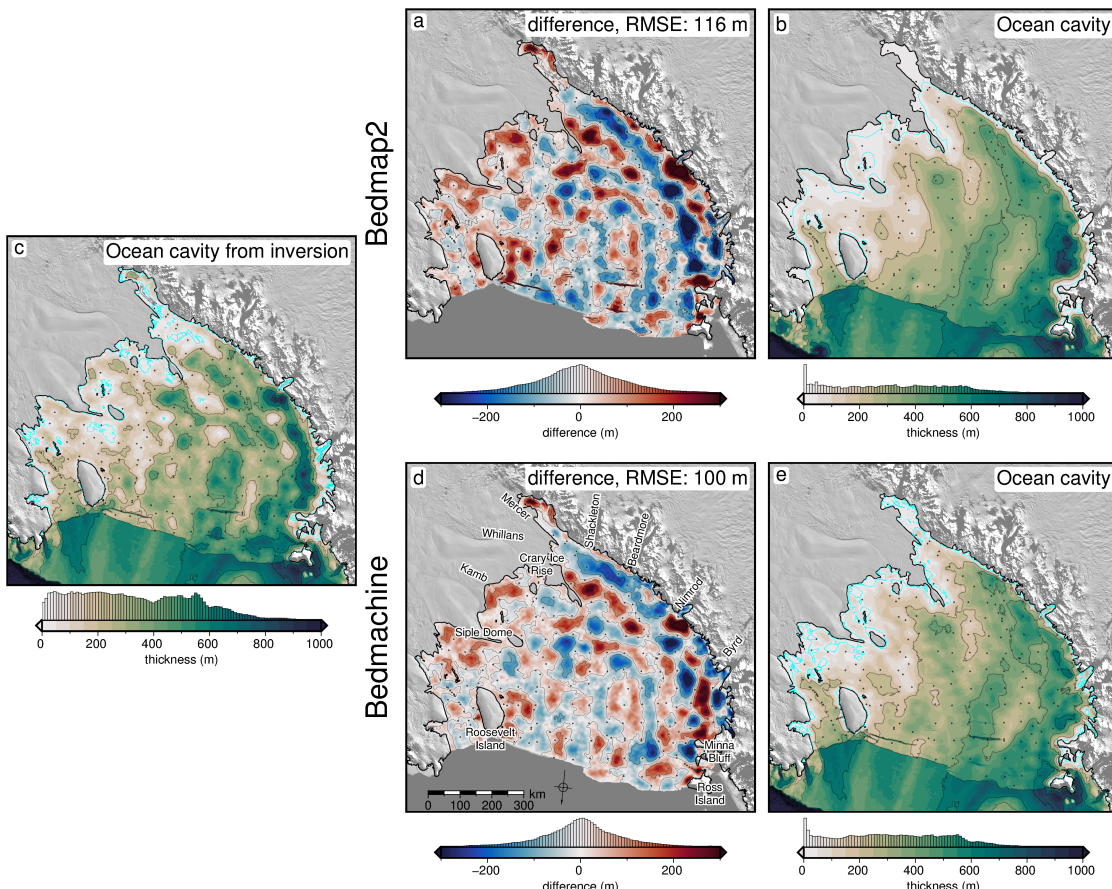


**Figure 4.19:** Comparison of our updated water column thickness with past models. **a)** Difference between our model and the water column thickness from Bedmap2, and **b)** the Bedmap2 water column thickness. **c)** Water column thickness calculated as the difference between BedMachine v3 icebase and our inverted bathymetry. **d)** Difference between our model and the water column thickness from BedMachine v3, and **e)** the BedMachine v3 water column thickness. Blue regions in the difference maps indicate where our results' water column is thinner, while red regions indicate where our results are thicker than the past models. Grounding line and coastline are shown in black (Morlighem, 2022). Background imagery is from Scambos et al. (2007). Water column thickness grids are contoured at 200 m intervals, and the 20 m contour is shown in bright blue. The difference grids are contoured at 100 m intervals. Water column thickness grids and difference grids share common colour scales.

### 3765 4.5.3 Implications

3766 Here, we discuss several of the important implications of our updated sub-RIS  
 3767 bathymetry. These implications relate to the stability of the Ross Ice Shelf, ge-  
 3768 ology, and tectonics.

**3769 4.5.3.1 New pinning points**

3770 We have identified several areas of thin water column thickness (< 20 m) with our  
3771 updated results beneath the Ross Ice Shelf. These areas are shown by the 20 m  
3772 water column thickness contour, in bright blue in Figure 4.19a. These include a  
3773 ~100x100 km region SW of Roosevelt Island, several ~50x50 km regions on the  
3774 north flank of Crary Ice Rise (Figure 4.18g at km ~ 900), and a widespread region  
3775 south of Crary Ice Rise (Figure 4.18g at km ~ 1350). Thin water depths south of  
3776 Crary Ice Rise have also been modelled by a local gravity survey along the Whillans  
3777 Ice Stream grounding zone (Muto et al., 2013b). Additionally, two smaller regions  
3778 of sub-20 m water column thickness are found nearer the centre of the ice shelf. One  
3779 is approximately 100 km off the point of Crary Ice Rise and is ~ 400 km<sup>2</sup> (Figure  
3780 4.18c at km ~ 200). The second is ~ 200 km north of Crary Ice Rise and is slightly  
3781 smaller (Figure 4.18b at km ~ 350). None of these shallow water column regions are  
3782 present in either of the past models. Interestingly, these regions coincide with some  
3783 of the lowest uncertainties we report ~ 20 m. A portion of this low uncertainty may  
3784 be related to the inversion constraining the bathymetry to the ice base, which in  
3785 regions of thin water column will reduce the variability of the suite of inversions in  
3786 the Monte Carlo simulation which were used to define the uncertainty.

3787

3788 These new-identified shallow regions highlight where the Ross Ice Shelf was likely  
3789 grounded in the recent past, or could likely become re-grounded in the future. While  
3790 some of these regions are small, analysis of pinning points on the Ross Ice Shelf has  
3791 shown some of the smallest pinning points can create the largest effective resistance  
3792 on the ice shelf (Still et al., 2019). Additionally, some of these locations (north side  
3793 of Crary Ice Rise) are predicted to have on the order of 1 m/yr of basal accretion  
3794 (Adusumilli et al., 2020). An already thickening shelf within ~20 m of the bed will  
3795 likely affect the ice sheet dynamics as part of future projections of the ice shelf. In-  
3796 corporation of these localities of likely past pinning points may aid in resolving the  
3797 ongoing debate of the style of grounding line retreat and readvance of the Ross Ice  
3798 Shelf throughout the Holocene (Kingslake et al., 2018; Lowry et al., 2019; Venturelli  
3799 et al., 2020).

3800

**3801 4.5.3.2 Basal melting**

3802 Our updated bathymetry, water column thickness, and uncertainty maps provide  
3803 additional information vital to understanding the distribution of basal melt beneath  
3804 the ice shelf. Melt beneath the Ross Ice Shelf is thought to predominantly occur  
3805 1) along the ice front, where Antarctic Surface Water causes rapid melting in the  
3806 summer (Figure 4.20 Horgan et al., 2011; Moholdt et al., 2014), and along the deep  
3807 grounding zones of the Transantarctic Mountain front, where contact with High  
3808 Salinity Shelf Water induces melting (Figure 4.20b Adusumilli et al., 2020; Tinto  
3809 et al., 2019). Throughout the centre of the ice shelf are zones of refreezing (Figure  
3810 4.20 Adusumilli et al., 2020; Das et al., 2020). Overall basal melting of the Ross Ice  
3811 Shelf is thought to be low compared to other shelves due to the blocking of warm  
3812 Circumpolar Deep Water from entering the cavity. This blocking is from a layer of  
3813 dense High Salinity Shelf Water (Dinniman et al., 2011; Tinto et al., 2019). The  
3814 Hayes Bank (Figure 4.1b) has been identified as one location where the Circumpolar  
3815 Deep Water is able to penetrate the ice shelf cavity and induce melting, but this

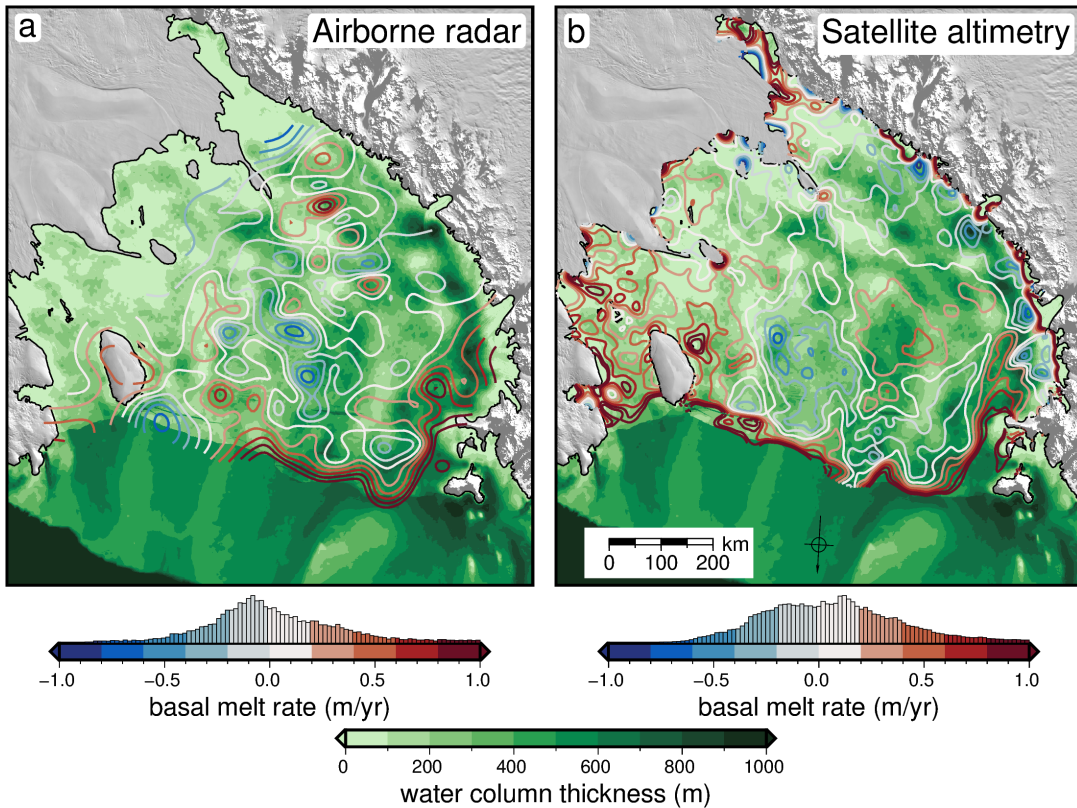


**Figure 4.20:** Basal melt rate and water column thickness compared for the Ross Ice Shelf. **a)** Blue to red contours show interpolated basal melt rate from Das et al. (2020) derived from ROSETTA-ice airborne ice-penetrating radar. Background shows water column thickness from this study. **b)** Same as **a** but with basal melt rate from Adusumilli et al. (2020) derived from satellite altimetry. Black line is the grounding line from Mouginot et al. (2017). Background imagery is from MODIS-MOA (Scambos et al., 2007).

penetration is thought to be limited to the region near Roosevelt Island (Das et al., 2020; Tinto et al., 2019). Our ocean cavity is  $\sim 100$  m thicker than Tinto et al. (2019) immediately to the west of Roosevelt Island (Figures 4.18a and 4.19d). This region should be investigated with sub-shelf circulation models using our updated bathymetry. Our larger cavity allowing the inflow of warm Circumpolar Deep Water beyond Roosevelt Island could help explain the relatively large basal melt rate found in the region as shown by satellite altimetry (Figure 4.20b).

3823

The high melt rates measured along the Transantarctic Mountain front (Adusumilli et al., 2020) are caused by the inflow of High Salinity Shelf Water (Tinto et al., 2019). This water is thought to be guided by bathymetric troughs and is able to induce melting only at large depths, due to the pressure suppression of the melting temperature of ice. Figures 4.20 show a comparison of both airborne radar and satellite altimetry-derived basal melt rates to the updated water column thickness resulting from our bathymetry inversion. The deeper bathymetry proximal to the Transantarctic Mountain front found in both our inversion and (Tinto et al., 2019), compared to the depths of Bedmap2, help explain the high melt rates measured there. The other locations we report with deeper bathymetry near grounding zones, such as the south side of Minna Bluff, and the far southern end of the ice shelf, at the Mercer Ice Stream grounding zone, may be potential locations where High Salinity Shelf Water is able to induce basal melt. Additionally, some of the very shallow

water column thicknesses (< 20m) we find (Figure 4.19c), for instance to the south of Crary Ice Rise, correspond with low basal melt rates (Figure 4.20). This may be due to the lack of stratification in the water column, which occurs due to tidal mixing possible only in thin water columns (Holland, 2008; Muto et al., 2013b).

#### 4.5.3.3 Geologic and tectonic significance

While there are many interesting implications to explore in this new dataset, we limit our discussion to several sub-Ross Ice Shelf bathymetric features of possible importance to solid-Earth investigations. These features include the bathymetry along the Transantarctic Mountain front, a deep feature on the southwest flank of Crary Ice Rise, and a newly identified orientation of bathymetry features, aligned with the Siple Coast ice streams.

#### Transantarctic Mountain front

The Transantarctic Mountains (Figure 4.1a) make up the world's largest rift shoulder. Despite their prominence, the uplift mechanisms are still debated (Goodge, 2020). It is likely that these mechanisms vary along-strike, and consist of some combination of thermal, flexural, or isostatic support (Goodge, 2020). For the central TAM, a mechanism of cantilevered flexure is proposed for the uplift of the mountains (Wannamaker et al., 2017; Yamasaki et al., 2008). This theoretically should be accompanied by a deep trough parallel just offshore the range front, and an outer bathymetric high, approximately 200 km from the range front (Stern & ten Brink, 1989). These features have not yet been observed (ten Brink et al., 1993; Wannamaker et al., 2017). Our results show a deep trough along the range front between the Nimrod Glacier and Minna Bluff, with bathymetry highs further offshore. These features may support the theory of flexural uplift along this portion of the TAM (Wannamaker et al., 2017). Further south, where the trough disappears, the mechanism of flexural uplift is not required, since the mountains have a crustal root, which likely provides the uplift mechanism, via Airy isostasy (Block et al., 2009; Wannamaker et al., 2017).

#### Fault bound Crary Ice Rise

Figure 4.18c shows a profile of the updated bathymetry model across the Crary Ice Rise. Our results show a steep drop off the south flank of the ice rise (at km  $\sim$  320), to depths up to  $\sim 1000 \pm 200$  m. This steep drop-off is aligned with an NW-SE fault proposed by Muto et al. (2013b) from a local gravity survey along the Whillan Ice Stream grounding zone. Depth to basement analysis from magnetic data (Chapter 2, Tankersley et al., 2022) also highlights this north flank of Crary Ice Rise as a likely location for faults. We believe this steep bathymetry feature adds evidence to the proposition of the Crary Ice Rise as a fault-bound horst (Muto et al., 2013b). This would imply the current grounding of the Ross Ice Shelf along the Crary Ice Rise is in part controlled by regional tectonics.

#### New bathymetric trend

From the gridding of point data, the bathymetry of the central Ross Ice Shelf is dominated by an N-S - NNE-SSW trend, aligned with the flow directions of the outlet glaciers of the Transantarctic Mountains (Figure 4.1). Our updated bathymetry model (Figure 4.15a) adds an overprinted NW-SE trend to the bathymetry features

of the central portion of the ice shelf. This trend is prevalent, but subtle, in the inversion of Tinto et al. (2019). The features comprising this trend are a series of 2-3 ridges and troughs of  $\sim 100$  m amplitudes and  $\sim 50$  km wavelengths, as shown in Figure 4.18d. These features are oblique to flight lines, adding to their validity, and are well-aligned with the Crary Ice Rise and the general ice flow direction of the Siple Coast ice streams. This trend could signify several things; 1) the most recently grounded ice in this region had a flow direction aligned with the Siple Coast ice streams, leaving behind erosional or depositional features with these orientations, 2) these features are tectonic in origin, and are the surface expressions of rift structures. These structures overprint the large bathymetric depression which runs from the Nimrod glacier to the calving front. If these are features left behind from the most recent grounding line retreat, they might inform the style of retreat. As seen in the Ross Sea, physiography of the sea floor exerts the primary control on ice stream flow and the patterns of retreat (Halberstadt et al., 2016).

## 4.6 Conclusion

Here we present an updated model of bathymetry depths beneath Antarctica's Ross Ice Shelf, as modelled from airborne gravity data. Our inversion algorithm provides a comprehensive spatial uncertainty analysis and parameter sensitivity estimation. This uncertainty highlights regions of high uncertainty that would benefit from additional seismic constraints. These regions include the entire Transantarctic Mountain front and two points near the centre of the shelf which are up to 40 km from the nearest constraints. We summarize some key findings from the research below;

1. Monte Carlo sampling is a robust method of uncertainty quantification and parameter sensitivity analysis for bathymetric gravity inversions.
2. Sensitivity analysis shows that gravity data is the largest contributor to bathymetry uncertainty, followed by assumptions of the geology of the region.
3. Our updated bathymetry model better matches *a priori* sub-ice shelf measurements compared to past models.
4. Compared to Bedmap2, our results are deeper proximal to the grounding line and shallower along the ice front.
5. Differences with the inversion of Tinto et al. (2019) (BedMachine v3) are mostly due to different chosen density contrasts.
6. Newly identified potential past pinning points are found along the Siple Coast and in the central Ross Ice Shelf.
7. Thick ocean cavity is found along the west flank of Roosevelt Island, where Circumpolar Deep Water flows under the shelf and may highlight a region of importance for ocean circulation modelling.
8. Possible tectonic implications including a fault-bound Crary Ice Rise and a flexural trough associated with Transantarctic Mountain uplift.

Our results provide the datasets necessary to begin answering key questions regarding the role of the Ross Ice Shelf in various components of the Earth system. These questions include; 1) where are melt-inducing bodies of water guided beneath the ice shelf? 2) where was the ice shelf grounded in the recent past, and what was the geometry of Holocene grounding line retreat and re-advance? Are the modern bathymetry features remnants of the last grounding line retreat, or are they tectonic in origin? While we don't provide direct answers to these questions, without adequate knowledge of the sea floor morphology and the associated uncertainties, investigators won't have the relevant boundary conditions to answer these questions. All of the research conducted here is published as open-source Python code (see Chapter 1 Section 1.6), with hopes that the methods presented here can be used by researchers to better model the bathymetry and uncertainty of other Antarctic ice shelves.



<sup>3933</sup> Chapter 5

<sup>3934</sup> Synthesis

<sup>3935</sup> Improving decadal to centennial projections of global sea level rise is of utmost im-  
<sup>3936</sup> portance for mitigating future environment and socio-economic impacts (Durand  
<sup>3937</sup> et al., 2022). Antarctica's projected contributions to global sea level rise by the  
<sup>3938</sup> end of the century under a high-emission scenario is between 0.03 and 0.28 m (RCP  
<sup>3939</sup> 8.5, Intergovernmental Panel on Climate Change (IPCC), 2022). This wide range  
<sup>3940</sup> of possible values expresses the uncertainty of the Antarctic Ice Sheet's response to  
<sup>3941</sup> a warming world. Over 80% of ice loss from Antarctica occurs through ice shelves  
<sup>3942</sup> (Rignot et al., 2013), highlighting their importance in reducing the uncertainty in  
<sup>3943</sup> sea level rise projections. Antarctica's largest ice shelf, the Ross Ice Shelf, is fed  
<sup>3944</sup> from both the East and West Antarctic Ice Sheets. Its catchment contains a total  
<sup>3945</sup> volume of ice equivalent to 11.6 m of global sea level rise (Fretwell et al., 2013;  
<sup>3946</sup> Rignot et al., 2011; Tinto et al., 2019). While the Ross Ice Shelf is relatively stable  
<sup>3947</sup> currently (Moholdt et al., 2014; Rignot et al., 2013), geologic evidence shows the  
<sup>3948</sup> rapid destabilization of the ice shelf within the past ~7,000 years (e.g., Naish et al.,  
<sup>3949</sup> 2009; Venturelli et al., 2020).

<sup>3950</sup>  
<sup>3951</sup> The destabilization of the ice shelf is thought to have been primarily caused  
<sup>3952</sup> by ocean forcings (Lowry et al., 2019), as bathymetric troughs guide the inflow of  
<sup>3953</sup> melt-inducing ocean circulations (Tinto et al., 2019). The subsequent grounding  
<sup>3954</sup> line retreat however is predominantly controlled by the physiography, geology, and  
<sup>3955</sup> glaciological feedbacks (Halberstadt et al., 2016). This highlights the solid earth,  
<sup>3956</sup> through its bathymetric control on basal melt and its effects on grounding line re-  
<sup>3957</sup> treat dynamics, as an important component of the dynamics of the Ross Ice Shelf.  
<sup>3958</sup> To reliably understand the contribution of the Ross Ice Shelf to future sea level rise,  
<sup>3959</sup> we must provide ocean and ice modellers with the necessary geologic boundary con-  
<sup>3960</sup> ditions. This thesis aimed to provide both these boundary conditions and estimates  
<sup>3961</sup> of their uncertainties to the modelling community. A series of research questions  
<sup>3962</sup> were proposed; as restated below:

- <sup>3963</sup> 1. What is the geologic structure of the upper crust beneath the Ross Ice Shelf?  
<sup>3964</sup> If there are sediments, what is their thickness and distribution? Where are  
<sup>3965</sup> the major faults likely located?
- <sup>3966</sup> 2. How can bathymetry beneath an ice shelf best be modelled? Are there further  
<sup>3967</sup> improvements that can be made to the gravity-inversion process? What are  
<sup>3968</sup> the predominant sources of uncertainty, and how can these be limited?

- 3969     3. How deep is the bathymetry beneath the Ross Ice Shelf and where are we most  
3970        and least certain about it?
- 3971     4. What are the geologic controls on the Ross Ice Shelf's stability?

3972        Here we draw from the various research chapters to provide answers to these  
3973        questions.

## 3974     5.1 Investigating geologic structures

### 3975     Research question 1

3976     To address research question 1 we sought to model the depth of the crystalline base-  
3977        ment rock beneath the ice shelf. We accomplished this with a depth-to-magnetic  
3978        source technique, which used airborne magnetic data and was calibrated to seismi-  
3979        cally imaged basement depths of the Ross Sea. Our resulting basement topography  
3980        revealed large-scale, fault-controlled extensional basins throughout the sub-Ross Ice  
3981        Shelf crust (Figure 5.1f). Above this basement sits various sediments, likely rang-  
3982        ing from coherent sedimentary rock to unconsolidated recent glacial and marine  
3983        deposits. While there is a continuous drape of sediments across the entire ice shelf,  
3984        we also image several distinct depocenters; the Western Ross Basin, covering the  
3985        East Antarctic half of the ice shelf, and several basins on the West Antarctic side,  
3986        including the Siple Dome Basin and the Crary Trough (Figure 5.1f). These results  
3987        were incorporated into an Antarctic-wide review of sedimentary basins (Figure 5.1a  
3988        Aitken et al., 2023b), showing the widespread distribution of similar basins across  
3989        much of Antarctica. From our findings, we were able to draw a wide range of imp-  
3990        lications, ranging from tectonic influence on ice dynamics along the Siple Coast to  
3991        the buried and subsided remnants of an above-sea-level Oligocene mountain range,  
3992        which likely accommodated alpine glaciers. These results provided the first view of  
3993        the upper crust beneath the entirety of the Ross Ice Shelf.

3994

## 3995     5.2 Developing a gravity inversion

### 3996     Research question 2

3997     To provide modellers with accurate bathymetry depths beneath the Ross Ice Shelf,  
3998        we utilized a gravity inversion technique. While there is an existing gravity-inverted  
3999        bathymetry model for the Ross Ice Shelf (Tinto et al., 2019), the reported uncertain-  
4000        ties were spatially uniform. To provide spatial uncertainties, we chose to develop  
4001        a new gravity inversion algorithm. In addition, since the majority of gravity inver-  
4002        sions use proprietary and expensive software, in an effort towards open-source and  
4003        reproducible science, we chose to develop our gravity inversion using Python and  
4004        release the code in an online repository.

4005

4006        Chapter 3 described this algorithm in detail. Extensive testing of various syn-  
4007        thetic and semi-realistic datasets revealed several intricacies of performing a gravity  
4008        inversion to attain a bathymetry model. The estimation and removal of the regional  
4009        component of gravity, which occurs in the data reduction steps before the inversion,  
4010        accounts for the majority of the error in the model. There are various techniques to

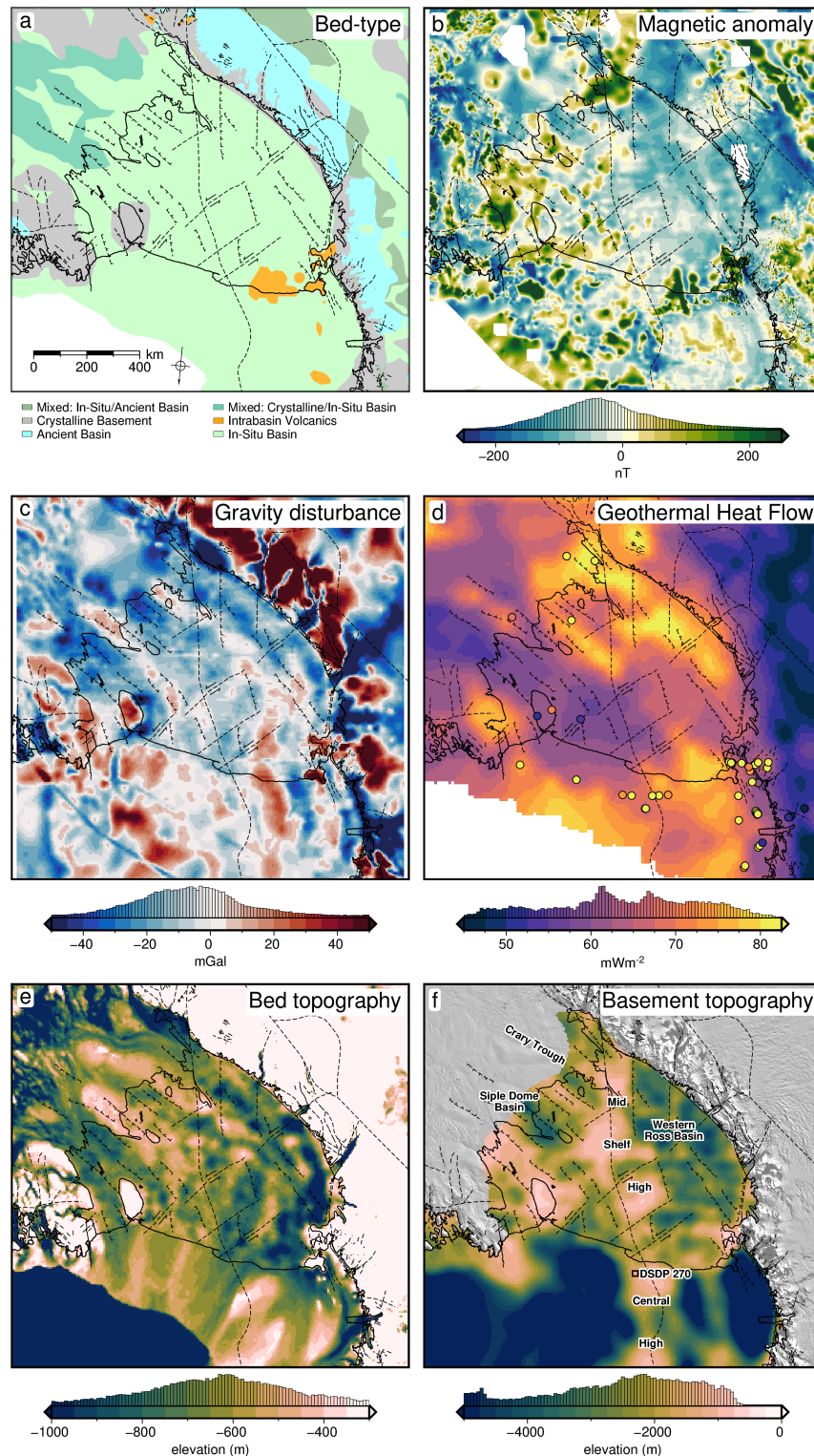


**Figure 5.1:** Summary of southern Ross Embayment geophysical and geologic information. **a)** Generalized geologic classification of the bed from Aitken et al. (2023a), **b)** ROSETTA-Ice airborne magnetic anomalies (Tinto et al., 2019) merged with ADMAP2 magnetic anomaly compilation (Golynsky et al., 2018), **c)** Gravity disturbance compilation from Forsberg (2020), include ROSETTA-Ice data. **d)** Geothermal heat flux from a seismically-derived model (Shen et al., 2020), and point measurements compiled from Burton-Johnson et al. (2020). **e)** Inverted bathymetry from Chapter 4, **f)** Basement topography from Chapter 2. Solid black line shows the grounding line and ice front from Mouginot et al. (2017). Fainter black lines show inferred (dashed) and exposed (solid) faults from a combination of Chapter 2 and Cox et al. (2023). Background imagery in **f** from MODIS-MOA (Scambos et al., 2007).

remove the regional field. We explore several of these methods and provide recommendations to best reduce the errors. Our uncertainty analysis highlighted regions of either steep topography or high gradient gravity anomalies as key regions where additional bathymetry measurements will make a significant contribution to reducing uncertainties. These suggestions of where to collect additional data should be considered alongside key regions of investigation identified through ocean modelling. Our findings suggest the quantity of bathymetry measurements is more important for reducing inversion uncertainty than the quality of these measurements. Conversely, we show larger sensitivity of the inversion results to the noise in the gravity data, relative to the density of gravity data collected. This suggests optimizing quantity over quality for bathymetry constraints while optimizing quality over quantity for gravity observation data. We hope these suggestions are able to better inform future Antarctic data collection for the goal of improving sub-ice shelf bathymetry models.

4024

As part of Chapter 4, we compared our methods, of both the gravity reduction process and the inversion procedure, to all past bathymetry models conducted in Antarctica, as well as several from Greenland. Several other inversions have used a regional separation method similar to ours, however, none of these have provided an assessment of the associated uncertainties related to this method, which we found to be significant. We also found that all other inversions utilized a non-rigorous method of correcting the gravity data for the effects of ice, water, and topography. While the error introduced is likely small, with modern computing, applying this correction correctly is trivial.

4034

From the other studies, excluding those with undocumented inversion algorithms, we found only one study which used a conventional regularized least-squares approach, similar to ours. Comparing our uncertainty analysis to past inversions revealed only two studies that report spatially variable uncertainties of their bathymetry model. It is our hope that the improvements made for the gravity inversion process are incorporated in future inversions in order to attain better estimates of uncertainties.

4042

## 5.3 Modelling Ross Ice Shelf Bathymetry

### Research question 3

With the gravity inversion methodology laid out in Chapter 3, we created a new model of sub-Ross Ice Shelf bathymetry (Figure 5.1e). This model highlighted some important differences from past bathymetry models. In general, our model has more varied topography, compared to the smooth Bedmap2 model, and the intermediate BedMachine model. Compared to Bedmap2, we report significantly deeper bathymetry proximal to the entire grounding zone, including notably deeper areas near the Kamb Ice Stream, along the west side of Roosevelt Island, and south of Minna Bluff. Compared to the past inverted bathymetry (Tinto et al., 2019), our results are deeper along the Siple Coast but vary between deeper and shallower along the Transantarctic Mountain front. Our uncertainty analysis identified gravity data quality as the largest component of the overall uncertainty, while the distance from the nearest constraint and interpolation parameter values contributed significantly

4057 to the spatial variability of the uncertainty. From this, the largest uncertainties were  
4058 found either far from constraints, or along the steep topography of the Transantarctic  
4059 Mountains. This highlighted several locations where future seismic surveys would  
4060 be able to effectively reduce uncertainties.

## 4061 5.4 Geologic controls on Ross Ice Shelf Stability

### 4062 Research question 4

4063 Next, we synthesize our findings which relate to the geologic influence on the Ross  
4064 Ice Shelf, in an attempt to answer research question 4. We start with the controls  
4065 on the ice shelf as it is today, before speculating on what these geologic controls  
4066 were in the past or will be in the future.

#### 4067 5.4.1 Present controls

##### 4068 5.4.1.1 Basal melt

4069 Basal mass loss of the Ross Ice Shelf is dominated at the deep grounding zones,  
4070 where relatively cool High Salinity Shelf Water is able to induce melting due to the  
4071 high pressure at depth (Adusumilli et al., 2020; Tinto et al., 2019). These inflows of  
4072 cold and dense water occur along the seafloor and are guided south beneath the ice  
4073 shelf by bathymetric features (Holland, 2008). Tinto et al. (2019) model the domi-  
4074 nant inflow of High Salinity Shelf Water starting near Ross Island, flowing south  
4075 along the mountain front, where at the southern flank of Crary Ice Rise the flow  
4076 turns north and flows back to the ice front through the centre of the ice shelf. This  
4077 inflow is responsible for much of the basal melting of the Ross Ice Shelf (Adusumilli  
4078 et al., 2020; Tinto et al., 2019). Our bathymetry model (Figure 5.1e) confirms the  
4079 presence of a deep trough ranging from the western ice front along the Transantarctic  
4080 Mountain front which accommodates this High Salinity Shelf Water inflow. Our  
4081 mountain front trough however is both narrower and deeper than past models. At  
4082 the Nimrod Glacier outlet our trough steps to the east by ~ 100km, and eventually  
4083 ends along the south flank of Crary Ice Rise.

4084  
4085 This eastward step is likely important for two reasons. 1) South of Nimrod  
4086 Glacier, we model a shallow bathymetric shelf proximal to the grounding line. This  
4087 likely blocks grounding line access to southward flowing High Salinity Shelf Water,  
4088 limiting basal melt for the southernmost outlet glaciers. 2) The eastward step likely  
4089 re-directs southward flowing High Salinity Shelf Water closer to the Siple Coast  
4090 grounding zone, particularly the south flank of Crary Ice Rise. In this region, past  
4091 bathymetry models show a continuous bathymetric ridge for ~ 300 km off the edge  
4092 of Crary Ice Rise which blocks the inflow of High Salinity Shelf Water to the Siple  
4093 Coast north of Crary Ice Rise (Tinto et al., 2019). Our results however show this  
4094 ridge being dissected by two low saddles. If included in ocean circulation models,  
4095 the lack of a continuous ridge and the presence of these low saddles may allow the  
4096 inflow of circulations to the Siple Coast; a scenario which should be further explored.

4097  
4098 The Hayes Bank, to the west of Roosevelt Island, has been identified as the  
4099 primary location of inflow of warm Circumpolar Deep Water (Das et al., 2020;

4100 Tinto et al., 2019). We model a region of deeper-than-previously seen bathymetry  
 4101 along the west edge of Roosevelt Island and propose this as a location that may  
 4102 allow the incursion of this ocean water with a high potential for melt. Additionally,  
 4103 along the Shirase Coast, south of Roosevelt Island, we model a thicker ocean cavity  
 4104 than past estimates. This may allow further penetration of water which enters the  
 4105 shelf near Hayes Bank. To address these highlighted regions of importance for basal  
 4106 melt, future ocean circulation models should incorporate our bathymetry model.  
 4107 Further, to test the sensitivity of sub-shelf circulations to bathymetry, the upper  
 4108 and lower bounds of uncertainty should be used in separate circulation models to  
 4109 test the range of possible sub-shelf circulations.

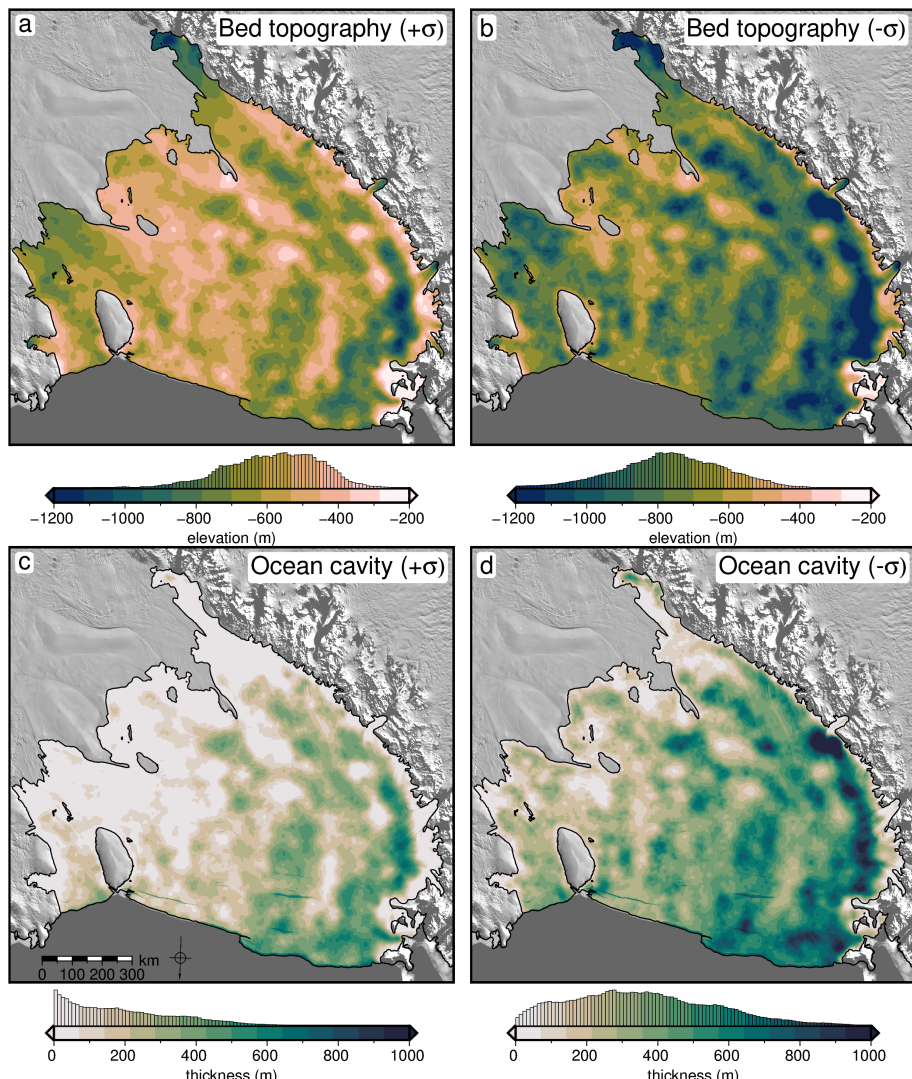


**Figure 5.2:** Lower and upper uncertainty bounds of Ross Ice Shelf bathymetry and ocean cavity thickness. **a)** Upper bathymetry uncertainty bound, **b)** lower bathymetry uncertainty bound, **c)** upper ocean cavity uncertainty bound, **d)** lower ocean cavity uncertainty bound.

#### 4110 5.4.1.2 Modern pinning points

4111 Analysis of Ross Ice Shelf's pinning points has shown that the effective resistance as  
 4112 well as the temporal persistence of pinning points are not tied solely to their size, but  
 4113 are strongly influenced by the competency of the bedrock (Still et al., 2019; Still &  
 4114 Hulbe, 2021). A really small pinning points which exert large effective resistance are

assumed to be grounded on bed with a high friction coefficient, while large pinning points which exert only minor resistance are assumed to be grounded on an easily deformable substrate. Based on the ratio of area to effective resistance, Still et al. (2019) suggested the bed beneath the Shirase Coast Ice Rumples, to the south-east of Roosevelt Island (Figure 5.3), is likely composed of competent bedrock with a high friction coefficient. Conversely, they suggest pinning point #14, just north of Crary Ice Rise, to be grounded on easily deformable till. The downstream extent of streaklines from pinning points provides an estimate of the temporal persistence of these features. Based on these streaklines, the Shirase Coast Ice Rumples and the Crary Ice Rise have likely been grounded for hundreds of years, while the large Steershead Ice Rise, just west of Siple Dome, only became grounded within the last 400 years (Fahnstock et al., 2000; Still et al., 2019).

4127

#### 4128 Persistent pinning points

4129 Our basement and sediment thickness results provide support for many of these  
4130 observations of ice dynamics. The Shirase Coast Ice Rumples, predicted to have  
4131 been long-lasting and grounded on competent bedrock, are shown in our basement  
4132 results to sit upon a large basement high, with thin sedimentary cover. This implies  
4133 both that the bedrock beneath the pinning point is either crystalline basement, or  
4134 very coarse sediment from minimally re-worked basement material, and that the  
4135 elevation of the bed is stable. This stability is likely due to both the tectonic nature  
4136 of the bed as a fault-bound horst, and the higher strength of the bedrock, able to  
4137 resist erosion by the overriding ice. Similarly, the persistence of Crary Ice Rise in  
4138 the glaciologic record may be owed to its location above a basement ridge. Of the  
4139 areas of possible recent grounding we identified, the region to the south of Crary Ice  
4140 Rise, and the smaller area  $\sim$  200 km north of Crary Ice Rise, both are located on  
4141 similar large basement highs with thin sedimentary cover. When grounded, these  
4142 past pinning points likely imparted a large effective resistance on the overriding ice.

4143

#### 4144 Recent pinning points

4145 The predicted deformable substrate of both Steershead Ice Rise and pinning point  
4146 #14 (Still et al., 2019), as well as the recent grounding of Steershead Ice Rise  
4147 (Fahnstock et al., 2000), are supported by our observations of these features being  
4148 located over thick fault-bound sedimentary basins. These thick sediments provide  
4149 material that is easily weathered into glacial till by the overriding ice, which lowers  
4150 the effective resistance of the pinning point. If the basin bounding faults we predicted  
4151 in Chapter 2 are truly active, they could accommodate local vertical bed movements  
4152 associated with glacial isostatic adjustment following changing ice loads (Peltier et  
4153 al., 2022; Steffen et al., 2021). For the very low-viscosity upper mantle and thin  
4154 lithosphere beneath West Antarctica (Chen et al., 2018; Pappa et al., 2019), these  
4155 solid earth responses to changing ice thickness may occur on decadal timescales  
4156 (Barletta et al., 2018). This may help explain the short-lived history of these pinning  
4157 points. One of the possible recent pinning points we identified is within the same  
4158 sedimentary basin as Steershead Ice Rise (between Steershead Ice Rise and Roosevelt  
4159 Island), and when grounded, likely shared these qualities. With these observations,  
4160 we support the notion of a strong geologic control on the buttressing ability and  
4161 persistence of pinning points throughout the Ross Ice Shelf. As the West Antarctic

4162 Ice Sheet thins, swift glacial isostatic rebound may lead to re-grounding; a response  
4163 which may promote stability of the ice sheet (Barletta et al., 2018; Coulon et al.,  
4164 2021; Kachuck et al., 2020). Accurate bathymetry beneath the Ross Ice Shelf is  
4165 vital for knowing where this re-grounding may occur, and thus where new pinning  
4166 points will develop.

4167 **5.4.1.3 Sediment distribution**

4168 The dynamics of Siple Coast ice streams are intrinsically tied to the bed which  
4169 they flow over. The presence of sediments and sedimentary basins allows for several  
4170 mechanisms to achieve the fast flow seen in these ice streams. 1) The sediments are  
4171 able to deform in response to the shear stress of the overriding ice, allowing faster  
4172 flow (Alley et al., 1986), 2) groundwater stored within the sedimentary basins both  
4173 lubricates the ice base, reducing basal friction and increases till deformation, through  
4174 increased pore-fluid pressure (Tulaczyk et al., 2000). Our results of Chapter 2 show  
4175 a continuous drape of sediments across the ice shelf including along the Siple Coast  
4176 grounding zone. The presence of these sediments helps explain the fast-flowing ice  
4177 along this region. Additionally, we image several large sediment basins beneath the  
4178 Siple Coast (Figure 5.1f). The groundwater storage capabilities of such basins could  
4179 provide up to half of the groundwater in the subglacial system of West Antarctica  
4180 (Christoffersen et al., 2014). The southernmost of these sedimentary basins has been  
4181 confirmed by a recent magnetotelluric survey, which identified >1 km of sediments  
4182 with extensive groundwater storage (Gustafson et al., 2022). The other two basins  
4183 we imaged, the Siple Dome Basin, and the Crary Trough (Figure 5.3), could be key  
4184 drivers on subglacial hydrology beneath the Siple Coast.

4185 **5.4.1.4 Geothermal heat flux at Siple Coast**

4186 **Spatial control on geothermal heat**

4187 The last main geologic control on Ross Ice Shelf stability we propose is the distribu-  
4188 tion of geothermal heat along the Siple Coast (Figure 5.1d). Geothermal heat flux  
4189 is one of the least constrained boundary conditions for Antarctica (Larour et al.,  
4190 2012; Pollard et al., 2005; Seroussi et al., 2017). High geothermal heat supplied to  
4191 the ice base can accelerate flow by 1) increasing englacial temperatures, reducing ice  
4192 viscosity, 2) increasing basal lubrication through meltwater production and 3) in-  
4193 creasing the ability of subglacial tills to deform, through water-saturation (Golledge  
4194 et al., 2014; Pollard et al., 2005). While we don't provide any direct measurements  
4195 of geothermal heat flux, our fault-bound sedimentary basins along the Siple Coast  
4196 provide important insights into the temporal and spatial variability expected for  
4197 geothermal heat flux along the Siple Coast.

4198  
4199 Measurements and predictions of geothermal heat flux along the Siple Coast are  
4200 shown to vary significantly, even between nearby (within ~ 100 km) measurements  
4201 (Figure 5.1d, Begeman et al., 2017; Fox Maule et al., 2005). This high spatial  
4202 variability is attributed to the localization of heat due to upper crustal structures  
4203 (Begeman et al., 2017). Faults and basement margins act as efficient fluid conduits,  
4204 which can localize the already regionally elevated heat (e.g., Burton-Johnson et al.,  
4205 2020; Fox Maule et al., 2005), resulting in vastly enhanced heat flow to the ice  
4206 base (Gooch et al., 2016), which is likely the cause of the anomalously high heat

4207 flow measured at Subglacial Lake Whillans ( $285 \text{ mW/m}^2$ , Fisher et al., 2015). We  
4208 hypothesized in Chapter 2 that these faults not only provide a spatial control on  
4209 geothermal heat flux, but a temporal control as well.

4210

#### 4211 Temporal control on geothermal heat

4212 As ice thickness has varied throughout the Holocene, the changing ice overburden  
4213 pressure on the subglacial sediments drives the discharge and recharge of these sedi-  
4214 mentary aquifers (Gooch et al., 2016; Li et al., 2022). This fluid movement is  
4215 accommodated along fault-damage zones and impermeable basement margins (Fig-  
4216 ure 5.1 Jolie et al., 2021). This may present a positive feedback, where thickening  
4217 ice drives groundwater into the aquifers, advecting heat away from the ice base,  
4218 which slows the flow of ice, leading to increased thickness. Similarly, as ice thins,  
4219 the reduced overburden on the aquifers results in water discharge to the ice base and  
4220 an associated localization of heat. The resulting increased flow speed and thinning  
4221 of the ice further reduces the overburden pressure. These mechanisms express how  
4222 crustal structures often thought of as static on a millennial timescale from the view-  
4223 point of ice dynamics may enable rapid changes in ice dynamics. The co-location of  
4224 highly dynamic ice streams (Bougamont et al., 2015; Catania et al., 2012), extensive  
4225 groundwater reservoirs (Christoffersen et al., 2014; Gustafson et al., 2022), elevated  
4226 geothermal heat flux (Burton-Johnson et al., 2020; Shen et al., 2020), and fluid  
4227 pathways (Chapter 2), highlight the Siple Coast as an ideal study site to investigate  
4228 these possible relations between changes in ice thickness, groundwater discharge,  
4229 and the advection of geothermal heat. We now discuss various implications of our  
4230 geologic findings for understanding past and future ice dynamics of the Ross Ice  
4231 Shelf region.

4232

#### 4233 5.4.2 Constraining past and future ice sheet behaviour

4234 While the above geologic controls on the ice sheet likely existed in the past and will  
4235 continue into the future, our study has implications that are exclusive to past or  
4236 future ice sheet configurations. The pinning points we discussed, and the regions of  
4237 thin draft, were all likely pinning points during periods of thicker ice. Since the Last  
4238 Glacial Maximum ( $\sim 22 \text{ kya}$ ) retreat of the grounding line from the outer shelf edge  
4239 has been primarily controlled by the physiography of the bed, as well as its geologic  
4240 composition (Anderson et al., 2019; Halberstadt et al., 2016). While the retreat  
4241 dynamics have been well studied in the Ross Sea, where the open ocean conditions  
4242 allow seismic and high-resolution multi-beam sonar surveying (Anderson et al., 2019;  
4243 Halberstadt et al., 2016), and drill cores provide sedimentary records (McKay et al.,  
4244 2016), under the Ross Ice Shelf there has been very little investigation on retreat  
4245 dynamics, apart from modelling studies (Kingslake et al., 2018; Lowry et al., 2020).  
4246 Here we have provided the physiography of the region, through the sub-Ross Ice  
4247 Shelf bathymetry model, enabling insight into the retreat dynamics throughout the  
4248 Holocene.

4249

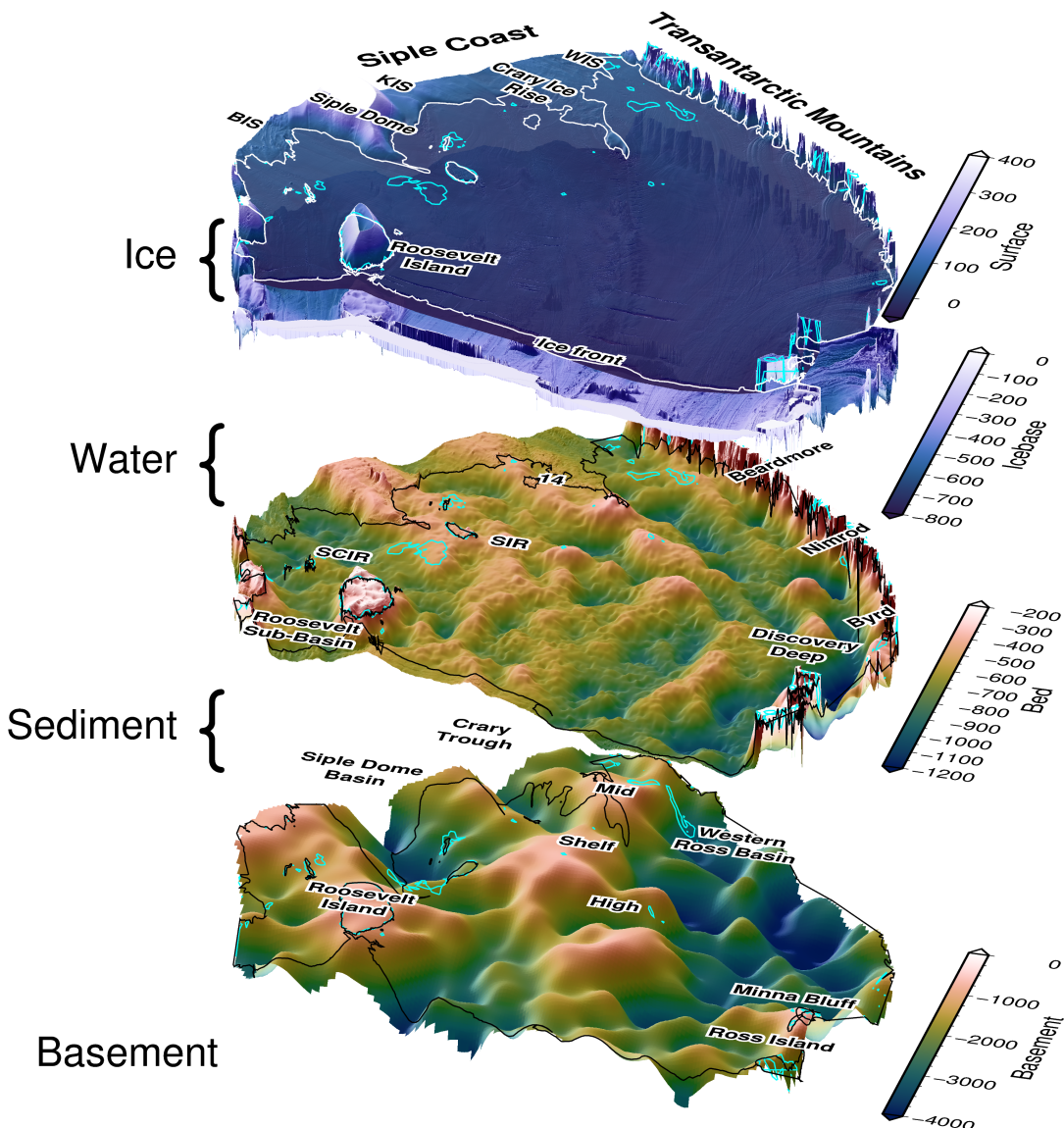


**Figure 5.3:** A 3D perspective view of the structure of the Ross Ice Shelf. Starting at the top, ice surface, and ice base from BedMachine v3 (Morlighem, 2022; Morlighem et al., 2020), inverted bathymetry results from Chapter 4, and basement topography from Chapter 2. Grounding line shown in all layers if from Morlighem (2022). Bright blue contour shows 20 m water column thickness. Note each layer has an independent vertical exaggeration to aid in visualization.

#### 4250 5.4.2.1 Retreat dynamics

4251 While we don't constrain the age of the sea floor sediments, the general physiography  
 4252 of the sea floor can provide some insights. The eastern side of the ice shelf, apart  
 4253 from Roosevelt Island, shows similar physiography to the eastern Ross Sea, with  
 4254 relatively flat bathymetry without major banks or troughs (Figure 5.1e). There,  
 4255 the subdued bathymetry likely resulted in a stepwise style of grounding line retreat  
 4256 throughout the Miocene, with the stabilizing build-up of grounding zone wedges, fol-  
 4257 lowed by decoupling and rapid retreat of 10's of kilometres (Anderson et al., 2019;  
 4258 Bart et al., 2017). The bathymetry of the western Ross Ice Shelf, characterized by  
 4259 depth troughs and shallow banks, is similar to that of the western Ross Sea (Figure

5.1e). There, the retreat style, also controlled by the bathymetry, was continuous and complex, as ice streams followed the bathymetry in a continuous retreat back to the outlet valleys in the Transantarctic Mountains (Anderson et al., 2019; Halberstadt et al., 2016). In the western Ross Sea, repeated cycles of advance and retreat within these confined bathymetry troughs led to the scouring of sediments from the inner shelf, and an over-deepened, landward sloping inner shelf (Anderson et al., 2019). These contrasting styles of retreat proposed for the eastern and western Ross Ice Shelf may be in part responsible for the varied bathymetry found on either side of the ice shelf. The above section discussed our bathymetry results in relation to past and future ice dynamics. Next, we discuss the implication of our basement topography on the glacial history of the region.

4271

#### 4272 5.4.2.2 Glacial initialization

4273 During the Oligocene, the Ross Embayment contained a long and broad mountain range emergent above sea level, trending N-S from the Ross Sea through the ice shelf. This feature was first recognized from the drill cores of DSDP (Deep Sea Drilling Project) site 270 in the Ross Sea (Figure 5.1f, Leckie, 1983), where a 400 m sedimentary sequence with depositional environments ranging from above sea level to  $\sim 500$  below sea level was found, dating from late Oligocene to early Miocene (Kulhanek et al., 2019). Beneath this sequence was crystalline basement. The broad dome-like shape of this basement high was revealed by shipborne seismic surveys (Brancolini et al., 1995), which imaged a similar basement high further north. These basement features were termed the Northern and Southern Central High. Seismic data also revealed small U-shaped channels within the acoustic basement, which were attributed to alpine glaciation (De Santis et al., 1995). Off the flanks of these fault-bound basement highs, wider troughs in the basement were imaged and attributed to the erosion of ice streams flowing off these basement highs. During the late Oligocene, ice caps nucleated on these subaerial basement features (De Santis et al., 1995; Olivetti et al., 2023). Thermal subsidence following the onset of mid-Cretaceous West Antarctic Rift System extension (Karner et al., 2005; Wilson & Luyendyk, 2009) gradually submerged these basement highs (De Santis, 1999; Olivetti et al., 2023). In addition to the North and South Central High features in the Ross Sea, paleotopographic reconstructions of the Oligocene (Paxman et al., 2019; Wilson et al., 2012) have predicted the continuation of this broad subaerial mountain range under the Ross Ice Shelf. Our depth to magnetic basement (Chapter 2) provided the first observations of the feature, which we termed the Mid Shelf High, beneath the Ross Ice Shelf (Figure 5.1f).

4297

4298 The strong continuity of the Mid Shelf High with the Ross Sea's Central High suggests that these features have similar histories. We propose the three blocks of the 4300 Mid Shelf High were emergent and hosted ice caps in the Oligocene. Following their 4301 submersion, likely in the latest Oligocene (Olivetti et al., 2023) these features would 4302 have acted as major bathymetry pinning points, similar to the modern Roosevelt 4303 Island. We suggest this chain of shallow basement blocks formed a long-lasting 4304 catchment divide of both sediment transport and ice flow between East and West 4305 Antarctica. This divide has been predicted as far back as the Paleogene, from 4306 distinct microfossil assemblages on either side of the Ross Embayment (Coenen et 4307 al., 2019). Since the Last Glacial Maximum, the Central High has been thought to

4308 be an ice flow divide, separating ice originating from the East and West Antarctic  
4309 Ice Sheets (Li et al., 2020; Licht et al., 2014; Licht et al., 2005). The prominent Mid  
4310 Shelf High / Central High appears to have played a central role in the history of the  
4311 Ross Embayment since the Oligocene.

## 4312 5.5 Future work

4313 Here we provide several suggestions for future research and fieldwork related to this  
4314 thesis. A primary piece of future work resulting from this thesis should be the incor-  
4315 poration of the updated bathymetry into a sub-ice shelf circulation model. To access  
4316 the sensitivity of sub-shelf circulations to bathymetry, models should be run for our  
4317 mean bathymetry model, as well as the upper and lower ranges of our uncertainties,  
4318 as defined by the mean model plus and minus the spatial uncertainty we present  
4319 (Figure 5.2). To better improve the bathymetry model and reduce uncertainties, we  
4320 suggest three alternatives for field seasons on the Ross Ice Shelf.

- 4321 1. Collect additional seismic depth measurements along the Transantarctic Moun-  
4322 tain front. This would serve to lower uncertainties in the bathymetry associ-  
4323 ated with the nearby steep topography. A traverse-style field season would be  
4324 best for this to accommodate the linear nature of the grounding zone. Collect-  
4325 ing occasional cross lines, running perpendicular to the grounding line, would  
4326 likely image the range front faults, commonly inferred by only rarely imaged.
- 4327 2. A seismic survey of the central block of the Mid Shelf High (Figure 5.1f).  
4328 This survey would accomplish several goals. First, it would fill one of the  
4329 two major gaps in bathymetry measurements in the central ice shelf, reducing  
4330 the bathymetry uncertainty. Secondly, it would inform on the nature of the  
4331 Mid Shelf High as a past pinning point and nucleation site of Oligocene ice  
4332 caps. Lastly, it would act as a site survey for potential sea-floor drilling. The  
4333 thin sedimentary cover of the Mid Shelf High may provide a good target for  
4334 future drilling since a temporally wide-ranging sequence may be concentrated  
4335 into a thin sedimentary package. Additionally, sampling of the crystalline  
4336 basement, trace element and provenance analysis will give further insights into  
4337 1) the proposed East-West Antarctic geologic boundary along the middle of the  
4338 Ross Embayment (Tinto et al., 2019), 2) the region's Cretaceous extensional  
4339 history (Olivetti et al., 2023), and 3) the region's Oligocene to Miocene climatic  
4340 evolution (Olivetti et al., 2023).
- 4341 3. Conduct a regional seismic survey across portions of the Siple Coast to better  
4342 image the sedimentary basins and basin bounding faults, especially where the  
4343 faults proposed in Chapter 2 may interact with the ice streams.

4344 We make several suggestions for future inversions based on our comprehensive re-  
4345 view of past Antarctic bathymetry gravity inversions. To test the inversion method  
4346 developed here, it would be useful to perform another inversion for an ice shelf that  
4347 has been previously inverted. The three best options would be the Getz Ice Shelf,  
4348 the Thwaites Glacier, and the Pine Island Glacier. The bathymetry beneath each of  
4349 these ice shelves has been inverted three separate times, allowing the comparison of  
4350 several different methods. The Getz Ice shelf bathymetry has been inverted in 2D  
4351 (Cochran et al., 2020; Wei et al., 2020), and with a 3D frequency-based inversion

(Millan et al., 2020). The Thwaites cavity has also been inverted in both 2D (Tinto & Bell, 2011) and 3D, with both the "topo-shift method" (Jordan et al., 2020a), and a frequency-based method (Millan et al., 2017). Lastly, the Pine Island Glacier bathymetry has been inversion twice with Simulated Annealing (Muto et al., 2013a; Muto et al., 2016), and once with a frequency-based inversion (Millan et al., 2017). To compare to a wider range of methods, the Thwaites glacier would be optimal. To gain insights into the effectiveness of our uncertainty analysis, Pine Island Glacier should be chosen since spatially variable uncertainty estimates exist from the studies which used Simulated Annealing.

Of the major Antarctic ice shelves, there are four that stand out as prime candidates for a future inversion if the goal is to increase our sub-ice shelf bathymetric knowledge. These include the Larse C Ice Shelf, the Ronne Filchner Ice Shelf, the Riiser-Larsen Ice Shelf, and the Shackleton Ice Shelf.

1. Larsen C is the largest ice shelf on the Antarctic Peninsula, yet bathymetry knowledge beneath it is still limited. A bathymetry inversion has been conducted (Cochran & Bell, 2012), but comparison with seismic constraints revealed large uncertainties in the model. A recent constraint compilation and new seismic data (Brisbourne et al., 2020) make this an ideal candidate without needing any field work. Additional gravity data has also been collected over the ice shelf during 2016, 2017, and 2018 Operation Ice Bridge flights ("IceBridge Sander AIRGrav L1B Geolocated Free Air Gravity Anomalies, Version 1", 2020).
2. The Ronne Filchner is the second-largest ice shelf, yet has not been included in a gravity inversion. An extensive array of seismic constraints, similar to the RIGGS survey of the Ross Ice Shelf exists (Fretwell et al., 2013; Rosier et al., 2018), and gravity data from compiled from Russian airborne and ground-based surveys (Aleshkova et al., 2000; Studinger & Miller, 1999) is accessible as part of the continent-wide AntGG gravity compilation (Scheinert et al., 2016).
3. and 4. The Riiser-Larsen and the Shackleton Ice Shelves are the 5th and 7th largest ice shelves, respectively. To our knowledge, there is no bathymetry knowledge beneath the entirety of either shelf. Gravity data exists for both shelves from the AntGG compilation (Scheinert et al., 2016). Performing inversions for these shelves would require extensive seismic data acquisition to be adequately constrained.

Lastly, we highlight a few alternative use cases and limitations for our gravity inversion algorithm. While this has been developed for a regional-scale sub-ice shelf application, at its core the inversion is a standard geometric (sometimes referred to as structural) inversion. Therefore, this code can be used to invert any topographic surface of a user-defined density contrast based on input gravity anomaly data. It is compatible with domains ranging from small-scale, local areas, to large domains such as ours ( $1000 \times 1000$  km). However, domains significantly larger than ours (continental scale) will introduce inaccuracies due to our use of vertical right-rectangular prisms, which makes assumptions of a planar Earth. For these continental to global scale inversions, vertical prisms should be replaced with spherical prisms (tesseroids), as implemented by (Uieda & Barbosa, 2017). With this, our

4399 inversion will work for other applications, such as predicting regional Moho depths,  
4400 the sediment-basement contact, or determining bed depths beneath grounded ice,  
4401 under subglacial lakes, or in the open ocean. We hope this code is used by others  
4402 for these various applications.

## 4403 5.6 Concluding remark

4404 The primary aim of this thesis was to use existing airborne geophysical data to better  
4405 characterize the geology and physiography beneath Antarctica's Ross Ice Shelf. We  
4406 used and developed several geophysical techniques to accomplish this. We first used  
4407 variations in Earth's magnetic field measured over the ice shelf to model the spatial  
4408 distribution and thickness of sediments beneath the ice shelf. We then developed  
4409 and extensively tested a geophysical inversion, which uses measurements of Earth's  
4410 gravity field to model the depth to the seafloor. With this, we created an updated  
4411 model of the bathymetry beneath the ice shelf.

4412  
4413 From this geophysically informed knowledge of the upper crust of the sub-Ross  
4414 Ice Shelf, we were able to draw inferences on the complex interactions between the  
4415 solid Earth, ocean, and ice for the Ross Embayment. We highlighted the Siple  
4416 Coast as a location with strong geologic control on ice dynamics, through 1) the  
4417 distribution of sediments, which control the competency of bedrock material beneath  
4418 grounded ice, and 2) the location of deep sedimentary basins, which likely supply  
4419 the ice base with lubricating water and localize the geothermal heat delivered to the  
4420 ice. Our bathymetry model confirms the findings of past models which show a deep  
4421 trough spanning from the ice front near Ross Island south along the Transantarctic  
4422 Mountain Front. This trough likely guides High Salinity Shelf Water from the ice  
4423 front to the deep grounding zone of the Transantarctic Mountain outlet glaciers,  
4424 where it induces significant basal melting. Our spatial uncertainty results highlight  
4425 the Transantarctic Mountain Front as the least-certain portion of the sub-ice shelf  
4426 bathymetry model. Combined with this region's importance for basal melt, we  
4427 suggest future seismic surveys target the mountain front. This thesis provides the  
4428 necessary boundary conditions and estimates of their uncertainties for ice and ocean  
4429 modellers to better characterize the Ross Ice Shelf's response to past, present, and  
4430 future changes in the climate.

# 4431 Appendix A

4432 This appendix section provides supplementary information to Chapter 2, and is  
4433 tasked directly from the published supplementary materials of Tankersley et al.  
4434 (2022).

## 4435 A.1 Introduction

4436 This supplement provides additional information on the assumptions behind the  
4437 process of determining basement depth from magnetic anomalies (Section A.2), the  
4438 collection and processing of aeromagnetic line data (Section A.3), the methodolo-  
4439 gy of tying ROSETTA-Ice magnetic basement to ANTOSTRAT acoustic base-  
4440 ment (Brancolini et al., 1995), through the use of Operation IceBridge (OIB) mag-  
4441 netic data (Cochran et al., 2014a) (Section A.4 & A.5), the gridding, merging,  
4442 and filtering of the resulting basement grid (Section A.6), the calculation of sedi-  
4443 ment thickness and  $\beta$ -factors for the region (Section A.7), and our quantification  
4444 of uncertainties and comparison with points of previously measured sediment thick-  
4445 ness (Section A.8). Sediment thickness comparisons with past seismic surveys are  
4446 included in Table S1. Also included are supplementary figures showing various  
4447 additional Ross Ice Shelf grids (Figure A.1), the Werner deconvolution solutions  
4448 of OIB flight 403.3 (A.2), several selected ROSETTA-Ice flight lines with Werner  
4449 deconvolution solutions (A.3), unfiltered basement solutions with flight line loca-  
4450 tions and individual Werner deconvolution solutions (A.4), uncertainties applied to  
4451 basement and sediment thickness results (A.5), and misfit distributions between  
4452 OIB, ANTOSTRAT, and ROSETTA basement models (A.6). Python code, within  
4453 a Jupyter notebook, documents our workflow and figure creation and is accessi-  
4454 ble here: <https://zenodo.org/badge/latestdoi/470814953> or at the GitHub reposi-  
4455 tory: [https://github.com/mdtanker/RIS\\_basement\\_sediment](https://github.com/mdtanker/RIS_basement_sediment). Results in the form  
4456 of netCDF's and csv's are available at <https://doi.pangaea.de/10.1594/PANGAEA.941238>, including figures of all ROSETTA-ice flight line basement solutions.

## 4458 A.2 Depth to basement assumptions

4459 Our resulting basement grid is the depth to the shallowest magnetic signal. It is  
4460 assumed that the crystalline basement in this region produces significantly larger  
4461 magnetic anomalies compared to the overlying sediment fill. Note that in some  
4462 instances, such as igneous bodies intruded into sedimentary basin fill, Werner de-  
4463 termined solutions fall upon the crest of the intrusion, and the actual top of the  
4464 crystalline basement could be at a deeper level. Intrusions of small lateral extent

will have small widths, resulting in small values of parameter S (susceptibility  $\times$  width) and therefore will be removed by our filter (Section A.4). For larger intrusions into existing basins, (i.e. Ross Island and Minna Bluff Cox et al., 2023), the modelled magnetic basement surface will be shallower than the bottom of the sedimentary basin. While this underestimates sediment volume, it better characterizes the competency of the substrate from an ice dynamics perspective. This is similar to how extensive intrusions into basins would be imaged by seismic surveys as shallow basement. However, these extensive regions of late-Cretaceous-Cenozoic magmatism are not expected to be prevalent under the RIS (Andrews & LeMasurier, 2021).

## A.3 Magnetic data collection, processing, and Werner deconvolution

Both ROSETTA-Ice and OIB data sets were collected with a Scintrex CS3 Cesium magnetometer. Average flight speeds were 123 m/s and 93 m/s for OIB and ROSETTA-Ice respectively. Altitudes for the sections of OIB flight 403 used here average around 400 m above sea level, while ROSETTA-Ice altitude averaged at 750 m above the ice sheet surface. OIB data were resampled from 20 Hz to 1 Hz to match the frequency of the ROSETTA-Ice data. Both datasets have been despiked, diurnally corrected, and had the International Geomagnetic Reference Field model removed. See Tinto et al. (2019) for more details of the ROSETTA-Ice survey and flight line locations. Due to variable flight elevations, both between and within the datasets, all magnetic data were upward continued to 1000 m above sea level. To avoid artifacts of downwards continuing, any data with flight elevations above 1000 m were removed ( $\sim 10\%$  of the data).

Here we use 2D Werner deconvolution Werner (1953), applied to aeromagnetic line data, to image the shallowest magnetic signals in the crust. Assuming that the overlying sediments produce smaller magnetic anomalies than the crystalline basement, we treat the resulting solutions as a depth to the magnetic basement. During Werner deconvolution, moving and expanding windows are passed over the magnetic anomaly line data. Within each window, after linearly detrending the data, the source parameters of the anomalies are estimated with a least-squares approach, assuming the source bodies are infinite-depth dikes or contacts. The source parameters include position (distance along profile and depth), magnetic susceptibility, and source geometry (contact or dike). Solutions are considered valid between 1200 m and 20 km of upward continued flight elevation (approx. 200 m - 19 km bsl). Windows ranged from 500 m - 50 km, with a window shift increment of 1 km and an expansion of 1 km.

Due to passing over the data many times with varying window widths, Werner deconvolution produces a depth-scatter of solutions, which tend to cluster vertically beneath the true magnetic sources. Each of these solutions consists of location, depth, susceptibility (S), window width (W), and a simplified source geometry (dike or contact). For contact-type solutions, parameter S is the estimated magnetic susceptibility of the body, while for dike-type solutions, S is the product of susceptibility and dike width. During filtering (Sections A.4 & A.5), a cut-off based on parameter S is used to remove shallow solutions. Since the value of parameter S for

4511 contact solutions are typically much smaller than for dike solutions (since they are  
4512 not multiplied by dike width), only dike solutions have been considered here. To  
4513 achieve a basement surface from this resulting depth-scatter of solutions, we have  
4514 utilized parameter-based filtering and clustering, described in Sections A.4 & A.5.  
4515 This Werner deconvolution process was the same for both OIB and ROSETTA-Ice  
4516 magnetics data. Werner deconvolution was performed in Geosoft's Oasis Montaj and  
4517 subsequent processing of these results was performed in Python, and is included in  
4518 a Jupyter notebook; <https://zenodo.org/badge/latestdoi/470814953>.

4519  
4520 This magnetic basement approach has been used to map sedimentary basins  
4521 throughout Antarctica, including the Ross Sea Karner et al. (2005), western Marie  
4522 Byrd Land (Bell et al., 2006), and Wilkes Subglacial Basin (Frederick et al., 2016;  
4523 Studinger et al., 2004a). Our approach is similar to past studies, but our proximity  
4524 to well-constrained offshore seismic basement depths (Brancolini et al., 1995) allows  
4525 us to develop the method further. Most studies display their results as 2D profiles  
4526 with the depth-scatter of solutions mentioned above, and simply use the tops of the  
4527 clusters as the basement depth. By comparison with seismic basement, we have  
4528 developed a reliable, automated method of 'draping' a surface over these depth-  
4529 scattered solutions to produce a 3D surface. This process is described below.

## 4530 **A.4 Tying magnetic basement to seismic basement**

4531 To validate the method described in Section A.3 and address uncertainty we per-  
4532 form Werner deconvolution for OIB magnetics data (Figure 2.1b, Cochran et al.,  
4533 2014a) over the Ross Sea. Here, ice-free conditions have permitted shipborne seis-  
4534 mic surveys to image basement depths in the region. These have been compiled by  
4535 the Antarctic Offshore Acoustic Stratigraphy project (ANTOSTRAT) (Brancolini  
4536 et al., 1995) (Figure 2.1b). The basement was not imaged for the deeper portions  
4537 of the basins and data coverage of actual basement reflectors, versus interpolation  
4538 between basement reflectors, is not reported. Werner deconvolution (Section A.3)  
4539 produces a series of many solutions (black dots in Figures 2.2 & A.2) at each window  
4540 along the line.

4541  
4542 To achieve a basement surface, instead of a depth-scatter of solutions, solutions  
4543 were filtered based on Werner window width (W) and the product of magnetic sus-  
4544 ceptibility and body width (parameter S). Filtered solutions (black circles, scaled to  
4545 parameter S in Figures 2.2 & A.2) were then horizontally binned with variable bin  
4546 sizes (parameter B) (vertical grey lines in Figures 2.2 & A.2). Bins with a minimum  
4547 count of solutions (parameter C) were retained, and the depth of the bin centre was  
4548 set to the 95th-percentile depth of the solutions in the bin. This removed spurious  
4549 shallow solutions, while effectively retaining the 'top' of the magnetic signal. These  
4550 bin centres (orange crosses in Figures 2.2 & A.2) were then interpolated, producing  
4551 our model of magnetic basement depths (orange line in Figures 2.2 & A.2). The  
4552 above filtering techniques removed the solutions above the basement, and the clus-  
4553 tering technique fitted a surface over the remaining points, which represents the  
4554 top of the basement. This interpolated line allowed a direct comparison between  
4555 ANTOSTRAT seismic basement and OIB magnetic basement.

4556  
4557 We varied each of the four parameters (W, S, B, and C) with 21 different values

and conducted the above procedures for all unique combinations of them on OIB line 403, segments 1 and 3, in the Ross Sea (location in Figure 2.1b). This resulted in 194,481 iterations, for each of which we calculated a mean absolute difference at points every 5 km between ANTOSTRAT seismic basement and the resulting OIB magnetic basement. We found the parameter values which produced the closest match between OIB magnetic basement and ANTOSTRAT seismic basement, as shown in Figures 2.2 & A.2. These resulting values were a maximum Werner deconvolution window width (parameter W) of 10 km, a minimum product of magnetic susceptibility and body width (parameter S) of 1.0, a horizontal bin width (parameter B) of 36 km, and a minimum number of solutions per bin (parameter C) of 6. The median absolute misfit between OIB and ANTOSTRAT basement for the two line-segments was 480 m (260 m for Line 403.1 (Figure 2.2), and 1040 m for Line 403.3 (Figure A.2)). This equates to 11% of average ANTOSTRAT depths for the two lines. The close fit between the OIB magnetic basement and the ANTOSTRAT seismic basement both supports the validity of this method and gives us the parameters necessary to repeat this method for data over the RIS.

## A.5 Tying Ross Sea magnetic basement to Ross Ice Shelf magnetic basement

Having optimized our method to match OIB magnetic basement to ANTOSTRAT seismic basement in the Ross Sea (Section A.4, Figures 2.2 & A.2), we now optimize the method to match ROSETTA-Ice magnetic basement to OIB magnetic basement. This additional optimization is necessary due to differences in processing and survey design, including flight elevations, speed, aircraft, mounting equipment used, and frequency of recording. With the optimized parameters for OIB data (Section A.4), we calculate magnetic basement for OIB flight 404 over the ice shelf. We treat this as the 'true' basement and update the filtering and clustering parameters (Section A.3) to minimize the misfit between OIB basement and the resulting ROSETTA-Ice basement. This tuning was performed on ROSETTA-Ice lines 590 and 650, which were coincident with segments from OIB line 404 (location in Figures 2.1b & A.4). Optimal parameters to match ROSETTA-Ice solutions to OIB basement are found to be  $W < 26$  km,  $S > 1.2$ ,  $B = 36$  km, and  $C > 40$ , resulting in a median absolute misfit between OIB basement and ROSETTA-Ice solutions of 400 m (630 m for line 404.590 (Figure A.3e) and 310 m for line 404.590 (Figure A.3f)). This equates to 18% of OIB depths for the two lines. With these parameters which best match ROSETTA magnetic basement to OIB magnetic basement, we performed the same procedure on all the ROSETTA-ice flight lines. A selection of these lines, and the two ties to OIB 404, are shown in Figure A.3. All ROSETTA-ice flight line solutions are available as images at the PANGAEA link.

## A.6 Gridding, merging, and filtering

The above processes were performed on all ROSETTA-ice flight lines (white lines in Figure A.4), including the N-S tie lines at  $\sim 55$  km spacing. Where the tie lines crossed over the E-W flight lines, some resulting basement solutions (black dots in Figure A.4) are nearby those from the crossing line. Since we are interested in the

shallowest magnetic signals, we have retained only the shallowest solution with 8 km cells across our region. Since bin widths (parameter B) were set to 36 km, the nearest solutions along individual lines were further apart than the 8 km cell. The closest spacing of E-W flight lines was 10 km, so this process only affected solutions at the crossover between N-S and E-W lines. These points were then gridded with a 5 km cell size and a minimum curvature spline with a tension factor of 0.35 Smith and Wessel, 1990 (Figure A.4). This grid was then merged with a Ross Sea seismic basement grid. The Ross Sea grid, while mostly ANTOSTRAT data, was sourced from a regional compilation of sediment thicknesses (Lindeque et al., 2016; Wilson & Luyendyk, 2009) we have subtracted from bathymetry depths (Morlighem et al., 2020) to achieve basement depths. Where the grids overlap near the ice shelf edge, we retain our RIS values. To aid in the merging at the overlaps, and to match RIS basement wavelengths to the characteristic basement wavelengths of ANTOSTRAT, we filtered the merged grid with an 80 km Gaussian filter (Figure 2.3a). This filtering was performed with a variety of wavelengths (20-120 km), where we found filters  $<80$  km didn't significantly alter the regional basement, while filters  $>80$  km excessively smoothed the basement topography. A few locations with anomalously shallow basement were set equal to BedMachine bathymetry.

## 4619 **A.7 Sediment thickness and $\beta$ -factor calculations**

With the regional basement model (Figure 2.3a) including RIS magnetic basement and offshore seismic basement, we calculated sediment thickness (Figure 2.3b) by subtracting the grid from BedMachine bathymetry depths (Figure 2.1a & A.1e, Morlighem et al., 2020). Previous estimates of sediment thickness for the sub-RIS come from the extrapolation of gravity anomalies with bathymetry trends (Wilson & Luyendyk, 2009). These were included in the Lindeque et al. (2016) compilation (Figure A.1d). Eocene Oligocene boundary paleotopographic reconstructions (Paxman et al., 2019; Wilson et al., 2012) assumed this sediment estimate was post-Eocene and used it as their maximum sub-RIS sediment thickness, incorporated into their minimum surface reconstruction. The thickness of sediment affects onshore erosion estimates, surface raising due to deposition, and isostatic surface subsidence due to loading. For their maximum paleotopographic reconstructions, they used a thinner sediment model, with the same general trends (Wilson & Luyendyk, 2009). Figure A.1 (c, d, & f) shows the comparison between the sediment thickness models. Figure A.1f colorbar histogram shows the distribution, with our values having a mean thickness  $\sim 115$  m greater than the past model. Yet, along the Siple Coast, we show much greater discrepancies, up to 2 km thicker.  $\beta$ -factor, the ratio of initial crustal thickness to final crustal thickness, is useful for quantifying the thinning of crust in extensional settings. We calculate a distribution of  $\beta$ -factors beneath the RIS by assuming a uniform initial crustal thickness and dividing it by current crustal thickness. We pick an initial crustal thickness of 38 km, which represents a global average for un-thinned plateau-type crust (Mooney et al., 1998), and has been used for the West Antarctic Rift System  $\beta$ -factor calculations (Müller et al., 2007). For the final (current) crustal thickness, we use a continent-wide Moho model from surface wave observations to define the bottom of the crust (An et al., 2015). For the top of the crust, we use our resulting RIS basement grid.

Name	Reference	Seismic sediment thickness (m)	Magnetic sediment thickness (m)	Absolute difference (m)
CIR	(Rooney et al., 1987)	400	514	114
I10S	(Robertson & Bentley, 1989)	$750 \pm 100$	1281	818
J9DC	(Greischar et al., 1992)	1350	770	580
BC	(Robertson & Bentley, 1989)	$1900 \pm 400$	1082	818
RI	(Greischar et al., 1992)	850	822	28
C49	(Crary, 1961)	754	1162	408
LAS	(Crary, 1961)	1325	1799	474
Q13	(Greischar et al., 1992)	$255 \pm 145$	721	466

**Table A.1:** Previous seismic sediment thickness results for the Ross Ice Shelf. Stations names are labelled in Figure 2.3b. Magnetic sediment thickness column shows our sampled results at the location of each station. Comparing the seismic estimates with our sediment thickness at the eight stations gives a median absolute misfit of 470 m.

## 4646 A.8 Uncertainties

4647 We estimated a representative uncertainty for our basement model by examining  
 4648 the misfit of our modelled basement compared to offshore seismic basement depths  
 4649 (Brancolini et al., 1995). We did this by sampling our OIB magnetic basement  
 4650 estimate and the coincident ANTOSTRAT basement at 1 km intervals along lines  
 4651 403.1 and 403.3 (Figures 2.2 and A.2) and compared the values. The resulting ab-  
 4652 solute values of the differences don't exhibit a normal distribution (Figure A.6a);  
 4653 therefore, we use the median of the absolute misfit ( $\pm 480$  m) as the basement model  
 4654 uncertainty. This equates to 22% of average basement depths for the sub-RIS. We  
 4655 performed a similar analysis between OIB magnetic basement and ROSETTA-Ice  
 4656 magnetic basement for coincident lines 590 and 650 (Figure A.3 e & f). This resulted  
 4657 in a median absolute misfit of 400 m (Figure A.6b). Tinto et al. (2019) report an un-  
 4658 certainty of 68 m for their bathymetry model. Incorporating this with our basement  
 4659 model gives an uncertainty of 550 m (37% of average thickness) for our sediment  
 4660 thickness results. Comparison with sub-RIS sediment thickness and distribution re-  
 4661 sults from a variety of methods, including active source seismic surveys (Table A.1  
 4662 and references within), seismic radial anisotropy (Zhou et al., 2022), geophysical  
 4663 machine learning (Li et al., 2022), and magnetotelluric surveying (Gustafson et al.,  
 4664 2022), all show general agreement with our results.

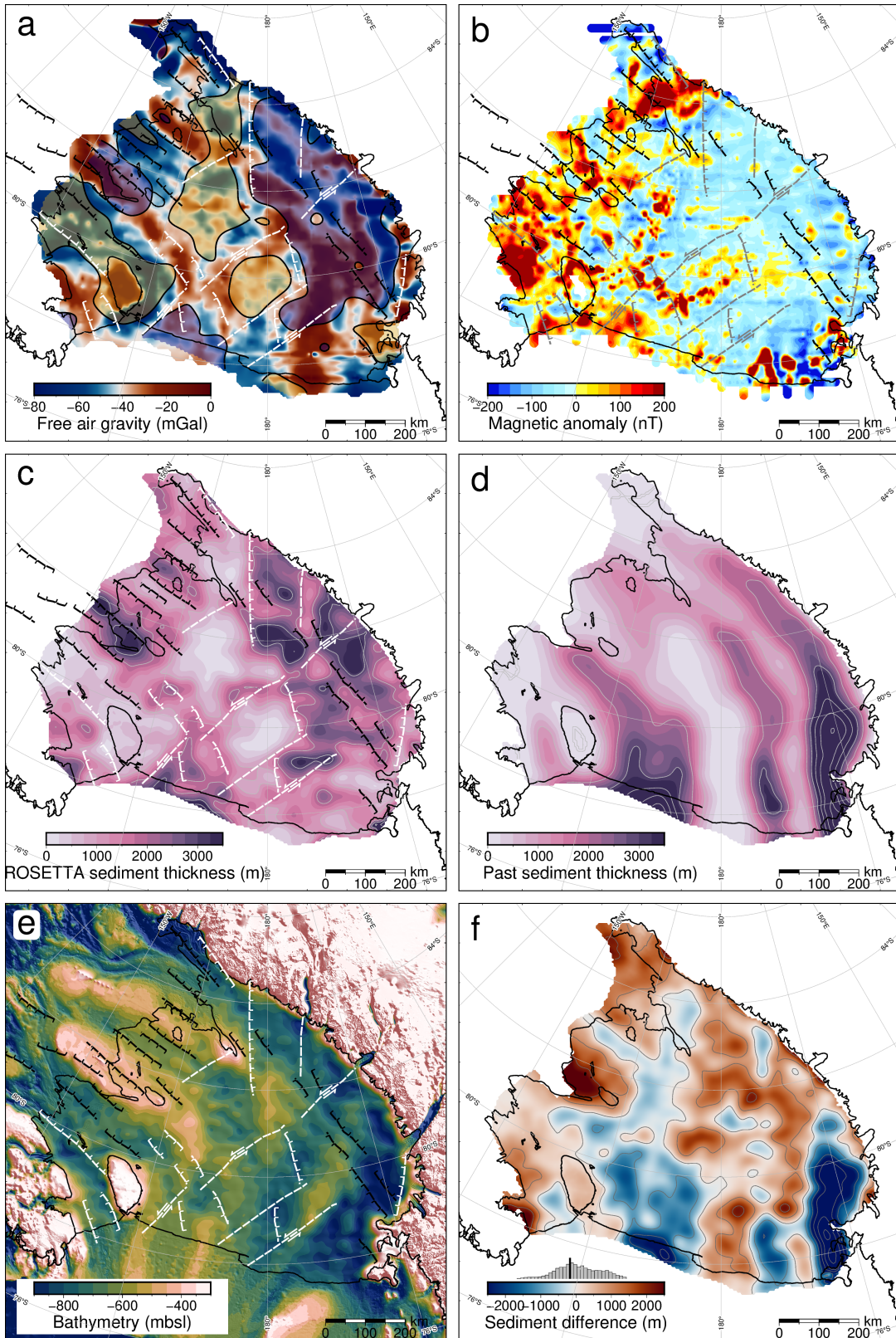


**Figure A.1:** **a)** ROSETTA-Ice free air gravity (Tinto et al., 2019). Shaded yellow regions are shallow basement ( $<\sim 1600$  mbsl), shaded blue regions are deep basement ( $>\sim 2600$  mbsl). **b)** ROSETTA-Ice airborne magnetic anomaly data (Tinto et al., 2019). **c)** Sediment thickness from this study (same as Figure 2.3b), with 1 km contours. **d)** Sediment thickness from a regional compilation (Section A.7, Lindeque et al., 2016; Wilson & Luyendyk, 2009), with 1 km contours. **e)** BedMachine2 bathymetry (Morlighem et al., 2020), from which sediment thickness in c) was calculated. **f)** Difference between c) and d). Red signifies our results have more sediment, while blue signifies our results have less sediment. Histogram shows data distribution, with mean value (black) at 115 m. Inferred faults in a), b), c), and e) same as Figure 2.4a. Grounding line and coastlines in black (Rignot et al., 2013). Projection is Antarctic Polar Stereographic: EPSG 3031.

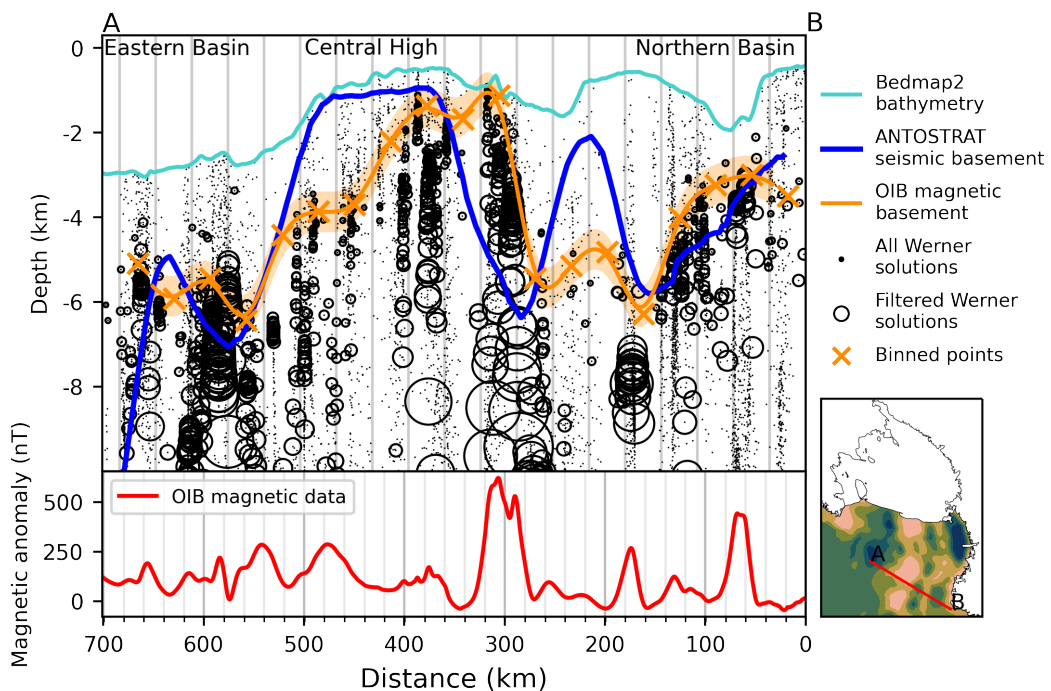


**Figure A.2:** Ross Sea magnetic and seismic basement comparison. Operation IceBridge airborne magnetic data (lower panel) from segment 403.3 (Figure 2.1b). Small dots show Werner deconvolution solutions, which were filtered based on parameters S and W (Section A.3) to produce black circles, which are scaled to parameter S. These circles were binned at a width equal to parameter B, shown by the vertical grey lines in the upper panel. Orange crosses show bin centres, which were fitted to a line to facilitate the comparison between the magnetic basement (orange line) and seismic basement (blue line). Orange band shows  $\pm 480$  m uncertainty for the basement model. Ross Sea basement features are labelled on top.

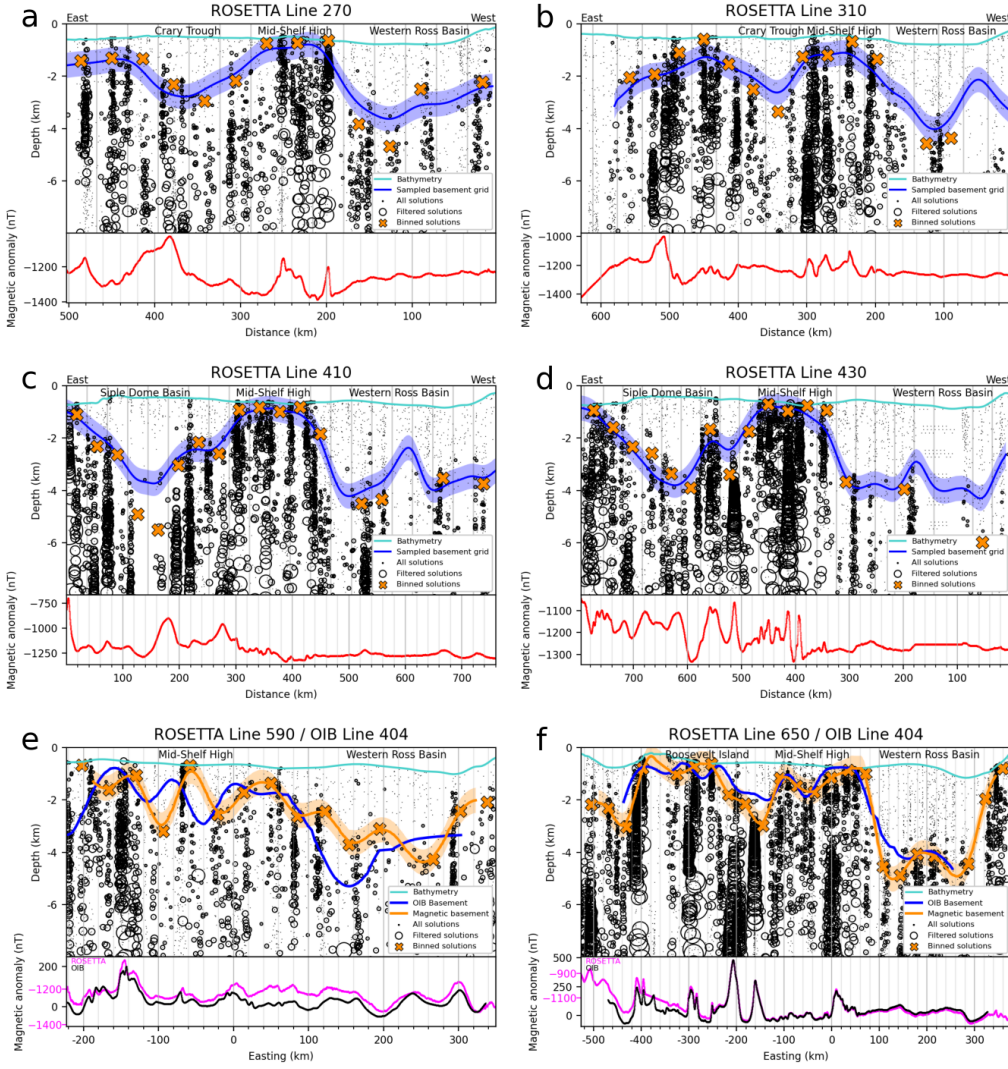


**Figure A.3:** Werner deconvolution solutions for a selection of ROSETTA-Ice lines, locations highlighted in Figure A.4. Bathymetry from Bedmap2 (Fretwell et al., 2013). Dots, circles, and vertical grey lines same as Figure A.2. **a-d)** Comparison between magnetic basement before and after filtering and gridding. Orange crosses are magnetic basement solutions, shown as black dots in Figure A.4, and highlighted for these lines. Blue lines are magnetic basement sampled from the grid of Figure 1a, after gridding and filtering. Red lines show 258 ROSETTA-Ice magnetics data. **e-f)** Comparison between magnetic basement resulting from Werner deconvolution of coincident OIB and ROSETTA-Ice flight lines. Location is shown in Figures 2.1b and A.4. These two lines were used to tie the ROSETTA-Ice survey to the OIB survey (Section A.5). Blue lines are OIB magnetic basement results, orange crosses and fitted orange lines with uncertainty bands are ROSETTA-Ice magnetic basement. ROSETTA-Ice (pink) and OIB (black) magnetics data are shown in lower panels.

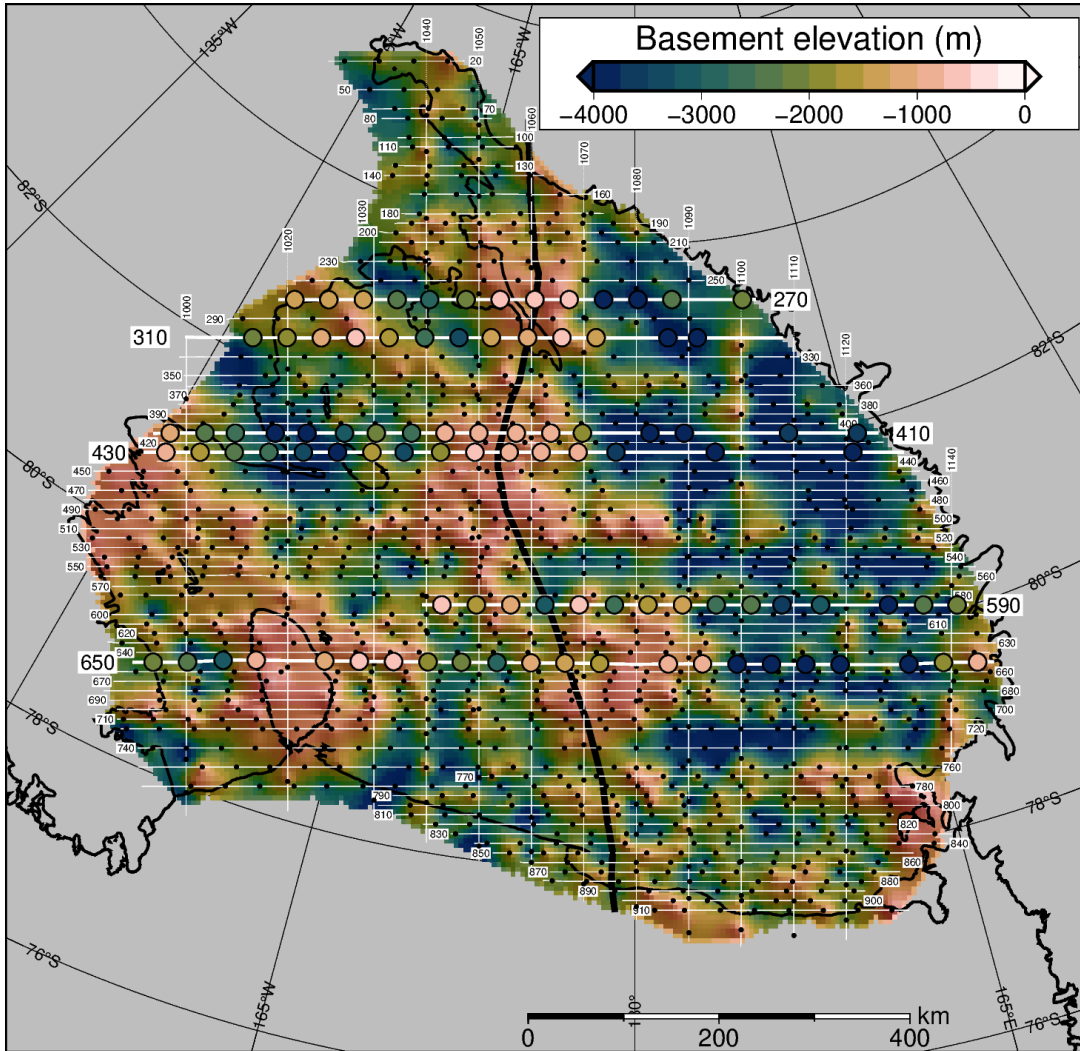


**Figure A.4:** Unfiltered magnetic basement. Point solutions (black dots here, orange crosses in Figure A.3) along ROSETTA-Ice flight lines (labelled) were gridded with a 5 km cell size and a minimum curvature spline with a tension factor of 0.35. Figure A.3 flight lines (bold white) and point solutions (coloured circles) are shown. Black line through the Mid-Shelf High shows the East-West Antarctic divide used in colorbar histograms of Figures 2.3 and 2.4a. Grounding line and coastlines in black (Rignot et al., 2013).

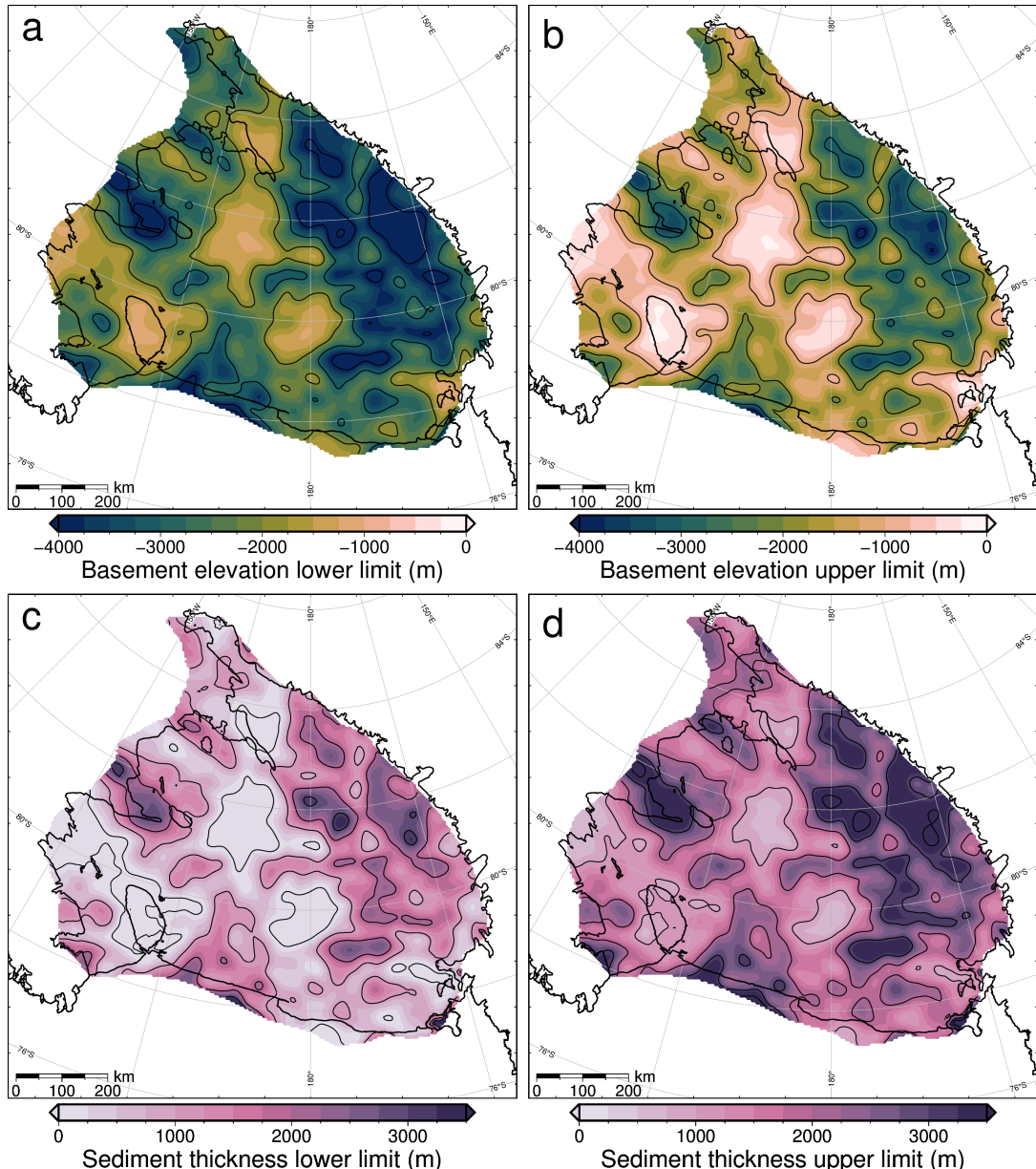


**Figure A.5:** Upper and lower limits of uncertainty applied to a-b) magnetic basement and c-d) sediment thickness. See Section A.8 for how these uncertainties were determined.

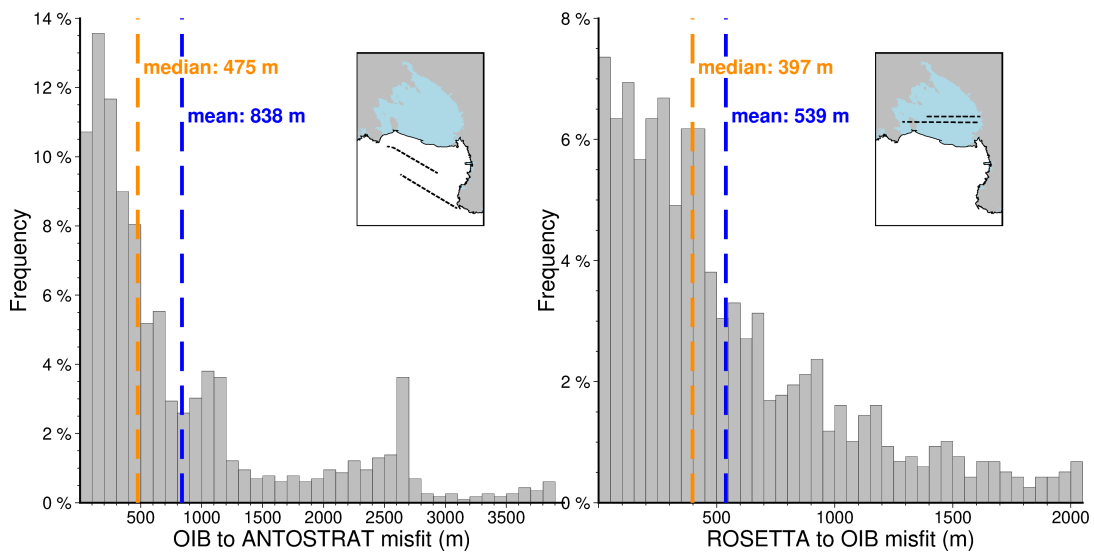


**Figure A.6:** Misfit distributions for comparisons between **a)** OIB magnetic basement and ANTOSTRAT seismic basement and between **b)** ROSETTA magnetic basement and OIB magnetic basement. Inset maps show the locations of flight lines. Basement models were sampled at 1 km intervals for the comparison.

# 4665 Appendix B

4666 This appendix section provides supplementary information to Chapter 3.

## 4667 B.1 Synthetic inversion with a regional field

### 4668 Regional separation techniques

4669 Figure B.1 shows profiles comparing the various regional separation techniques  
4670 shown in Figure 3.19 of Chapter 3.

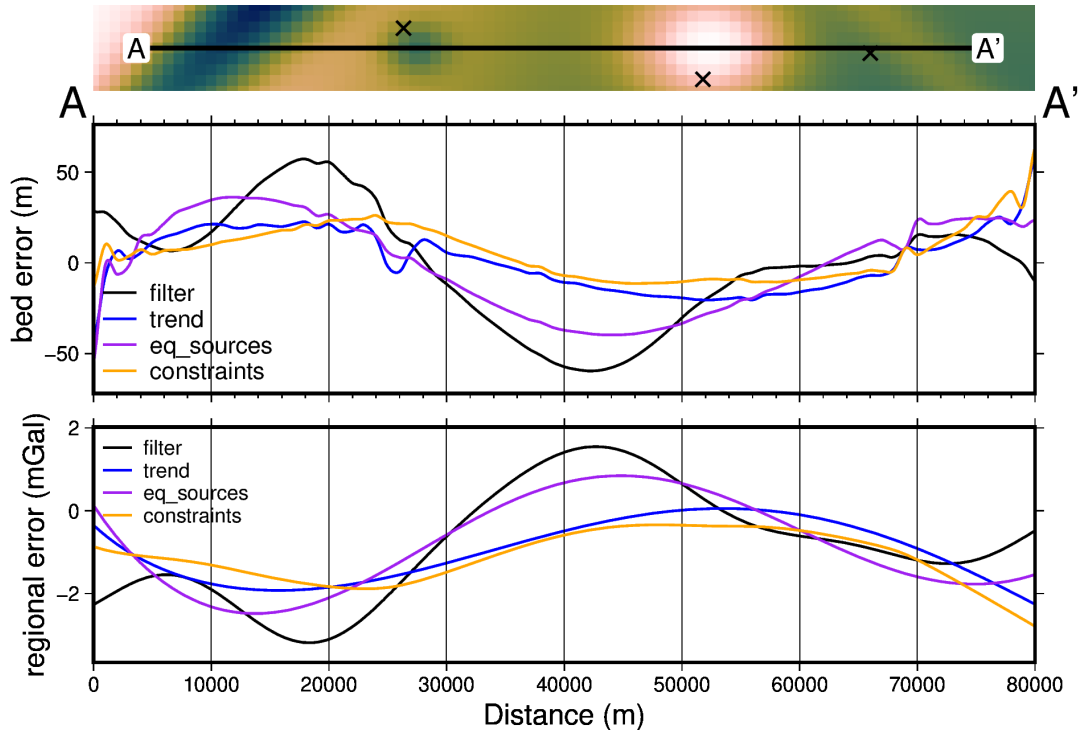


**Figure B.1:** Comparison of four methods of regional separation. **Upper panel** shows the error in the inverted bathymetry models for each method. **Lower panel** shows the errors in the regional field estimation of each method. Profile location shown at the top.

### 4671 Constraint point minimization grinding techniques

4672 Figure B.1 shows profiles comparing the various gridding techniques for the con-  
4673 straint point minimization regional separation method. These various gridding tech-  
4674 niques are shown in map view in Figure 3.20 of Chapter 3.

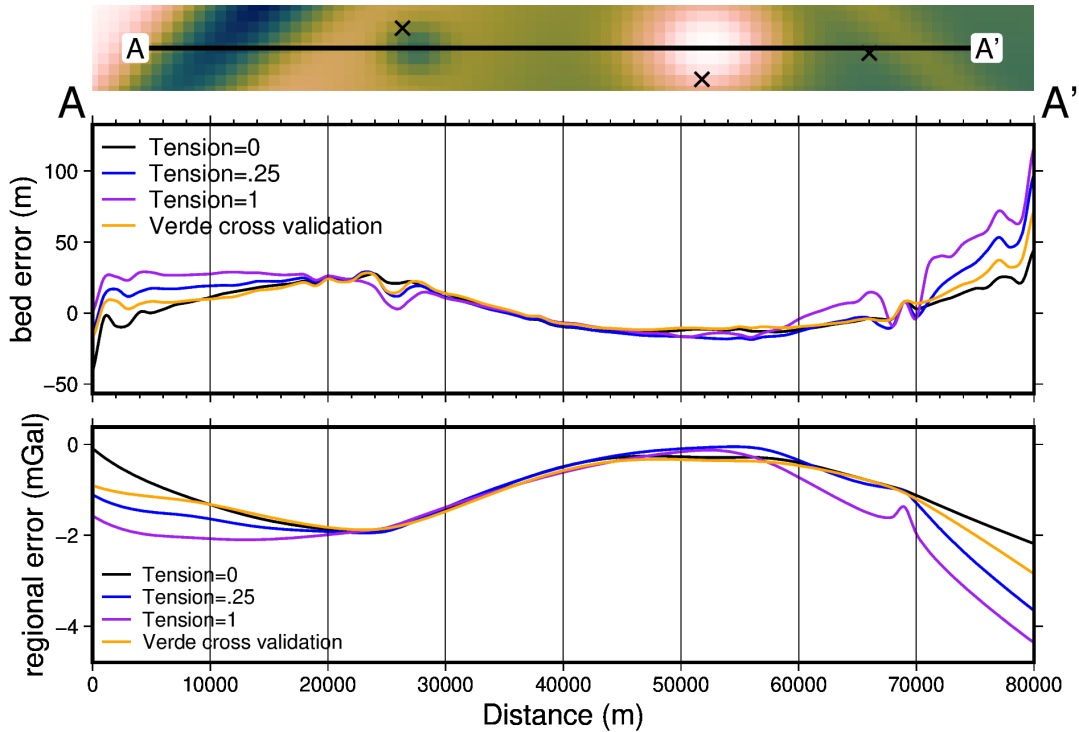


**Figure B.2:** Comparison of gridding techniques for the constraint point minimization method of regional separation. **Upper panel** shows the error in the inverted bathymetry models for each method. **Lower panel** shows the errors in the regional field estimation of each method. Profile location shown at the top.

#### 4675    Added noise

4676    Here, we repeat the inversion from Section 3.4 with noise added to the observed  
 4677    gravity data. Noise was from a Gaussian distribution with a mean of 0 and a stan-  
 4678    dard deviation of 2% of the max absolute values of the data, equating to 0.24 mGal.  
 4679    The cross-validation curve and a profile across the inverted bathymetry as shown in  
 4680    Figure B.3. The inverted bathymetry and difference with the true bathymetry as  
 4681    shown in Figure B.4. The error in the inverted bathymetry is compared to the error  
 4682    in the regional field estimation in Figure B.5.

#### 4683    Lower-resolution gravity survey

4684    This same inversion is now repeated with a lower-resolution gravity survey. Instead  
 4685    of the original 1 km survey grid, a 4 km grid is used.

## 4686    B.2    Ross Sea synthetic model

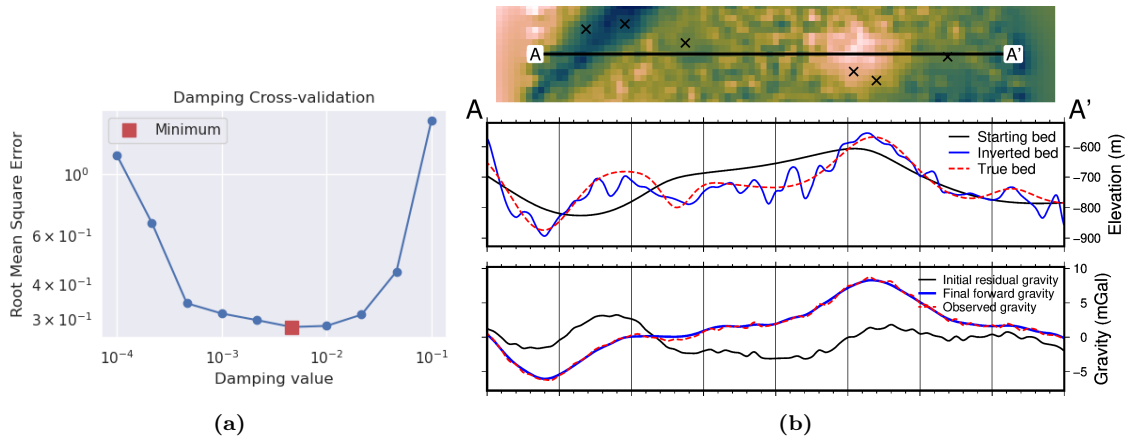


**Figure B.3:** Cross-validation and profiles for the simple synthetic inversion with a regional component removed and 2% noise added to the observed gravity data. a) Cross-validation curve showing the optimal damping parameter (red square). b) 2D profile of the inversion results. The top panel shows profile location and constraint points (black crosses). The middle panel contains topographic profiles of the starting, inverted, and true bathymetries. The bottom panel contains gravity anomaly profiles.

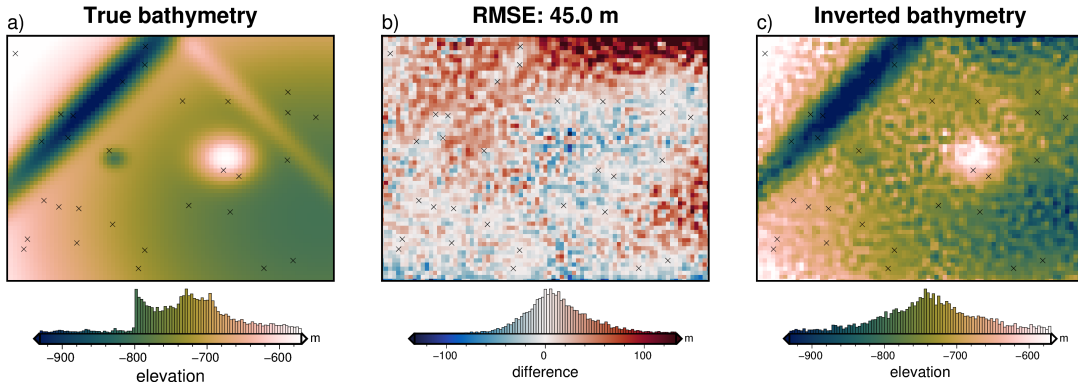


**Figure B.4:** Simple synthetic model inversion with a removed regional component and noise contamination. a) True bathymetry, b) difference between a) and c), c) final inverted bathymetry. Black crosses are constraint points. The RMS difference with the true bathymetry at these constraints is 2 m.

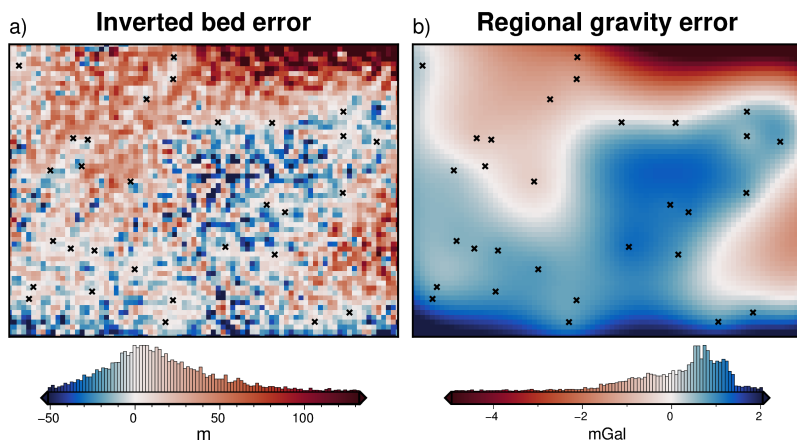


**Figure B.5:** Source of inverted bathymetry error for model with regional field and noise. a) Inverted bathymetry error from Figure 3.22b. b) Error in the estimation of the regional component of gravity from comparison with the true regional component (Figure 3.18b). Black cross show constraint points. Colourmaps are opposed to highlight the similarities and the mean has been removed from the regional error.

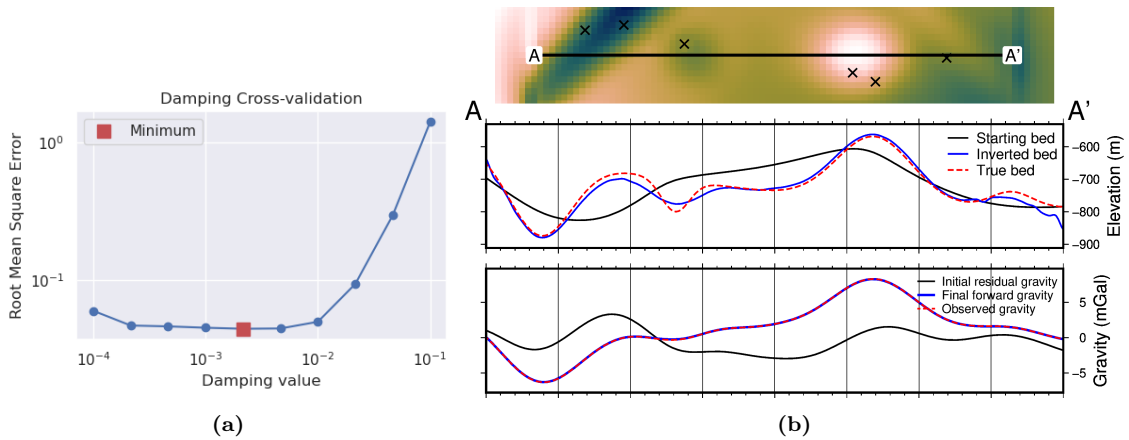


**Figure B.6:** Cross-validation and profiles for the simple synthetic inversion with a regional component removed and low-resolution gravity data. a) Cross-validation curve showing the optimal damping parameter (red square). b) 2D profile of the inversion results. The top panel shows profile location and constraint points (black crosses). The middle panel contains topographic profiles of the starting, inverted, and true bathymetries. The bottom panel contains gravity anomaly profiles.

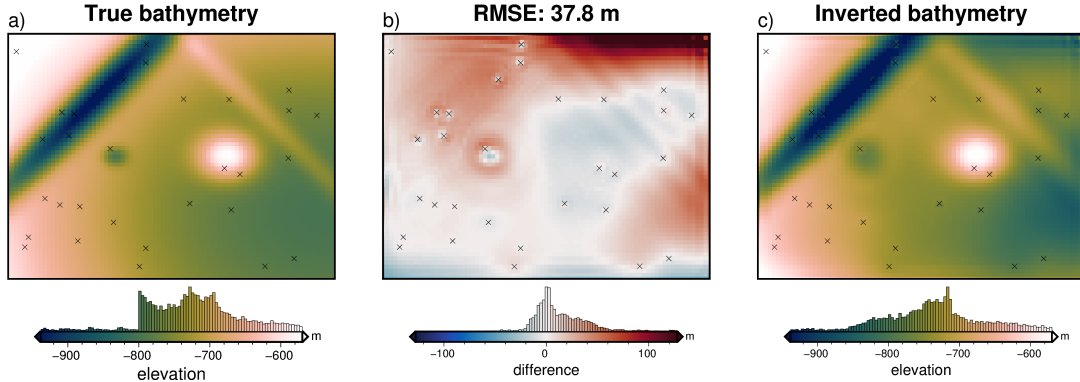


**Figure B.7:** Simple synthetic model inversion with a removed regional component and gravity resampling. a) True bathymetry, b) difference between a) and c), c) final inverted bathymetry. Black crosses are constraint points. The RMS difference with the true bathymetry at these constraints is 2 m.

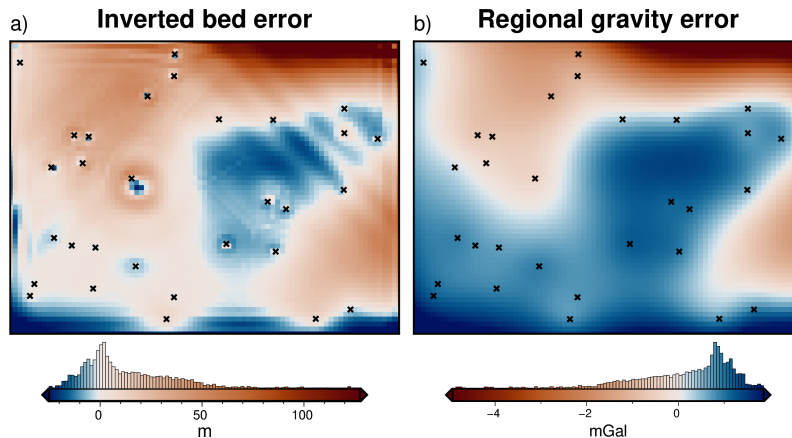


**Figure B.8:** Source of inverted bathymetry error for model with regional field and re-sampled gravity data. a) Inverted bathymetry error from Figure 3.22b. b) Error in the estimation of the regional component of gravity from comparison with the true regional component (Figure 3.18b). Black crosses show constraint points. Colourmaps are opposed to highlight the similarities and the mean has been removed from the regional error.

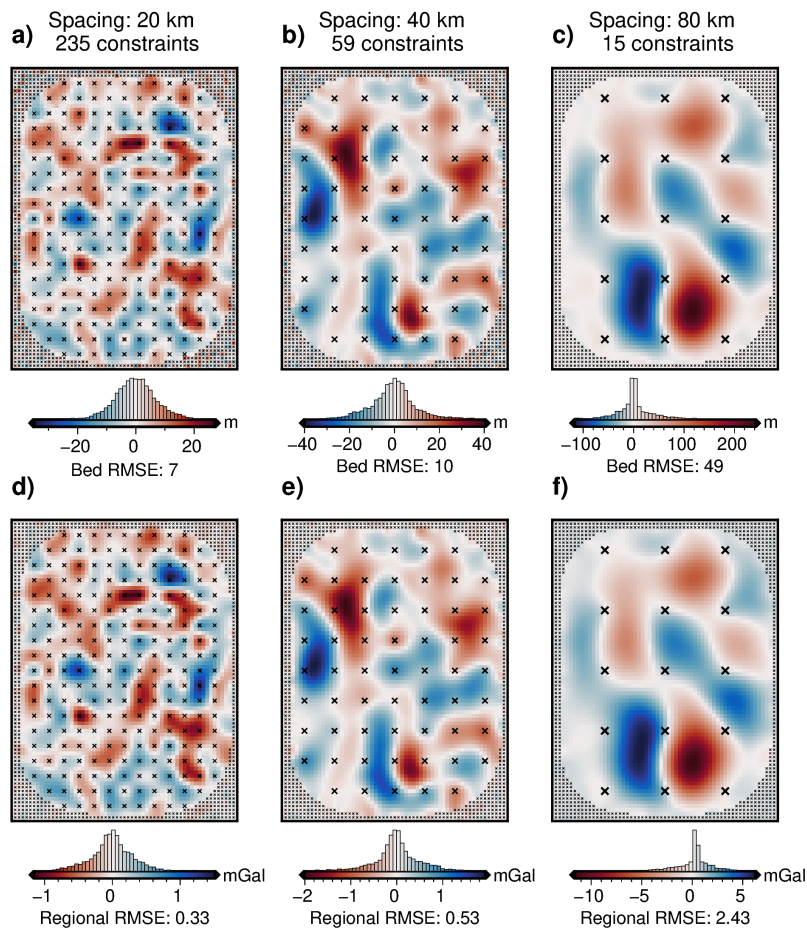


**Figure B.9:** Source of inverted bathymetry error for three inversion with varying constraint spacings. a) Inverted bathymetry error from three of the models in the constraint ensemble of Figure 3.31. b) Error in the estimation of the regional component of gravity from comparison with the true regional component for each model. Black crosses show constraint points. Colormaps are opposed to highlight the similarities and the mean has been removed from the regional error.



4687 **Appendix C**

4688 This appendix provides supplemental information to Chapter 4.

4689 **C.1 Gravity disturbance vs anomaly**

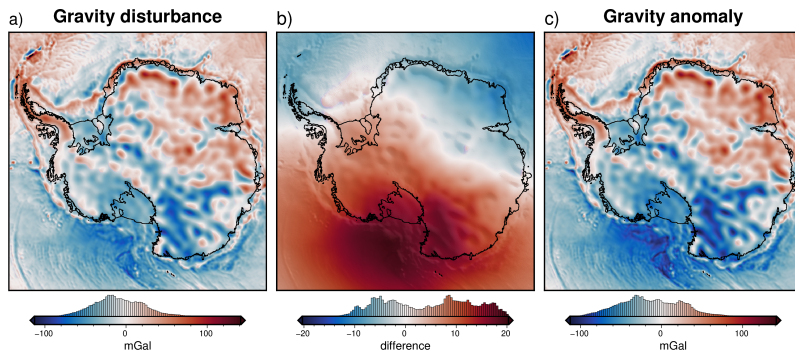


**Figure C.1:** Difference between the gravity disturbance and anomaly for Antarctica. Observed gravity is from Förste et al. (2014) and the normal gravity for each was calculated with the python package Boule (Fatiando a Terra Project et al., 2022). See Section 4.2.1 for further details.



# 4690 Appendix D

## 4691 Antarctic-Plots

4692 This appendix briefly describes the Python package Antarctic-Plots (Tankersley,  
4693 2023) which I developed during this thesis and is used in all of the chapters. The  
4694 documentation of the package is hosted at the following link; <https://antarctic-plots.readthedocs.io/en/latest/index.html> and the code is stored and developed in the fol-  
4695 lowing GitHub repository; [https://github.com/mdtanker/antarctic\\_plots](https://github.com/mdtanker/antarctic_plots).  
4696

4697 The Antarctic-Plots Python package aims to help automate common tasks as-  
4698 sociated with researching Antarctica. There are four main modules of the package;  
4699 **Fetch**, **Map**, **Profile**, and **Regions**.

### 4701 D.1 Fetch

4702 The Fetch module contains functions to download data related to Antarctica. These  
4703 downloads are accomplished with the Python package Pooch Uieda et al. (2020).  
4704 Calls to these functions will download the respective data and store it in a com-  
4705 mon folder in your system. Subsequent calls to the same function will retrieve the  
4706 already downloaded file. There is no need for remembering file paths or having  
4707 multiple copies of the same data throughout your projects. Additionally, some of  
4708 this data is pre-processed. This pre-processing includes re-projecting all data (grid-  
4709 ded or tabular) to a common projection, South Polar Stereographic (EPSG:3031),  
4710 and converting pre-gridded tabular data into more useful formats, such as Xarray  
4711 dataarrays. (Hoyer & Hamman, 2017).

4712 This module currently contains over 40 datasets, which include; topography  
4713 products, imagery, grounding line, coastline, and basin shapefiles, gravity, magnetics,  
4714 geothermal heat flow, ice velocity, sediment thickness, moho depths, basal melt,  
4715 ice mass change, and geologic units and faults. Below is an example that downloads,  
4716 or retrieves if already download, BedMachine v3 surface elevation data, converted  
4717 to be referenced to the WGS-84 ellipsoid (as opposed to the original data which is  
4718 referenced to the geoid), and resampled at a 5 km spacing.

```
4720 from antarctic_plots import fetch
4721
4722 surface_data = fetch.bedmachine(
4723     layer="surface",
4724     reference="ellipsoid",
4725     spacing=5000,
4726 )
```

## 4728 D.2 Map

4729 The Map module provides convenient methods for plotting geospatial data. Most of  
4730 these plotting functions use the Python package PyGMT (Uieda et al., 2021). All  
4731 of the maps in Chapters 3, 4, & 5 were created with the help of these functions. In  
4732 addition to static figures, there are several functions for creating interactive figures,  
4733 which help with data visualization.

## 4734 D.3 Profile

4735 The Profile module is used to sample gridded data along specified profiles, and plot  
4736 cross-sections and profiles of the data. The cross-section plots of Chapters 3 & 4 were  
4737 created using these functions. Profiles can be defined by clicking on an interactive  
4738 map to help with quickly exploring and visualizing datasets.

## 4739 D.4 Regions

4740 The Regions module provides pre-defined variables of region boundaries in EPSG:3031  
4741 for commonly studied Antarctic areas. These region variables are used by the  
4742 other modules to subset the desired region. For example, if you only want to fetch  
4743 BedMap2 surface topography only for the Ross Ice Shelf, instead of the whole continent,  
4744 you can pass the parameter "region = regions.ross\_ice\_shelf".

4745 Additionally, there are geospatial tools provided for re-projecting, masking, and  
4746 gridding data. This package is still early in its development and many more datasets  
4747 and functions will still be added.

# 4748 Bibliography

- 4749 Adusumilli, S., Fricker, H. A., Medley, B., Padman, L., & Siegfried, M. R. (2020). Interannual  
4750 variations in meltwater input to the Southern Ocean from Antarctic ice shelves. *Nature  
4751 Geoscience*, *13*(9), 616–620. <https://doi.org/10.1038/s41561-020-0616-z> (cit. on pp. 16,  
4752 39, 90, 131, 132, 141)
- 4753 Aitken, A., Li, L., Kulessa, B., Schroeder, D., Jordan, T., Whittaker, J., Anandakrishnan, S.,  
4754 Dawson, E., Wiens, D., Eisen, O., & Siegert, M. (2023a). *Antarctic sedimentary basin  
4755 distribution and classification* (Version v1.04). Zenodo. <https://doi.org/10.5281/zenodo.7984586>. (Cit. on p. 139)
- 4756 Aitken, A. R., Li, L., Kulessa, B., Schroeder, D. M., Jordan, T. A., Whittaker, J. M., Anandakr-  
4757 ishnan, S., Dawson, E. J., Wiens, D. A., Eisen, O., & Siegert, M. J. (2023b). *Antarctica's  
4758 sedimentary basins and their influence on ice sheet dynamics* (Preprint). Preprints. <https://doi.org/10.1002/essoar.10510905.2>. (Cit. on pp. 17, 20, 138)
- 4759 Akiba, T., Sano, S., Yanase, T., Ohta, T., & Koyama, M. (2019). Optuna: A Next-generation  
4760 Hyperparameter Optimization Framework. *Proceedings of the 25th ACM SIGKDD Interna-  
4761 tional Conference on Knowledge Discovery & Data Mining*, 2623–2631. <https://doi.org/10.1145/3292500.3330701> (cit. on p. 51)
- 4762 Aleshkova, N. D., Golynsky, A. V., Kurinin, R. G., & Mandrikov, V. S. (2000). Gravity Mapping in  
4763 the Southern Weddell Sea Region. (Explanatory note for free-air and Bouguer anomalies  
4764 maps). *Polarforschung*, 15 pages. <https://doi.org/10.2312/POLARFORSCHUNG.67.3.163>  
4765 (cit. on p. 149)
- 4766 Alley, R. B., Blankenship, D. D., Bentley, C. R., & Rooney, S. T. (1986). Deformation of till  
4767 beneath ice stream B, West Antarctica. *Nature*, *322*(6074), 57–59. <https://doi.org/10.1038/322057a0> (cit. on pp. 20, 144)
- 4768 An, L., Rignot, E., Elieff, S., Morlighem, M., Millan, R., Mouginot, J., Holland, D. M., Holland,  
4769 D., & Paden, J. (2017). Bed elevation of Jakobshavn Isbrae, West Greenland, from high-  
4770 resolution airborne gravity and other data. *Geophysical Research Letters*, *44*(8), 3728–  
4771 3736. <https://doi.org/10.1002/2017GL073245> (cit. on pp. 105, 106, 120)
- 4772 An, L., Rignot, E., Chauche, N., Holland, D. M., Holland, D., Jakobsson, M., Kane, E., Wood,  
4773 M., Klaucke, I., Morlighem, M., Velicogna, I., Weinrebe, W., & Willis, J. K. (2019a).  
4774 Bathymetry of Southeast Greenland From Oceans Melting Greenland (OMG) Data. *Geo-  
4775 physical Research Letters*, *46*(20), 11197–11205. <https://doi.org/10.1029/2019GL083953>  
4776 (cit. on pp. 46, 63, 105–107, 120, 122)
- 4777 An, L., Rignot, E., Millan, R., Tinto, K., & Willis, J. (2019b). Bathymetry of Northwest Greenland  
4778 Using “Ocean Melting Greenland” (OMG) High-Resolution Airborne Gravity and Other  
4779 Data. *Remote Sensing*, *11*(2), 131. <https://doi.org/10.3390/rs11020131> (cit. on pp. 105–  
4780 107)
- 4781 An, M., Wiens, D. A., Zhao, Y., Feng, M., Nyblade, A. A., Kanao, M., Li, Y., Maggi, A., & Lévéque,  
4782 J.-J. (2015). S-velocity model and inferred Moho topography beneath the Antarctic Plate  
4783 from Rayleigh waves: Antarctic S-velocities and Moho. *Journal of Geophysical Research:  
4784 Solid Earth*, *120*(1), 359–383. <https://doi.org/10.1002/2014JB011332> (cit. on pp. 29, 155)
- 4785 Anandakrishnan, S., Blankenship, D. D., Alley, R. B., & Stoffa, P. L. (1998). Influence of subglacial  
4786 geology on the position of a West Antarctic ice stream from seismic observations. *Nature*,  
4787 *394*(6688), 62–65. <https://doi.org/10.1038/27889> (cit. on p. 20)
- 4788 Anderson, J. B., Conway, H., Bart, P. J., Witus, A. E., Greenwood, S. L., McKay, R., Hall, B. H.,  
4789 Ackert, R. P., Licht, K., Jakobsson, M., & Stone, J. O. (2014). Ross Sea paleo-ice drainage  
4790 and deglacial history during and since the LGM. *Quaternary Science Reviews*, *100*, 31–54.  
4791 <https://doi.org/10.1016/j.quascirev.2013.08.020> (cit. on p. 16)

- 4796 Anderson, J. B., Simkins, L. M., Bart, P. J., De Santis, L., Halberstadt, A. R. W., Olivo, E., &  
 4797 Greenwood, S. L. (2019). Seismic and geomorphic records of Antarctic Ice Sheet evolution  
 4798 in the Ross Sea and controlling factors in its behaviour. *Geological Society, London, Special*  
 4799 *Publications*, 475(1), 223–240. <https://doi.org/10.1144/SP475.5> (cit. on pp. 16, 20, 145–  
 4800 147)
- 4801 Andrews, J. T., & LeMasurier, W. (2021). Resolving the argument about volcanic bedrock under  
 4802 the West Antarctic Ice Sheet and implications for ice sheet stability and sea level change.  
*Earth and Planetary Science Letters*, 568, 117035. [https://doi.org/10.1016/j.epsl.2021.](https://doi.org/10.1016/j.epsl.2021.117035)  
 4804 117035 (cit. on p. 152)
- 4805 Aster, R. C., Borchers, B., & Thurber, C. H. (2018). *Parameter estimation and inverse problems*.  
 4806 Elsevier. (Cit. on pp. 42, 48, 103, 106).
- 4807 Austermann, J., Pollard, D., Mitrovica, J. X., Moucha, R., Forte, A. M., DeConto, R. M., Rowley,  
 4808 D. B., & Raymo, M. E. (2015). The impact of dynamic topography change on Antarctic  
 4809 ice sheet stability during the mid-Pliocene warm period. *Geology*, 43(10), 927–930. <https://doi.org/10.1130/G36988.1> (cit. on p. 26)
- 4811 Bamber, J. L., Oppenheimer, M., Kopp, R. E., Aspinall, W. P., & Cooke, R. M. (2022). Ice  
 4812 Sheet and Climate Processes Driving the Uncertainty in Projections of Future Sea Level  
 4813 Rise: Findings From a Structured Expert Judgement Approach. *Earth's Future*, 10(10).  
 4814 <https://doi.org/10.1029/2022EF002772> (cit. on pp. 15, 16)
- 4815 Bamber, J., & Bentley, C. R. (1994). A comparison of satellite-altimetry and ice-thickness mea-  
 4816 surements of the Ross Ice Shelf, Antarctica. *Annals of Glaciology*, 20, 357–364. <https://doi.org/10.3189/1994AoG20-1-357-364> (cit. on p. 38)
- 4818 Barbosa, V. C., Menezes, P. T., & Silva, J. B. (2007). Gravity data as a tool for detecting faults:  
 4819 In-depth enhancement of subtle Almada's basement faults, Brazil. *GEOPHYSICS*, 72(3),  
 4820 B59–B68. <https://doi.org/10.1190/1.2713226> (cit. on p. 42)
- 4821 Barletta, V. R., Bevis, M., Smith, B. E., Wilson, T., Brown, A., Bordoni, A., Willis, M., Khan,  
 4822 S. A., Rovira-Navarro, M., Dalziel, I., Smalley, R., Kendrick, E., Konfal, S., Caccamise,  
 4823 D. J., Aster, R. C., Nyblade, A., & Wiens, D. A. (2018). Observed rapid bedrock uplift in  
 4824 Amundsen Sea Embayment promotes ice-sheet stability. *Science*, 360(6395), 1335–1339.  
 4825 <https://doi.org/10.1126/science.aa01447> (cit. on pp. 18, 143, 144)
- 4826 Bart, P., & De Santis, L. (2012). Glacial intensification during the Neogene: A review of seismic  
 4827 stratigraphic evidence from the Ross Sea, Antarctica, continental shelf. *Oceanography*,  
 4828 25(3), 166–183. <https://doi.org/10.5670/oceanog.2012.92> (cit. on p. 34)
- 4829 Bart, P. J., Krogmeier, B. J., Bart, M. P., & Tulaczyk, S. (2017). The paradox of a long grounding  
 4830 during West Antarctic Ice Sheet retreat in Ross Sea. *Scientific Reports*, 7(1), 1262. <https://doi.org/10.1038/s41598-017-01329-8> (cit. on p. 146)
- 4832 Beaudoin, B. C., ten Brink, U. S., & Stern, T. A. (1992). Characteristics and processing of seismic  
 4833 data collected on thick, floating ice: Results from the Ross Ice Shelf, Antarctica. *Geo-  
 4834 physics*, 57(10), 1359–1372. <https://doi.org/10.1190/1.1443205> (cit. on p. 31)
- 4835 Begeman, C. B., Tulaczyk, S. M., & Fisher, A. T. (2017). Spatially Variable Geothermal Heat  
 4836 Flux in West Antarctica: Evidence and Implications. *Geophysical Research Letters*, 44(19),  
 4837 9823–9832. <https://doi.org/10.1002/2017GL075579> (cit. on pp. 28, 144)
- 4838 Bell, R. E., Blankenship, D. D., Finn, C. A., Morse, D. L., Scambos, T. A., Brozena, J. M., &  
 4839 Hodge, S. M. (1998). Influence of subglacial geology on the onset of a West Antarctic ice  
 4840 stream from aerogeophysical observations. *Nature*, 394(6688), 58–62. <https://doi.org/10.1038/27883> (cit. on p. 19)
- 4842 Bell, R. E., Studinger, M., Karner, G., Finn, C. A., & Blankenship, D. D. (2006). Identifying  
 4843 major sedimentary basins beneath the West Antarctic Ice Sheet from aeromagnetic data  
 4844 analysis. In D. K. Fütterer, D. Damaske, G. Kleinschmidt, H. Miller, & F. Tessensohn  
 4845 (Eds.), *Antarctica* (pp. 117–121). Springer-Verlag. [https://doi.org/10.1007/3-540-32934-X\\_13](https://doi.org/10.1007/3-540-32934-X_13). (Cit. on pp. 28, 30–32, 153)
- 4847 Bell, R. E., Ferraccioli, F., Creyts, T. T., Braaten, D., Corr, H., Das, I., Damaske, D., Frearson,  
 4848 N., Jordan, T., Rose, K., Studinger, M., & Wolovick, M. (2011). Widespread Persistent  
 4849 Thickening of the East Antarctic Ice Sheet by Freezing from the Base. *Science*, 331(6024),  
 4850 1592–1595. <https://doi.org/10.1126/science.1200109> (cit. on p. 26)
- 4851 Bennett, H. F. (1964). *A gravity and magnetic survey of the Ross Ice Shelf area, Antarctica* (tech.  
 4852 rep. No. 64-3). The University of Wisconsin. Madison. (Cit. on p. 108).
- 4853 Bentley, C. R., Cray, A. P., Ostenso, N. A., & Thiel, E. C. (1960). Structure of West Antarctica.  
 4854 *Science*, 131(3394), 131–136. <https://doi.org/10.1126/science.131.3394.131> (cit. on p. 21)

- 4855 Bentley, C. R. (1984). The Ross Ice Shelf: Glaciology and Geophysics Paper 1: Introduction and  
 4856 summary of measurements performed. In C. R. Bentley & D. E. Hayes (Eds.), *Antarctic*  
 4857 *Research Series* (pp. 1–20). American Geophysical Union. <https://doi.org/10.1029/AR042p0001>. (Cit. on pp. 18, 21, 91, 108, 111)
- 4859 Block, A. E., Bell, R. E., & Studinger, M. (2009). Antarctic crustal thickness from satellite gravity:  
 4860 Implications for the Transantarctic and Gamburtsev Subglacial Mountains. *Earth and*  
 4861 *Planetary Science Letters*, 288(1-2), 194–203. <https://doi.org/10.1016/j.epsl.2009.09.022>  
 4862 (cit. on p. 133)
- 4863 Boghosian, A., Tinto, K., Cochran, J. R., Porter, D., Elieff, S., Burton, B. L., & Bell, R. E. (2015).  
 4864 Resolving bathymetry from airborne gravity along Greenland fjords. *Journal of Geophysical*  
 4865 *Research: Solid Earth*, 120(12), 8516–8533. <https://doi.org/10.1002/2015JB012129>  
 4866 (cit. on pp. 78, 104–107, 120)
- 4867 Borg, S. G., Depaolo, D. J., & Smith, B. M. (1990). Isotopic structure and tectonics of the central  
 4868 Transantarctic mountains. *Journal of Geophysical Research*, 95(B5), 6647. <https://doi.org/10.1029/JB095iB05p06647> (cit. on pp. 32, 34)
- 4870 Borghi, A. (2022). Moho depths for Antarctica Region by the inversion of ground-based gravity  
 4871 data. *Geophysical Journal International*, 231(2), 1404–1420. <https://doi.org/10.1093/gji/ggac249> (cit. on p. 42)
- 4873 Bougamont, M., Christoffersen, P., Price, S. F., Fricker, H. A., Tulaczyk, S., & Carter, S. P. (2015).  
 4874 Reactivation of Kamb Ice Stream tributaries triggers century-scale reorganization of Siple  
 4875 Coast ice flow in West Antarctica: Restructuring of Siple Coast Ice Flow. *Geophysical*  
 4876 *Research Letters*, 42(20), 8471–8480. <https://doi.org/10.1002/2015GL065782> (cit. on  
 4877 p. 145)
- 4878 Bourgeois, B. S., Elmore, P. A., Avera, W. E., & Zambo, S. J. (2016). Achieving comparable uncer-  
 4879 tainty estimates with Kalman filters or linear smoothers for bathymetry data. *Geochemistry,*  
 4880 *Geophysics, Geosystems*, 17(7), 2576–2590. <https://doi.org/10.1002/2015GC006239>  
 4881 (cit. on pp. 84, 85)
- 4882 Brancolini, G., Busetti, M., Marchetti, A., Santis, L. D., Zanolla, C., Cooper, A. K., Cochrane,  
 4883 G. R., Zayatz, I., Belyaev, V., Knyazev, M., Vinnikovskaya, O., Davey, F. J., & Hinze, K.  
 4884 (1995). Descriptive text for the seismic stratigraphic atlas of the Ross Sea, Antarctica. In  
 4885 A. K. Cooper, P. F. Barker, & G. Brancolini (Eds.), *Geology and Seismic Stratigraphy of*  
 4886 *the Antarctic Margin* (A271–A286). American Geophysical Union. <https://doi.org/10.1002/9781118669013.app1>. (Cit. on pp. 26–28, 67, 68, 147, 151, 153, 156)
- 4888 Brisbourne, A. M., Kulessa, B., Hudson, T., Harrison, L., Holland, P., Luckman, A., Bevan, S.,  
 4889 Ashmore, D., Hubbard, B., Pearce, E., White, J., Booth, A., Nicholls, K., & Smith, A.  
 4890 (2020). An updated seabed bathymetry beneath Larsen C Ice Shelf, Antarctic Peninsula.  
 4891 *Earth System Science Data*, 12(2), 887–896. <https://doi.org/10.5194/essd-12-887-2020>  
 4892 (cit. on pp. 70, 124, 149)
- 4893 Brisbourne, A. M., Smith, A. M., King, E. C., Nicholls, K. W., Holland, P. R., & Makinson,  
 4894 K. (2014). Seabed topography beneath Larsen C Ice Shelf from seismic soundings. *The*  
 4895 *Cryosphere*, 8(1), 1–13. <https://doi.org/10.5194/tc-8-1-2014> (cit. on pp. 45, 80, 99, 120)
- 4896 Burton-Johnson, A., Dziadek, R., & Martin, C. (2020). Geothermal heat flow in Antarctica: Current  
 4897 and future directions. *The Cryosphere Discussions*, 1–45. <https://doi.org/10.5194/tc-2020-59> (cit. on pp. 32, 139, 144, 145)
- 4899 Calder, B., & Elmore, P. (2017). Development of an Uncertainty Propagation Equation for Scalar  
 4900 Fields. *Marine Geodesy*, 40(5), 341–360. <https://doi.org/10.1080/01490419.2017.1345811>  
 4901 (cit. on p. 85)
- 4902 Catania, G., Hulbe, C., Conway, H., Scambos, T., & Raymond, C. (2012). Variability in the  
 4903 mass flux of the Ross ice streams, West Antarctica, over the last millennium. *Journal of*  
 4904 *Glaciology*, 58(210), 741–752. <https://doi.org/10.3189/2012JoG11J219> (cit. on p. 145)
- 4905 Chen, B., Haeger, C., Kaban, M. K., & Petrunin, A. G. (2018). Variations of the effective elastic  
 4906 thickness reveal tectonic fragmentation of the Antarctic lithosphere. *Tectonophysics*, 746,  
 4907 412–424. <https://doi.org/10.1016/j.tecto.2017.06.012> (cit. on p. 143)
- 4908 Cheng, W., Hu, X. G., & Liu, L. T. (2021). Anisotropy Gradients in the Middle of the Ross Sea  
 4909 Embayment, West Antarctica: Evidence From QL Scattered Surface Waves. *Geophysical*  
 4910 *Research Letters*, 48(6). <https://doi.org/10.1029/2020GL091232> (cit. on p. 34)
- 4911 Chiappini, M., Ferraccioli, F., Bozzo, E., & Damaske, D. (2002). Regional compilation and analysis  
 4912 of aeromagnetic anomalies for the Transantarctic Mountains–Ross Sea sector of the Antarc-

- tic. *Tectonophysics*, 347(1-3), 121–137. [https://doi.org/10.1016/S0040-1951\(01\)00241-4](https://doi.org/10.1016/S0040-1951(01)00241-4) (cit. on p. 30)
- Christoffersen, P., Bougamont, M., Carter, S. P., Fricker, H. A., & Tulaczyk, S. (2014). Significant groundwater contribution to Antarctic ice streams hydrologic budget. *Geophysical Research Letters*, 41(6), 2003–2010. <https://doi.org/10.1002/2014GL059250> (cit. on pp. 19, 26, 144, 145)
- Clough, J. W., & Hansen, B. L. (1979). The Ross Ice Shelf Project. *Science*, 203(4379), 433–434. <https://doi.org/10.1126/science.203.4379.433> (cit. on pp. 18, 91)
- Cochran, J. R., Burton, B., Frearson, N., & Tinto, K. (2014a). IceBridge Scintrex CS-3 Cesium magnetometer L1B geolocated magnetic anomalies, version 2. [Line 403, 404]. *Boulder, Colorado USA. NASA National Snow and Ice Data Center Distributed Active Archive Center*. <https://doi.org/10.5067/OY7C2Y61YSYW> (cit. on pp. 28, 151, 153)
- Cochran, J. R., Jacobs, S. S., Tinto, K. J., & Bell, R. E. (2014b). Bathymetric and oceanic controls on Abbot Ice Shelf thickness and stability. *The Cryosphere*, 8(3), 877–889. <https://doi.org/10.5194/tc-8-877-2014> (cit. on pp. 105, 106)
- Cochran, J. R., & Bell, R. E. (2012). Inversion of IceBridge gravity data for continental shelf bathymetry beneath the Larsen Ice Shelf, Antarctica. *Journal of Glaciology*, 58(209), 540–552. <https://doi.org/10.3189/2012JoG11J033> (cit. on pp. 104–106, 149)
- Cochran, J. R., Tinto, K. J., & Bell, R. E. (2020). Detailed Bathymetry of the Continental Shelf Beneath the Getz Ice Shelf, West Antarctica. *Journal of Geophysical Research: Earth Surface*, 125(10). <https://doi.org/10.1029/2019JF005493> (cit. on pp. 46, 104–106, 148)
- Coenen, J. J., Scherer, R. P., Baudoin, P., Warny, S., Castañeda, I. S., & Askin, R. (2019). Paleogene marine and terrestrial development of the West Antarctic Rift System. *Geophysical Research Letters*, 47(3). <https://doi.org/10.1029/2019GL085281> (cit. on pp. 26, 33, 147)
- Colleoni, F., De Santis, L., Montoli, E., Olivo, E., Sorlien, C. C., Bart, P. J., Gasson, E. G. W., Bergamasco, A., Sauli, C., Wardell, N., & Prato, S. (2018). Past continental shelf evolution increased Antarctic ice sheet sensitivity to climatic conditions. *Scientific Reports*, 8(1), 11323. <https://doi.org/10.1038/s41598-018-29718-7> (cit. on p. 26)
- Constantino, R. R., & Tinto, K. J. (2023). Cook Ice Shelf and Ninnis Glacier Tongue Bathymetry From Inversion of Operation Ice Bridge Airborne Gravity Data. *Geophysical Research Letters*, 50(11), e2023GL103815. <https://doi.org/10.1029/2023GL103815> (cit. on pp. 106, 120)
- Constantino, R. R., Tinto, K. J., Bell, R. E., Porter, D. F., & Jordan, T. A. (2020). Seafloor Depth of George VI Sound, Antarctic Peninsula, From Inversion of Aerogravity Data. *Geophysical Research Letters*, 47(21). <https://doi.org/10.1029/2020GL088654> (cit. on pp. 104, 105, 107, 120, 122)
- Cooper, A. K., Barker, P. F., & Brancolini, G. (Eds.). (1995). *Geology and seismic stratigraphy of the Antarctic margin*. AGU. <https://doi.org/10.1029/AR068>. (Cit. on p. 31)
- Coulon, V., Bulthuis, K., Whitehouse, P. L., Sun, S., Haubner, K., Zipf, L., & Pattyn, F. (2021). Contrasting response of West and East Antarctic Ice Sheets to glacial isostatic adjustment. *Journal of Geophysical Research: Earth Surface*, 126(7). <https://doi.org/10.1029/2020JF006003> (cit. on pp. 18, 33, 144)
- Cox, S. C., Smith Lyttle, B., Elkind, S., Smith Siddoway, C., Morin, P., Capponi, G., Abu-Alam, T., Ballinger, M., Bamber, L., Kitchener, B., Lelli, L., Mawson, J., Millikin, A., Dal Seno, N., Whitburn, L., White, T., Burton-Johnson, A., Crispini, L., Elliot, D., ... Wilson, G. (2023). A continent-wide detailed geological map dataset of Antarctica. *Scientific Data*, 10(1), 250. <https://doi.org/10.1038/s41597-023-02152-9> (cit. on pp. 139, 152)
- Crary, A. P. (1961). Marine-sediment thickness in the eastern Ross Sea area, Antarctica. *Geological Society of America Bulletin*, 72(5), 787. [https://doi.org/10.1130/0016-7606\(1961\)72\[787:MTITER\]2.0.CO;2](https://doi.org/10.1130/0016-7606(1961)72[787:MTITER]2.0.CO;2) (cit. on p. 156)
- Crary, A. P., Robinson, E. S., Bennett, H. F., & Boyd, W. (1962). *Glaciological studies on the Ross Ice Shelf, Antarctica; 1957-1960* (tech. rep. No. 6). American Geographical Society. New York, NY, USA. (Cit. on pp. 91, 108).
- Crary, A. (1959). Oversnow Traverses from IGY Little American Station. *Transactions, American Geophysical Union*, 40(3), 311–315. <https://doi.org/10.1029/TR040i003p00269> (cit. on pp. 21, 91, 108)
- Crary, A., & Robinson, E. (1962). Oversnow Traverse from McMurdo to the South Pole. *Science*, 135(3500), 291–295. <https://doi.org/10.1126/science.135.3500.291> (cit. on pp. 91, 108)

- 4971 Dampney, C. N. G. (1969). The equivalent source technique, 15. <https://doi.org/10.1190/1.1439996>  
 4972 (cit. on pp. 57, 112)
- 4973 Das, I., Padman, L., Bell, R. E., Fricker, H. A., Tinto, K. J., Hulbe, C. L., Siddoway, C. S.,  
 4974 Dhakal, T., Frearson, N. P., Mosbeux, C., Cordero, S. I., & Siegfried, M. R. (2020). Multi-  
 4975 decadal basal melt rates and structure of the Ross Ice Shelf, Antarctica using airborne ice  
 4976 penetrating radar. *Journal of Geophysical Research: Earth Surface*, 1–20. <https://doi.org/10.1029/2019JF005241> (cit. on pp. 21, 38, 131, 132, 141)
- 4977 De Rydt, J., Holland, P. R., Dutrieux, P., & Jenkins, A. (2014). Geometric and oceanographic  
 4978 controls on melting beneath Pine Island Glacier. *Journal of Geophysical Research: Oceans*,  
 4980 119(4), 2420–2438. <https://doi.org/10.1002/2013JC009513> (cit. on pp. 16, 90, 91)
- 4981 De Santis, L. (1999). The Eastern Ross Sea continental shelf during the Cenozoic: Implications for  
 4982 the West Antarctic ice sheet development. *Global and Planetary Change*, 23(1-4), 173–196.  
 4983 [https://doi.org/10.1016/S0921-8181\(99\)00056-9](https://doi.org/10.1016/S0921-8181(99)00056-9) (cit. on p. 147)
- 4984 De Santis, L., Anderson, J. B., Brancolini, G., & Zayatz, I. (1995). Seismic record of late Oligocene  
 4985 through Miocene glaciation on the central and eastern continental shelf of the Ross Sea. In  
 4986 A. K. Cooper, P. F. Barker, & G. Brancolini (Eds.), *Antarctic Research Series* (pp. 235–  
 4987 260). American Geophysical Union. <https://doi.org/10.1029/AR068p0235>. (Cit. on pp. 34,  
 4988 147)
- 4989 DeConto, R. M., & Pollard, D. (2003). A coupled climate–ice sheet modeling approach to the  
 4990 Early Cenozoic history of the Antarctic ice sheet. *Palaeogeography, Palaeoclimatology,*  
 4991 *Palaeoecology*, 198(1-2), 39–52. [https://doi.org/10.1016/S0031-0182\(03\)00393-6](https://doi.org/10.1016/S0031-0182(03)00393-6) (cit. on  
 4992 p. 26)
- 4993 Deng, X., & Tang, Z.-a. (2011). Moving Surface Spline Interpolation Based on Green's Function.  
 4994 *Mathematical Geosciences*, 43(6), 663–680. <https://doi.org/10.1007/s11004-011-9346-5>  
 4995 (cit. on p. 63)
- 4996 Dinniman, M. S., Klinck, J. M., & Smith, W. O. (2011). A model study of Circumpolar Deep Water  
 4997 on the West Antarctic Peninsula and Ross Sea continental shelves. *Deep Sea Research Part*  
 4998 *II: Topical Studies in Oceanography*, 58(13-16), 1508–1523. <https://doi.org/10.1016/j.dsr2.2010.11.013> (cit. on pp. 90, 131)
- 5000 Dorschel, B., Hehemann, L., Viquerat, S., Warnke, F., Dreutter, S., Tenberge, Y. S., Accettella, D.,  
 5001 An, L., Barrios, F., Bazhenova, E., Black, J., Bohoyo, F., Davey, C., De Santis, L., Dotti,  
 5002 C. E., Fremand, A. C., Fretwell, P. T., Gales, J. A., Gao, J., ... Arndt, J. E. (2022). The  
 5003 International Bathymetric Chart of the Southern Ocean Version 2. *Scientific Data*, 9(1),  
 5004 275. <https://doi.org/10.1038/s41597-022-01366-7> (cit. on pp. 67, 68, 70)  
 5005 IBCSO
- 5006 Dowdeswell, J., Evans, J., Mugford, R., Griffiths, G., McPhail, S., Millard, N., Stevenson, P., Brandon,  
 5007 M., Banks, C., Heywood, K., Price, M., Dodd, P., Jenkins, A., Nicholls, K., Hayes,  
 5008 D., Abrahamsen, E., Tyler, P., Bett, B., Jones, D., ... Ackley, S. (2008). Autonomous  
 5009 underwater vehicles (AUVs) and investigations of the ice–ocean interface in Antarctic  
 5010 and Arctic waters. *Journal of Glaciology*, 54(187), 661–672. <https://doi.org/10.3189/002214308786570773> (cit. on p. 18)
- 5012 Drenth, B. J., Grauch, V., Turner, K. J., Rodriguez, B. D., Thompson, R. A., & Bauer, P. W.  
 5013 (2019). A shallow rift basin segmented in space and time: The southern San Luis Basin,  
 5014 Rio Grande rift, northern New Mexico, U.S.A. *Rocky Mountain Geology*, 54(2), 97–131.  
 5015 <https://doi.org/10.24872/rmgjournal.54.2.97> (cit. on p. 29)
- 5016 Dupont, T. K., & Alley, R. B. (2005). Assessment of the importance of ice-shelf buttressing to  
 5017 ice-sheet flow. *Geophysical Research Letters*, 32, 1–4. <https://doi.org/10.1029/2004GL022024> (cit. on pp. 17, 38, 90)
- 5019 Durand, G., van den Broeke, M. R., Le Cozannet, G., Edwards, T. L., Holland, P. R., Jourdain,  
 5020 N. C., Marzeion, B., Mottram, R., Nicholls, R. J., Pattyn, F., Paul, F., Slangen, A. B. A.,  
 5021 Winkelmann, R., Burgard, C., van Calcar, C. J., Barré, J.-B., Bataille, A., & Chapuis, A.  
 5022 (2022). Sea-Level Rise: From Global Perspectives to Local Services. *Frontiers in Marine*  
 5023 *Science*, 8, 709595. <https://doi.org/10.3389/fmars.2021.709595> (cit. on pp. 15, 137)
- 5024 Dutrieux, P., De Rydt, J., Jenkins, A., Holland, P. R., Ha, H. K., Lee, S. H., Steig, E. J., Ding,  
 5025 Q., Abrahamsen, E. P., & Schröder, M. (2014). Strong Sensitivity of Pine Island Ice-Shelf  
 5026 Melting to Climatic Variability. *Science*, 343(6167), 174–178. <https://doi.org/10.1126/science.1244341> (cit. on p. 90)
- 5028 Edwards, T. L., Nowicki, S., Marzeion, B., Hock, R., Goelzer, H., Seroussi, H., Jourdain, N. C.,  
 5029 Slater, D. A., Turner, F. E., Smith, C. J., McKenna, C. M., Simon, E., Abe-Ouchi, A.,

- 5030        Gregory, J. M., Larour, E., Lipscomb, W. H., Payne, A. J., Shepherd, A., Agosta, C., ...  
 5031        Zwinger, T. (2021). Projected land ice contributions to twenty-first-century sea level rise.  
 5032        *Nature*, 593(7857), 74–82. <https://doi.org/10.1038/s41586-021-03302-y> (cit. on p. 15)
- 5033        Eisermann, H., Eagles, G., Ruppel, A., Smith, E. C., & Jokat, W. (2020). Bathymetry Beneath Ice  
 5034        Shelves of Western Dronning Maud Land, East Antarctica, and Implications on Ice Shelf  
 5035        Stability. *Geophysical Research Letters*, 47(12). <https://doi.org/10.1029/2019GL086724>  
 5036        (cit. on pp. 45, 104–106, 120)
- 5037        Eisermann, H., Eagles, G., Ruppel, A. S., Läufer, A., & Jokat, W. (2021). Bathymetric Control  
 5038        on Borchgrevink and Roi Baudouin Ice Shelves in East Antarctica. *Journal of Geophysical*  
 5039        *Research: Earth Surface*, 126(10). <https://doi.org/10.1029/2021JF006342> (cit. on pp. 105,  
 5040        106, 120)
- 5041        Fahnestock, M. A., Scambos, T. A., Bindschadler, R. A., & Kvaran, G. (2000). A millennium of  
 5042        variable ice flow recorded by the Ross Ice Shelf, Antarctica. *Journal of Glaciology*, 13.  
 5043        <https://doi.org/10.3189/172756500781832693> (cit. on p. 143)
- 5044        Fatiando a Terra Project, Dinneen, C., Gomez, M., Li, L., Pesce, A., Soler, S. R., & Uieda, L.  
 5045        (2022). Boule v0.4.1: Reference ellipsoids for geodesy and geophysics. <https://doi.org/10.5281/zenodo.7258175>. (Cit. on p. 169)
- 5047        Fatiando a Terra Project, Esteban, F. D., Li, L., Oliveira, V. C., Pesce, A., Shea, N., Soler, S. R.,  
 5048        Tankersley, M., & Uieda, L. (2023). Harmonica v0.6.0: Forward modeling, inversion, and  
 5049        processing gravity and magnetic data. <https://doi.org/10.5281/zenodo.7690145>. (Cit. on  
 5050        pp. 43, 48, 51, 95)
- 5051        Ferraccioli, F., Bozzo, E., & Damaske, D. (2002). Aeromagnetic signatures over western Marie Byrd  
 5052        Land provide insight into magmatic arc basement, mafic magmatism and structure of the  
 5053        Eastern Ross Sea Rift flank. *Tectonophysics*, 347, 139–165. [https://doi.org/10.1016/S0040-1951\(01\)00242-6](https://doi.org/10.1016/S0040-1951(01)00242-6) (cit. on p. 30)
- 5055        Filina, I. Y., Blankenship, D. D., Thoma, M., Lukin, V. V., Masolov, V. N., & Sen, M. K. (2008).  
 5056        New 3D bathymetry and sediment distribution in Lake Vostok: Implication for pre-glacial  
 5057        origin and numerical modeling of the internal processes within the lake. *Earth and Plan-  
 5058        etary Science Letters*, 276(1-2), 106–114. <https://doi.org/10.1016/j.epsl.2008.09.012>  
 5059        (cit. on pp. 106, 120)
- 5060        Finn, C. (2002). *Examples of the utility of magnetic anomaly data for geologic mapping* (Open-File  
 5061        Report No. 02-400). USGS. Denver, Colorado. (Cit. on p. 29).
- 5062        Fisher, A. T., Mankoff, K. D., Tulaczyk, S. M., Tyler, S. W., Foley, N., & and the WISSARD  
 5063        Science Team. (2015). High geothermal heat flux measured below the West Antarctic Ice  
 5064        Sheet. *Science Advances*, 1, 1–9. <https://doi.org/10.1126/sciadv.1500093> (cit. on pp. 33,  
 5065        145)
- 5066        Ford, A., & Barrett, P. J. (1975). *Basement rocks of the south-central Ross Sea, site 270, DSDP  
 5067        leg 28* (tech. rep.). Texas A & M University, Ocean Drilling Program. College Station, TX,  
 5068        United States. <https://doi.org/10.2973/dsdp.proc.28.130.1975>. (Cit. on p. 26)
- 5069        Forsberg, R. (2020). Preliminary compilation of Antarctica gravity and gravity gradient data (cit.  
 5070        on p. 139).
- 5071        Förste, C., Bruinsma, S., Abrikosov, O., Lemoine, J.-M., Marty, J. C., Flechtner, F., Balmino, G.,  
 5072        Barthelmes, F., & Biancale, R. (2014). EIGEN-6C4 The latest combined global gravity  
 5073        field model including GOCE data up to degree and order 2190 of GFZ Potsdam and GRGS  
 5074        Toulouse. <https://doi.org/10.5880/ICGEM.2015.1>. (Cit. on pp. 95, 169)
- 5075        Fox Maule, C., Purucker, M. E., Olsen, N., & Mosegaard, K. (2005). Heat Flux Anomalies in  
 5076        Antarctica Revealed by Satellite Magnetic Data. *Science*, 309(5733), 464–467. <https://doi.org/10.1126/science.1106888> (cit. on p. 144)
- 5078        Frederick, B. C., Young, D. A., Blankenship, D. D., Richter, T. G., Kempf, S. D., Ferraccioli, F.,  
 5079        & Siegert, M. J. (2016). Distribution of subglacial sediments across the Wilkes Subglacial  
 5080        Basin, East Antarctica. *Journal of Geophysical Research: Earth Surface*, 121(4), 790–813.  
 5081        <https://doi.org/10.1002/2015JF003760> (cit. on pp. 28, 153)
- 5082        Frémard, A. C., Fretwell, P., Bodart, J., Pritchard, H. D., Aitken, A., Bamber, J. L., Bell, R.,  
 5083        Bianchi, C., Bingham, R. G., Blankenship, D. D., Casassa, G., Catania, G., Christianson,  
 5084        K., Conway, H., Corr, H. F. J., Cui, X., Damaske, D., Damm, V., Drews, R., ... Zirizzotti,  
 5085        A. (2022). Antarctic Bedmap data: FAIR sharing of 60 years of ice bed, surface and  
 5086        thickness data. *Earth System Science Data Discussions*, 1–25. <https://doi.org/10.5194/essd-2022-355> (cit. on p. 17)

- 5088 Fretwell, P., Pritchard, H. D., Vaughan, D. G., Bamber, J. L., Barrand, N. E., Bell, R. E., Bianchi,  
 5089 C., Bingham, R. G., Blankenship, D. D., Casassa, G., Catania, G., Callens, D., Conway,  
 5090 H., Cook, A. J., Corr, H. F. J., Damaske, D., Damm, V., Ferraccioli, F., Forsberg, R.,  
 5091 ... Zirizzotti, A. (2013). Bedmap2: Improved ice bed, surface and thickness datasets for  
 5092 Antarctica. *The Cryosphere*, 7(1), 375–393. <https://doi.org/10.5194/tc-7-375-2013> (cit.  
 5093 on pp. 15, 18, 20, 77, 90, 91, 97, 98, 107, 108, 124, 137, 149, 159)
- 5094 Fricker, H. A., Popov, S., Allison, I., & Young, N. (2001). Distribution of marine ice beneath the  
 5095 Amery Ice Shelf. *Geophysical Research Letters*, 28(11), 2241–2244. <https://doi.org/10.1029/2000GL012461> (cit. on p. 121)
- 5096 Fürst, J. J., Durand, G., Gillet-Chaulet, F., Tavard, L., Rankl, M., Braun, M., & Gagliardini, O.  
 5097 (2016). The safety band of Antarctic ice shelves. *Nature Climate Change*, 6(5), 479–482.  
 5098 <https://doi.org/10.1038/nclimate2912> (cit. on p. 90)
- 5099 Gladish, C. V., Holland, D. M., Rosing-Asvid, A., Behrens, J. W., & Boje, J. (2015). Oceanic  
 5100 Boundary Conditions for Jakobshavn Glacier. Part I: Variability and Renewal of Ilulissat  
 5101 Icefjord Waters, 2001–14. *Journal of Physical Oceanography*, 45(1), 3–32. <https://doi.org/10.1175/JPO-D-14-0044.1> (cit. on p. 90)
- 5102 Goldberg, D. N., Gourmelen, N., Kimura, S., Millan, R., & Snow, K. (2019). How Accurately  
 5103 Should We Model Ice Shelf Melt Rates? *Geophysical Research Letters*, 46(1), 189–199.  
 5104 <https://doi.org/10.1029/2018GL080383> (cit. on p. 91)
- 5105 Goldberg, D. N., Smith, T. A., Narayanan, S. H. K., Heimbach, P., & Morlighem, M. (2020).  
 5106 Bathymetric Influences on Antarctic Ice-Shelf Melt Rates. *Journal of Geophysical Research: Oceans*, 125(11). <https://doi.org/10.1029/2020JC016370> (cit. on pp. 16, 91,  
 5107 92)
- 5108 Golledge, N. R., Marsh, O. J., Rack, W., Braaten, D., & Jones, R. S. (2014). Basal conditions of two  
 5109 Transantarctic Mountains outlet glaciers from observation-constrained diagnostic mod-  
 5110elling. *Journal of Glaciology*, 60(223), 855–866. <https://doi.org/10.3189/2014JoG13J131>  
 5111 (cit. on p. 144)
- 5112 Golynsky, A. V., Ferraccioli, F., Hong, J. K., Golynsky, D. A., von Frese, R. R. B., Young, D. A.,  
 5113 Blankenship, D. D., Holt, J. W., Ivanov, S. V., Kiselev, A. V., Masolov, V. N., Eagles, G.,  
 5114 Gohl, K., Jokat, W., Damaske, D., Finn, C., Aitken, A., Bell, R. E., Armadillo, E., ...  
 5115 Roberts, J. L. (2018). New Magnetic Anomaly Map of the Antarctic: ADMAP2. *Geophys-  
 5116 ical Research Letters*, 45(13), 6437–6449. <https://doi.org/10.1029/2018GL078153> (cit. on  
 5117 p. 139)
- 5118 Gooch, B. T., Young, D. A., & Blankenship, D. D. (2016). Potential groundwater and heteroge-  
 5119 neous heat source contributions to ice sheet dynamics in critical submarine basins of East  
 5120 Antarctica. *Geochemistry, Geophysics, Geosystems*, 17(2), 395–409. <https://doi.org/10.1002/2015GC006117> (cit. on pp. 19, 28, 33, 144, 145)
- 5121 Goodge, J. W. (2020). Geological and tectonic evolution of the Transantarctic Mountains, from  
 5122 ancient craton to recent enigma. *Gondwana Research*, 80, 50–122. <https://doi.org/10.1016/j.gr.2019.11.001> (cit. on pp. 26, 30, 133)
- 5123 Granot, R., & Dyment, J. (2018). Late Cenozoic unification of East and West Antarctica. *Nature  
 5124 Communications*, 9(1), 3189. <https://doi.org/10.1038/s41467-018-05270-w> (cit. on pp. 26,  
 5125 32)
- 5126 Greenbaum, J. S., Blankenship, D. D., Young, D. A., Richter, T. G., Roberts, J. L., Aitken, A. R. A.,  
 5127 Legresy, B., Schroeder, D. M., Warner, R. C., van Ommen, T. D., & Siegert, M. J. (2015).  
 5128 Ocean access to a cavity beneath Totten Glacier in East Antarctica. *Nature Geoscience*,  
 5129 8(4), 294–298. <https://doi.org/10.1038/ngeo2388> (cit. on pp. 104–106, 120)
- 5130 Greene, C. A., Gardner, A. S., Schlegel, N.-J., & Fraser, A. D. (2022). Antarctic calving loss rivals  
 5131 ice-shelf thinning. *Nature*, 609(7929), 948–953. <https://doi.org/10.1038/s41586-022-05037-w> (cit. on p. 16)
- 5132 Greischar, L. L., Bentley, C. R., & Whiting, L. R. (1992). An analysis of gravity measurements on  
 5133 the Ross Ice Shelf, Antarctica. In *Contributions to Antarctic Research III* (pp. 105–155).  
 5134 American Geophysical Union (AGU). <https://doi.org/10.1029/AR057p0105>. (Cit. on  
 5135 pp. 21, 32, 156)
- 5136 Griggs, J. A., & Bamber, J. L. (2011). Antarctic ice-shelf thickness from satellite radar altimetry.  
 5137 *Journal of Glaciology*, 57(203), 485–498. <https://doi.org/10.3189/002214311796905659>  
 5138 (cit. on pp. 38, 112)
- 5139 Gustafson, C. D., Key, K., Siegfried, M. R., Winberry, J. P., Fricker, H. A., Venturelli, R. A.,  
 5140 & Michaud, A. B. (2022). A dynamic saline groundwater system mapped beneath an

- 5147        Antarctic ice stream. *Science*, 376(6593), 640–644. <https://doi.org/10.1126/science.abm3301> (cit. on pp. 19, 26, 32, 33, 144, 145, 156)
- 5148        Halberstadt, A. R. W., Simkins, L. M., Greenwood, S. L., & Anderson, J. B. (2016). Past ice-  
5149        sheet behaviour: Retreat scenarios and changing controls in the Ross Sea, Antarctica. *The  
5150        Cryosphere*, 10(3), 1003–1020. <https://doi.org/10.5194/tc-10-1003-2016> (cit. on pp. 16,  
5151        20, 34, 134, 137, 145, 147)
- 5152        Hammer, S. (1939). Terrain corrections for gravimeter stations. *GEOPHYSICS*, 4(3), 184–194.  
5153        <https://doi.org/10.1190/1.1440495> (cit. on p. 47)
- 5154        Harlan, R. B. (1968). Eotvos corrections for airborne gravimetry. *Journal of Geophysical Research*,  
5155        73(14), 4675–4679. <https://doi.org/10.1029/JB073i014p04675> (cit. on p. 111)
- 5156        Helton, J., Johnson, J., Sallaberry, C., & Storlie, C. (2006). Survey of sampling-based methods for  
5157        uncertainty and sensitivity analysis. *Reliability Engineering & System Safety*, 91(10-11),  
5158        1175–1209. <https://doi.org/10.1016/j.ress.2005.11.017> (cit. on pp. 73, 100–102, 116)
- 5159        Hinze, W. J., Aiken, C., Brozena, J., Coakley, B., Dater, D., Flanagan, G., Forsberg, R., Hilden-  
5160        brand, T., Keller, G. R., Kellogg, J., Kucks, R., Li, X., Mainville, A., Morin, R., Pilk-  
5161        ington, M., Plouff, D., Ravat, D., Roman, D., Urrutia-Fucugauchi, J., ... Winester, D.  
5162        (2005). New standards for reducing gravity data: The North American gravity database.  
5163        *GEOPHYSICS*, 70(4), J25–J32. <https://doi.org/10.1190/1.1988183> (cit. on pp. 92, 93)
- 5164        Hinze, W. J., Von Frese, R., & Saad, A. H. (2013). *Gravity and magnetic exploration: Principles,  
5165        practices, and applications*. Cambridge University Press. (Cit. on p. 92).
- 5166        Hodgson, D. A., Jordan, T. A., De Rydt, J., Fretwell, P. T., Seddon, S. A., Becker, D., Hogan,  
5167        K. A., Smith, A. M., & Vaughan, D. G. (2019). Past and future dynamics of the Brunt Ice  
5168        Shelf from seabed bathymetry and ice shelf geometry. *The Cryosphere*, 13(2), 545–556.  
5169        <https://doi.org/10.5194/tc-13-545-2019> (cit. on pp. 46, 105, 106, 120)
- 5170        Hofmann-Wellenhof, B., & Moritz, H. (2006). *Physical geodesy* (2nd, corrected ed). SpringerWien-  
5171        NewYork. (Cit. on pp. 92, 94).
- 5172        Hofstede, C., Beyer, S., Corr, H., Eisen, O., Hattermann, T., Helm, V., Neckel, N., Smith, E. C.,  
5173        Steinhage, D., Zeising, O., & Humbert, A. (2021). Evidence for a grounding line fan at the  
5174        onset of a basal channel under the ice shelf of Support Force Glacier, Antarctica, revealed  
5175        by reflection seismics. *The Cryosphere*, 15(3), 1517–1535. <https://doi.org/10.5194/tc-15-1517-2021> (cit. on p. 121)
- 5176        Holland, P. R. (2008). A model of tidally dominated ocean processes near ice shelf grounding  
5177        lines. *Journal of Geophysical Research*, 113(C11), C11002. <https://doi.org/10.1029/2007JC004576> (cit. on pp. 16, 133, 141)
- 5178        Horgan, H. J., Hulbe, C., Alley, R. B., Anandakrishnan, S., Goodsell, B., Taylor-Offord, S., &  
5179        Vaughan, M. J. (2017). Poststagnation Retreat of Kamb Ice Stream's Grounding Zone.  
5180        *Geophysical Research Letters*, 44(19), 9815–9822. <https://doi.org/10.1002/2017GL074986>  
5181        (cit. on pp. 21, 129)
- 5182        Horgan, H. J., Walker, R. T., Anandakrishnan, S., & Alley, R. B. (2011). Surface elevation changes  
5183        at the front of the Ross Ice Shelf: Implications for basal melting. *Journal of Geophysical  
5184        Research*, 116(C2), C02005. <https://doi.org/10.1029/2010JC006192> (cit. on p. 131)
- 5185        Horgan, H. J., Christianson, K., Jacobel, R. W., Anandakrishnan, S., & Alley, R. B. (2013). Sediment  
5186        deposition at the modern grounding zone of Whillans Ice Stream, West Antarctica.  
5187        *Geophysical Research Letters*, 40(15), 3934–3939. <https://doi.org/10.1002/grl.50712> (cit.  
5188        on p. 121)
- 5189        Hoyer, S., & Hamman, J. (2017). Xarray: N-D labeled Arrays and Datasets in Python. *Journal of  
5190        Open Research Software*, 5(1), 10. <https://doi.org/10.5334/jors.148> (cit. on p. 171)
- 5191        IceBridge Sander AIRGrav L1B Geolocated Free Air Gravity Anomalies, Version 1. (2020). (Cit.  
5192        on p. 149).
- 5193        Intergovernmental Panel on Climate Change (IPCC). (2022). *The Ocean and Cryosphere in a  
5194        Changing Climate: Special Report of the Intergovernmental Panel on Climate Change* (First). Cambridge University Press. <https://doi.org/10.1017/9781009157964>. (Cit. on  
5195        pp. 15, 137)
- 5196        Jacobs, S., Helmer, H., Doake, C. S. M., Jenkins, A., & Frolich, R. M. (1992). Melting of ice  
5197        shelves and the mass balance of Antarctica. *Journal of Glaciology*, 38(130), 375–387. <https://doi.org/10.3189/S0022143000002252> (cit. on p. 90)
- 5198        Jacoby, W., & Smilde, P. L. (2009). *Gravity interpretation: Fundamentals and application of gravity  
5199        inversion and geological interpretation ; with CD-ROM*. Springer. (Cit. on pp. 42, 93)  
5200        OCLC: 845389531.

- 5206 Jansen, M. J. W., Rossing, W. A. H., & Daamen, R. A. (1994). Monte Carlo Estimation of Uncertainty Contributions from Several Independent Multivariate Sources. In J. Grasman & G. van Straten (Eds.), *Predictability and Nonlinear Modelling in Natural Sciences and Economics* (pp. 334–343). Springer Netherlands. [https://doi.org/10.1007/978-94-011-0962-8\\_28](https://doi.org/10.1007/978-94-011-0962-8_28). (Cit. on pp. 73, 100, 101)
- 5211 Jenkins, A., Dutrieux, P., Jacobs, S. S., McPhail, S. D., Perrett, J. R., Webb, A. T., & White, D. (2010). Observations beneath Pine Island Glacier in West Antarctica and implications for its retreat. *Nature Geoscience*, 3(7), 468–472. <https://doi.org/10.1038/ngeo890> (cit. on p. 38)
- 5215 Jolie, E., Scott, S., Faulds, J., Chambefort, I., Axelsson, G., Gutiérrez-Negrín, L. C., Regenspurg, S., Ziegler, M., Ayling, B., Richter, A., & Zemedkun, M. T. (2021). Geological controls on geothermal resources for power generation. *Nature Reviews Earth & Environment*, 2(5), 324–339. <https://doi.org/10.1038/s43017-021-00154-y> (cit. on pp. 19, 26, 145)
- 5219 Jordan, T. A., Ferraccioli, F., Vaughan, D. G., Holt, J. W., Corr, H., Blankenship, D. D., & Diehl, T. M. (2010). Aerogravity evidence for major crustal thinning under the Pine Island Glacier region (West Antarctica). *Geological Society of America Bulletin*, 122(5-6), 714–726. <https://doi.org/10.1130/B26417.1> (cit. on pp. 78, 85)
- 5223 Jordan, T. A., Riley, T. R., & Siddoway, C. S. (2020a). The geological history and evolution of West Antarctica. *Nature Reviews Earth & Environment*, 1, 117–133. <https://doi.org/10.1038/s43017-019-0013-6> (cit. on pp. 31, 149)
- 5226 Jordan, T. A., Porter, D., Tinto, K., Millan, R., Muto, A., Hogan, K., Larter, R. D., Graham, A. G. C., & Paden, J. D. (2020b). New gravity-derived bathymetry for the Thwaites, Crosson, and Dotson ice shelves revealing two ice shelf populations. *The Cryosphere*, 14(9), 2869–2882. <https://doi.org/10.5194/tc-14-2869-2020> (cit. on pp. 104–106, 120)
- 5230 Kachuck, S. B., Martin, D. F., Bassis, J. N., & Price, S. F. (2020). Rapid Viscoelastic Deformation Slows Marine Ice Sheet Instability at Pine Island Glacier. *Geophysical Research Letters*, 47(10). <https://doi.org/10.1029/2019GL086446> (cit. on pp. 18, 144)
- 5233 Karner, G. D., Studinger, M., & Bell, R. E. (2005). Gravity anomalies of sedimentary basins and their mechanical implications: Application to the Ross Sea basins, West Antarctica. *Earth and Planetary Science Letters*, 235, 577–596. <https://doi.org/10.1016/j.epsl.2005.04.016> (cit. on pp. 26, 28, 147, 153)
- 5237 Kingslake, J., Scherer, R. P., Albrecht, T., Coenen, J., Powell, R. D., Reese, R., Stansell, N. D., Tulaczyk, S., Wearing, M. G., & Whitehouse, P. L. (2018). Extensive retreat and re-advance of the West Antarctic Ice Sheet during the Holocene. *Nature*, 558(7710), 430–434. <https://doi.org/10.1038/s41586-018-0208-x> (cit. on pp. 33, 131, 145)
- 5241 Kirkpatrick, S., Gelatt, C. D., & Vecchi, M. P. (1983). Optimization by Simulated Annealing. *Science*, 220(4598), 671–680. <https://doi.org/10.1126/science.220.4598.671> (cit. on p. 106)
- 5244 Koch, P., Wujek, B., Golovinov, O., & Gardner, S. (2017). Automated Hyperparameter Tuning for Effective Machine Learning. *SAS Institute Inc.* (cit. on p. 103).
- 5246 Kulhanek, D. K., Levy, R. H., Clowes, C. D., Prebble, J. G., Rodelli, D., Jovane, L., Morgans, H. E., Kraus, C., Zwingmann, H., Griffith, E. M., Scher, H. D., McKay, R. M., & Naish, T. R. (2019). Revised chronostratigraphy of DSDP Site 270 and late Oligocene to early Miocene paleoecology of the Ross Sea sector of Antarctica. *Global and Planetary Change*, 178, 46–64. <https://doi.org/10.1016/j.gloplacha.2019.04.002> (cit. on pp. 34, 147)
- 5251 Larour, E., Morlighem, M., Seroussi, H., Schiermeier, J., & Rignot, E. (2012). Ice flow sensitivity to geothermal heat flux of Pine Island Glacier, Antarctica. *Journal of Geophysical Research: Earth Surface*, 117(F04023), 1–12. <https://doi.org/10.1029/2012JF002371> (cit. on p. 144)
- 5254 Le Brocq, A. M., Payne, A. J., & Vieli, A. (2010). An improved Antarctic dataset for high resolution numerical ice sheet models (ALBMAP v1). *Earth System Science Data*, 2(2), 247–260. <https://doi.org/10.5194/essd-2-247-2010> (cit. on pp. 91, 124)
- 5257 Leckie, F. M. (1983). Late Oligocene-early Miocene glacial record of the Ross Sea, Antarctica: Evidence from DSDP Site 270. *Geology*, 11, 578–582. [https://doi.org/10.1130/0091-7613\(1983\)11<578:LOMGRO>2.0.CO;2](https://doi.org/10.1130/0091-7613(1983)11<578:LOMGRO>2.0.CO;2) (cit. on pp. 34, 147)
- 5260 Li, L., Aitken, A. R. A., Lindsay, M. D., & Kulessa, B. (2022). Sedimentary basins reduce stability of Antarctic ice streams through groundwater feedbacks. *Nature Geoscience*. <https://doi.org/10.1038/s41561-022-00992-5> (cit. on pp. 19, 31, 145, 156)

- 5263 Li, X., Zattin, M., & Olivetti, V. (2020). Apatite fission track signatures of the Ross Sea ice flows  
 5264 during the Last Glacial Maximum. *Geochemistry, Geophysics, Geosystems*, 21(10), 1–21.  
 5265 <https://doi.org/10.1029/2019GC008749> (cit. on pp. 33, 148)
- 5266 Li, X., & Götze, H.-J. (2001). Ellipsoid, geoid, gravity, geodesy, and geophysics. *Geophysics*, 66(6),  
 5267 1660–1668. <https://doi.org/10.1190/1.1487109> (cit. on pp. 93, 95)
- 5268 Licht, K. J., Hennessy, A. J., & Welke, B. M. (2014). The U-Pb detrital zircon signature of  
 5269 West Antarctic ice stream tills in the Ross embayment, with implications for Last Glacial  
 5270 Maximum ice flow reconstructions. *Antarctic Science*, 26(6), 687–697. <https://doi.org/10.1017/S0954102014000315> (cit. on pp. 33, 148)
- 5271 Licht, K. J., Lederer, J. R., & Jeffrey Swope, R. (2005). Provenance of LGM glacial till (sand  
 5272 fraction) across the Ross embayment, Antarctica. *Quaternary Science Reviews*, 24(12-13),  
 5273 1499–1520. <https://doi.org/10.1016/j.quascirev.2004.10.017> (cit. on p. 148)
- 5274 Lindeque, A., Gohl, K., Wobbe, F., & Uenzelmann-Neben, G. (2016). Preglacial to glacial sediment  
 5275 thickness grids for the Southern Pacific Margin of West Antarctica: Preglacial, transitional  
 5276 and full glacial isopach maps, West Antarctica. *Geochemistry, Geophysics, Geosystems*,  
 5277 17(10), 4276–4285. <https://doi.org/10.1002/2016GC006401> (cit. on pp. 155, 157)
- 5278 Lloyd, A. J., Wiens, D. A., Nyblade, A. A., Anandakrishnan, S., Aster, R. C., Huerta, A. D.,  
 5279 Wilson, T. J., Dalziel, I. W. D., Shore, P. J., & Zhao, D. (2015). A seismic transect across  
 5280 West Antarctica: Evidence for mantle thermal anomalies beneath the Bentley Subglacial  
 5281 Trench and the Marie Byrd Land Dome. *Journal of Geophysical Research: Solid Earth*,  
 5282 120(12), 8439–8460. <https://doi.org/10.1002/2015JB012455> (cit. on p. 33)
- 5283 Llubes, M., Lanseau, C., & Rémy, F. (2006). Relations between basal condition, subglacial hydro-  
 5284 logical networks and geothermal flux in Antarctica. *Earth and Planetary Science Letters*,  
 5285 241(3-4), 655–662. <https://doi.org/10.1016/j.epsl.2005.10.040> (cit. on p. 18)
- 5286 Lowry, D. P., Golledge, N. R., Bertler, N. A. N., Jones, R. S., & McKay, R. (2019). Deglacial  
 5287 grounding-line retreat in the Ross Embayment, Antarctica, controlled by ocean and atmo-  
 5288 sphere forcing. *Science Advances*, 5, 1–12. <https://doi.org/10.1126/sciadv.aav8754> (cit. on  
 5289 pp. 20, 33, 90, 131, 137)
- 5290 Lowry, D. P., Golledge, N. R., Bertler, N. A., Jones, R. S., McKay, R., & Stutz, J. (2020). Geo-  
 5291 logic controls on ice sheet sensitivity to deglacial climate forcing in the Ross Embayment,  
 5292 Antarctica. *Quaternary Science Advances*, 1, 1–17. <https://doi.org/10.1016/j.qsa.2020.100002> (cit. on pp. 33, 145)
- 5293 Luyendyk, B., Sorlien, C. C., Wilson, D. S., Bartek, L. R., & Siddoway, C. S. (2001). Structural  
 5294 and tectonic evolution of the Ross Sea rift in the Cape Colbeck region, Eastern Ross Sea,  
 5295 Antarctica. *Tectonics*, 20(6), 933–958. <https://doi.org/10.1029/2000TC001260> (cit. on  
 5296 p. 30)
- 5297 Luyendyk, B., Wilson, D. S., & Siddoway, C. S. (2003). Eastern margin of the Ross Sea Rift in  
 5298 western Marie Byrd Land, Antarctica: Crustal structure and tectonic development. *Geo-  
 5299 chemistry, Geophysics, Geosystems*, 4(10), 1–25. <https://doi.org/10.1029/2002GC000462>  
 5300 (cit. on p. 26)
- 5301 Martins, C. M., Barbosa, V. C., & Silva, J. B. (2010). Simultaneous 3D depth-to-basement and  
 5302 density-contrast estimates using gravity data and depth control at few points. *GEO-  
 5303 PHYSICS*, 75(3), I21–I28. <https://doi.org/10.1190/1.3380225> (cit. on p. 106)
- 5304 Matsuoka, K., Hindmarsh, R. C., Moholdt, G., Bentley, M. J., Pritchard, H. D., Brown, J., Con-  
 5305 way, H., Drews, R., Durand, G., Goldberg, D., Hattermann, T., Kingslake, J., Lenaerts,  
 5306 J. T., Martín, C., Mulvaney, R., Nicholls, K. W., Pattyn, F., Ross, N., Scambos, T., &  
 5307 Whitehouse, P. L. (2015). Antarctic ice rises and ripples: Their properties and signifi-  
 5308 cance for ice-sheet dynamics and evolution. *Earth-Science Reviews*, 150, 724–745. <https://doi.org/10.1016/j.earscirev.2015.09.004> (cit. on pp. 16, 90)
- 5309 McCubbine, J. (2016). *Airborne Gravity Across New Zealand - For An Improved Vertical Datum*  
 5310 (Doctoral dissertation). Victoria University of Wellington. (Cit. on p. 47).
- 5311 McKay, R., Golledge, N., Maas, S., Naish, T., Levy, R., Dunbar, G., & Kuhn, G. (2016). Antarctic  
 5312 marine ice-sheet retreat in the Ross Sea during the early Holocene. *Geology*, 44(1), 7–10.  
 5313 <https://doi.org/10.1130/G37315.1> (cit. on p. 145)
- 5314 Menke, W. (2012). *Geophysical data analysis: Discrete inverse theory* (Matlab ed., 3rd ed). Academic Press. (Cit. on p. 39).
- 5315 Millan, R., Rignot, E., Mouginot, J., Wood, M., Bjørk, A. A., & Morlighem, M. (2018). Vulner-  
 5316 ability of Southeast Greenland Glaciers to Warm Atlantic Water From Operation Ice-

- 5321 Bridge and Ocean Melting Greenland Data. *Geophysical Research Letters*, 45(6), 2688–  
 5322 2696. <https://doi.org/10.1002/2017GL076561> (cit. on pp. 105, 106, 120)
- 5323 Millan, R., Rignot, E., Bernier, V., Morlighem, M., & Dutrieux, P. (2017). Bathymetry of the  
 5324 Amundsen Sea Embayment sector of West Antarctica from Operation IceBridge gravity  
 5325 and other data. *Geophysical Research Letters*, 44(3), 1360–1368. <https://doi.org/10.1002/2016GL072071> (cit. on pp. 104–106, 120, 149)
- 5327 Millan, R., St-Laurent, P., Rignot, E., Morlighem, M., Mouginot, J., & Scheuchl, B. (2020). Con-  
 5328 straining an Ocean Model Under Getz Ice Shelf, Antarctica, Using A Gravity-Derived  
 5329 Bathymetry. *Geophysical Research Letters*, 47(13). <https://doi.org/10.1029/2019GL086522>  
 5330 (cit. on pp. 46, 63, 104–106, 120, 122, 149)
- 5331 Moholdt, G., Padman, L., & Fricker, H. A. (2014). Basal mass budget of Ross and Filchner-Ronne  
 5332 ice shelves, Antarctica, derived from Lagrangian analysis of ICESat altimetry: Ice shelf  
 5333 basal melting from altimetry. *Journal of Geophysical Research: Earth Surface*, 119(11),  
 5334 2361–2380. <https://doi.org/10.1002/2014JF003171> (cit. on pp. 20, 90, 131, 137)
- 5335 Mooney, W. D., Laske, G., & Masters, T. G. (1998). CRUST 5.1: A global crustal model at 5° ×  
 5336 5°. *Journal of Geophysical Research: Solid Earth*, 103(B1), 727–747. <https://doi.org/10.1029/97JB02122> (cit. on p. 155)
- 5338 Morlighem, M. (2022). MEaSUREs BedMachine Antarctica, Version 3. (Cit. on pp. 39, 92, 107–  
 5339 109, 112, 113, 115, 117, 118, 124, 125, 128, 130, 146)  
 5340 <https://doi.org/10.5067/FPSU0V1MWUB6>.
- 5341 Morlighem, M., Rignot, E., Binder, T., Blankenship, D., Drews, R., Eagles, G., Eisen, O., Ferraci-  
 5342 cioli, F., Forsberg, R., Fretwell, P., Goel, V., Greenbaum, J. S., Gudmundsson, H., Guo,  
 5343 J., Helm, V., Hofstede, C., Howat, I., Humbert, A., Jokat, W., ... Young, D. A. (2020). Deep  
 5344 glacial troughs and stabilizing ridges unveiled beneath the margins of the Antarctic  
 5345 ice sheet. *Nature Geoscience*, 13(2), 132–137. <https://doi.org/10.1038/s41561-019-0510-8>  
 5346 (cit. on pp. 18, 27, 28, 32, 39, 69, 92, 107–109, 112, 113, 115, 117, 118, 124, 146, 155, 157)  
 5347 BedMachine
- 5348 Mouginot, J., Rignot, E., & Scheuchl, B. (2019). Continent-wide, interferometric SAR phase, map-  
 5349 ping of Antarctic ice velocity. *Geophysical Research Letters*, 46(16), 9710–9718. <https://doi.org/10.1029/2019GL083826> (cit. on p. 32)
- 5351 Mouginot, J., Scheuchl, B., & Rignot, E. (2017). MEaSUREs Antarctic Boundaries for IPY 2007–  
 5352 2009 from Satellite Radar, Version 2. (Cit. on pp. 91, 108–110, 128, 132, 139)  
 5353 <https://doi.org/10.5067/AXE4121732AD>.
- 5354 Müller, R. D., Gohl, K., Cande, S. C., Goncharov, A., & Golynsky, A. V. (2007). Eocene to Miocene  
 5355 geometry of the West Antarctic Rift System. *Australian Journal of Earth Sciences*, 54(8),  
 5356 1033–1045. <https://doi.org/10.1080/08120090701615691> (cit. on pp. 29, 155)
- 5357 Muto, A., Anandakrishnan, S., & Alley, R. B. (2013a). Subglacial bathymetry and sediment layer  
 5358 distribution beneath the Pine Island Glacier ice shelf, West Antarctica, modeled using  
 5359 aerogravity and autonomous underwater vehicle data. *Annals of Glaciology*, 54(64), 27–  
 5360 32. <https://doi.org/10.3189/2013AoG64A110> (cit. on pp. 104, 106, 149)
- 5361 Muto, A., Christianson, K., Horgan, H. J., Anandakrishnan, S., & Alley, R. B. (2013b). Bathymetry  
 5362 and geological structures beneath the Ross Ice Shelf at the mouth of Whillans Ice Stream,  
 5363 West Antarctica, modeled from ground-based gravity measurements. *Journal of Geophys-  
 5364 ical Research: Solid Earth*, 118(8), 4535–4546. <https://doi.org/10.1002/jgrb.50315> (cit. on  
 5365 pp. 21, 32, 105, 131, 133)
- 5366 Muto, A., Peters, L. E., Gohl, K., Sasgen, I., Alley, R. B., Anandakrishnan, S., & Riverman, K. L.  
 5367 (2016). Subglacial bathymetry and sediment distribution beneath Pine Island Glacier ice  
 5368 shelf modeled using aerogravity and in situ geophysical data: New results. *Earth and  
 5369 Planetary Science Letters*, 433, 63–75. <https://doi.org/10.1016/j.epsl.2015.10.037> (cit. on  
 5370 pp. 46, 105–107, 149)
- 5371 Nagy, D., Papp, G., & Benedek, J. (2000). The gravitational potential and its derivatives for the  
 5372 prism. *Journal of Geodesy*, 74(7–8), 552–560. <https://doi.org/10.1007/s001900000116>  
 5373 (cit. on pp. 43, 46, 48, 97)
- 5374 Naish, T., Powell, R., Levy, R., Wilson, G., Scherer, R., Talarico, F., Krissek, L., Niessen, F.,  
 5375 Pompilio, M., Wilson, T., Carter, L., DeConto, R., Huybers, P., McKay, R., Pollard, D., Ross, J., Winter, D., Barrett, P., Browne, G., ... Williams, T. (2009). Obliquity-  
 5377 paced Pliocene West Antarctic ice sheet oscillations. *Nature*, 458(7236), 322–328. <https://doi.org/10.1038/nature07867> (cit. on pp. 20, 90, 137)

- 5379 Nerem, R. S., Beckley, B. D., Fasullo, J. T., Hamilton, B. D., Masters, D., & Mitchum, G. T. (2018).  
 5380 Climate-change-driven accelerated sea-level rise detected in the altimeter era. *Proceedings*  
 5381 *of the National Academy of Sciences*, 115(9), 2022–2025. <https://doi.org/10.1073/pnas.1717312115> (cit. on p. 15)
- 5383 Neuhaus, S. U., Tulaczyk, S. M., Stansell, N. D., Coenen, J. J., Scherer, R. P., Mikucki, J. A., &  
 5384 Powell, R. D. (2021). Did Holocene climate changes drive West Antarctic grounding line  
 5385 retreat and readvance? *The Cryosphere*, 15(10), 4655–4673. <https://doi.org/10.5194/tc-15-4655-2021> (cit. on p. 33)
- 5387 Nicholls, K. W., Abrahamsen, E. P., Buck, J. J. H., Dodd, P. A., Goldblatt, C., Griffiths, G.,  
 5388 Heywood, K. J., Hughes, N. E., Kaletzky, A., Lane-Serff, G. F., McPhail, S. D., Millard,  
 5389 N. W., Oliver, K. I. C., Perrett, J., Price, M. R., Pudsey, C. J., Saw, K., Stansfield, K.,  
 5390 Stott, M. J., ... Wilkinson, J. P. (2006). Measurements beneath an Antarctic ice shelf  
 5391 using an autonomous underwater vehicle. *Geophysical Research Letters*, 33(8), L08612.  
 5392 <https://doi.org/10.1029/2006GL025998> (cit. on p. 18)
- 5393 Oldenburg, D. W. (1974). The inversion and interpretation of gravity anomalies. *Geophysics*, 39(4),  
 5394 526–536 (cit. on p. 106).
- 5395 Oldenburg, D. W., & Li, Y. (2005). Inversion for applied geophysics: A tutorial. In D. K. Butler  
 5396 (Ed.), *Near-Surface Geophysics*. Society of Exploration Geophysicists. <https://doi.org/10.1190/1.9781560801719>. (Cit. on pp. 39, 40, 103)
- 5398 Oldenburg, D. W., & Pratt, D. (2007). Geophysical inversion for mineral exploration: A decade  
 5399 of progress in theory and practice. In B. Milkereit (Ed.), *Proceedings of Exploration 07*  
 5400 (pp. 61–95). (Cit. on p. 42).
- 5401 Oliveira, V. C., & Uieda, L. (2014). Tópicos de inversão em geofísica. *figshare*. <https://doi.org/http://dx.doi.org/10.6084/m9.figshare.1192984> (cit. on p. 40)
- 5403 Oliveira, V. C., Uieda, L., & Hallam, K. A. T. (2018). Should geophysicists use the gravity disturbance or the anomaly?, 11. <https://doi.org/10.5281/zenodo.1255305> (cit. on p. 94)
- 5405 Olivetti, V., Balestrieri, M. L., Chew, D., Zurli, L., Zattin, M., Pace, D., Drakou, F., Cornamusini,  
 5406 G., & Perotti, M. (2023). Ice volume variations and provenance trends in the Oligocene-  
 5407 early Miocene glaciomarine sediments of the Central Ross Sea, Antarctica (DSDP Site 270).  
 5408 *Global and Planetary Change*, 104042. <https://doi.org/10.1016/j.gloplacha.2023.104042>  
 5409 (cit. on pp. 147, 148)
- 5410 Otosaka, I. N., Shepherd, A., Ivins, E. R., Schlegel, N.-J., Amory, C., van den Broeke, M. R.,  
 5411 Horwath, M., Joughin, I., King, M. D., Krinner, G., Nowicki, S., Payne, A. J., Rignot, E.,  
 5412 Scambos, T., Simon, K. M., Smith, B. E., Sørensen, L. S., Velicogna, I., Whitehouse, P. L.,  
 5413 ... Wouters, B. (2023). Mass balance of the Greenland and Antarctic ice sheets from 1992  
 5414 to 2020. *Earth System Science Data*, 15(4), 1597–1616. <https://doi.org/10.5194/essd-15-1597-2023> (cit. on pp. 15, 16)
- 5416 Paige, C. C., & Saunders, M. A. (1982). LSQR: An Algorithm for Sparse Linear Equations and  
 5417 Sparse Least Squares. *ACM Transactions on Mathematical Software*, 8(1), 43–71. <https://doi.org/10.1145/355984.355989> (cit. on p. 48)
- 5419 Pappa, F., Ebbing, J., & Ferraccioli, F. (2019). Moho Depths of Antarctica: Comparison of Seismic,  
 5420 Gravity, and Isostatic Results. *Geochemistry, Geophysics, Geosystems*, 20(3), 1629–1645.  
 5421 <https://doi.org/10.1029/2018GC008111> (cit. on pp. 106, 143)
- 5422 Parker, R. L. (1972). The Rapid Calculation of Potential Anomalies. *Geophysical Journal International*, 31(4), 447–455. <https://doi.org/10.1111/j.1365-246X.1973.tb06513.x> (cit. on p. 106)
- 5425 Pašteka, R., Mikuška, J., & Meurers, B. (2017). *Understanding the Bouguer Anomaly*. Elsevier.  
 5426 <https://doi.org/10.1016/B978-0-12-812913-5.00008-7>. (Cit. on p. 94)
- 5427 Patterson, M. O., Levy, R. H., Kulhanek, D. K., van de Flierdt, T., Horgan, H., Dunbar, G. B.,  
 5428 Naish, T. R., Ash, J., Pyne, A., Mandeno, D., Winberry, P., Harwood, D. M., Florindo,  
 5429 F., Jimenez-Espejo, F. J., Läufer, A., Yoo, K.-C., Seki, O., Stocchi, P., Klages, J. P., ...  
 5430 the SWAIS 2C Science Team. (2022). Sensitivity of the West Antarctic Ice Sheet to +2  
 5431 °C (SWAIS 2C). *Scientific Drilling*, 30, 101–112. <https://doi.org/10.5194/sd-30-101-2022>  
 5432 (cit. on pp. 18, 21)
- 5433 Paulsen, T., Encarnación, J., & Grunow, A. (2004). Structure and timing of transpressional deformation in the Shackleton Glacier area, Ross orogen, Antarctica. *Journal of the Geological Society*, 161(6), 1027–1038. <https://doi.org/10.1144/0016-764903-040> (cit. on p. 34)
- 5436 Paxman, G. J. G., Jamieson, S. S., Hochmuth, K., Gohl, K., Bentley, M. J., Leitchenkov, G., &  
 5437 Ferraccioli, F. (2019). Reconstructions of Antarctic topography since the Eocene–Oligocene

- boundary. *Palaeogeography, Palaeoclimatology, Palaeoecology*, 535, 109346. <https://doi.org/10.1016/j.palaeo.2019.109346> (cit. on pp. 26, 34, 147, 155)
- Pekar, S. F., DeConto, R. M., & Harwood, D. M. (2006). Resolving a late Oligocene conundrum: Deep-sea warming and Antarctic glaciation. *Palaeogeography, Palaeoclimatology, Palaeoecology*, 231, 29–40. <https://doi.org/10.1016/j.palaeo.2005.07.024> (cit. on p. 34)
- Peltier, W. R., Wu, P. P.-C., Argus, D. F., Li, T., & Velay-Vitow, J. (2022). Glacial isostatic adjustment: Physical models and observational constraints. *Reports on Progress in Physics*, 85(9), 096801. <https://doi.org/10.1088/1361-6633/ac805b> (cit. on pp. 19, 143)
- Pérez, F., & Granger, B. E. (2007). IPython: A system for interactive scientific computing. *Computing in Science and Engineering*, 9(3), 21–29. <https://doi.org/10.1109/MCSE.2007.53> (cit. on p. 51)
- Pérez, L. F., De Santis, L., McKay, R. M., Larter, R. D., Ash, J., Bart, P. J., Böhm, G., Brancatelli, G., Browne, I., Colleoni, F., Dodd, J. P., Geletti, R., Harwood, D. M., Kuhn, G., Sverre Laberg, J., Leckie, R. M., Levy, R. H., Marschalek, J., Mateo, Z., ... 374 Scientists, I. O. D. P. E. (2021). Early and middle Miocene ice sheet dynamics in the Ross Sea: Results from integrated core-log-seismic interpretation. *GSA Bulletin*. <https://doi.org/10.1130/B35814.1> (cit. on p. 26)
- Perozzi, L., Guglielmetti, L., & Moscariello, A. (2021). Quantitative uncertainty analysis of gravity disturbance. The case of the Geneva Basin (Switzerland). *Journal of Applied Geophysics*, 193, 104431. <https://doi.org/10.1016/j.jappgeo.2021.104431> (cit. on p. 85)
- Phillips, G., & Läufer, A. (2009). Brittle deformation relating to the Carboniferous–Cretaceous evolution of the Lambert Graben, East Antarctica: A precursor for Cenozoic relief development in an intraplate and glaciated region. *Tectonophysics*, 471(3-4), 216–224. <https://doi.org/10.1016/j.tecto.2009.02.012> (cit. on p. 33)
- Pollard, D., DeConto, R. M., & Nyblade, A. A. (2005). Sensitivity of Cenozoic Antarctic ice sheet variations to geothermal heat flux. *Global and Planetary Change*, 49(1-2), 63–74. <https://doi.org/10.1016/j.gloplacha.2005.05.003> (cit. on pp. 18, 144)
- Pritchard, H. D., Ligtenberg, S. R. M., Fricker, H. A., Vaughan, D. G., van den Broeke, M. R., & Padman, L. (2012). Antarctic ice-sheet loss driven by basal melting of ice shelves. *Nature*, 484(7395), 502–505. <https://doi.org/10.1038/nature10968> (cit. on pp. 38, 90)
- Rashidifard, M., Giraud, J., Lindsay, M., Jessell, M., & Ogarko, V. (2021). Constraining 3D geometric gravity inversion with a 2D reflection seismic profile using a generalized level set approach: Application to the eastern Yilgarn Craton. *Solid Earth*, 12(10), 2387–2406. <https://doi.org/10.5194/se-12-2387-2021> (cit. on p. 55)
- Ravier, E., & Buonchristiani, J.-F. (2018). Glaciohydrogeology. In *Past Glacial Environments* (pp. 431–466). Elsevier. <https://doi.org/10.1016/B978-0-08-100524-8.00013-0>. (Cit. on pp. 19, 33)
- Rignot, E., Jacobs, S., Mouginot, J., & Scheuchl, B. (2013). Ice-Shelf Melting Around Antarctica. *Science*, 341(6143), 266–270. <https://doi.org/10.1126/science.1235798> (cit. on pp. 16, 20, 27, 90, 108, 137, 157, 160)
- Rignot, E., Mouginot, J., & Scheuchl, B. (2011). Antarctic grounding line mapping from differential satellite radar interferometry. *Geophysical Research Letters*, 38, 1–6. <https://doi.org/10.1029/2011GL047109> (cit. on pp. 20, 137)
- Rignot, E., Mouginot, J., Scheuchl, B., van den Broeke, M., van Wessem, M. J., & Morlighem, M. (2019). Four decades of Antarctic Ice Sheet mass balance from 1979–2017. *Proceedings of the National Academy of Sciences*, 116(4), 1095–1103. <https://doi.org/10.1073/pnas.1812883116> (cit. on p. 38)
- Robertson, J. D., & Bentley, C. R. (1989). The Ross Ice Shelf: Glaciology and geophysics paper 3: Seismic studies on the grid western half of the Ross Ice Shelf: RIGGS I and RIGGS II. In C. R. Bentley & D. E. Hayes (Eds.), *Antarctic Research Series* (pp. 55–86). American Geophysical Union. <https://doi.org/10.1029/AR042p0055>. (Cit. on p. 156)
- Rooney, S. T., Blankenship, D. D., & Bentley, C. R. (1987). Seismic refraction measurements of crustal structure in West Antarctica. In G. D. McKenzie (Ed.), *Geophysical Monograph Series* (pp. 1–7). American Geophysical Union. <https://doi.org/10.1029/GM040p0001>. (Cit. on p. 156)
- Rosier, S. H. R., Hofstede, C., Brisbourne, A. M., Hattermann, T., Nicholls, K. W., Davis, P. E. D., Anker, P. G. D., Hillenbrand, C.-D., Smith, A. M., & Corr, H. F. J. (2018). A New Bathymetry for the Southeastern Filchner-Ronne Ice Shelf: Implications for Modern Oceanographic Processes and Glacial History. *Journal of Geophysical Research: Oceans*, 123(7), 4610–4623. <https://doi.org/10.1029/2018JC013982> (cit. on p. 149)

- 5497 Roy, L., Sen, M. K., Blankenship, D. D., Stoffa, P. L., & Richter, T. G. (2005). Inversion and  
 5498 uncertainty estimation of gravity data using simulated annealing: An application over Lake  
 5499 Vostok, East Antarctica. *Geophysics*, 70(1), J1–J12. <https://doi.org/10.1190/1.1852777>  
 5500 (cit. on p. 106)
- 5501 Salvini, F., Brancolini, G., Busetti, M., Storti, F., Mazzarini, F., & Coren, F. (1997). Cenozoic  
 5502 geodynamics of the Ross Sea region, Antarctica: Crustal extension, intraplate strike-slip  
 5503 faulting, and tectonic inheritance. *Journal of Geophysical Research: Solid Earth*, 102(B11),  
 5504 24669–24696. <https://doi.org/10.1029/97JB01643> (cit. on pp. 30, 31)
- 5505 Sandwell, D. T. (1987). Biharmonic spline interpolation of GEOS-3 and SEASAT altimeter data.  
 5506 *Geophysical Research Letters*, 14(2), 139–142. <https://doi.org/10.1029/GL014i002p00139>  
 5507 (cit. on pp. 62, 63, 100, 108)
- 5508 Santos, D. F., Silva, J. B. C., Martins, C. M., dos Santos, R. D. C. S., Ramos, L. C., & de  
 5509 Araújo, A. C. M. (2015). Efficient gravity inversion of discontinuous basement relief. *GEO-  
 5510 PHYSICS*, 80(4), G95–G106. <https://doi.org/10.1190/geo2014-0513.1> (cit. on pp. 42,  
 5511 106)
- 5512 Sauli, C., Sorlien, C., Busetti, M., De Santis, L., Geletti, R., Wardell, N., & Luyendyk, B. P. (2021).  
 5513 Neogene development of the Terror Rift, western Ross Sea, Antarctica. *Geochemistry,  
 5514 Geophysics, Geosystems*, 22(3). <https://doi.org/10.1029/2020GC009076> (cit. on pp. 30,  
 5515 32)
- 5516 Scambos, T. A., Bohlander, J., Shuman, C., & Skvarca, P. (2004). Glacier acceleration and thin-  
 5517 ning after ice shelf collapse in the Larsen B embayment, Antarctica. *Geophysical Research  
 5518 Letters*, 31(18), L18402. <https://doi.org/10.1029/2004GL020670> (cit. on p. 90)
- 5519 Scambos, T., Haran, T., Fahnestock, M., Painter, T., & Bohlander, J. (2007). MODIS-based Mosaic  
 5520 of Antarctica (MOA) data sets: Continent-wide surface morphology and snow grain size.  
 5521 *Remote Sensing of Environment*, 111(2-3), 242–257. <https://doi.org/10.1016/j.rse.2006.12.020> (cit. on pp. 27, 91, 113, 117, 118, 125, 130, 132, 139)
- 5522 Scheinert, M., Ferraccioli, F., Schwabe, J., Bell, R., Studinger, M., Damaske, D., Jokat, W.,  
 5523 Aleshkova, N., Jordan, T., Leitchenkov, G., Blankenship, D. D., Damiani, T. M., Young,  
 5524 D., Cochran, J. R., & Richter, T. D. (2016). New Antarctic gravity anomaly grid for  
 5525 enhanced geodetic and geophysical studies in Antarctica. *Geophysical Research Letters*,  
 5526 43(2), 600–610. <https://doi.org/10.1002/2015GL067439> (cit. on p. 149)
- 5527 Schlegel, N.-J., Seroussi, H., Schodlok, M. P., Larour, E. Y., Boening, C., Limonadi, D., Watkins,  
 5528 M. M., Morlighem, M., & van den Broeke, M. R. (2018). Exploration of Antarctic Ice Sheet  
 5529 100-year contribution to sea level rise and associated model uncertainties using the ISSM  
 5530 framework. *The Cryosphere*, 12(11), 3511–3534. <https://doi.org/10.5194/tc-12-3511-2018>  
 5531 (cit. on p. 15)
- 5532 Schnaidt, S., & Heinson, G. (2015). Bootstrap resampling as a tool for uncertainty analysis in 2-D  
 5533 magnetotelluric inversion modelling. *Geophysical Journal International*, 203(1), 92–106.  
 5534 <https://doi.org/10.1093/gji/ggv264> (cit. on pp. 73, 101)
- 5535 Schön, J. H. (2015). Density. In *Developments in Petroleum Science* (pp. 109–118). Elsevier. <https://doi.org/10.1016/B978-0-08-100404-3.00004-4>. (Cit. on pp. 112, 116, 129)
- 5536 Seroussi, H., Ivins, E. R., Wiens, D. A., & Bondzio, J. (2017). Influence of a West Antarctic mantle  
 5537 plume on ice sheet basal conditions. *Journal of Geophysical Research: Solid Earth*, 122(9),  
 5538 7127–7155. <https://doi.org/10.1002/2017JB014423> (cit. on p. 144)
- 5539 Shen, W., Wiens, D. A., Anandakrishnan, S., Aster, R. C., Gerstoft, P., Bromirski, P. D., Hansen,  
 5540 S. E., Dalziel, I. W. D., Heeszel, D. S., Huerta, A. D., Nyblade, A. A., Stephen, R., Wilson,  
 5541 T. J., & Winberry, J. P. (2018a). The crust and upper mantle structure of Central and  
 5542 West Antarctica from bayesian inversion of Rayleigh wave and receiver functions. *Journal  
 5543 of Geophysical Research: Solid Earth*, 123(9), 7824–7849. <https://doi.org/10.1029/2017JB015346> (cit. on pp. 32, 35)
- 5544 Shen, W., Wiens, D. A., Lloyd, A. J., & Nyblade, A. A. (2020). A geothermal heat flux map  
 5545 of Antarctica empirically constrained by seismic structure. *Geophysical Research Letters*,  
 5546 47(14). <https://doi.org/10.1029/2020GL086955> (cit. on pp. 139, 145)
- 5547 Shen, W., Wiens, D. A., Stern, T., Anandakrishnan, S., Aster, R. C., Dalziel, I., Hansen, S., Heeszel,  
 5548 D. S., Huerta, A., Nyblade, A., Wilson, T. J., & Winberry, J. P. (2018b). Seismic evidence  
 5549 for lithospheric foundering beneath the southern Transantarctic Mountains, Antarctica.  
 5550 *Geology*, 46(1), 71–74. <https://doi.org/10.1130/G39555.1> (cit. on p. 33)
- 5551 Shipp, S., Anderson, J., & Domack, E. (1999). Late Pleistocene-Holocene retreat of the West  
 5552 Antarctic Ice-Sheet system in the Ross Sea: Part 1 - Geophysical results. *Geological Society*

- 5556       of America Bulletin, 111(10), 32. <https://doi.org/10.1130/0016-7606%281999%29111%3C1486%3ALPHROT%3E2.3.CO%3B2> (cit. on p. 16)
- 5557       Siddoway, C. S. (2008). Tectonics of the West Antarctic Rift System: New light on the history  
5558       and dynamics of distributed intracontinental extension. In A. K. Cooper, P. J. Barrett, H.  
5559       Stagg, B. C. Storey, W. Stump, W. Wise, & 10th ISAES editorial team (Eds.), *Antarctica: A  
5560       Keystone in a Changing World*. The National Academies Press. <https://doi.org/10.3133/ofr20071047KP09>. (Cit. on p. 30)
- 5561       Siegent, M. J., Kulessa, B., Bougamont, M., Christoffersen, P., Key, K., Andersen, K. R., Booth,  
5562       A. D., & Smith, A. M. (2018). Antarctic subglacial groundwater: A concept paper on  
5563       its measurement and potential influence on ice flow. *Geological Society, London, Special  
5564       Publications*, 461(1), 197–213. <https://doi.org/10.1144/SP461.8> (cit. on p. 26)
- 5565       Siegent, M. J., Taylor, J., Payne, A. J., & Hubbard, B. (2004). Macro-scale bed roughness of the  
5566       simple coast ice streams in West Antarctica. *Earth Surface Processes and Landforms*, 29(13),  
5567       1591–1596. <https://doi.org/10.1002/esp.1100> (cit. on p. 20)
- 5568       Slater, T., & Shepherd, A. (2018). Antarctic ice losses tracking high. *Nature Climate Change*,  
5569       8(12), 1025–1026. <https://doi.org/10.1038/s41558-018-0284-9> (cit. on p. 15)
- 5570       Smith, B., Fricker, H. A., Gardner, A. S., Medley, B., Nilsson, J., Paolo, F. S., Holschuh, N.,  
5571       Adusumilli, S., Brunt, K., Csatho, B., Harbeck, K., Markus, T., Neumann, T., Siegfried,  
5572       M. R., & Zwally, H. J. (2020a). Pervasive ice sheet mass loss reflects competing ocean and  
5573       atmosphere processes. *Science*, eaaz5845. <https://doi.org/10.1126/science.aaz5845> (cit. on  
5574       p. 38)
- 5575       Smith, E. C., Hattermann, T., Kuhn, G., Gaedicke, C., Berger, S., Drews, R., Ehlers, T. A.,  
5576       Franke, D., Gromig, R., Hofstede, C., Lambrecht, A., Läufer, A., Mayer, C., Tiedemann,  
5577       R., Wilhelms, F., & Eisen, O. (2020b). Detailed Seismic Bathymetry Beneath Ekström Ice  
5578       Shelf, Antarctica: Implications for Glacial History and Ice-Ocean Interaction. *Geophysical  
5579       Research Letters*, 47(10). <https://doi.org/10.1029/2019GL086187> (cit. on p. 121)
- 5580       Smith, W. H. F., & Wessel, P. (1990). Gridding with continuous curvature splines in tension.  
5581       *GEOPHYSICS*, 55(3), 293–305. <https://doi.org/10.1190/1.1442837> (cit. on pp. 60, 62,  
5582       63, 99, 100, 108, 122, 155)
- 5583       Soler, S. R., & Uieda, L. (2021). Gradient-boosted equivalent sources. *Geophysical Journal  
5584       International*, 227(3), 1768–1783. <https://doi.org/10.1093/gji/ggab297> (cit. on pp. 51, 57, 60,  
5585       112)
- 5586       Sorlien, C. C., Luyendyk, B., Wilson, D. S., Decesari, R. C., Bartek, L. R., & Diebold, J. B.  
5587       (2007). Oligocene development of the West Antarctic Ice Sheet recorded in eastern Ross  
5588       Sea strata. *Geology*, 35(5), 467. <https://doi.org/10.1130/G23387A.1> (cit. on p. 26)
- 5589       Spector, P., Stone, J., Cowdery, S. G., Hall, B., Conway, H., & Bromley, G. (2017). Rapid early-  
5590       Holocene deglaciation in the Ross Sea, Antarctica. *Geophysical Research Letters*, 44(15),  
5591       7817–7825. <https://doi.org/10.1002/2017GL074216> (cit. on p. 90)
- 5592       Steffen, H., Olesen, O., & Sutinen, R. (2021). Glacially Triggered Faulting: A Historical Overview  
5593       and Recent Developments. In H. Steffen, O. Olesen, & R. Sutinen (Eds.), *Glacially  
5594       Triggered Faulting* (First, pp. 3–19). Cambridge University Press. <https://doi.org/10.1017/9781108779906.003>. (Cit. on pp. 19, 143)
- 5595       Stern, T. A., Davey, F. J., & Delisle, G. (1991). Lithospheric flexure induced by the load of the  
5596       Ross Archipelago, southern Victoria land, Antarctica. In M. Thomson, A. Crame, & J.  
5597       Thomson (Eds.), *Geological Evolution of Antarctica* (pp. 323–328). Cambridge University  
5598       Press. (Cit. on p. 31).
- 5599       Stern, T. A., Ten Brink, U. S., Beaudoin, B. C., & Bannister, S. (1994). Seismic Reflection Experiments  
5600       on the Ross Ice Shelf: 1985-1991. *Terra Antarctica*, 1(3), 513–516 (cit. on p. 21).
- 5601       Stern, T. A., & ten Brink, U. S. (1989). Flexural uplift of the Transantarctic Mountains. *Journal  
5602       of Geophysical Research: Solid Earth*, 94(B8), 10315–10330. <https://doi.org/10.1029/JB094iB08p10315> (cit. on p. 133)
- 5603       Stevens, C., Hulbe, C., Brewer, M., Stewart, C., Robinson, N., Ohneiser, C., & Jendersie, S. (2020).  
5604       Ocean mixing and heat transport processes observed under the Ross Ice Shelf control its  
5605       basal melting. *Proceedings of the National Academy of Sciences*, 117(29), 16799–16804.  
5606       <https://doi.org/10.1073/pnas.1910760117> (cit. on p. 91)
- 5607       Still, H., Campbell, A., & Hulbe, C. (2019). Mechanical analysis of pinning points in the Ross Ice  
5608       Shelf, Antarctica. *Annals of Glaciology*, 60(78), 32–41. <https://doi.org/10.1017/aog.2018.31> (cit. on pp. 20, 26, 33, 91, 131, 142, 143)

- 5614 Still, H., & Hulbe, C. (2021). Mechanics and dynamics of pinning points on the Shirase Coast,  
 5615 West Antarctica. *The Cryosphere*, 15(6), 19. <https://doi.org/10.5194/tc-15-2647-2021>  
 5616 (cit. on p. 142)
- 5617 St-Laurent, P., Klinck, J. M., & Dinniman, M. S. (2013). On the Role of Coastal Troughs in the  
 5618 Circulation of Warm Circumpolar Deep Water on Antarctic Shelves. *Journal of Physical*  
 5619 *Oceanography*, 43(1), 51–64. <https://doi.org/10.1175/JPO-D-11-0237.1> (cit. on p. 38)
- 5620 Studinger, M., Bell, R., Fitzgerald, P., & Buck, W. (2006). Crustal architecture of the Transantarctic  
 5621 Mountains between the Scott and Reedy Glacier region and South Pole from aerogeophysical data.  
 5622 *Earth and Planetary Science Letters*, 250(1-2), 182–199. [https://doi.org/](https://doi.org/10.1016/j.epsl.2006.07.035)  
 5623 10.1016/j.epsl.2006.07.035 (cit. on p. 34)
- 5624 Studinger, M., Bell, R. E., Buck, W., Karner, G. D., & Blankenship, D. D. (2004a). Sub-ice geology  
 5625 inland of the Transantarctic Mountains in light of new aerogeophysical data. *Earth and*  
 5626 *Planetary Science Letters*, 220(3-4), 391–408. [https://doi.org/10.1016/S0012-821X\(04\)](https://doi.org/10.1016/S0012-821X(04)00066-4)  
 5627 00066-4 (cit. on pp. 28, 153)
- 5628 Studinger, M., Bell, R. E., & Tikku, A. A. (2004b). Estimating the depth and shape of subglacial  
 5629 Lake Vostok's water cavity from aerogravity data: ESTIMATING LAKE VOSTOK'S WA-  
 5630 TER DEPTH. *Geophysical Research Letters*, 31(12), n/a–n/a. [https://doi.org/10.1029/](https://doi.org/10.1029/2004GL019801)  
 5631 2004GL019801 (cit. on pp. 106, 120)
- 5632 Studinger, M., & Miller, H. (1999). Crustal structure of the Filchner-Ronne Shelf and Coats Land,  
 5633 Antarctica, from gravity and magnetic data: Implications for the breakup of Gondwana.  
 5634 *Journal of Geophysical Research: Solid Earth*, 104(B9), 20379–20394. <https://doi.org/10.1029/1999JB900117> (cit. on p. 149)
- 5635 Talwani, M., Worzel, J. L., & Landisman, M. (1959). Rapid gravity computations for two-dimensional  
 5636 bodies with application to the Mendocino submarine fracture zone. *Journal of Geophysical*  
 5637 *Research*, 64(1), 49–59. <https://doi.org/10.1029/JZ064i001p00049> (cit. on p. 106)
- 5638 Tankersley, M., Horgan, H. J., Siddoway, C. S., Caratori Tontini, F., & Tinto, K. J. (2022). Basement  
 5639 Topography and Sediment Thickness Beneath Antarctica's Ross Ice Shelf. *Geophysical*  
 5640 *Research Letters*, 49(10). <https://doi.org/10.1029/2021GL097371> (cit. on pp. 22, 115,  
 5641 129, 133, 151)
- 5642 Tankersley, M. D. (2023). Antarctic\_plots: V0.0.6. <https://doi.org/10.5281/zenodo.7750998>.  
 5643 (Cit. on pp. 23, 51, 171)
- 5644 Tankersley, M. (2022). Mdtanker/RIS\_basement\_sediment: V2.0. <https://doi.org/10.5281/zenodo.6499863>. (Cit. on p. 23)
- 5645 Tankersley, M., Horgan, H., & Caratori-Tontini, F. (2023). Mdtanker/RIS\_gravity\_inversion:  
 5646 First release associated with PhD thesis. <https://doi.org/10.5281/zenodo.8084469>.  
 5647 (Cit. on p. 23)
- 5648 Tarantola, A. (2005). *Inverse Problem Theory and Methods for Model Parameter Estimation*. Society  
 5649 for Industrial and Applied Mathematics. <https://doi.org/10.1137/1.9780898717921>.  
 5650 (Cit. on p. 39)
- 5651 ten Brink, U. S., Bannister, S., Beaudoin, B. C., & Stern, T. A. (1993). Geophysical investigations  
 5652 of the tectonic boundary between East and West Antarctica. *Science*, 261(5117), 45–50.  
 5653 <https://doi.org/10.1126/science.261.5117.45> (cit. on pp. 21, 31, 133)
- 5654 Thomas, R. H. (1979). Ice Shelves: A Review. *Journal of Glaciology*, 24(90), 273–286. <https://doi.org/10.3189/S002214300014799> (cit. on p. 17)
- 5655 Timmermann, R., Brocq, A. L., Deen, T., Domack, E., Dutrieux, P., Galton-Fenzi, B., Hellmer,  
 5656 H., Humbert, A., Jansen, D., Jenkins, A., Lambrecht, A., Makinson, K., Niederjasper, F.,  
 5657 Nitsche, F., Nøst, O. A., Smedsrød, L. H., & Smith, W. H. F. (2010). A consistent data set  
 5658 of Antarctic ice sheet topography, cavity geometry, and global bathymetry. *Earth System*  
 5659 *Science Data*, 2(2), 13. <https://doi.org/10.5194/essd-2-261-2010> (cit. on pp. 91, 124)
- 5660 Tinto, K. J., & Bell, R. E. (2011). Progressive unpinning of Thwaites Glacier from newly identified  
 5661 offshore ridge: Constraints from aerogravity. *Geophysical Research Letters*, 38, 1–6. <https://doi.org/10.1029/2011GL049026> (cit. on pp. 46, 105, 106, 120, 149)
- 5662 Tinto, K. J., Padman, L., Siddoway, C. S., Springer, S. R., Fricker, H. A., Das, I., Caratori Tontini,  
 5663 F., Porter, D. F., Frearson, N. P., Howard, S. L., Siegfried, M. R., Mosbeux, C., Becker,  
 5664 M. K., Bertinato, C., Boghosian, A., Brady, N., Burton, B. L., Chu, W., Cordero, S. I.,  
 5665 ... Bell, R. E. (2019). Ross Ice Shelf response to climate driven by the tectonic imprint on  
 5666 seafloor bathymetry. *Nature Geoscience*, 12(6), 441–449. <https://doi.org/10.1038/s41561-019-0370-2> (cit. on pp. 20, 21, 26–28, 30, 32, 34, 38, 46, 68, 90–92, 104, 105, 107, 108, 111,  
 5667 120, 122, 124, 126, 129, 131, 132, 134, 137–141, 148, 152, 156, 157)

- 5673 Tinto, K. J., Bell, R. E., Cochran, J. R., & Münchow, A. (2015). Bathymetry in Petermann fjord  
 5674 from Operation IceBridge aerogravity. *Earth and Planetary Science Letters*, 422, 58–66.  
 5675 <https://doi.org/10.1016/j.epsl.2015.04.009> (cit. on pp. 16, 45, 46, 105, 106, 120)
- 5676 Tulaczyk, S., Kamb, W. B., & Engelhardt, H. F. (2000). Basal mechanics of Ice Stream B, west  
 5677 Antarctica: 2. Undrained plastic bed model. *Journal of Geophysical Research: Solid Earth*,  
 5678 105(B1), 483–494. <https://doi.org/10.1029/1999JB900328> (cit. on pp. 18, 144)
- 5679 Uieda, L. (2018). Verde: Processing and gridding spatial data using Green's functions. *Journal of  
 5680 Open Source Software*, 3(29), 957. <https://doi.org/10.21105/joss.00957> (cit. on pp. 51, 60,  
 5681 61, 63, 70, 99)
- 5682 Uieda, L., & Barbosa, V. C. (2017). Fast nonlinear gravity inversion in spherical coordinates with  
 5683 application to the South American Moho. *Geophysical Journal International*, 208(1), 162–  
 5684 176. <https://doi.org/10.1093/gji/ggw390> (cit. on pp. 42, 48, 49, 53, 55, 85, 100, 106, 149)
- 5685 Uieda, L., Soler, S., Rampin, R., van Kemenade, H., Turk, M., Shapero, D., Banihirwe, A., & Lee-  
 5686 man, J. (2020). Pooch: A friend to fetch your data files. *Journal of Open Source Software*,  
 5687 5(45), 1943. <https://doi.org/10.21105/joss.01943> (cit. on p. 171)
- 5688 Uieda, L., Tian, D., Leong, W. J., Jones, M., Schlitzer, W., Toney, L., Grund, M., Yao, J., Magen,  
 5689 Y., Materna, K., Newton, T., Anant, A., Ziebarth, M., Wessel, P., & Quinn, J. (2021).  
 5690 PyGMT: A Python interface for the Generic Mapping Tools. <https://doi.org/10.5281/zenodo.5607255>. (Cit. on pp. 36, 51, 172)
- 5692 Vajda, P., Ellmann, A., Meurers, B., Vaníček, P., Novák, P., & Tenzer, R. (2008a). Global ellipsoid-  
 5693 referenced topographic, bathymetric and stripping corrections to gravity disturbance. *Stu-  
 5694 dia Geophysica et Geodaetica*, 52(1), 19–34. <https://doi.org/10.1007/s11200-008-0003-5>  
 5695 (cit. on p. 104)
- 5696 Vajda, P., Ellmann, A., Meurers, B., Vaníček, P., Novák, P., & Tenzer, R. (2008b). Gravity dis-  
 5697 turbances in regions of negative heights: A reference quasi-ellipsoid approach. *Stu-  
 5698 dia Geophysica et Geodaetica*, 52(1), 35–52. <https://doi.org/10.1007/s11200-008-0004-4> (cit. on  
 5699 p. 94)
- 5700 Vajda, P., Vaníček, P., & Meurers, B. (2006). A new physical foundation for anomalous gravity.  
 5701 *Stu- dia Geophysica et Geodaetica*, 50(2), 189–216. <https://doi.org/10.1007/s11200-006-0012-1> (cit. on p. 96)
- 5703 Vajda, P., Vaníček, P., Novák, P., Tenzer, R., & Ellmann, A. (2007). Secondary indirect effects  
 5704 in gravity anomaly data inversion or interpretation. *Journal of Geophysical Research*,  
 5705 112(B6), B06411. <https://doi.org/10.1029/2006JB004470> (cit. on pp. 95, 103)
- 5706 Vajda, P., Vaníček, P., & Meurers, B. (2004). On the removal of the effect of topography on gravity  
 5707 disturbance in gravity data inversion or interpretation. *Contributions to Geophysics and  
 5708 Geodesy*, 34 (cit. on p. 94).
- 5709 Vaňková, I., Winberry, J. P., Cook, S., Nicholls, K. W., Greene, C. A., & Galton-Fenzi, B. K. (2023).  
 5710 High Spatial Melt Rate Variability Near the Totten Glacier Grounding Zone Explained by  
 5711 New Bathymetry Inversion. *Geophysical Research Letters*, 50(10), e2023GL102960. <https://doi.org/10.1029/2023GL102960> (cit. on pp. 105, 106)
- 5713 Venturelli, R. A., Siegfried, M. R., Roush, K. A., Li, W., Burnett, J., Zook, R., Fricker, H. A., Priscu,  
 5714 J. C., Leventer, A., & Rosenheim, B. E. (2020). Mid-Holocene grounding line retreat and  
 5715 readvance at Whillans Ice Stream, West Antarctica. *Geophysical Research Letters*, 47(15).  
 5716 <https://doi.org/10.1029/2020GL088476> (cit. on pp. 20, 32, 33, 36, 90, 131, 137)
- 5717 Virtanen, P., Gommers, R., Oliphant, T. E., Haberland, M., Reddy, T., Cournapeau, D., Burovski,  
 5718 E., Peterson, P., Weckesser, W., Bright, J., van der Walt, S. J., Brett, M., Wilson, J.,  
 5719 Millman, K. J., Mayorov, N., Nelson, A. R. J., Jones, E., Kern, R., Larson, E., ... SciPy  
 5720 1.0 Contributors. (2020). SciPy 1.0: Fundamental algorithms for scientific computing in  
 5721 python. *Nature Methods*, 17, 261–272. <https://doi.org/10.1038/s41592-019-0686-2> (cit. on  
 5722 p. 51)
- 5723 Wannamaker, P., Hill, G., Stodt, J., Maris, V., Ogawa, Y., Selway, K., Boren, G., Bertrand,  
 5724 E., Uhlmann, D., Ayling, B., Green, A. M., & Feucht, D. (2017). Uplift of the central  
 5725 transantarctic mountains. *Nature Communications*, 8(1), 1588. <https://doi.org/10.1038/s41467-017-01577-2> (cit. on pp. 21, 133)
- 5727 Wei, W., Blankenship, D. D., Greenbaum, J. S., Gourmelen, N., Dow, C. F., Richter, T. G., Greene,  
 5728 C. A., Young, D. A., Lee, S., Kim, T.-W., Lee, W. S., & Assmann, K. M. (2020). Getz Ice  
 5729 Shelf melt enhanced by freshwater discharge from beneath the West Antarctic Ice Sheet.  
 5730 *The Cryosphere*, 14(4), 1399–1408. <https://doi.org/10.5194/tc-14-1399-2020> (cit. on  
 5731 pp. 105, 106, 120, 148)

- 5732 Werner, S. (1953). Interpretation of magnetic anomalies at sheet-like bodies. In *Sveriges Geologiska  
5733 Undersök* (pp. 413–449). Stockholm Norstedt. (Cit. on pp. 28, 152).
- 5734 Wessel, P., Luis, J. F., Uieda, L., Scharroo, R., Wobbe, F., Smith, W. H. F., & Tian, D. (2019).  
5735 The Generic Mapping Tools version 6. *Geochemistry, Geophysics, Geosystems*, 20(11),  
5736 5556–5564. <https://doi.org/10.1029/2019GC008515> (cit. on pp. 36, 63)
- 5737 Wessel, P., & Bercovici, D. (1998). Interpolation with splines in tension: A Green's function ap-  
5738 proach. *Mathematical Geology*, 30(1), 77–93. <https://doi.org/10.1023/A:1021713421882>  
5739 (cit. on p. 63)
- 5740 White-Gaynor, A. L., Nyblade, A. A., Aster, R. C., Wiens, D. A., Bromirski, P. D., Gerstoft, P.,  
5741 Stephen, R. A., Hansen, S. E., Wilson, T., Dalziel, I. W., Huerta, A. D., Paul Winberry,  
5742 J., & Anandakrishnan, S. (2019). Heterogeneous upper mantle structure beneath the Ross  
5743 Sea Embayment and Marie Byrd Land, West Antarctica, revealed by P-wave tomography.  
5744 *Earth and Planetary Science Letters*, 513, 40–50. <https://doi.org/10.1016/j.epsl.2019.02.013> (cit. on p. 34)
- 5745 Whitehouse, P. L., Gomez, N., King, M. A., & Wiens, D. A. (2019). Solid Earth change and the  
5746 evolution of the Antarctic Ice Sheet. *Nature Communications*, 10(1), 503. <https://doi.org/10.1038/s41467-018-08068-y> (cit. on pp. 19, 33)
- 5747 Wilkinson, M. D., Dumontier, M., Aalbersberg, I. J., Appleton, G., Axton, M., Baak, A., Blomberg,  
5748 N., Boiten, J.-W., da Silva Santos, L. B., Bourne, P. E., Bouwman, J., Brookes, A. J., Clark,  
5749 T., Crosas, M., Dillo, I., Dumon, O., Edmunds, S., Evelo, C. T., Finkers, R., ... Mons,  
5750 B. (2016). The FAIR Guiding Principles for scientific data management and stewardship.  
5751 *Scientific Data*, 3(1), 160018. <https://doi.org/10.1038/sdata.2016.18> (cit. on p. 23)
- 5752 Wilson, D. S., Jamieson, S. S., Barrett, P. J., Leitchenkov, G., Gohl, K., & Larter, R. D. (2012).  
5753 Antarctic topography at the Eocene–Oligocene boundary. *Palaeogeography, Palaeoclima-  
5754 tology, Palaeoecology*, 335–336, 24–34. <https://doi.org/10.1016/j.palaeo.2011.05.028>  
5755 (cit. on pp. 34, 147, 155)
- 5756 Wilson, D. S., & Luyendyk, B. (2009). West Antarctic paleotopography estimated at the Eocene-  
5757 Oligocene climate transition. *Geophysical Research Letters*, 36(16), L16302. <https://doi.org/10.1029/2009GL039297> (cit. on pp. 26, 34, 147, 155, 157)
- 5758 Wilson, D. S., Pollard, D., DeConto, R. M., Jamieson, S. S., & Luyendyk, B. (2013). Initiation of  
5759 the West Antarctic Ice Sheet and estimates of total Antarctic ice volume in the earliest  
5760 Oligocene. *Geophysical Research Letters*, 40(16), 4305–4309. <https://doi.org/10.1002/grl.50797> (cit. on pp. 26, 34)
- 5761 Yamasaki, T., Miura, H., & Nogi, Y. (2008). Numerical modelling study on the flexural uplift of  
5762 the Transantarctic Mountains. *Geophysical Journal International*, 174(1), 377–390. <https://doi.org/10.1111/j.1365-246X.2008.03815.x> (cit. on p. 133)
- 5763 Yang, J., Guo, J., Greenbaum, J. S., Cui, X., Tu, L., Li, L., Jong, L. M., Tang, X., Li, B., Blanken-  
5764 ship, D. D., Roberts, J. L., Ommen, T., & Sun, B. (2021). Bathymetry Beneath the Amery  
5765 Ice Shelf, East Antarctica, Revealed by Airborne Gravity. *Geophysical Research Letters*,  
5766 48(24). <https://doi.org/10.1029/2021GL096215> (cit. on pp. 38, 46, 63, 104–106, 120, 122)
- 5767 Yang, J., Jekeli, C., & Liu, L. (2018). Seafloor Topography Estimation From Gravity Gradients  
5768 Using Simulated Annealing. *Journal of Geophysical Research: Solid Earth*. <https://doi.org/10.1029/2018JB015883> (cit. on p. 106)
- 5769 Yang, J., Luo, Z., & Tu, L. (2020a). Ocean Access to Zachariæ Isstrøm Glacier, Northeast Green-  
5770 land, Revealed by OMG Airborne Gravity. *Journal of Geophysical Research: Solid Earth*,  
5771 125(11). <https://doi.org/10.1029/2020JB020281> (cit. on pp. 78, 105, 106)
- 5772 Yang, J., Luo, Z., Tu, L., Li, S., Guo, J., & Fan, D. (2020b). On the Feasibility of Seafloor To-  
5773 polography Estimation from Airborne Gravity Gradients: Performance Analysis Using Real  
5774 Data. *Remote Sensing*, 12(24), 4092. <https://doi.org/10.3390/rs12244092> (cit. on p. 104)
- 5775 Yokoyama, Y., Anderson, J. B., Yamane, M., Simkins, L. M., Miyairi, Y., Yamazaki, T., Koizumi,  
5776 M., Suga, H., Kusahara, K., Prothro, L., Hasumi, H., Southon, J. R., & Ohkouchi, N.  
5777 (2016). Widespread collapse of the Ross Ice Shelf during the late Holocene. *Proceedings  
5778 of the National Academy of Sciences*, 113(9), 2354–2359. <https://doi.org/10.1073/pnas.1516908113> (cit. on p. 90)
- 5779 Zhao, C., Gladstone, R. M., Warner, R. C., King, M. A., Zwinger, T., & Morlighem, M. (2018).  
5780 Basal friction of Fleming Glacier, Antarctica – Part 1: Sensitivity of inversion to temper-  
5781 ature and bedrock uncertainty. *The Cryosphere*, 12(8), 2637–2652. <https://doi.org/10.5194/tc-12-2637-2018> (cit. on p. 15)

- 5790 Zhao, K. X., Stewart, A. L., & McWilliams, J. C. (2019). Sill-Influenced Exchange Flows in Ice Shelf  
5791 Cavities. *Journal of Physical Oceanography*, 49(1), 163–191. [https://doi.org/10.1175/JPO-](https://doi.org/10.1175/JPO-D-18-0076.1)  
5792 D-18-0076.1 (cit. on pp. 16, 91)
- 5793 Zhou, Z., Wiens, D. A., Shen, W., Aster, R. C., Nyblade, A., & Wilson, T. J. (2022). Radial  
5794 Anisotropy and Sediment Thickness of West and Central Antarctica Estimated From  
5795 Rayleigh and Love Wave Velocities. *Journal of Geophysical Research: Solid Earth*, 127(3).  
5796 <https://doi.org/10.1029/2021JB022857> (cit. on pp. 31, 156)